SOFT X-RAY MICROANALYSIS AND MICROSCOPY: A UNIQUE PROBE OF THE ORGANIC CHEMISTRY OF HETEROGENEOUS SOLIDS

G. D. Cody, R. E. Botto, H. Ade,[†] S. Wirick,[‡] A. Davis,[§] and G. Mitchell[§]
Chemistry Division, Argonne National Laboratory, Argonne IL 60439
[†]Department of Physics, North Carolina State University, Raleigh, NC 27695
[‡]Department of Physics, SUNY at Stony Brook, NY 11794
[§]Coal and Organic Petrology Labs., Pennsylvania State University, University Park, PA 16802

Keywords: X-ray microscopy, carbon, coke

INTRODUCTION

Many problems in fuel chemistry relate directly to the heterogeneous nature of materials such as coals and cokes. Recent advances in X-ray micro-focusing techniques coupled with synchrotron light sources have resulted in a scanning transmission X-ray microscope (STXM) located at the National Synchrotron Light Source at Brookhaven National Laboratory. Carbon's 1s near absorption edge region is rich with fine structure associated with photo-excited transitions to various low lying, unoccupied molecular orbitals. Preliminary carbon near edge absorption micro-spectroscopy (C-NEXAFS) and microscopy on complex organic solids such as coal has been performed using the scanning transmission microscope on the X1A beamline at NSLS. In many cases, spectacular chemical heterogeneity was observed down to the submicron level using the intensity of the prominent absorption fine structure on carbon's absorption edge for contrast.[1-3] STXM/C-NEXAFS has also been applied to biological specimen[4-6] and heterogeneous polymers.[7]

In the present paper, the STXM and C-NEXAFS microanalysis will be used to analyze the microchemistry of cokes and highly carbonaceous materials. The issue of molecular orientation will be addressed by using the intrinsic polarization of the X-ray beam at X1A.

EXPERIMENTAL

Sample: Two samples of carbonized materials were selected for STXM analysis. The first is a naturally coked coal from western Pennsylvania. The other is a laboratory derived sample of carbonized (1000 °C) pyrene.

Sample Preparation: A crucial aspect of STXM and C-NEXAFS is the necessity of preparing extremely thin specimens. The relatively high molar absorption coefficient of carbon at these wavelengths, $\mu = 1 \times 10^4$ cm^2/g, and the high bulk density of carbon in coal requires that sample thicknesses be less than 800 nm. There are a variety of methods available to obtain specimens of this thicknesses, however, ultra-microtoming was found to yield the most favorable results. Thicknesses in the range of 100 to 200 nm were readily produced. Artifacts associated with the technique, for example, scoring marks paralleling the cutting direction of the diamond knife and chatter marks perpendicular to the cutting direction, were readily identifiable.

Scanning Transmission X-ray Microscopy: The microscope, a scanning transmission X-ray microscope (STXM), is located at the terminus of the X1A beam line at the National Synchrotron Light Source (NSLS). The elements of the STXM relevant to this paper are described as follows. At the head of the instrument, soft X-rays are generated using an undulator which resides on the 2.5 GeV electron storage ring. Energy selectivity (0.3 eV resolution) is controlled with a tunable spherical monochromator. X-ray micro-focusing is managed with near field optics, i.e., a Fresnel phase zone plate and an order sorting aperture.[8] Currently, the STXM has a resolution limit of 55 nm, however, in the future, the resolution down to 10 nm may be possible.[9] X-ray transmission is detected using a gas-filled proportional counter. Details on the instrument's specifications have been reported elsewhere.[8]

C-NEXAFS: The physics of NEXAFS is similar to valence shell electronic state spectroscopy, with one important distinction, the initial state of the photo-ionized electron is in an atomic, not molecular, orbital. Herein lies the major advantage of inner shell over valence shell spectroscopy, the photo-ionized core hole is highly localized, thus, the initial orbital is more readily identified and, in principle, specific information on functional groups may be obtained. Absorption of X-rays occurs through the interaction of an X-ray photon with an electron in an atomic core resulting in the promotion of the inner shell electron to a relatively low-lying unoccupied molecular orbital (LUMO). Molecules containing π orbitals generally have their lowest energy inner shell transition to the first unoccupied, or antibonding, π^* orbital.

In alkanes, a relatively intense absorption band is observed which correspond to the transition from carbon's 1s to a 3p Rydberg-like orbital which overlaps with a C-H σ^* transition. These transitions are referred to as 1s - 3p/σ^* transitions.[10]

The intensity of a given electronic transition is a function of its dipole moment. Given some preferred orientation in a molecular assemblage, linear dichroic effects are expected and can be measured. For aromatic systems, the 1s - π^* transitions are naturally polarized in the direction of the $2p_z$ orbitals, i.e., out of the ring. The 1s - σ^* transitions are polarized parallel with the $2p_{x,y}$ plane, i.e., opposite that of the 1s - π^* transitions. Degrees of preferred orientation can be calculated from the change in intensity with orientation via the relationship,

$$I_0/I_{90} = \cot^2\alpha \qquad (1)$$

where α is the angular degree of preferred orientation, i.e., $\alpha = 45$ is completely random, while $\alpha = 0$ is perfectly aligned.

RESULTS AND DISCUSSION

Figure 1 presents a reasonably high resolution image of the naturally coked coal acquired with the monochromator tuned to the 1s - π^* transition of aromatic carbon. Clearly there is considerable microstructure which may be related to either chemistry or molecular orientation. Figure 2 presents the laboratory carbonized material. In this sample, there is also considerable microheterogeneity, with a domain scale somewhat finer than the coke (Figure 1).

The C-NEXAFS spectra of light and dark regions in Figure 1 are presented in Figure 3. At the low energy end, enormous differences in intensity of the 1s - π^* transitions are clearly evident. At the high energy end of the near edge region, the 1s - σ^* transitions also exhibit significant differences in intensity. The fact that the two types of transition exhibit a contrast reversal indicates that the differences in absorption are related to molecular orientation. Using Equation 1, we calculate an preferred orientation of 20 degrees off of completely random.

The C-NEXAFS spectra of the laboratory coke is presented in Figure 4. In this case, there are also significant differences in absorption; however, there is no contrast reversal between the 1s - π^* and 1s - σ^* transitions. This indicates that the contrast evident in Figure 2 is related to variation in the chemistry and density, but not to variations in molecular orientation.

ACKNOWLEDGMENTS

This work was performed at the National Synchrotron Light Source (NSLS) which is supported by the U.S. Department of Energy. GDC gratefully acknowledges the Chemistry Division of Argonne National Laboratory for support granted through the award of the Enrico Fermi Scholarship. GDC and REB acknowledge support from the Office of Basic Energy Sciences, Division of Chemical Sciences, U.S. Department of Energy, under contract number W-31-109-ENG-38. SW and the STXM Facility are supported by the U.S. Department of Energy, under contract number 89ER60858.

REFERENCES

1. Botto, R. E.; Cody, G. D.; Ade, H.; Behal, S.; Disko, M.; Wirick, S. *Energy Fuels*, **1994**, *8*, 152.
2. Cody, G. D.; Botto, R. E.; Ade, H.; Behal, S.; Disko, M.; Wirick, S. *Energy Fuels*, **1995a**, *9*, 75.
3. Cody, G. D.; Botto, R. E.; Ade, H.; Behal, S.; Disko, M.; Wirick, S. *Energy Fuels*, **1995b**, in press.
4. Williams, S.; Zhang, X.; Jacobsen, C.; Kirz, J.; Lindass, S.; Hof, J. V.; Lamm, S. S. *J. Microsc.*, **1993**, *170*, 155.
5. Zhang, X.; Ade, H.; Jacobsen, C.; Kirz, J.; Lindass, S.; Williams, S.; Wirick, S. *Nucl. Instr. Meth. In Phys. Res.*, **1994**, *A 347*, 431.
6. Buckley, C. J. *Bone*, **1992**, *13*, 100.
7. Ade, H.; Zhang, X.; Cameron, S.; Costello, C.; Kirz, J.; Williams, S. *Science*, **1992**, *258*, 972.
8. Jacobsen, C.; Williams, S.; Anderson, E.; Browne, M. T.; Buckley, C. J.; Kern, D.; Kirz, J.; Rivers, M.; Zhang, X. *Opt. Commun.*, **1991**, *86*, 351.
9. Ade, H. *Synchrotron Radiation News*, **1994**, *7*, 11.

10. Hitchcock, A. P.; Newbury, D. C.; Ishii, I.; Stohr, J.; Horsley, J. A.; Redwing, R. D.; Johnson, A. L.; Sette, F. *J. Chem. Phys.*, **1986**, *85*, 4849.

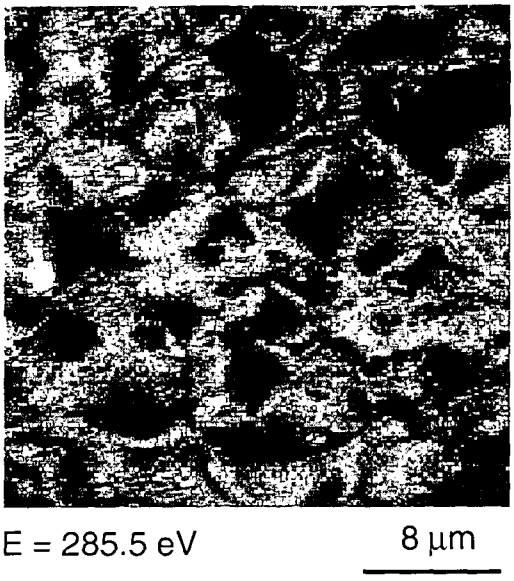

Figure 1. X-ray image of the naturally coked coal. Monochromator tuned to the aromatic 1s-pi* electronic transition.

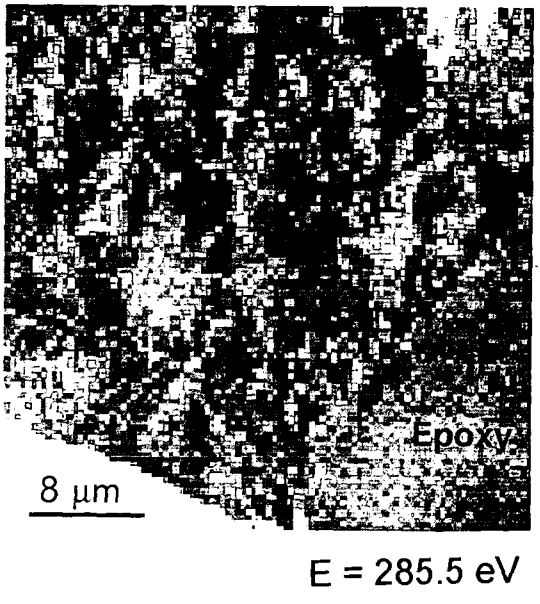

Figure 2. X-ray image of the carbonized pyrene sample. Monochromator tuned to the aromatic 1s-pi* electronic transition.

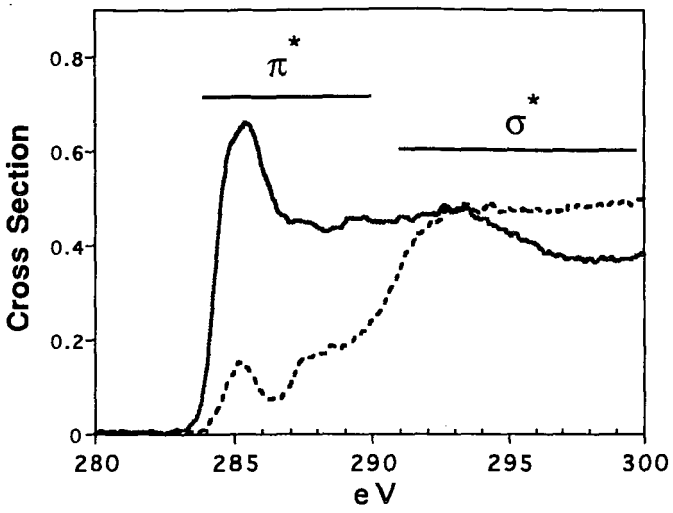

Figure 3. The C-NEXAFS spectra of light and dark regions in Figure 1.

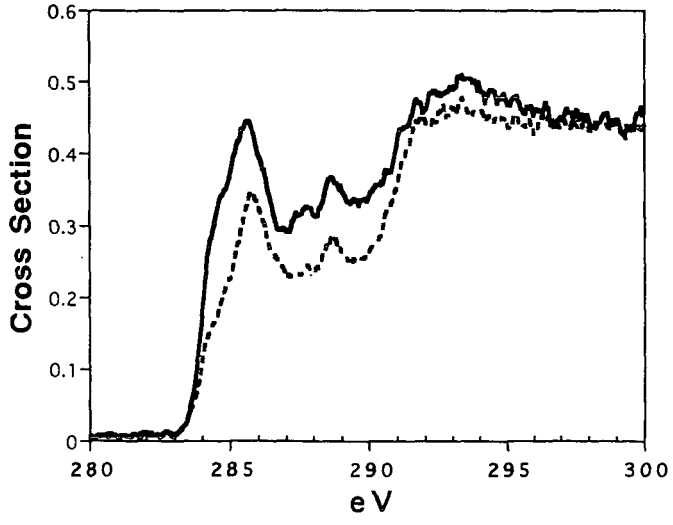

Figure 4. The C-NEXAFS spectra of the laboratory coke.

THE DEVELOPMENT OF POROSITY IN PITTSBURGH #8 AND WYODAK CHARS AS STUDIED USING CONTRAST MATCHING SMALL ANGLE NEUTRON SCATTERING

Peter J. Hall and M. Mirari Antxustegi
Department of Pure and Applied Chemistry, University of Strathclyde
295 Cathedral Street, Glasgow G1 1XL, SCOTLAND

Joseph M. Calo
Division of Engineering, Box D, Brown University, Providence, RI, USA

Keywords: Contrast Matching Small Angle Neutron Scattering, Interparticle Scattering, Porosity.

INTRODUCTION

The development of porosity in coal chars is important in both combustion and gasification processes and there have been a large number of investigations and techniques applied to the subject[1]. A persistent problem in understanding the development of porosity is the existence of closed porosity, which cannot be accessed from the external surface. Intrusive techniques, such as mercury porosimetry[2], or adsorbative techniques[3] cannot, by definition, give information about such porosity. On the other hand, small angle x-ray scattering (saxs)[4] and small angle neutron scattering (sans)[5] techniques monitor scattering from both open and closed porosity and consequently cannot distinguish them. Additionally, saxs data may be complicated by interparticle scattering.

Recently, progress has been made in the understanding of closed and open porosity by using contrast-matching small angle neutron scattering (sans) to investigate the development of porosity[6,7]. In Hall *et al.*[6], sans was first performed on dry powdered phenolic resin char (prc). As with saxs, scattering is off open and closed porosity, as well as some interparticle scattering. Sans was then performed on phenolic resin char saturated with deuterated toluene. Following ultrasonication of the toluene/char mixture, the deuterated solvent fills any accessible porosity and interparticle voids. Hall *et al.*[6] showed that deuterated toluene has the same neutron scattering density as typical polycrystalline carbon ($\sim 5.6\ 10^{10}$ cm^{-2}) and therefore contrast matches the carbon very closely. With respect to neutrons there is no scattering contrast between the carbon and deuterated toluene in the pores and therefore no coherent scattering. Open porosity is therefore becomes "invisible" to the neutrons. Neutron scattering from the deuterated toluene/char mixture was therefore due to carbon and any porosity that could not be accessed by the deuterated toluene. Hall *et al.*[6] showed that there was significant residual scattering in the contrast matched sample which was due to a well developed closed pore system. The difference between the dry and contrast matched samples was therefore due to scattering in open pores and interparticle scattering from the external surfaces of the packed prc particles.

Pittsburgh #8 coal is a coking coal and following slow pyrolysis (heating rates $\sim$10 Kmin^{-1}) under nitrogen it goes through a fluid phase[8] before the onset of significant carbonization. The resulting chars have low surface areas and are highly graphitic[9]. From investigation of the desorption of oxygen complexes, Hall and Calo[9] have speculated that Pittsburgh #8 char has very low levels of microporosity and that gasification proceeds by the creation of new pores. This thesis has not been explicitly tested.

Conversely, Wyodak is a Subbituminous coal and forms a char of high surface area.

The objective of the present work is to use a technique to investigate the development of Pittsburgh #8 and Wyodak coal chars: contrast matching sans.

EXPERIMENTAL

BET surface areas were obtained from adsorption of nitrogen at 77K using a Quantasorb apparatus over the range $0.01<P/P_o<0.95$.

The sans was performed at the Intense Pulsed Neutron Source (IPNS) at the Argonne National Laboratory at the small angle diffractometer (SAD)[10]. The sample holders were made of Suprasil with a path length of 0.2 cm. The scattering data were corrected for the scattering from the sample holder and other instrumental backgrounds. Normalization for the sample thickness and transmission were made and the data were scaled to yield absolute calibration.

Pittsburgh # 8 and Wyodak coals were selected from the Argonne Premium Coal sample programme. Great care was taken to avoid contact with air during the pyrolysis procedure. The coal was heated under a slight positive pressure of nitrogen at 10 K min^{-1} to 1273K with a heat soak time of 1 hour. The resulting char was ground to between 60 and 100 Tyler mesh. For sans on the contrast matched samples, the chars were mixed with excess deuterated toluene and placed in an ultrasonic bath for 4 hours. Activation of the chars was by air in a tube furnace at 673K.

RESULTS AND DISCUSSION

Pittsburgh #8 char: 77K nitrogen adsorption isotherms were made for Pittsburgh #8. The surface area of the ungasified char was 8 m^2g^{-1}, which suggests no significant open porosity. This has been previously observed by Hall and Calo and is typical of chars from coking coals. The isotherm is of Type 2 according to the BDDT[11] classification, which is typical for non-porous materials or materials which have pore systems with significant amounts of meso- or macro- porosity. As discussed, the gas adsorption gives no indication as to the possible existence of closed porosity or whether porosity development proceeds by opening porosity or developing new porosity.

Small angle neutron scattering for the ungasified char is shown in Figure 1. To summarize, the dry curve represents coherent scattering from open and closed porosity as well as interparticle scattering. The contrast matched curve represents scattering from closed porosity and the difference curve represents scattering from open porosity and interparticle scattering.

From the dry curve it can be seen that there is no significant scattering for $q>0.15$ $Å^{-1}$. This suggests the absence of scatterers of size less than ~40 Å and the absence of well developed microporosity. There is therefore consistency between the isotherm and sans data. The scattering data increases monotonically over the q range studies which suggests that the size of the largest scatterer cannot be resolved. This may be either due to interparticle scattering or scattering from a small number of large pores.

From Figure 1 it can be seen that the effect of contrast matching by the addition of deuterated toluene reduced significantly the scattered intensity at all q-values. To illustrate this more graphically, the scattering is shown on a linear scale as an insert in Figure 1. The integral under the "dry" scattering curve is 2.19 (arbitrary units) and the integral under the contrast matched curve is 0.10 (arbitrary units). Therefore scattering has been reduced by a factor of 22. Therefore, 4.8% of the total scattering is due to closed porosity. This compares to 59.9% for the ungasified phenolic resin char of Hall *et al.*[6] and shows clear differences between the pore structures of prc and Pittsburgh #8 coal char. Figure 1 also shows that there is no significant scattering for $q>0.078$ Å, for the contrast matched sample, which suggests the absence of porosity less than ~75Å. It is probable therefore that scattering is due to a small number of large pores.

Gasification to 0.8% burn-off increases the surface area to 80 m^2g^{-1}, which suggests the development of porosity. Analysis of the BET isotherm curve shows a BDDT Type 2 adsorption isotherm for this char although the knee is more clearly defined than for the ungasified char. This may suggest the development of significant levels of microporosity. The sans data for the 0.8% burn-off char are shown in Figure 2. The results are qualitatively the same as for the ungasified char. Contrast matching reduces the scattered intensity very significantly, which

suggests that there is very little porosity. The scattering integral for the dry sample is 3.33 (arbitrary units) and this reduces to 0.15 for the contrast matched sample. Therefore 4.8% of the total scattering is due to closed porosity, which is similar to the ungasified char. The scattering data suggests that deuterated toluene can access all of the porosity developed during gasification.

Comparison of the scattering from the contrast matched samples in Figures 2 and 3 (shown as an insert in Figure 2) shows that they are very similar. Invariance of scattering from contrast matched samples has previously been observed by Hall *et al.*[6] for phenolic resin. This constitutes evidence that the scattering is indeed from closed porosity which is unaffected by gasification. The scattering data from the 0% and 0.8% samples therefore show that gasification proceeds by the creation of new porosity, rather than the opening of closed porosity as is the case for phenolic resin char[6].

The dry scattering curve in Figure 2 is typical for a material with a well developed micropore system. For convenience, the scattering behaviour for Porod type of behaviour is also shown in Figure 2. The upward deviation from this is due to the presence of micropores formed during gasification. Since the ungasified char has a low surface area, and the adsorption isotherm for the ungasified char is typical for a non-porous material, the scattering in the "difference" curve of Figure 1 is therefore dominated by interparticle effects, i.e. scattering determined by the external surface of the particles and the packing of the char particles. Again, this effect has been observed by Hall *et al*[6] for phenolic resin char. The form of the scattering curve for the ungasified sample approximates to Porod behaviour, which suggests that it is due to the presence of relatively large scale scatterers. Since the surface area of the 0.8% gasified char suggests the development of open porosity then the difference curve of Figure 2 must therefore contain information about interparticle scattering as well as the additional porosity. The difference curves are compared in Figure 3. The curves converge at low-q, which suggests that the nature of the background scattering has not changed significantly. The difference between the two difference curves ($0.8\%_{diff}$-$0\%_{diff}$ in Figure 3) is therefore due to scattering from any additional pores created during the gasification process. Using the technique of subtracting interparticle scattering effects, the development of porosity in Pittsburgh #8 coal char can be studied in detail.

BET surface areas increase with gasification. The surface area at 13.5% burn-off is 252 m^2g^{-1}. The isotherms are all of type 2, although the "knee" seems to be more clearly defined for the 0.8% and 4.5% gasified chars. Sans for the gasified chars are shown in Figure 4. The data are difference scattering curves that have been corrected for interparticle scattering by further subtraction of the "difference" scattering curve of Figure 1. The scattering curves therefore give information about pores that have been developed during gasification. The Guinier analysis[12] for the 0.8% gasified char shows a linear section with a radius of gyration, R_g=16.3Å. Therefore, the early stage of gasification appears to produce microporosity. The scattering curve for the 4.5% gasified char in Figure 4 is also typical for a microporous network and the Guinier plot is also linear with R_g=13.5Å. The conclusion is that further microporosity is being produced. In contrast, the scattering curve for the the 13.5% gasified char is typical for a pore system with a wide range of pore sizes. The Guinier plot confirms this by showing curvature over the entire q-range. The log-log plot is linear over the range $0.0058Å<q<0.054Å$ and the slope of the line is -3.8. This deviates slightly from the Porod ideal and is probably due to fractal roughening of the pore surfaces. The fractal dimension is 2.2, which agrees with other fractal investigations of the surfaces of gasified carbon surfaces. Therefore in the burn-off range 4.5%-13.5% micropores appear to being opened to produce a pore system with a wide size range.

Wyodak Char: In this case, the picture is quite different. It is not possible to define the amount of interparticle scattering as in the case of Pittsburgh #8 because in the case of ungasified wyodak char, there is some initial opened and closed porosity. As before, the extent of scattering due to closed porosity can be obtained by examining the scattering from the contrast matched sample. But after substracting the scattering due to closed porosity, the difference curve will tell about the interparticle scattering at the same time as the open porosity. Another input in the scattering curve could be scattering of the mineral matter in the coal char. This may have much more importance than in the case of Pittsburgh #8 because in the results presented here the

gasification is taken to much later stages. At 70% weight loss, the ash content of the sample is high. It is observed that there is a bump in the scattering curve between $0.03Å^{-1}<q<0.09Å^{-1}$ that remains invariant with gasification. The origin of this feature could be scattering from ash particles, but further work is needed to test this.

The contrast matched curve for the ungasifyed Wyodak char in Figure 5 shows considerable scattering. This suggest the presence of closed porosity in the sample. Other experiments show that the extent of closed porosity diminishes as gasification increases to 58% weight loss where it can be seen that the scattering from the closed pore is almost nil (Figure 6). After this stage, around 68% weight loss, the extent of closed porosity seems to increase. The explanation for this could be associated with the scattering of ash particles. The BET surface area decreases from $397m^2g^{-1}$ for 58% weight loss char to $267m^2g^{-1}$ for 68% weight loss char.

The results show that scattering from open porosity increases faster than the decrease of scattering from closed porosity. This may suggest that during the gasification process, both pore opening and pore creation take place simultaneously.

CONCLUSIONS

Contrast matching has been shown to be a very powerful technique for investigating the development of porosity in carbons both in terms of understanding the effects of closed porosity and the elimination of interparticle scattering. Contrast matching sans shows that Pittsburgh #8 char has very little closed porosity and consequently that pore development during gasification proceeds by the creation of new pores. In the early stages of gasification (<4.5% burn-off) a pore system with significant microporosity is produced. In later stages of gasification (4.5%-13.5% burn-off) the tendency is to open these micropores, producing a pore system with a broad size distribution. Ungasified Wyodak coal char has a significant amount of closed porosity that opens as gasification proceeds, giving a minimum of closed porosity around 58% weight loss. It is also shown that the increase of surface area during gasification is due to pore opening and creation.

ACKNOWLEDGEMENTS

The work was supported by a British Coal extra mural grant and MMA acknowledges support of a University of Strathclyde scholarship. Travel funding for MMA was from the Bellahouston Trust.

REFERENCES

1. Lowell, S. and Shields *Powder Surface Area and Porosity*, Chapman and Hall, London, 1984.
2. Bale, H.D. and Schmidt, P.W. *Phys Rev Lett*, 53, 596, (1984).
3. Hall, P.J. *Chemical Physics Letters*, 124, 467-469, (1986).
4. Porod, G. in Small Angle X-ray Scattering, edited by Glatter, O. and Kratky O., Academic Press, N.Y., 1982, pp: 17-52.
5. Kostortz, G. in Treatise on Material Science and Technology, Vol 15 -- Neutron Scattering, edited by Kostortz, G., Academic Press, N.Y., 1979, pp: 227-290.
6. Hall, P.J., Antxustegi, M.M. and Calo, J.M. *Proc. Int Conf. Carbon '94*, Granada, Spain, 1994
7. Gethner, J.S., Journal of Applied Physics, 59 (4), 15 February 1986, pp: 1068-1085.
8. Mahajan O.P. in Coal Structure, edited by Meyers, R.A., Academic Press, N.Y., 1982, pp: 51-86.
9. Hall P.J. and Calo, J.M., Abstracts of Papers of ACS 1990, vol 35, no 3, Washington DC, pp: 705-712.
10. Epperson, J.E., Thiyagarajan, P. and Klippert, T.E., SAD Manual, IPNS, Argonne National Laboratory, Argonne, IL 60439.
11. Brunauer, S., Deming, L.S., Deming, W.S. and Teller, E. (1940), J. Amer. Chem. Soc., 62, pp: 1723.
12. Guinier, A. and Fournet, G.,in Small Angle Neutron Scattering (translated by Walker, C.B., Kudowitch, K.L., Edited by Wiley, N.Y., 1955, pp: 19-23.

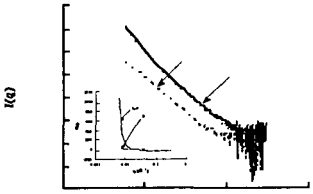

Figure 1. Small angle neutron scattering from unactivated Pittsburgh #8 coal char dry (a), contrast matched by mixing with deuterated toluene (b) and the difference (c) between scattering curves (a) and (b).

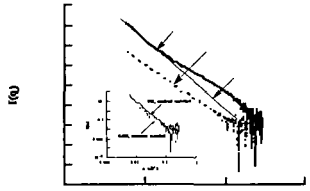

Figure 2. Small angle neutron scattering from Pittsburgh #8 coal char gasified to 0.8% weight loss in air at 673K dry (a), contrast matched by mixing with deuterated toluene (b) and the difference between scattering curves (a) and (b). A comparison of the scattering from the contrast matched ungasified and 0.8% gasified Pittsburgh #8 coal chars is sbown as an insert.

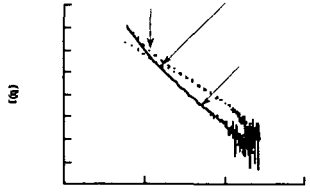

Figure 3. The method for correcting the "difference" scattering curve (curve (c) in Figure 3) by subtraction of the interparticle scattering (curve (c) in Figure 1) to show scattering from pores produced during gasification ($0.8\%_{diff}$-$0\%_{diff}$) for Pittsburgh #8 coal char gasified to 0.8% burn-off in air at 673K.

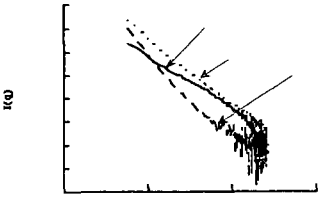

Figure 4. "Difference" scattering curves corrected for interparticle scattering to show small angle neutron scattering from pores produced during gasification for Pittsburgh #8 coal char gasified to different levels of burn-off in air at 673K.

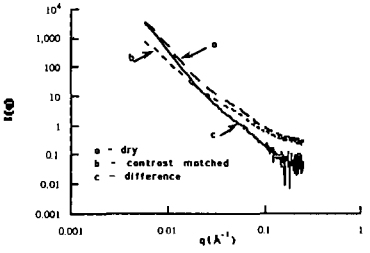

Figure 5: Small angle neutron scattering from ungasified Wyodak coal char dry (a), contrast matched by mixing with deuterated toluene(b) and the difference (c) between scattering curves (a) and (b).

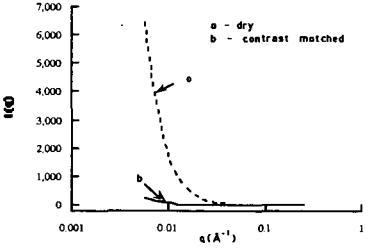

Figure 6: Small angle neutron scattering from Wyodak coal char gasified to 58% weight loss dry (a) and contrastmatched by mixing with duterated toluene (b). The intensity is shown in linear scale to show how the scattering of the contrast matched almost disappears.

SMALL ANGLE NEUTRON SCATTERING APPLICATIONS IN FUEL SCIENCE

P. Thiyagarajan
IPNS Division
George D. Cody, Jerry E. Hunt and Randall E. Winans
Chemistry Division
Argonne National Laboratory
Argonne, IL 60439.

Keywords: SANS Asphaltenes Coal

INTRODUCTION

Small angle neutron scattering (SANS) is a versatile technique[1], extensively used in condensed matter research, spanning the scientific fields including polymer science, metallic alloys, magnetic materials, porous materials, ceramics, composites, structural biology and colloidal systems of industrial and technological importance. SANS is useful to study both solid and liquid systems to obtain the size, morphology, molecular weight, particle size distribution in a size range of 10 to 1000 Å, as well as to study the phenomena such as phase separation, crystallization etc. In the presence of inter-particle interactions (e.g. ionic micelles) this will yield information on the surface potentials (e.g. surface charge density) of the colloids[2].

Three properties of neutrons make SANS to be unique and the information complementary to other techniques. The scattering cross-sections of the elements do not depend on their atomic number, but vary between the isotopes[3]; e.g., b_H=-0.3740x10^{-12}cm and b_D=0.6674X10^{-12}cm. This permits investigations of systems containing hydrogen (polymers, biological macromolecules, micelles, coals, asphaltenes) and multicomponent systems (clay-polymer composites, virus, microemulsions, coals). The high penetration of cold neutrons is valuable for the study of bulk materials under a variety of conditions, such as a wide range of temperature, magnetic field, pressure, shear etc. The magnetic moment of neutrons permits them as a powerful probe for the study of magnetic materials.

The SANS experiments can be carried out at either reactor facilities (e.g. ORNL, NIST, ILL-France), or at Pulsed Neutron Sources (e.g. ANL, ISIS-Great Britain). The neutron beams, usually, have circular cross-section with a diameter of 8-12mm, and the sample thicknesses are typically 1-5mm, depending on the chemical composition of the sample. Majority of SANS experiments require data in a wide q ($q=4\pi.\sin\theta/\lambda$, where θ is the half the scattering angle and λ is the wavelength of the neutrons) range, in order to carry out analysis on morphology, fractal dimension, particle size distribution, phase separation etc. To measure data in a wide q range at the SANS instruments at reactors, one has to repeat the experiments 2 to 3 times by changing the sample-to-detector distance or the wavelength of the neutrons or both. The SANS instruments at the pulsed neutron sources, on the other hand, yield data in a wide q range in a single measurement, by using neutrons with a wide range of wavelengths which are determined by time-of-flight techniques. This may serve as an advantage for studying systems which cannot be exactly reproduced for the repetitive measurements. In this paper we discuss briefly a few fundamental principles of SANS and demonstrate the technique with a few examples.

BASIC PRINCIPLES

A number of reviews[4,5,6] describe the basic principles of small angle scattering and hence we only give relevant formulae useful for obtaining the structural information. Briefly, the intensity of the scattered neutrons, I(q), in the low q region is determined by the number density of particles, n, the distance correlations due to time-averaged position vectors of the atoms within a particle [intra-particle structure factor, P(q)] and those due to the distribution of particles [inter-particle structure factor, S(q)] within the sample volume.

$$I(q) = n\,P(q)\,S(q) \qquad (1)$$

In dilute systems S(q) tend to oscillate around 1.0 in the low q region and the measured I(q) is determined essentially by P(q). Analysis of the measured I(q) for dilute systems will yield direct information on the structural properties of the particles, in terms of size and shape. If the data is calibrated to be on an absolute scale, additional infomation such as molecular weight and volume can also be obtained. In the absence of inter-particle interactions the differential scattering cross-section can be written as

$$I(q) = k\,|\int(\rho_s-\rho_m)\,e^{iqr}\,d^3r\,|^2 \qquad (2)$$

where ρ_s and ρ_m are the scattering length densities (scattering length per unit volume) for the particle and the matrix, and the k includes all the constants to place the data on an absolute scale. Table I contains scattering length densities ($\rho=\sum b.N_A.d/M$, where b is the scattering length[3], N_A.is the Avogadro's number, d is the physical density and M is the molecular weight) for a number of normal and per-deuteriated solvents. At low q region, equation 2 reduces to a simple form, Guinier equation[4],

$$I(q) = I(0) \exp(-q^2 R_g^2/3) \quad (3)$$

$$I(0) = n v^2(\rho_s-\rho_m)^2 \quad (4)$$

In eq. 3, R_g is known as the radius of gyration of the particle and v in eq. 4 is the volume of the solvent excluded by the particles. This is defined as the root-mean square value of all the pair-wise distances from the centroid of the scattering volume and this parameter does not specify the shape. In the case of monodisperse system, R_g can be used to determine the dimensions of the particles, provided the shape is known. In the case of spherical particles $R_g = \sqrt{(3/5)}$. radius. A plot of Ln.I(q) vs. q^2 (Guinier plot) will yield a straight line in the q region where $q.R_g \leq 1.0$. The absolute slope of the straight line can be used to determine the R_g and the y-intercept yields I(0) which can be used to determine the molecular weight of the particle. In the case of polydisperse systems the measured R_g is the z-avearaged value given by $R_g^2 = \Sigma N_i.M_i^2.R_g^2{}_i \; / \; \Sigma N_i.M_i^2$ and the molecular weight from I(0) is the weight-averaged value. It can be seen from eq. 4 that the magnitude of I(0) can be manipulated by changing either the scattering length density of the solute, ρ_s, or the solvent, ρ_m, and can be made zero by exactly matching these two parameters. This method is called contrast varation[7] which can be done by changing the deuteration levels of either the solute or solvent. In the case of binary system the contrast variation method can be used to determine I(0) at different ρ_m values and a plot of $\sqrt{I(0)}$ vs ρ_m will give a straight line whose slope is proportional to the solvent excluded volume, v (see eq. 4) and the x-intercept gives ρ_s value. The value in turn can be used to determine the partial specific volume of the particle provided the chemical composition of the constituents is known. The contrast matching technique has been used to advantage in the case of coals. The composition and the density of the coals is such that its scattering length density is similar to the scattering length density of perdeuteriated toluene (see Table I). If coal is imbibed in the perdeuteriated toluene then for neutrons the particulate region of the coal and the solvent filling the accessible pores resemble as a system of uniform scattering length density. Hence the scattering from the pores accessible to the solvent will be negligible. However if there exists pores inaccessible to the solvent then they will produce SANS signals. Thus SANS can be used to characterize the closed pores in coals as well as other porous materials[8]. Such manipulation has also been done to see the effects of confined space on the phase separation in binary solvents[9] and micellization.

As mentioned earlier, the low q region gives the size parameter, R_g, but delineation of the shape information requires data in a wide q region. The log(I).vs.log(q) plots yield important information on the probable shapes. In the case of infinitely long particles the scattering signal in the low q region is convoluted by a powerlaw of q^{-1}. In the case of sheet like particles the scattering signal in the low q region is convoluted by a powerlaw of q^{-2}. Thus the measured differential scattering cross-sections for the rod and a sheet, respectively, are given by

$$I(q) = q^{-1}.\exp(-q^2.R_c^2/2) \quad (5)$$

$$I(q) = q^{-2}.\exp(-q^2.R_t^2) \quad (6)$$

These equations can be used to obtain the cross-sectional radius of gyration, R_c, of the rod-like particle from a modified Guinier plot[5] for a rod, Ln.[q.I(q)] vs. q2 and the thickness factor, R_t, of the lamellar particle can be obtained from a modified Guinier plot for a sheet, Ln.[q2.I(q)]. vs. q^2. The radius of the rod can be obtained by multiplying R_c by $\sqrt{2}$, and the thickness of the sheet can be obtained by multiplying the R_t by $\sqrt{12}$. The y-intercepts in these plots can be used to obtain the mass per unit length and mass per unit area respectively.

For obtaining information on the morphology of the particles, the data in the whole q region can be modelled by using the form factors for shapes such as sphere, ellipsoid, cylinder, random coil etc., and obtain the size parameters best describing the scattering signal. Form factors for several known geometries are available in Guinier and Fournet (1955)[4]

In the case of self-similar aggregates the scattering signals exhibit powerlaw behavior in a wide q region. The log(I) vs log(q) plots can be fitted in the linear regions and the absolute values of the slope can be used to describe the system in terms of fractal dimensions[10-12]. If the absolute value of the slope is a fraction in the region of 1-3, then the system is a mass fractal and the magnitude tells about the packing density of the fractal objects. If the fractal objects are formed through aggregation then it is possible to delineate the kinetics of aggregation. For example if the absolute value of the slope is around 1.7 then the cluster-cluster aggregation model may explain the aggregation mechanism, and if it is around 2.5 then it could be due to diffusion limited aggregation. If the absolute value of the slope is between 3-4 then the system is quite large and the system may be a surface fractal. A value close to 4 corresponds to a smooth surface and that close to 3 implies a particles with a rough surface.

The scattering signal in the case of polydisperse systems cannot easily be fitted with either the form factor of known geometrical objects or at times it may not exhibit linear curves in the Guinier plot [Ln I(q) vs q2]. If the measured scattering data contains data in the q region where $q.R_g \leq 1.0$ such that R_g is the largest particle size then unique information on the particle size distribution can be obtained by using maximum entopy technique. If the particles are too large and the data cannot be measured to very low q values fulfilling the relationship $q.R_g \leq 1.0$, then it may not be possible to get the correct particle size distribution. The pore size distribution in coals is quite wide and the pores are quite large and hence the scattering techniques cannot give the correct pore size distribution for coals.

EXPERIMENTAL

We have conductued a number of SANS experiments on coals, coal macromolecules and asphaltenes at the Small Angle Diffractometer (SAD) at the Intense Pulsed Neutron Source of Argonne National Laboratory. This instrument uses neutrons produced in pulses by spallation due to the deposition of 450 MeV protons on a depleted uranium target, followed by a solid methane moderator (22 K) yielding a wavelength range of 1 to 14 Å. Detection of scattered neutrons was accomplished with an area sensitive, gas-filled proportional counter, and the wavelength of the scattered neutrons was determined by their times-of-flight. The accessible q range using SAD is from 0.005 to 0.25 $Å^{-1}$ in a single measurement. The samples at ambient to 100 C were measured in Suprasil cells, while the high temperature measurements were done in a stainless steel cell

EXAMPLES

Coals are complex materials and a variety of techniques have been applied to understand their chemical and physical structures. Scattering studies on coals have brought out the fractal nature of the network structure[12] and the structural modifications occurring due to solvents such as pyridine. SANS showed that Pittsburgh #8 in C_5D_5N swelling is due to the breaking of the hydrogen bonded network of coal structure[13]. In order to gain a better understanding of the coal structure we took an an approach to study the pyridine-extracted species[14] in deuteriopyridine as well as the extracts with their acidic groups methylated. The scattering behavior of both neat and O-methylated extracts of APCS #3 (5 wt.% in C_5D_5N) is shown in Fig. 1a and the Guinier plot for the neat sample is shown in Fig. 1b. The slope of the fitted line in Fig. 1b gives an R_g of 41±3Å and I(0)=0.01 $cm^2.mg^{-1}$ which corresponds to a molecular weight of 6365 daltons and a solvent excluded volume of 9000 $Å^3$. This clearly shows that the macromolecule is not a solid sphere, rather a random coil. The data thus can be fitted well with the form factor for a random coil and the fit is also shown in Fig.1 for the neat sample. The R_g value from the fit is consistent with that from Guinier analysis. The O-methylated macromolecules exhibit a powerlaw behavior in the low q region with an absolute slope of -1.7 (Fig. 1a). However the scattering behavior is similar in the q region above 0.03 $Å^{-1}$. This indicates that the particles are similar in both neat and O-methylated samples, however they aggregate further in the O-methylated sample. The blocking of the hydrogen bonding interactions between the macromolecular surface and deuteropyridine leads to large net work structures resembling a system aggregated due to cluster-cluster aggregation. The size of the smallerst cluster is around 70 Å. We obeserved that the differences between the neat and O-methylated cases decreases with decreasing in rank of the coals, however the net work strctures seem to be more dense than seen in the case of APCS #3 in C_5D_5N.

Another system in the fuel chemstry which is quite complex and widely studied is the asphaltenes. We carried out SANS studies on heptane precipitated asphaltenes[15] form Maya vacuum resids in deuteriated 1-methylnaphthalene (d10-1MN) in a wide temperature range of 20 to 400 C. This study showed that a 5 wt.% asphaltenes solution in d10-1MN at ambient temperatures form large colloidal systems, but they break down with increasing temperature. To compare the behavior of extracted coal macromolecules and asphaltene colloids we have shown the temperature effect on R_g and I(0) values in Figs. 2a and 2b respectively. It can be seen that at 20C the size and I(0) for the asphaltene colloids in d10-1MN are larger than those for the pyridine extracted coal macromolecules in C_5D_5N. With increase in temperature the asphaltene colloids become smaller than the coal macromolecules (Fig.2a). However the I(0) values, which are directly proportional to the solvent excluded volume of the particles and the contrast, continue to be larger than the coal macromolecules. The larger I(0) values for the asphaltenes (smaller size) suggest that the asphaltene colloids may be more densely packed than the coal macromolecules in C_5D_5N. This can be confirmed with contrast variation studies on asphaltenes in organic solvents and such studies are in progress. Our studies on asphaltenes[15] showed that they have a rod shape with a radius around 18A, but with varying lengths depending on the temperature. We used modified Guinier analysis (Fig.3a) to obtain the cross-sectional radius of the particle and MaxEnt analysis for the polydispersity (Fig.3b).

CONCLUSIONS

In the field of fuel chemistry we encounter several systems which are quite complex as well as multicomponent in nature (crude oil). A wide range of physical and chemical methods have

been used to understand these systems and we are still far from complete understanding. For example coals have been studied in pure solid to chemically modified states. Since chemical modification and/or solvent extraction result in a number of different systems, it would be very important to understand the products in terms of thier colloidal properties as a function of the type of solvent used to disperse them, as well as other physical conditions. Such knowledge will be helpful in the design of processing techniques. Another area of research where SANS can be useful is in the characterization of synthetic and modified clays[16,17] which are being developed for processing in the petroleum industry. The major limitations for performing SANS experiments are the nonavalilability/high cost of certain deuteriated solvents and the paucity of beam time at the neutron scattering centers.

ACKNOWLEDGEMENT
This work benefited from the use of the Intense Pulsed Neutron Source, ANL funded by the Office of Basic Energy Sciences, Division of Materials Science, U.S. Department of Energy under contract # W-31-109-ENG-38. This work was done under the auspices of U.S. DOE, BES-Division of Chemical Sciences under the same contract.

REFERENCES:
1) L.A. Feigin & D. I. Svergun (1987) Structure Analysis by Small Angle X-ray and Neutron Scattering, Plenum Press, New York.
2) S. H. Chen, E. Y. Sheu, J. Kalus & H. Hoffmann (1988) J. Appl. Cryst. 21, 751-769.
3) V. F. Sears,Neutron Scattering Lengths and Cross sections. In K.Skold & D. L. Price (ed) Neutron Scattering Methods of experimental Physics, R. Celotta & J. Levine (Series ed) 23A, 521-549) Academic Press, Inc, New York.
4) A. Guinier & G. Fournet (1955) Small Angle Scattering, Wiley, New York.
5) O. Glatter & O. Kratky (1982) Small Angle X-ray Scattering, Academic Press, New York.
6) G. D. Wignall, (1987) In Encyclopedia of Polymer Science and Engineering, 2nd ed. Vol.10 112-184, Wiley, New York.
7) H.B. Stuhrmann & A. Miller (1978) Small ANgle Scattering of Biological Molecules, J. Appl. Cryst. 11, 325-345.
8) P.J. Hall, M.M. Antxustegi & J.M. Calo (1994) (Private Communication to P. Thiyagarajan)
9) M.Y. Lin, S.K. Sinha, J.M. Drake, X.-I. Wu, P. Thiyagarajan & H.B. Stanley (1994) Phys Rev Letters, 72, 2207-2210.
10) J. Feder (1988) *Fractals*, Plenum Press, New York.
11) T. Freltoft, J. K. Kjems & S.K. Sinha (1986)*Physical Rev. B*, **33**, 269
12) H.D. Bale & P.W. Schmidt (1984) *Phys. Rev. Lett.*, **53**, 596.
13) R.E. Winans & P. Thiyagarajan (1988) *Energy & Fuels* **2**, 356
14) G.D. Cody, P. Thiyagarajan, R. E. Botto, J. E. Hunt & R.E. Winans (1994) Energy and Fuels 8, 1370-78.
15) P. Thiyagarajan, J.E. Hunt, R.E. Winans, K.B. Anderson & J.T. Miller (1995) Energy and Fuels (In Press)
16) K.A. Carrado, P. Thiyagarajan, R.E. Winans & R.E. Botto (1991) Inorganic Chemistry, 30, 794-799.
17) A. Moini, T.J. Pinnavaia, P. Thiyagarajan & J.W. White (1988) J. Appl. Cryst 21, 840-842.

TABLE I
Neutron Scattering Length Densities (ρ)

System	Chemical formula	Density(g/cm^3)	ρ(10^{10}cm^{-2})
Benzene	C_6H_6	0.8786	1.18
Benzene-d6	C_6D_6	0.950	5.43
Cyclohexane	C_6H_{12}	0.7786	-0.277
Cyclohexane-d12	C_6D_{12}	0.89	6.678
Methanol	CH_3OH	0.7914	-0.373
Metanol-d4	CD_3OD	0.89	5.81
1-methylnaphthalene	$C_{11}H_{10}$	1.02	1.54
1-methylnaphthalene-d10	$C_{11}D_{10}$	1.1	6.08
Pyridine	C_5H_5N	0.9819	1.79
Pyridine-d5	C_5D_5N	1.05	5.71
Toluene	$C_6H_5CH_3$	0.8669	0.94
Toluene-d8	$C_6D_5CD_3$	0.94	5.64
Water	H_2O	1.0	-0.56
Water-d2	D_2O	1.105	6.358
polycrystalline carbon		1.4	5.6

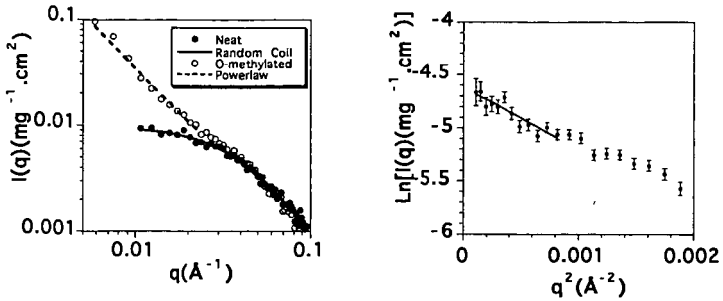

Fig.1a: SANS of APCS #3 in C_5D_5N (•), solid line is the fit for a random coil. Data for O-methylated extracts (o), dotted line is the powerlaw fit. Fig. 1b: Guinier plot fot the pyridine extracts from APCS #3 in C_5D_5N. The size of error bars is smaller than the size of the symbols.

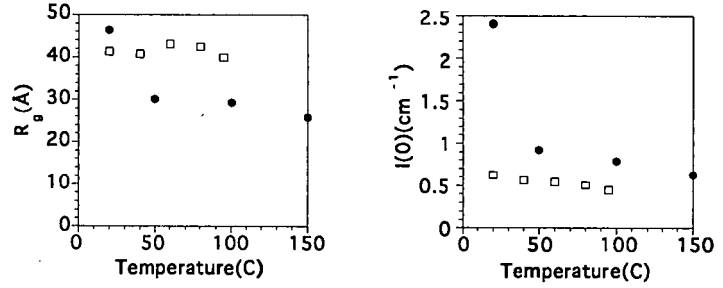

Fig.2a: Temperature effect on the Rg of the 5 wt% APCS #3 macromolecules in C_5D_5N (square) and 5 wt.% asphaltenes in $C_{11}D_{10}$ (filled o). Fig 2b: Temperature effect on the I(0) of the APCS #3 pyridine extracts in C_5D_5N (square) and 5 wt.% asphaltenes in $C_{11}D_{10}$ (o). The size of error bars is smaller than the size of the symbols.

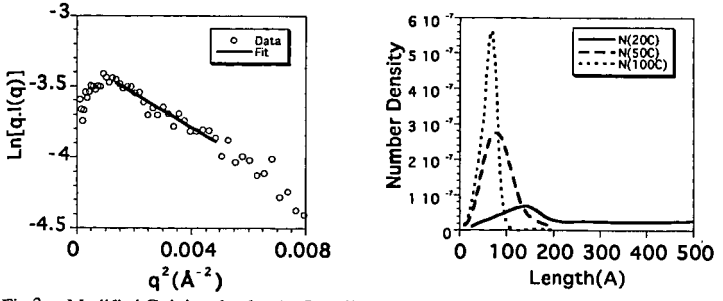

Fig.3a: Modified Guinier plot for the 5 wt.% asphaltenes in $C_{11}D_{10}$ at 20C. The size of error bars is smaller than the size of the symbols. Fig. 3b: Length distribution for the 5 wt.% asphaltenes in $C_{11}D_{10}$ as a funtion of temperature (radius of the rods is 18Å). 20C (solid line), 50C (dashed line), 100C (dotted line).

CHLORINE IN FIVE ILLINOIS COALS AND THREE BRITISH COALS: AN X-RAY ABSORPTION NEAR-EDGE STRUCTURE (XANES) SPECTROSCOPY INVESTIGATION.

M.-I.M. Chou, J.M. Lytle, and Y.C. Li
Illinois State Geological Survey
615 E. Peabody Drive
Champaign, IL 61820

F.E. Huggins and G.P. Huffman
University of Kentucky

Ken K. Ho, Illinois Clean Coal Institute

KEYWORDS: chlorine, coal, x-ray

ABSTRACT

The chlorine x-ray absorption near-edge structure (XANES) spectra of five Illinois coals and three British coals, and two series of char samples were examined. The char samples were prepared by stepwise heating one Illinois and one British coal in air at temperatures from 200 to 650°C. The chlorine XANES spectra for all the coals are similar and chloride anion was determined to be the predominant form of chlorine. The identity of the positive counter ions with which the chlorine anions are associated in the coals could not be unambiguously determined from XANES spectra. Nevertheless, the XANES spectra of the raw coal and its partially combusted char samples show significant changes in the form (and concentration) of chlorine with increasing char preparation temperature. The appearance of NaCl was observed in the chars from the British sample between 200 to 350°C but was not observed in the chars from the Illinois sample. The appearance of sodium chloride in British chars and not Illinois chars may indicate an isolated incidence due to dehydration and to the high sodium content of these coals, but it could also imply that in the British coal sodium cations are paired with chloride anions and this sodium could be associated with the sodium sulfate mechanism of boiler corrosion.

INTRODUCTION AND BACKGROUND

The total Cl content in coal has been used in Great Britain to predict the boiler corrosivity of a coal. It has been reported that British coals with more than 0.3% Cl are not recommended for pulverized-coal-fired boilers.[1,2] However, a recent survey conducted through a joint effort of the Electric Power Research Institute and the Illinois Clean Coal Institute indicates that many midwestern United States utilities have decades of experience burning high-Cl Illinois coals in a large variety of boiler equipment with no reported Cl-related fireside corrosion problems.[3] This suggests that the extent of boiler corrosion may not be directly related to the amount of Cl in the coal but to how the Cl occurs in the coal or to other factors such as the alkali and sulfur content of the coal, the type of boiler in which the coals were burned, and boiler operating parameters.[4]

If the nature of the Cl in coals with different corrosion potentials varies, then determination of how the Cl occurs in coals may provide a method to assess a coal's boiler corrosion potential. The current American Society for Testing and Materials (ASTM) standard method can determine the total chlorine content, but not the forms of chlorine in coal[5]. In many previous attempts at determining the forms of chlorine in coals, indirect methods were used, and some mixed results were reported. For example, Hamling and Kaegi[6] stated that chlorine in coal samples from one of the high-chlorine Illinois mines was predominantly in the form of organic chloride(s), and the organically associated chlorine does not apparently contribute to boiler corrosion and fouling problems. Chou[7] suggested that chlorine in coals occurs in two major forms: chloride anions dissolved in the pore water of coal, and chloride anions adsorbed on the inner surfaces of the micropores in macerals (organic fraction of the coal). It is clearly desirable to generate representative data with a more direct method of determination. Huggins and Huffman[8] recently used K-edge X-ray absorption fine structures (XAFS) spectroscopy to examine the occurrence of chlorine in coals from various locations worldwide. This nondestructive technique was applied in this study to directly examine five Illinois coals and three British coals and chars produced from the coals by stepwise heating under air.

EXPERIMENTAL PROCEDURES

Samples - Five Illinois coals, representing five specific geological locations[9] in Illinois, and three coals previously obtained from Great Britain were analyzed for chlorine by XANES. Data on chlorine and ash composition of the coals are listed in Table 1. Illinois coals have

much higher moisture contents than the British coals. Two of the three British coals have high ash contents. Among these coals, the two high ash content British coals also contain the highest sodium and potassium content.

Char preparation - Partially combusted coal samples (chars) were prepared from two coals, an Illinois coal (C-32795) and a British coal (C-32500). The coal sample was placed in a constant temperature zone of a Lindberg tube furnace. Under a flow of air, the furnace temperature was increased from room temperature to 200°C and remained at 200°C for 30 minutes before the first sample was collected. After the first sample was taken out, the temperature was increased to 250°C and held at 250°C for 30 minutes in order for the second sample to be collected. This stepwise heating was continued and a sample was collected at each 50°C interval until the final temperature of 1000°C was reached. These partially combusted samples were submitted to the University of Kentucky for XANES analysis.

XANES analysis - Chlorine XAFS spectra were obtained at beam-line X19A of the National Synchrotron Light Source (NSLS), Brookhaven National Laboratory. The spectra were obtained from the samples as-received by suspending them in the monochromatic X-ray beam in ultrathin (6 μm) polypropylene baggies. The chlorine XAFS spectra were collected in fluorescence geometry using a Lytle-type fluorescent detector with nitrogen as the ionization gas and helium in the sample chamber. The beam-line was operated in the focussed spot mode, although the spot was de-focussed somewhat in order to obtain a better sampling of the coal and char samples. Each spectrum consisted of about 500 points collected at energies between about 50 eV below the chlorine edge (2825 eV) to about 300 eV above the edge. Dilute samples of sodium chloride in boric acid were used as the primary standard for the chlorine edges. The principal peak position of the derivative XANES spectrum of NaCl was defined as the zero point of energy for the purpose of calibrating the chlorine XANES spectra. All spectra were collected and stored in a MicroVAX computer at NSLS and were transferred electronically to a similar computer at the University of Kentucky for analysis.

The chlorine spectra were first calibrated with respect to the primary standard (NaCl), then normalized to the edge step, corrected for background slope above and below the edge, and finally divided into separate XANES and extended X-ray absorption fine structure (EXAFS) regions. Analysis of the EXAFS regions of these spectra is generally not very informative, so that the data reported here comes from only the XANES region, that is, the structure within ±50 eV of the chlorine K absorption edge.

RESULTS AND DISCUSSIONS

Variation of forms of chlorine in coals - Based on the XANES spectra of standard compounds[8], a strong broad peak at about 1 eV followed by a much weaker, broad peak at about 20 eV is indicative of an ionic form of chlorine. The chlorine XANES spectra of the Illinois coals and the British coals are shown in Figures 1 and 2, respectively. The spectra of the Illinois coals and those of the British coals show a predominant form of chlorine as chloride anions. These anions may be in solution and have significant interaction with maceral surfaces presumably via ionic functional groups, such as quaternary amines or oxygen functional groups anchored via cations. The identity of these positive counter ions with which the chlorine anions are associated in the coals could not be unambiguously determined from XANES spectra. Nevertheless, the appearance of a sharp peak at 12.5 eV is indicative of the crystalline form of NaCl which is observed only in the spectrum of a British coal (C-33499). The ash composition of the coals indicated that this British coal is one of the coals which have high ash and high sodium contents.

Variation of forms and concentration of chlorine during stepwise heating under air - A procedure for the quantification of different forms of chlorine, similar to that done for sulfur[10], has not been established because most coals appear to have only one major form of chlorine, chloride anion. In this study, a separate set of experiment, using stepwise heating of one British coal (C-32500) and one Illinois coal (C-32795) under air, was conducted to attempt to remove the more volatile chlorine step by step from the less volatile chlorine and examine the residues by XANES. The XANES analysis on the changes, if any, of the forms of chlorine in chars during stepwise heating may help in understanding the nature of chlorine in these coals. The XANES spectra of the Illinois and the British coal and their partially combusted char samples were compared, as shown in Figure 3. The XANES spectra show significant changes in the form of chlorine (and concentration) with increasing char preparation temperature. In addition, there are differences between the variation of chlorine in the British coal compared to that in the

Illinois coal. A small peak at about 12.5 eV, diagnostic of the presence of NaCl, is apparent in the spectra of the chars formed at 200 to 350°C from the British coal. This feature is absent from the spectra of chars from the Illinois coal. The ash composition of these coal indicated that the British coal (C-32500) used has high ash and high sodium contents.

Above 350°C, the spectra of chars from both coals show a prominent sharp peak at about -1 eV that dominates the spectra in the range 400 - 600°C. Above 600°C, the spectra degrade in quality, as virtually all of the chlorine has been evolved from the samples. The peak position and shape of the spectra for the chars prepared at 400°C are similar to those noted for chlorine in organic (aromatic) compounds[8]. However, other less similar chlorine forms (hypochlorite, e.g. NaOCl) could be possible. The possible presence of organic chlorine in these chars raises some interesting speculations as to its possible origin. Alternative possibilities are: (i) it was present in the coal originally, but at such a low level (<10% of the total chlorine) that it did not register in the Cl XANES spectrum of the coal until the more volatile forms of chlorine had been evolved during low-temperature char preparation; or (ii) it was formed by reaction between the char and HCl evolved during char preparation. This phenomenon, the appearance of "organic" chloride, was not seen in a previous investigation[8], which was done by *in situ* heating under helium followed by XANES Cl analysis. In that study, however, the heating temperature was low, reaching only 350°C.

The chlorine content in the chars was estimated using a parameter known as step-height in the analysis of the chlorine XANES spectra. The results (Figure 4) showed that both coals experienced a large decrease in chlorine content at early stages of heating over the temperature range 250 to 400°C. The decrease of the remaining chlorine content in chars during further heating from 400°C to 600°C was very limited. In comparison with a previous study by Liu[11] in which chlorine evolution was based on HCl gas analysis, this study measured the chlorine content of the chars. In that study, the differences in chlorine evolution as a function of temperature between Illinois and British coals when heated under air were observed using a temperature-programmed thermogravimetric analyzer equipped with Fourier transform infrared spectrometry (TGA-FTIR). When comparing these two results, it should be noted the experiments in the two studies were conducted under different conditions. For example, the samples in this study during stepwise heating were heated much more slowly and at a longer residence time, which may have allowed more chlorine in the Illinois coals to be evolved at lower temperatures as compared with the TGA-FTIR analysis.

SUMMARY AND CONCLUSIONS

The data based on X-ray absorption near edge spectrum (XANES) analysis indicate that, in general, chlorine in coal mainly occurs in an ionic form. To balance the negative charge of these chloride anions, the occurrence of sodium and other cations, such as amino functional group, in the pore water of the coal are important. The identity of the positive counter ions with which the chlorine anions are associated in the coals could not be unambiguously determined from XANES spectra. Nevertheless, the current XANES data clearly indicated the appearance of NaCl in a British coal and in chars formed at 200 to 350°C from another British coal. The appearance of sodium chloride in the British char and not in the Illinois char may indicate an isolated incidence due to the dehydration of the coal sample and to the high sodium concentration of the coal samples, but it could also imply that in the British coal sodium cations are paired with chloride anions and this sodium could be associated with the sodium sulfate mechanism of boiler corrosion during coal combustion. Further investigation using *in situ* techniques to determine volatile alkali metals and chlorine-containing compounds produced during coal combustion may shed light on this speculation.

ACKNOWLEDGEMENT & DISCLAIMER

This report was prepared by M.-I. M. Chou and the ISGS with support, in part, by grants made possible by the U.S. Department of Energy (DOE) Cooperative Agreement Number DE-FC22-PC92521 and the Illinois Coal Development Board (ICDB) and the Illinois Clean Coal Institute (ICCI). Neither authors nor any of the subcontractors nor the U.S. DOE, ISGS, ICDB, ICCI, nor any person acting on behalf of either assumes any liabilities with respect to the use of, or for damages resulting from the use of, any information disclosed In this report. Technical assistance by J.B. Bruinius and J. Zhao is acknowledged.

REFERENCES

1. Bettelheim, J.; Halstead, W.D.; Lcs, D.J.; Mortimer, D. Combustion problems associated with high chlorine coals: Erdol and Kohle-Erdgas *Petrochemie*, v. 33, p. 436, 1980.

2. Raask, E. *Mineral Impurities in Coal Combustion: Behavior, Problems and Remedial Measures*, Hemisphere Publishing Corporation, New York, 1985.
3. Wright, I.G.; Ho, K.K.; Mehta, A.K. Survey of the effects of coal chlorine on fireside corrosion in pulverized coal-fired boilers, in Proceedings of EPRI Symposium The Effects of Coal Quality on Power Plants: Fourth International Conference" August 17-19, 1994 Charleston, SC.
4. Meadowcroft, D.B.; Manning, M.I.(editors) Corrosion Resistant Materials for Coal Conversion Systems, Applied Science Publishers, New York, 1983.
5. American Society for Testing Materials, 1991, Annual Book of ASTM Standards, D-2492, p. 289-294.
6. Hamling, J.W. and D.D. Kaegi, Characterization and Removal of Chlorides in Illinois Coal, Proceeding of the First Annual Pittsburgh Coal Conference, 849-855, September 17-24, 1984.
7. Chou, C.-L. 1991 Distribution and forms of chlorine in Illinois Basin coals. In: Stringer, J. and Banerjee, D.D. (eds), Coal Science and Technology 17: Chlorine in Coal, Elsevier Science Publishing Co., New York, p 11-29.
8. Huggins F.E. and G.P. Huffman, Chlorine in Coal: A XAFS Spectroscopic Investigation, Fuel, 1995, 74, 556-569.
9. I. Demir, R.R. Ruch, J. Steele, and S. Kahn, Washabiltiy of Trace Elements in Product (Marketed) Coals from Illinois, ISGS Open File Series in press 1995.
10. Huffman, G.P., N. Shan, F.E. Huggins,L.M. Stock, K. Chatterjee, J.J. Kilbane, M.-I.M. Chou, and D.H. Buchanan. Sulfur speciation of desulfurized coals by XANES spectroscopy, Fuel, 1995, 74, 549-555.
11. Liu, J., Behavior of Chlorine in Illinois Coals Comparing with that in British Coals During Combustion and Pyrolysis, A Master's Degree thesis presented to the faculty of the Department of Chemistry, Western Kentucky University, Bowling Green, Kentucky, 1994.
11. Chou, M.-I., W.P. Pan, F.E. Huggins, J.M. Lytle, L. Liu, and K.K. Ho. 1994. Chlorine in coal and boiler corrosion. proceedings of the 11th International Pittsburgh Coal Conference. Pittsburgh, PA. September 12 - 16, 1994. pp. 359-364.

Table 1. Ash composition and chlorine content in coals

Coal sample	Moisture	*Ash	*Na_2O	*K_2O	*Cl
Illinois coals					
C-32783	15.22	12.86	0.20	0.21	0.16
C-32779	12.62	9.63	0.14	0.20	0.08
C-32795	9.42	5.76	0.14	0.14	0.45
C-32661	6.79	8.17	0.07	0.20	0.26
C-32662	7.99	7.00	0.08	0.21	0.35
British coals					
C-33499	4.55	14.79	0.31	0.48	0.61
C-33500	4.16	22.24	0.31	0.89	0.43
C-33502	3.21	3.13	0.10	0.02	0.81

* % moisture free basis; Data on Illinois coals were provided by Dr. Ilham Demir of the ISGS.

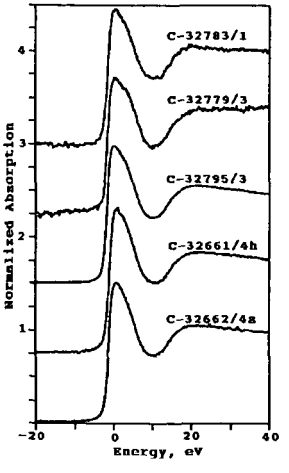

Figure 1: XANES spectra of the five Illinois coals and their specific geographic locations.

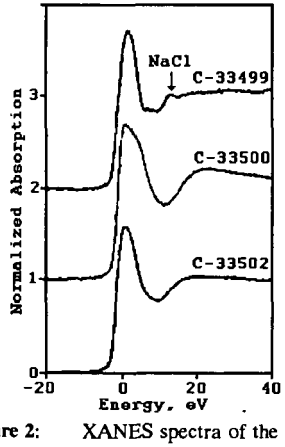

Figure 2: XANES spectra of the British coals.

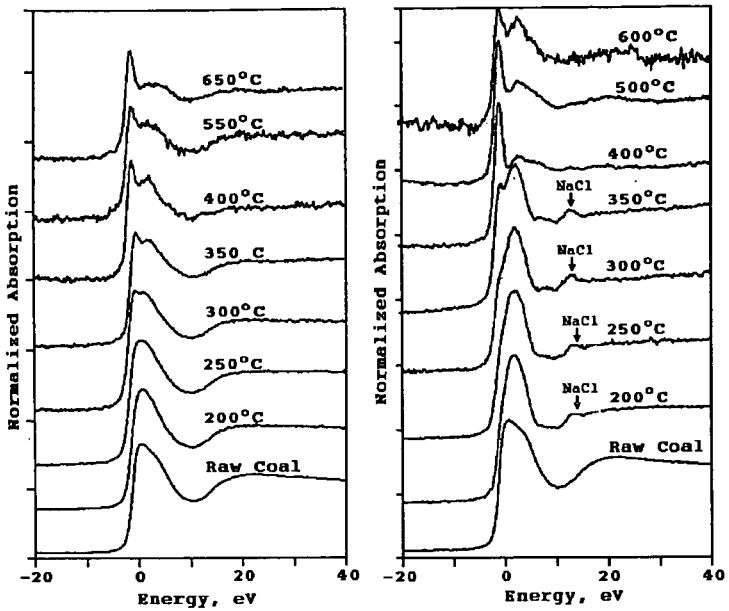

Figure 3: XANES spectra of one Illinois (C-32795, left) and one British (C-33500, right) coal and chars from step-wise heating under air.

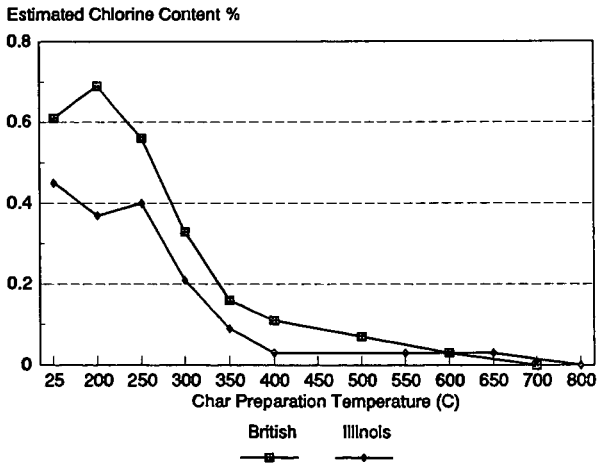

Figure 4: Comparing chlorine content in chars produced from stepwise heating of a British coal (C-32500) and an Illinois coal (C-32795) under air.

CONCURRENT CHANGES IN AGGREGATION AND SWELLING OF COAL PARTICLES IN SOLVENTS

Masaharu Nishioka

Nihon Rikagaku Laboratories,
2-5-601 Ohara-cho, Ashiya 659 Japan

Keywords: Solvent Swelling, Laser Scattering, Coal Association

INTRODUCTION

The behavior of solvent(-induced) swelling of coal without complete dissolution in any solvents has been used as evidence for the three-dimensionally cross-linked macromolecular network model of coal structure. Sanada and Honda[1] applied the statistical theory of rubber elasticity to coal swelling. Since then coal swelling has been used to characterize the macromolecular nature of coal by many workers[2-10]. Four major methods have been used: the volumetric method using glass tubes[11-13], the gravimetric method[1,3,4], the method requiring a piston type of apparatus[10,14,15], and direct observation using a microscope[6,16-18]. The easiest and most commonly used one is probably the volumetric method.

The conventional volumetric technique with glass tubes was selected to investigate the physical structure of coal in this author's recent papers[19-22]. Some steps in the method were modified. Coal samples and solvents were weighed, and each initial height before swelling was calculated from the mass and bulk density of the samples. This was necessary to obtain reproducible results, particularly at low coal (slurry) concentration. In the previous paper[20], coal/solvent mass ratios (*C/S*) were used as an index of *concentration*. From this study, it was found that coal swelling is strongly dependent on C/S[20]. The high dependence of C/S on coal swelling is very important, because changes in swelling with C/S is not thermodynamically allowed for the three-dimensionally cross-linked network model.

The results showed that swelling ratios, Q, did not change in the common range of C/S = 10-20 % which is generally used for the conventional volumetric swelling method, but significantly increased at < C/S = 5 %[20]. At the low C/S, the dependence of coal concentration on Q is given by

$$Q = [Q]/(C/S)^n \qquad (1)$$

where

$$[Q] = \lim_{\log(C/S)\to 0} Q \qquad (2)$$

and n is a constant. $[Q]$ is defined as the intrinsic swelling ratio, which is independent of C/S. The $[Q]$ values were consistently more than two times larger than those conventionally observed. Therefore, conventionally observed swelling ratios are apparent values. It is thought that intra- and intermolecular (secondary) interactions are solvated more at a lower C/S value and coal swells more. The process of attaining associative equilibria is presumably very difficult when using the volumetric method. The dependence of C/S on coal swelling means that swelling changes depending on uniformity of coal and solvent. Coal and solvent are usually mixed only at the initial time with a thin rod. It is not practical to continuously mix coal and solvent for a long time, because it may take more than 24 h to reach its equilibrium value[21,22]. These strongly suggest that coal swelling should be measured at a very *low* coal concentration with *continuous mixing* for a given period to avoid the effect of these unknown factors. Furthermore, measurements of volumetric swelling at low C/S values are difficult. Therefore, an apparatus specifically designed for these factors is necessary.

The objective of this paper was to observe coal swelling in solvents at *low coal concentration with continuous mixing*. It can be thought that coal swelling is given by the difference of particle sizes between poor and good solvents. The measurement of particle sizes in solvents by a laser scattering method is applied to the system. The swelling ratio measurement by a particle size distribution was probably first suggested by Turpin *et al.*[17], but the details were not reported. The observation of coal swelling under the conditions is very important to better understanding of coal structure and also the behavior of coal particles in coal/oil systems in various processes.

EXPERIMENTAL

Blind Canyon (DECS-16) and Illinois No. 6 (DECS-2) coals (-20 mesh) were obtained from the DOE Coal Bank at Pennsylvania State University. These pyridine extracted coals (PI) were prepared by Soxhlet extraction for 3 days. Pyridine extracts (PS) were also used. PI and PS were dried under vacuum at 95°C overnight. All samples were ground with a agate set to arbitrary particle sizes (-100 mesh). The same lots of samples were used for particle size measurements. Standard polyvinylpyrrolidone with average molecular mass of 10,000 and cross-linked polyvinylpyrrolidone were obtained from Aldrich Chemical Co. These polymers as received were used for particle size measurements.

For a new method of swelling, Model LAB-TEC 1000 particle size analyzer (LASENTEC, Bellevue. WA) was used. This analyzer is a scanning laser type of apparatus[23]. When the focal spot intercepts a particle, some light is scattered back to the probe and converted into an electronic pulse, which is converted to size by the relationship:

$$d = v/t \qquad (3)$$

The duration of the pulse represents the time (t) the focal spot illuminated the particle. Since the velocity

(v) of the focal spot is known, the distance (d) for the focal spot scanned across the particle can be determined. This distance represents the length of a chord of the particle. Pulses representing the chord lengths are classified by counting circuits, then transferred to a computer for processing and presentation on a display or a printer. The LAB-TEC 1000 classifies particles into 29 channels, ranging from 0.2 to 250 μm. The distribution is presented in two ways in this study. Scanned count is the uncorrected random chord frequency distribution. Volume diameters are the distribution of volume, derived from the scanned count data, when particles are assumed to be spherical. The mean volume diameter and the mean diameter with scanned counts are shown as Dv and Dc, respectively. LASENTEC® measuring beakers (100 ml) were used for a sample container. Samples were agitated with a magnetic stirrer during measurement.

RESULTS AND DISCUSSION

Attempt of swelling ratios by particle size distribution

The reproducibility of measurements using this particle size analyzer was confirmed with a standard powder sample provided by the manufacturer before every measurement. The critical factor to obtain reliable results was to adjust a focal point of laser to the inner wall of the measuring beaker. Once the focal point is carefully tuned, measurements of the particle size distributions were reproducible.

The particle size distribution of the PI sample from Blind Canyon (DECS-16) coal ground to arbitrary was measured in methanol and pyridine. The coal concentration was 0.25 g/100 ml (coal/solvent). Since the evaluation method using glass tubes can be used only down to the value of C/S = 2-3 %, this coal concentration was relatively low for the swelling measurement. In addition to low coal concentration, coal particles were observed with continuous mixing. Laser was continuously scanned for several hours, and the distributions averaged every 20 scans were monitored several times. This was repeated for one week after preparation of samples. Any significant change in the distributions was not observed for these measurements.

Figure 1 shows the particle size distributions of this sample with volume diameters in (a) methanol and (b) pyridine. The distribution in methanol did not significantly change with time, while that in pyridine changed from time to time. The change in the distribution in pyridine was not dependent on time but apparently reversible from time to time. Two typical distributions in pyridine are shown here. The Dv value in methanol was 120 μm, while pyridine values were (b-1) 130 μm and (b-2) 60 μm. Methanol is a very poor solvent for coal, while pyridine is one of the best. The particle size distributions in pyridine were, however, approximately the same or smaller than that in methanol. This is surprising, because swelling ratios of high-volatile bituminous coals can be estimated to be more than 3 at this concentration range by the conventional volumetric method[20]. The above measurements were also evaluated using PI from Illinois No. 6 (DECS-2) coal. General results obtained from the DECS-16 coal were again similar for this sample.

Particle size distribution of standard polymers

To confirm the above proposed mechanism, the particle size distribution of standard polymers was evaluated under the same conditions. Fine powders of polyvinylpyrrolidone (average molecular mass; 10,000) and cross-linked polyvinylpyrrolidone as received were used. Polyvinylpyrrolidone readily dissolves in methanol and water, but does not dissolve in *n*-hexane and toluene. Toluene is a slightly better solvent than *n*-hexane. The distribution in toluene changed from time to time, and two representative distributions are shown. Mean volume diameters determined were 14 μm in *n*-hexane and 18 and 31 μm in toluene, respectively. The difference between these distributions is small, but the change in particle sizes with larger diameters is seen in toluene. The change was apparently reversible.

The particle size distribution of cross-linked polyvinylpyrrolidone was evaluated next in methanol and *n*-hexane. *Figure 2* compares these distributions with scanned counts at a concentration of 0.50 g/100 ml (polymer/solvent). As a significant portion of particle volume diameters exceeded 250 μm, the distributions with scanned counts are presented. The specific swelling ratio (Q)[20] of this sample in methanol and *n*-hexane were 4.0 and 3.0, respectively. This suggests that methanol is a better solvent than *n*-hexane and swells the polymer. Therefore, the particle size of this polymer in a good solvent (methanol) was expected to be larger due to swelling. The results, however, shows that particle sizes in methanol (Dc=34 μm) are actually smaller than those measured in *n*-hexane (Dc=53 μm). One interpretation is that this cross-linked polymer is initially swollen in methanol but concurrently disaggregates. The overall particle size distribution may reflect these adverse effects.

It was notable that particle sizes of pyridine extracted DECS-2 and -16 coals observed in pyridine and methanol were nearly equal, considering the volumetric swelling in pyridine was much larger than in methanol. Apparent reversible changes in the particle size distribution of coal were observed in pyridine. The results obtained from standard polymers are consistent with these results.

Change in numbers of coal particles in solvents

From the above results, the following behavior of coal particles in solvents is suggested: Coal particles are highly aggregated even at the relatively low C/S values. Coal particles are swollen, but interparticle disaggregation also occurs in good solvents. This may lead to apparent small coal swelling in good solvents observed by particle size distributions. If this interpretation is correct, numbers of coal particles should be different between poor and good solvents. Numbers of coal particles can be measured as numbers of light scattered back to the probe by this apparatus.

The numbers of particles of the PI from DECS-2 coal were evaluated in methanol, toluene, chloroform and pyridine at concentrations of 0.1 - 0.5 g/100 ml. *Figure 3* shows the accumulated channel % for ≤ 1.3 μm. Obviously, coal particles with small diameters increased in the order of better solvents for coal; methanol, toluene, chloroform and pyridine at all concentrations tested.

Effect of coal concentration on the particle size disiribution

Volumetric swelling increases at low coal concentration[20]. The evaluation method using glass tubes was used down to the value of *C/S* = 2-3 %. The particle size distribution was investigated to evaluate the effect of coal concentration at further low values. Volume diameter distributions for the DECS-16 coal were measured in coal concentration from 1 g to 0.1 g per 100 ml pyridine. Since the dependence of coal concentration on volumetric swelling was remarkable below C/S = 2-3 %, a notable increase in the particle size would be expected at the concentrations of 1 to 0.1 g/100 ml. No significant increase in the particle size with a decrease in coal concentration was found, but a decrease in the particle size is noted at lower coal concentrations. These results again demonstrate the significant variance in coal swelling observed by two different procedures; the volumetric swelling and the particle size distribution methods. The results can be interpreted on the bases of the proposed mechanism. Coal particles may swell at low coal concentration to large extent, but interparticle disaggregation due to a decrease in coal concentration seems to control the overall particle size distribution.

CONCLUSIONS

A new method of coal swelling has been developed under the condition of low coal concentrations with continuous mixing of coal and solvent. The change in particle size distributions by a laser scattering procedure was used for the evaluation of coal swelling. Particle size distributions in good and poor solvents were nearly equal, but reversibly changed in good solvents from time to time. It was concluded that aggregated coal particles disaggregate in good solvents, and that an increase in the particle size distribution due to swelling in good solvents are compensated by a decrease in the particle size due to disaggregation. Therefore, the behavior of coal particles in solvents is controlled by aggregation in addition to coal swelling. This implies that an increase in the particle size due to coal swelling in actual processes is not so large as expected by the results obtained from the conventional coal swelling methods.

ACKNOWLEDGEMENT

This work was partly supported by the U.S. Department of Energy under Contract No. DE-AC22-92PC91047 when this author was at Viking Systems International.

REFERENCES

1 Sanada, Y. and Honda, H. *Fuel* 1966, **45**, 295
2 Larsen, J. W. and Kovac, J. in 'Organic Chemistry of Coal' (Ed. J. W. Larsen), American Chemical Society, Washington, DC, 1978, Ch. 2
3 Lucht, L. M. and Peppas, N. A. in 'New Approaches in Coal Chemistry' (Eds. B. D. Blaustein, B. C. Bockrath and S. Friedman), American Chemical Society, Washington, DC, 1981, Ch. 3
4 Nelson, J. R. *Fuel* 1983, **62**, 112
5 Szeliga, J. and Marzec, A. *Fuel* 1983, **62**, 1229
6 Brenner, D. *Fuel* 1984, **63**, 1324
7 Matturro, M., Liotta, R. and Isaacs, J. J. *J. Org. Chem.* 1985, **50**, 5560
8 Hsieh, S. T. and Duda, J. L. *Fuel* 1987, **66**, 170
9 Painter, P. C., Park, Y. and Coleman, M. M. *Energy & Fuels* 1988, **2**, 693
10 Hall, P. J., Marsh, H. and Thomas, K. M. *Fuel* 1988, **67**, 863
11 Liotta, R., Brown, G. and Issacs, J. *Fuel* 1983, **62**, 781
12 Green T. K., Kovac, J. and Larsen, J. W. *Fuel* 1984, **63**, 935
13 Otake, Y. and Suuberg, E. M. *Fuel* 1989, **68**, 1609
14 Aida, T. and Squires, T. G. *Am. Chem. Soc. Div. Fuel Chem. Prepr.* 1985, **30**(1), 95
15 Eser, S., Jenkins, R. G., Wei, G., Schobert, H. H. and Joseph, J. T. *Fuel* 1991, **70**, 1445
16 Brenner, D. *Fuel* 1985, **64**, 167
17 Turpin, M., Ellis, B. and Rand, B. in 'International Conference on Coal Science' (Eds. J. A. Moulijin, K. A. Nater and H. A. and G. Chrmin), Elsevier, New York, 1987, p. 85
18 Cody, G. D. Jr, Larsen, J. W. and Siskin, M. *Energy & Fuels* 1988, **2**, 340
19 Nishioka, M. *Fuel* 1993, **72**, 997
20 Nishioka, M. *Fuel* 1993, **72**, 1001
21 Nishioka, M. *Fuel* 1993, **72**, 1719
22 Nishioka, M. *Fuel* 1993, **72**, 1725
23 LAB-TEC 1000 User's Manual

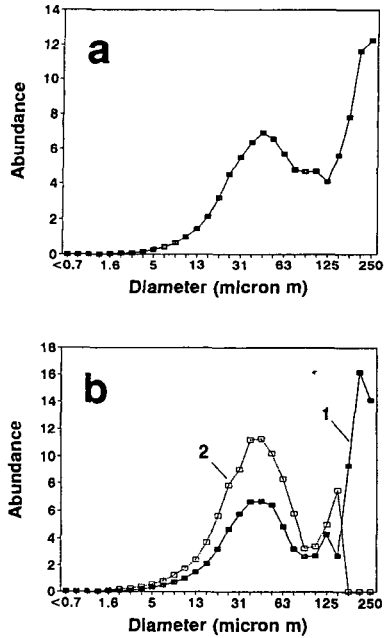

Figure 1 Particle size distribution with volume diameters of the pyridine extracted DECS-16 coal at coal/solvent = 0.25 g/100 ml, (a) in methanol (*Dv*; 120 μm), (b-1) in pyridine (*Dv*; 130 μm) and (b-2) in pyridine at another scanning (*Dv*; 60 μm) (average of 20 cycles)

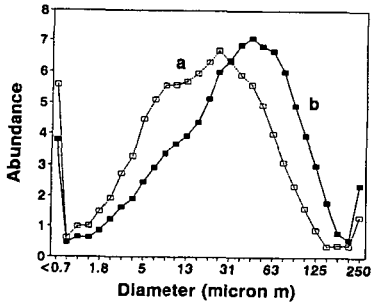

Figure 2 Comparison of particle size distributions with scanned counts of cross-linked polyvinylpyrrolidone at sample/solvent = 0.50 g/100 ml, (a) in methanol (*Dc*; 34 μm) and (b) *n*-hexane (*Dc*; 53 μm) (average of 20 cycles)

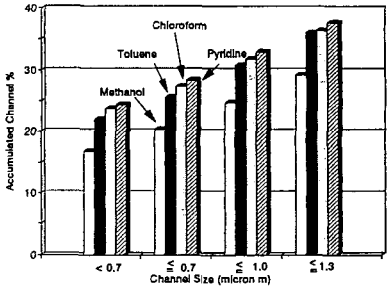

Figure 3 Accumulated channel % for channel sizes of ≤ 1.3 μm for the PI sample from DECS-2 coal

Applications of the ^{13}C NMR Magic Angle Turning Experiment to Coal Studies

R. J. Pugmire[a], W. Wang[b], M. S. Solum[b], D. M. Grant[b], and J. Z. Hu

Departments of Chemical and Fuels Engineering[a] and Chemistry[b]
University of Utah, Salt Lake City, Utah 84112, USA
and Wuhan Institute of Physics., Chinese Academy of Science, Wuhan, The People's Republic of China

Keywords: ^{13}C NMR, Two Dimensional Spectroscopy, Coal Structure

INTRODUCTION

One of the important contributions of high resolution ^{13}C CP/MAS to coal science is the measurement of the structural parameters of coal.[1-2] It has been demonstrated[3-5] that the structural parameters directly derived from ^{13}C CP/MAS experiments can be utilized to predict the details of coal devolatilization and char formation processes. One of the advantages of spinning a solid sample at the magic angle is the reduction of the line broadening contributions due to the chemical shift anisotropy (CSA). The chemical shift anisotropy is proportional to the strength of the external magnetic field and the CSA of aromatic carbons (200-240 ppm) is greater than that of the aliphatic carbons (20-100 ppm). When the sample is spun at the magic angle the CSA induced powder patterns break up into spinning sidebands and, in order to obtain a ^{13}C CP/MAS spectrum in which the aromatic carbon sidebands do not overlap the aliphatic carbon signals, it is necessary to spin the sample at approximately 4 KHz at a magnetic field of 2.35 Tesla. At a higher magnetic field strength a greater spinning rate is required. High speed magic angle spinning not only reduces the contributions of the spinning side bands but it also destroys very useful information on the local electronic environment that is embedded in the principal values of the CSA tensors.

The CSA exhibits three frequency components for each carbon in a powdered sample, the principal values, and spinning the sample at the magic angle averages these three values to the isotropic chemical shift of each nucleus. Hence, elimination of the CSA contribution increases the spectral resolution in conventional CP/MAS experiments but also throws away two thirds of the available data for each carbon. Thus, a major dilemma exists between spectral resolution and the richness of the data that is contained in powdered samples such as coal. Fortunately, the recently developed two-dimensional (2D) magic angle turning (MAT) experiments, (the triple echo-MAT[6] and PHORMAT[7]) when applied at an extremely slow rotation rate, can provide both types of information without serious penalty. In the MAT experiments, a sideband free isotropic chemical shift spectrum which has resolution in the isotropic shift dimension comparable to the standard CP/MAS spectrum is obtained by projecting the 2D data onto the evolution frequency axis. Concurrently, an essentially static powder pattern is projected onto the acquisition frequency axis and the powder pattern for each individual isotropic chemical shift is obtained by simply taking a spectral slice at the specified isotropic chemical shift value in the acquisition dimension.[6-8] In this paper, the power of the MAT experiments is further explored in a study of coals at a magnetic field strength of 9.4 Tesla.

EXPERIMENTAL

The experiments were performed on a Chemagnetics CMX-400 spectrometer with a ^{13}C frequency of 100.6 MHz. The probe used was a Chemagnetics pencil rotor design and samples were spun at *ca.* 30 Hz in a 9.5 mm rotor with a specially built low speed drive tip. The proton decoupling field strength on this probe is 50 KHz. The spinning speed was maintained within 0.25 Hz with a Chemagnetics speed control unit and the pulse sequences used are described elsewhere.[6-8]

Results and Discussion

The usefulness of the MAT experiments can best be described by examining the data obtained from a model compound with a diversity of carbon types. The PHORMAT pulse sequence[7] was used to generate the composite data in Figure 1 in which the two-dimensional (2D) contour plot of p-ethoxyphenylacetic acid is displayed. All ten carbons are clearly resolved in the contour plot. The isotropic chemical shifts of these carbons are projected onto the evolution axis while the composite powder pattern data are projected onto the axis representing the acquisition dimension. As previously described,[6-8] the principal values of the CSA tensors of each carbon can be found by examining the powder patterns taken at the individual isotropic chemical shift frequencies. Figure 3 displays a stacked plot of the powder patterns at the isotropic chemical shift frequency of each carbon. In this case none of the carbons overlap and, hence, no ambiguity is encountered in identifying the types of carbons associated with each powder pattern. Orendt, et. al.[2] have described the general shapes of powder patterns associated with different types of aromatic carbon functional groups, e.g., protonated, alkyl substituted, aryl ethers, and bridgehead carbons. The powder

patterns for the methyl, CH_2-, and CH_2O- groups in p-ethoxyphenylacetic acid also exhibit characteristic shapes which can be used to identify overlapping carbon signals. The analysis of overlapping powder patterns in carbons with accidental degeneracy of the chemical shifts has been described by Hu, et. al.[6], and Wang, et. al.[9] for model compounds and for coals.[8]

The application of the triple-echo version of the MAT experiment to coal samples has been previously reported.[6,8] The PHORMAT version of the MAT experiment does not require spectral shearing, as in the triple-echo MAT experiments, which simplifies the extraction of the principal values. The 2D PHORMAT data for Pocahontas #3 coal is presented in Figure 2. At first glance, one could assume that the useful information obtainable from the data is no greater than that of the standard CP/MAS experiment. However, by examining the spectral slices obtained at different isotropic chemical shifts, one can readily recognize the contributions from different types of carbon atoms. Figure 4 exhibits spectral slices taken at selected isotropic chemical shift values in the aromatic region from the data portrayed in Figure 3. One can easily recognize the characteristic line shapes of powder patters due to substituted, bridgehead, and substituted aromatic carbons. One can also identify the features of composite patterns derived from overlapping signals from different structural types of carbons, i. e., protonated/bridgehead (slices at 120, 125, and 130 ppm), bridgehead/substituted (slices at 130 and 135 ppm), and substituted (slices at 135, 140, and 145 ppm). In Figure 4 the heavy vertical lines represent the frequency for the δ_{22} components of the protonated, bridgehead, and substituted carbons.

2D data set on experimental data of this type in model compounds. Versions of these tools have been used for analysis of the spectral slices in coals and efforts are under way to expand these capabilities to include the entire 2D data set. It is interesting to note that the MAT experiments can also be used on polymer systems to refine the structural analysis and assess crystalline and non-crystalline components.

Acknowledgments

Support for this work was made available by the National Science Foundation through the Advanced Combustion Engineering Research Center, the U. S. Department of Energy Pittsburgh Energy Technology Center through the Consortium for Fossil Fuel Liquefaction Science (Contract No. DE-FCC22-93PC93053), and by Basic Energy Sciences, Office of Energy Research, U. S. Department of Energy (Contract No. DE03-94ER14452).

REFERENCES

1. M. S. Solum, R. J. Pugmire and D. M. Grant, Energy & Fuels, 3 (2), 187-193 (1989).
2. A. M. Orendt, M. S. Solum, N. K. Sethi, R. J. Pugmire and D. M. Grant, " Advances in Coal Spectroscopy" Edited by Henk L. C. Meuzelaar, Plenum Press · New York and London, 1992, Page 215-223.
3. T. H. Fletcher, A. R. Kerstein, R. J. Pugmire, M. S. Solum and D. M. Grant, Energy Fuels, 6 (4), 414-431 (1992).
4. T. H. Fletcher, M. S. Solum, D. M. Grant, and R. J. Pugmire, Energy Fuels, 1992, 643-650.
5. D. M. Grant, R. J. Pugmire, T. H. Fletcher and A. R. Kerstein, Energy Fuels, 3 (2), 175-186 (1989).
6. J . Z. Hu, A. M. Orendt, D. W. Alderman, R. J. Pugmire, C. Ye and D. M. Grant, Solid State NMR, 1994, 3, 298.
7. J. Z. Hu, W. Wang, F. Liu, M. S. Solum, D. W. Alderman, R. J. Pugmire, and D. M. Grant, J. Magn. Reson., 1995, A113 (in press).
8. J. Z. Hu, M. S. Solum, R. J. Pugmire, C. Ye, and D. M. Grant, Energy & Fuels, 1995 (in press).
9. W. Wang, J. Z. Hu, D. W. Alderman, R. J. Pugmire, and D. M. Grant, Solid State NMR, 1995, 4 (in press).

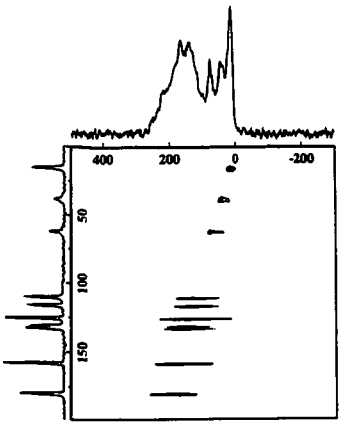

Figure 1. Two dimensional MAT data for p-ethoxyphenylacetic acid. The isotropic chemical shifts are projected on the evolution dimension while the powder patterns are projected on the acquisition dimension.

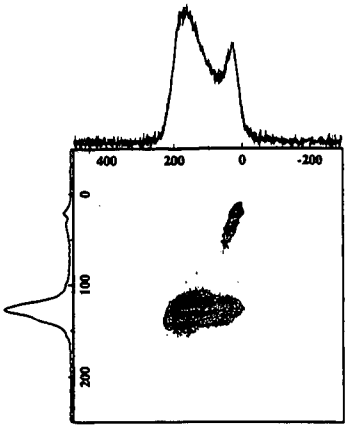

Figure 2. Two dimensional MAT data for Pocahontas #3 coal from the Argonne Premium Coal Sample Bank.

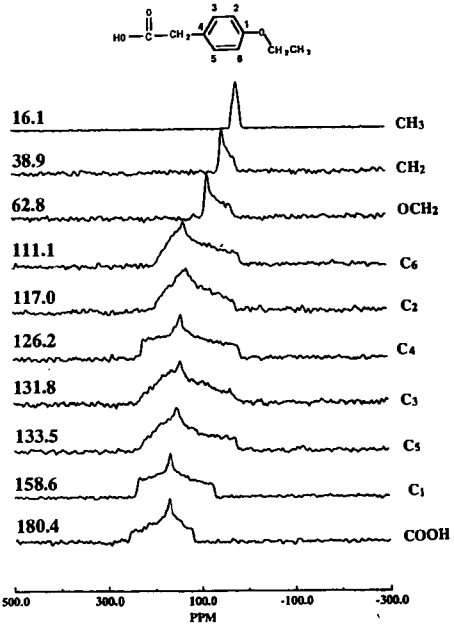

Figure 3. Powder patterns obtained from spectral slices taken from Figure 1.

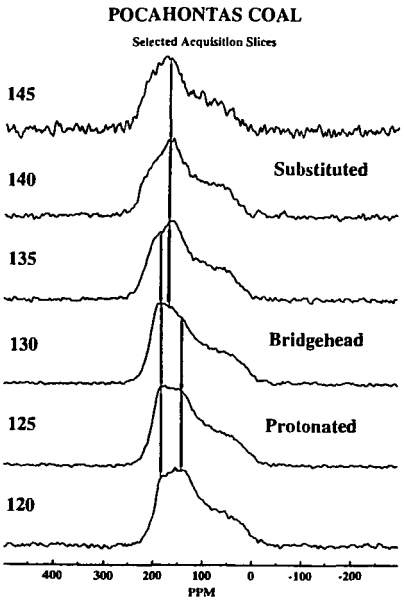

Figure 4. Powder patterns taken from Figure 2 at selected spectral slices illustrating composite patterns that still have features which can be attributed to protonated, bridgehead, and substituted aromatic carbons. The heavy vertical lines represent the approximate frequencies of the δ_{22} component of the principal values of the chemical shielding tensor for the different types of aromatic carbons.

APPLICATIONS OF TOROIDS IN HIGH-PRESSURE NMR SPECTROSCOPY

R. J. Klingler, J. W. Rathke, Klaus Woelk, Kurt W. Kramarz, and Rex Gerald
Chemical Technology Division
Argonne National Laboratory
Argonne, Illinois, 60439.

Keywords: high-pressure NMR, supercritical fluids, hydroformylation, NMR-imaging

Abstract

Toroid detectors have distinct NMR sensitivity and imaging advantages. The magnetic field lines are nearly completely contained within the active volume element of a toroid. This results in high NMR signal sensitivity. In addition, the toroid detector may be placed next to the metallic walls of a containment vessel with minimal signal loss due to magnetic coupling with the metal container. Thus, the toroid detector is ideal for static high pressure or continuous flow monitoring systems. Toroid NMR detectors have been used to follow the hydroformylation of olefins in supercritical fluids under industrial process conditions. Supercritical fluids are potentially ideal media for conducting catalytic reactions that involve gaseous reactants, including H_2, CO, and CO_2. The presence of a single homogeneous reaction phase eliminates the gas-liquid mixing problem of alternative two-phase systems, which can limit process rates and adversely affect hydroformylation product selectivities. A second advantage of toroid NMR detectors is that they exhibit a well-defined gradient in the rf field. This magnetic field gradient can be used for NMR imaging applications. Distance resolutions of 20 μ have been obtained.

Introduction

The vitality of the industrial process arena is strongly influenced by the development of new instrumental techniques. This work focuses on a special type of NMR detector whose unique properties make it an ideal choice for *in situ* NMR spectroscopic analysis of synthesis gas reactions. In addition, the same toroid NMR detectors are useful for imaging applications. In contrast to conventional NMR imaging techniques, the new toroid cavity NMR-imaging method retains all chemical shift and coupling constant information.

High-pressure NMR spectroscopy

One of the key properties of toroids for NMR applications is that the magnetic field lines are nearly completely contained within the windings of the coil. This contrast with the Helmholtz and solenoid coils that are typically used in commercial NMR spectrometers. In the latter type of coils, the magnetic field lines are more diffuse and extend well outside the coil windings, see Figure 1. The result is a signal-to-noise advantage of 3-5 for toroids compared with Helmholtz detectors [1-3]. More significantly for high pressure work, a toroid detector may be operated near the walls of a metallic containment vessel. Thus, in the cell design [4] of Figure 2, there is minimal dead volume. Furthermore, the small internal reactor volume of only 8 ml minimizes the amount of hazardous materials required for the experiments. The reactor in Figure 2 is routinely operated at 250 °C and 300 atm pressure. Typical *in situ* spectroscopic results obtained during the hydroformylation of propylene [5,6] are presented in Figures 3 and 4.

Special emphasis has been placed on exploring the use of supercritical fluids as homogeneous reaction media for catalytic synthesis gas transformations. Supercritical fluids consisting of carbon dioxide or water are environmentally benign solvents. Furthermore, separations of products may be accomplished by facile pressure alterations [7] instead of energy intensive distillations. In addition, mixing is not required for supercritical fluids. The oxo process is an important industrial reaction that is sensitive to gas-liquid mixing conditions [8]. Interestingly, we have found that the reaction exhibits improved straight chain aldehyde product selectivity [5,6] when the reaction is conduced in supercritical carbon dioxide as indicated in the last row of Table 1.

Supercritical fluids also have advantages for fundamental mechanistic analyses. Thus, the low viscosity of supercritical fluids results in NMR linewidths that are up to an order of magnitude sharper than those found in conventional organic solvents [5,9]. Thus, in benzene solvent where the ^{59}Co NMR linewidths are broader than those in Figure 4 by a factor of six,it would be difficult to resolve $HCo(CO)_4$ and $Co_2(CO)_8$. Furthermore, the acyl intermediate would not be detectable. The oxo process was investigated by a combination of

^{1}H, ^{13}C, and ^{59}Co spectroscopy under industrial process conditions. It was found that the high temperature reaction chemistry is dominated by mechanistically significant $\cdot Co(CO)_4$ radical concentrations which are formed by homolysis of the Co-Co bond in $Co_2(CO)_8$. The Co-Co bond dissociation enthalpy in $Co_2(CO)_8$ has been measured, $\Delta H^\circ = 19 \pm 2$ kcal/mole and $\Delta S^\circ = 29 \pm 4$ cal/(K·mol), by NMR magnetic susceptibility measurements over the temperature range of 120 to 225°C and from the contact chemical shift of the carbon monoxide ligand in the ^{13}C NMR spectra, $\Delta H^\circ = 19 \pm 2$ kcal/mole. The $\cdot Co(CO)_4$ radical induces a complex manifold of facile hydrogen atom transfer reactions that may be quantitated by ^{1}H and ^{59}Co NMR line shape analysis [10].

NMR-Imaging

Toroid cavity detectors may be used for rotating frame spectroscopic imaging [11]. The well-defined rf field gradient that is produced within a toroid cavity [12] minimizes the problems that were encountered in early applications of the rotating frame imaging technique using surface coils [13]. The salient feature of the rotating frame imaging technique is that the high-resolution NMR spectral information is not lost as is the case in conventional magnetic resonance imaging (MRI). As an example, five capillaries containing different solvents were placed at a spacing of 0.8 mm outward from the center of the cavity. The result in Figure 5 demonstrates that in a single experiment, the toroid cavity imaging technique can chemically distinguish between water and acetone, in addition to identifying the location of these samples along the distance axis. The chemical shift resolution of this technique is equivalent to that of a normal NMR spectrum. Alternatively, the ultimate resolution with respect to distance for the toroid cavity detector is under study. The data in Figure 6 demonstrates the distance resolution by ^{19}F NMR spectroscopy of two Teflon layers that were placed around the central conductor of the toroid cavity resonator. The measured thickness of the Teflon layers, as well as their 20 μm separation, is accurately reproduced by the imaging data. This distance resolution is already better than that which can be attained for solid samples using conventional MRI techniques. This toroid cavity imaging technique could find a wide range of applications in the characterization of surface layers and in the production of advanced materials. Potential areas of application include *in situ* NMR monitoring of growth sites during ceramic formation processes, analysis of the oxygen annealing step for wires coated with high-temperature superconductors, investigation of the reaction chemistry as a function of distance within the diffusion layer for electrochemical processes.

Acknowledgement

Support for this work was provided by the office of Basic Energy Sciences, Division of Chemical Sciences, U.S. Department of Energy.

References

1. D. W. Alderman and D. M. Grant, 21st Experimental NMR Conference, Tallahassee, Florida, 1980.
2. T. E. Glass and H. C. Dorn, *J. Magn. Reson.* **52**, 518 (1983).
3. J. W. Rathke, *J. Magn. Reson.* **85**, 150 (1989).
4. J. W. Rathke, U. S. Patent 5,045,793 issued Sept. 3 (1991).
5. J. W. Rathke, R. J. Klingler, and T. R. Krause, *Organometallics*, **10**, 1350 (1991).
6. J. W. Rathke and R. J. Klingler, U. S. Patent 5,198,589 issued Mar. 30 (1993).
7. M. McHugh, U. Krukonis, *Supercritical Fluid Extraction*; Butterworths: Stoneham, MA, 1986.
8. R. L. Pruett, In *Advances in Organometallic Chemistry*; F. G. A. Stone and R. West, Eds.; Academic Press: New York, 1079; Vol. 17, pp 1-60.
9. J. M. Robert and R. F. Evilia, *J. Am. Chem. Soc.* **107**, 3733 (1985).
10. R. J. Klingler and J. W. Rathke, *J. Am Chem. Soc.* **116**, 4772 (1994).
11. K. Woelk, J. W. Rathke, and R. J. Klingler, *J. Magn. Reson.* **105**, 113 (1994).
12. K. Woelk, J. W. Rathke, and R. J. Klingler, *J. Magn. Reson.* **109**, 137 (1994).
13. D. I. Hoult, *J. Magn. Reson.* **33**, 183 (1979).
14. P. Pino, F. Piacenti, and M. Bianchi, In *Organic Syntheses via Metal Carbonyls*: I. Wender, P. Pino, Eds.; Wiley: New York, 1977; Vol. 2, pp 98.
15. I. Kisshenbaum and E. J. Inchalik, "Oxo Process," In Encyclopedia of Chemical Technology, 3rd ed., Vol. 16, John Wiley & Sons, New York, pp637-653 (1981).

Table 1. Selectivity in the Hydroformylation of Propylene

Solvent	n/i-Butyraldehydes
2,2,4 - Trimethylpentane[a]	4.6
Benzene[a]	4.5
Toluene[a]	4.4
Diethyl ether[a]	4.4
Ethyl alcohol, 95%[a]	3.8
Acetone[a]	3.6
Commercial plants[b]	3.0 - 4.1
CO_2 (0.5 g/ml)[c]	7.2

[a] T = 108 °C, P(CO) = 140 atm, $P(H_2)$ = 100 atm, ref 14.
[b] T = 140-180 °C, P(CO) = 100-150 atm, $P(H_2)$ = 100-150 atm, ref 15.
[c] T = 80 °C, P(CO) = 56.1 atm, $P(H_2)$ = 56.1 atm, ref 5,6.

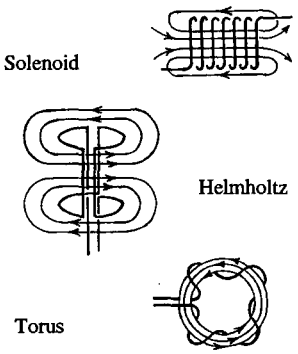

Figure 1. NMR detector coils.

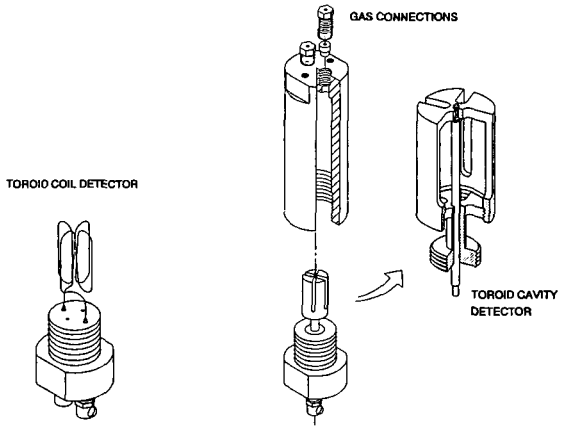

Figure 2. High-pressure NMR cell with toroid coil or cavity detector.

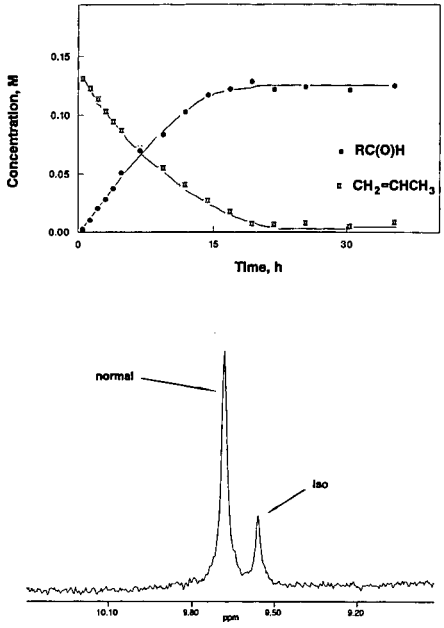

Figure 3. Butryaldehyde product mixture based on *in situ* ^{1}H NMR spectra during the hydroformylation of propylene in supercritical carbon dioxide at 80 °C.

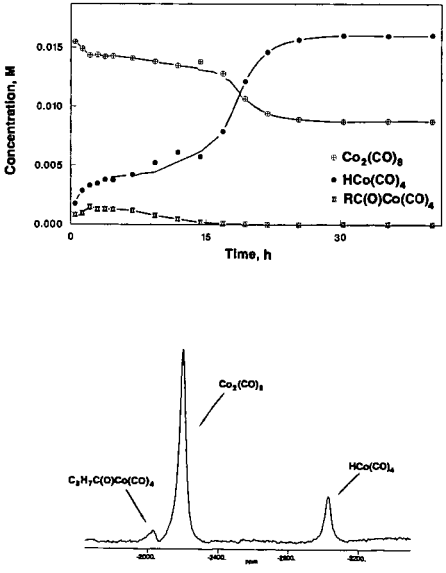

Figure 4. Organocobalt intermediates based on ^{59}Co NMR spectra during the hydroformylation of propylene in supercritical carbon dioxide at 80 °C.

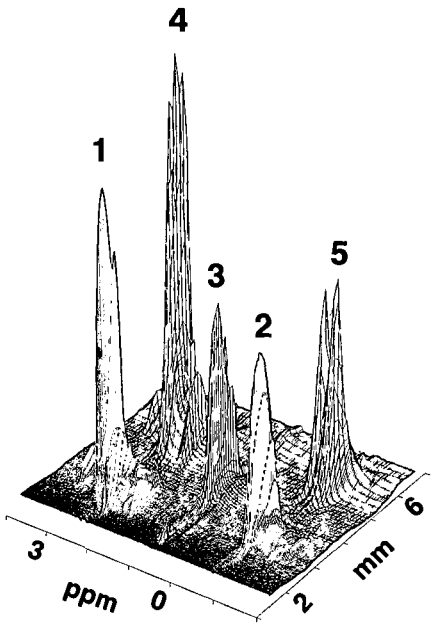

Figure 5. Simultaneous resolution of NMR chemical shift and radial displacement for five capillary tubes containing: 1, water; 2, isopropanol; 3, acetone; 4, water; and 5, isopropanol.

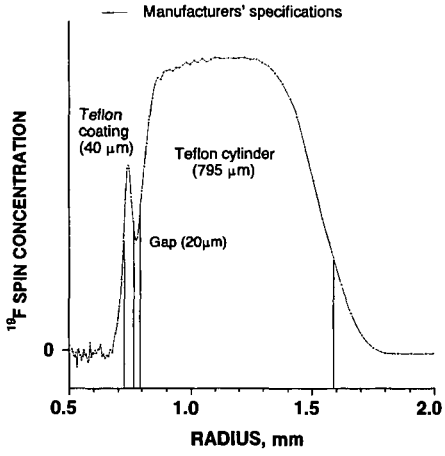

Figure 6. Plot of teflon concentration versus radial displacement based on ^{19}F NMR imaging.

VERY HIGH FREQUENCY EPR OF SULFUR COMPOUNDS IN COAL

R. B. Clarkson, R. L. Belford, P. Ceroke, W. Wang, W. Shi, K. Motsegood,
A. Smirnov, T. Smirnova, M. J. Nilges
Illinois EPR Research Center
University of Illinois, Urbana, IL 61801

Keywords: Aromatic sulfur, EPR, quantitative measurement

INTRODUCTION

The overall goal of our work during the last five years has been the non-destructive elucidation of molecular structure in coal and coal-derived materials [1]. Special emphasis has been placed on determining the concentration and molecular forms of organic sulfur in coal. Our approach has been to use the naturally occurring unpaired electrons in coal as reporters of their environment, making use of electron magnetic resonance (EMR) spectroscopy to develop a detailed picture of the types and arrangements of atoms "seen" by the electrons. During this period, we constructed the first 95 GHz (W-band) EMR spectrometer in the USA (and the second in the world). With this advanced spectrometer, we were the first to discover that the aromatic sulfur in coal produced a unique EMR signature. Extensive experimental and theoretical work on model aromatic sulfur compounds in the thiophene series (thiophene, benzothiophene, dibenzothiophene, etc.) has enabled us to develop a detailed understanding of the relationships between the molecular and electronic structure of these compounds and their EMR spectra. This new basic scientific knowledge in turn allowed us accurately to analyze the W-band EMR spectra from coal, desulfurized coal, and a variety of coal derived materials. We developed an automated computer program (based on spin quantum mechanics) which can analyze the EMR spectra and which reports the aromatic sulfur content of the coal as well as key spectral parameters. This analysis method has been tested on coal blends of know sulfur content as well as on a variety of coals from the IBCSP and elsewhere. The precision of the method is conservatively ± 0.1% of the aromatic sulfur in the sample. Identical samples measured both by EMR and XANES gave nearly identical results. The EMR technique has the twin advantages of simplicity and absolute concentration readout; an analysis takes less than five minutes to perform. Applications of the EMR technique include the determination of aromatic sulfur in coal, evaluation of the effectiveness of desulfurization technologies, and the evaluation of the effects of desulfurization on the rest of the molecular forms in coal.

EXPERIMENTAL PROCEDURES

A. Coal Sample Preparation

Significant progress has been made in the development of a standard protocol for coal sample preparation. Following the same protocol for all the samples allows the direct comparison of results from various types of coals. The development of a standard method also allows the calibration of the precision of the techniques and calculation of error limits. The techniques developed must allow for the sensitivity of coal samples to oxygen.

Since the EPR lineshape changes when samples are exposed to oxygen, preparation of coal samples for EPR analysis is done in a nitrogen atmosphere glove bag. All the necessary items needed for coal sample preparation, including the coal samples are exposed to nitrogen environment for two to three days. The oxygen concentration inside the bag is monitored continuously by keeping an oxygen sensitive electrode in the glove bag. The oxygen meter used is manufactured by "Yellow Springs Instrument Company" Yellow Springs, Ohio. The electrode utilizes a membrane with a KCl solution on the inside. The membrane must be kept wet so the electrode is stored in a beaker of distilled water. This meter gives oxygen concentration directly in ppm. EPR sample tubes are prepared at the oxygen level ~4-6 ppm. The EPR sample tubes (.7 mm O.D. quartz tube) are sealed at one end before being placed inside the glovebag. After the tubes are filled, a high quality vacuum grease is applied on the open end and tubes were carefully transferred in small labeled plastic vials. The vials are removed from the glovebag only when EPR spectroscopy is done.

B. W- Band EPR Spectroscopy

The key to our work plan is the W-band spectrometer. This unique instrument has been built over the last three years, and now incorporates several important technical innovations that make it well-suited for the present research work [2]. All spectroscopy at W-band (ca. 95 GHz) is done on the instrument constructed in our laboratory. Routine spectra were taken under nitrogen gas flow to avoid any possible oxygen sensitive changes. Lower power (15 db) is used to avoid saturation effects. Different modulation amplitudes were tried and finally a best compromise was achieved between the S/N ratio and the resolution of the spectrum. Data is acquired by a computer, which also controls the magnetic field sweep of the experiment.

C. Model Compounds

A 1000:1 mole ratio mixture of powdered boric acid (Aldrich) and the selected member of the thiophene series (thiophene, benzothiophene, dibenzothiophene, benznaphthothiophene, dinaphthothiophene, thianthrene) is heated to the melting point of boric acid (190°C). The molten mass is vortexed to maximize the dispersion of the selected thiophene in the molten solution and then allowed to cool to a glass. The glass is crushed into fine powder and loaded into a quartz sample tube. The tube is placed in a Ray-O-Net irradiation unit and subjected to UV irradiation at 254 nm for 20 to 30 minutes. The sample tube is then removed from the UV light and sealed for analysis. Degassing before and after the irradiation shows no effect on the EPR spectra. This method is a convenient way to produce matrix-isolated ionic radicals at room temperature. Their disordered state closely approximates the environment of similar compounds found in coal. Data on the model compounds is summarized in Table I [3].

We have used four microwave frequencies, S-band (2-4 GHz), X-band (9.5 GHz), Q-band (35 GHz), and W-band (95 GHz) to study the radicals produced by this method. CW saturation behavior of the organic radicals has been studied. Modulation amplitude profiles of the sample are routinely probed to achieve the best compromise between the S/N and resolution of possible hyperfine structure. Wide magnetic field scans have been performed for the sample at X-band to make sure all signals are accounted for. Low temperature experiments at liquid nitrogen temperature (77 K) were also performed for the sample at 9.5 GHz; no discernible difference in EPR parameters (g and linewidth) were observed, suggesting that the radical is a rigid structure at room temperature. Care has also been taken to avoid distortion of the signal by RC filters.

X-band and Q-band spectra were obtained from Varian E-line EPR spectrometers outfitted with a tracking Varian NMR gaussmeter and a HP frequency divider with a Fluke frequency counter. W-band EPR is performed using the spectrometer system built in our laboratory. All g-value measurements are based on direct field and frequency measurements. A statistical treatment of the g-matrix measured from seven independently prepared samples of DBT in BAG shows that experimental errors are very small (max. standard deviation, $\sigma_{n-1}=11\times10^{-5}$). S-band ESEEM is done on a locally-built Electron Spin Echo (ESE) spectrometer.

A computer-assisted analysis using an EPR powder spectrum simulation program and the spectral parameter optimization routine based on the SIMPLEX algorithm are performed to: 1) confirm the direct measurements of principal g values, 2) extract possible hyperfine interaction, and 3) accurately assess the linewidths and lineshapes. The calculation of principal values of the g matrix is based on Stone's theory (ref Stone) with certain modifications. The SCF-MO wave function and orbital energies are obtained from the semi-empirical method PM3 in MOPAC (ref QCPE 455) All calculations employ an IBM R6000 workstation.

RESULTS AND DISCUSSION

The anisotropic g matrix is one of the most important and fundamental EPR parameters. It is generally viewed as characteristic of the electronic structure of the molecule that contains one or more unpaired electrons. But for most organic radicals, the elements of the g matrices are very close to the free-electron value ($g_0 = 2.00232$). Experimentally resolving such small differences was difficult using conventional 9.5 GHz EPR, and this greatly limited the usefulness of g matrix as a structure indicator. The development of very high frequency EPR (VHF-EPR) has overcome this problem. From the simple resonance condition one can see easily that the difference in resonance fields for two slightly different g factors is proportional to the product of the microwave frequency and the difference between the two g factors.

$$\Delta B = B_1 - B_2 = \frac{2\pi\hbar\nu}{\beta}\left(\frac{1}{g_2} - \frac{1}{g_1}\right) = \left(2\pi\frac{\hbar}{\beta}\right)\left(\frac{\Delta g}{g_1 g_2}\right)\nu$$

Therefore the g resolution will be enhanced by a factor of 10 on going from X-band (9.5 GHz) to W-band (95 GHz) providing the line does not broaden substantially with microwave frequency.

At a sufficiently high field, the electronic Zeeman interaction will dominate the electron-nuclear hyperfine interaction, and both the electron and nuclear spins will be quantized along the external field. Under favorable conditions, the anisotropic hyperfine coupling matrix, A, can be resolved or partially resolved along the canonical directions of g matrix, yielding additional valuable information about molecular structure and other properties related to the ground electronic state of a molecule. Indeed, we have observed the anisotropic A matrix in the continuous wave VHF-EPR spectra of a series of thiophenic radicals. In addition, an auxiliary experiment using a low frequency pulsed spectrometer at S-band (2-4 GHz) also reveals the anisotropic hyperfine interactions between the

electron spin and the ring protons.

The multifrequency approach has resulted in a unified set of magnetic parameters (g and A matrices), from which it is possible to identify and characterize the radical species in terms of properties related to its molecular orbital structure. The total spin energy Hamiltonian for an electron with spin S is written:

$$\mathcal{H}_{spin} = \mathcal{H}_{ez} + \mathcal{H}_{so} = \beta_e \, B \cdot (L + g_e \, S) + \lambda \, L \cdot S$$

The shift due to organic heteroatoms (O and S) results from a change in resonance energies caused by anisotropy in g_e and the spin-orbit constant λ, coupling the spin and orbital angular momenta (L). The larger the field shift ΔB, the more sensitive our experiment will be to the presence of sulfur. It is for this reason that we observed the shift due to sulfur at higher spectrometer frequencies. Since XANES results from Illinois coals shows that thiophenic sulfur is the aromatic form in which the majority of organic sulfur is found in these coals, the connection between molecular and electronic structure found in the series of model thiophènes can be used as a basis for the analysis of VHF-EPR spectra from coal.

Several experiments have been performed to test the accuracy of the VHF-EPR method for aromatic sulfur analysis in coal. The first of these tests was suggested by Dr. Ken Ho, ICCI project monitor, and consisted of of making blends of two coals of known sulfur composition. VHF-EPR analyses of these blends then could be checked against the *known sulfur content*. Accordingly, a vitrinite (organic sulfur 2.9% dmf) and a sporinite (organic sulfur 4.25%) were blended, and the sulfur content of these blends measured by VHF-EPR was compared to the known composition. Figure 1 shows the results of this test. The VHF-EPR results agree with the known values to better than ± 0.1%.

The second type of test which was performed to evaluate the method was the direct analysis of organic sulfur content in a variety of coals of widely differing character, spanning the range of sulfur content from less than 0.5% to more than 11%. These coals were selected because each had been carefully analyzed for organic sulfur content by other chemical and physical methods. Figure 2 shows the excellent correlation between VHF-EPR analyses and the published organic sulfur content of these coals.

The third type of test which we performed to validate the VHF-EPR method was a direct comparison of results from the method and those obtained by XANES on identical samples. Sets of samples prepared by Dr. Steve Palmer, Southern Illinois University-Carbondale, were sent to Prof. G. Huffman, University of Kentucky, for analysis by XANES, as well as to us for analysis by VHF-EPR. Figure 3. shows the comparison of the two methods on four IBCSP coals. Nearly perfect agreement is seen in IBC 101, 102, and 106, while a considerable disagreement is seen in values for IBC 109. Figure 4 shows a similar comparison between VHF-EPR and IBCSP published values for *organic sulfur* in these coals. A comparison of Figures 3 and 4 show that the VHF-EPR determination of aromatic sulfur is at variance with both XANES and proximate analytical data in the case of IBC 109, and that a much better correlation exists for the XANES data than for the proximate analytical data. The reasons for disagreement in the case of IBC 109 are currently being investigated.

CONCLUSIONS

This research and development project has demonstrated a new analytical method for determining the aromatic sulfur content of coals and coal-related materials. It is based on VHF-EPR technology, and is non-destructive, quick, and precise. The method requires only a few tenths of a milligram of sample. The precision of this measurement seems less sensitive to sample oxidation than does XANES, although a much more detailed comparison of the two methods clearly is in order. VHF-EPR analysis for aromatic sulfur seems a good choice for routine coal characterization. It also should be very useful in the evaluation of various desulfurization technologies, and as a monitor of the extent of desulfurization. Several scientific questions remain for future work. These include: (a) the effects of spin exchange in modifying observed g-values in coals; (b) the effects of oxygen and sample oxidation; and (c) the advantages of working at magnetic fields *higher than 3.4 T.* Additional instrument development and fundamental research on items (a) - (c) could extend the technique into the analysis of heteroatomic oxygen as well as sulfur.

This work was prepared with the support, in part by grants made possible by the Illinois Department of Energy and Natural Resources through its Coal Development Board and Illinois Clean Coal Institute (K. Ho, project manager), and by the U. S. Department of Energy (DE-FC22-92PC-92521). However, any opinions, findings, conclusions, or recommendations expressed herein are those of the authors, and do not necessarily reflect the views of IDENR, ICCI, and the DOE.

REFERENCES

1. "Electron Magnetic Resonance of Standard Coal Samples at Multiple Microwave Frequencies," R. B. Clarkson, W. Wang, D. L. Brown, H. C. Crookham, and R. L. Belford, in Techniques in Magnetic Resonance for Carbonaceous Solids, R. Botto and Y. Sanada, eds., ACS Advances in Chemistry Series **229**, American Chemical Society, Washington, 1993, 507 - 528.

"Multi-Frequency Electron Magnetic Resonance," R. L. Belford and R. B. Clarkson, in Techniques in Magnetic Resonance for Carbonaceous Solids, R. Botto and Y. Sanada, eds., ACS Advances in Chemistry Series **229**, American Chemical Society, Washington, 1993, 107 - 138.

2. "Very High Frequency EPR - 94 GHz Instrument and Applications to Primary Reaction Centers from Photosynthetic Red Bacteria and Other Disordered Systems," W. Wang, R. L. Belford, R. B. Clarkson, P. H. Davis, J. Forrer, M. J. Nilges, M. D. Timken, T. Walczak, M. C. Thurnauer, J. R. Norris, A. L. Morris, and Y. Zhang, *Appl. Magn. Reson.*, **6**, 195 - 215 (1994).

3. "Electron Magnetic Resonance of Aromatic Radicals on Metal Oxide Surfaces," R. B. Clarkson, K. Mattson, W. Shi, W. Wang, and R. L. Belford, *Mol. Engineering*, **4**, 89 - 117 (1994).

Table I.
Summary of g-matrix values for selected thiophene radicals on alumina

Species	g_1	g_2	g_3
THI	2.00506±.00050	2.00506±.00050	2.00234±.00010
BTH	2.00642±.00038	2.00451±.00012	2.00226±.00013
DBT	2.01130±.00026	2.00624±.00015	2.00236±.00010
BNT	2.00583±.00012	2.00495±.00012	2.00224±.00011
DNT	2.00518±.00052	2.00326±.00047	2.00224±.00051

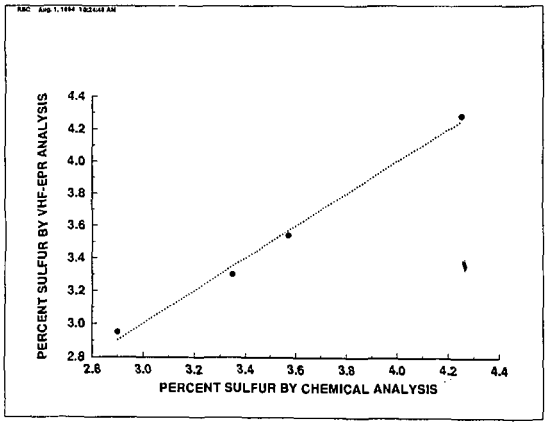

Figure 1. VHF-EPR sulfur analysis test on vitrinite/sporinite blends

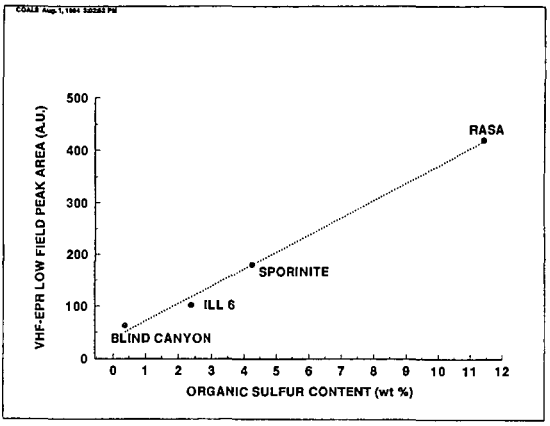

Figure 2. Correlation between VHF-EPR and other analytical methods for organic sulfur in a series of coals with widely differing sulfur contents.

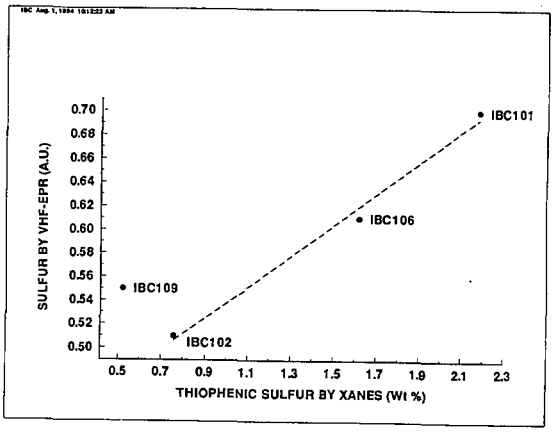

Figure 3. Comparison of VHF-EPR and XANES analyses on four IBCSP coals. The XANES figures are for thiophenic sulfur.

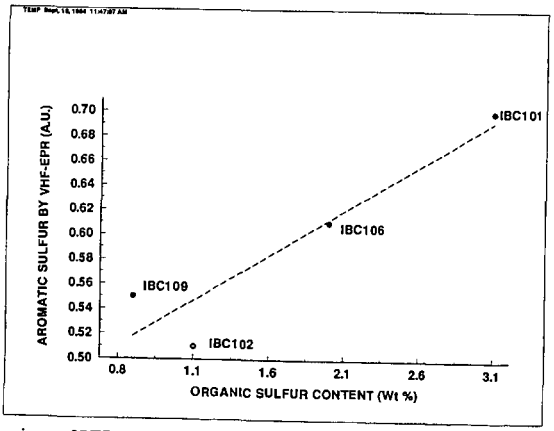

Figure 4. Comparison of VHF-EPR analytical results and IBCSP values for organic sulfur in four coals.

SWELLING BEHAVIOR OF O-ALKYLATED APCS COALS AS EXAMINED BY THE EPR SPIN PROBE METHOD

Ruisong Ding, David Tucker and Lowell D. Kispert
Department of Chemistry, Box 870336
The University of Alabama
Tuscaloosa, AL 35487-0336

KEYWORDS: O-Alkylated Coal, EPR Spin Probe, Hydrogen Bonding

ABSTRACT

Known O-alkylation procedures have been used to derivatize the carboxyl and hydroxyl groups in the APCS coals Lewiston-Stockton, Wyodak-Anderson, Beulah-Zap, Illinois #6, Upper Freeport, and Pittsburgh #8. In general the resulting decrease in hydrogen bonding reduced the cyclical variation in nitroxide spin probe retention observed for nonalkylated coals when small amounts (<1%) of pyridine are present in the toluene swelling solvent. An increase in spin probe retention by the O-alkylated coals relative to the underivatized coals indicates a more open arrangement in the coal due to a decrease in attractive forces, confirming that microporosity increases with increasing rank.

INTRODUCTION

A recent study of Tucker,[1] using an EPR spin probe method we have developed, and an earlier study by Green and Larsen[2] showed that an unexpectedly large number of guest molecules could be included in the swelled macromolecular structure of coal by spiking a "poor" swelling solvent such as toluene (or chlorobenzene) with as little as 100 ppm of a strong swelling solvent such as pyridine. The specific amount of included guest material depends on the rank of the coal undergoing swelling, but all ranks showed reproducible fluctuations in the number of trapped guest molecules as the pyridine content was increased by increments of 100 ppm. This oscillatory uptake behavior was explained as follows. At low ppm pyridine, weak hydrogen bonds which isolate interconnected micropore systems are disrupted. As the concentration of pyridine increases, disruption of weak hydrogen bonds which protect individual micropores will occur, followed at 1-5% pyridine by disruption of stronger hydrogen bonds within the macromolecular structure resulting in an opening of the structure. The cartoon given in Figure 1 emphasizes the active sites that can hydrogen bond (OH) with guest molecules, the interconnected micropore system, the hydrogen bonds of individual micropores and the stronger hydrogen bonds within the macromolecular structure.

In an effort to examine the integrity of the proposed swelling model for the action of binary solvents composed of less than 1% strong swelling solute in a poor swelling solvent, the Argonne Premium Coal Samples (APCS)[3,4] of Lewiston-Stockton (LS), Wyodak-Anderson (WA), Beulah-Zap (BZ), Illinois #6 (I6), Upper Freeport (UF) and Pittsburgh #8 (P8) were O-alkylated by a published procedure.[5] Due to space limitations, only the results for BZ, WA and LS coals will be presented here. The O-alkylated coal differs from the underivatized coal because interactions involving the acidic protons of the hydroxyl and carboxylic groups are no longer possible. Helium density and mercury porosimetry measurements revealed that the secondary structure (intermolecular associations) of the O-alkylated coals is significantly altered.[5] Furthermore, it is known that lower rank coals have lower microporosity (pores smaller than 18 Å) and largely consist of macropores, while higher rank coals have higher microporosity. Microporosity is a measure of the short-range intermolecular forces which contribute to the secondary structure of coal. Upon O-methylation the total porosity (<2200 Å) increases, and the increase is more pronounced for the higher ranked coals. The dramatic increase in the microporosity of O-methylated coals indicates a more open arrangement in the regions where short-range attractive molecular interactions are affective.[4] Since higher rank coals lack the very polar carboxylic acid functionalities and also have a low total concentration of polar functional groups, relative to subbituminous rank coals, microporosity increases with rank.

EPR SPIN PROBE METHOD

Electron paramagnetic resonance (EPR) techniques have been used previously to follow the inclusion of molecular probes in the micropore structure of coal in order to determine the changes in pore size, shape characteristics, pore wall chemistry, and hydrogen bonding which occur during the swelling process.[6]

The most common molecular probes are stable cyclic nitroxyl free radicals (depicted in Figure 2) which contain a ring nitrogen that is also singly bonded to oxygen and flanked by four methyl groups which sterically stabilize the radical. The unpaired electron density is distributed over both the nitrogen (40%) and the oxygen (60%) atoms. Reactive substituents (R) on the ring allow for chemical reactions to be studied, and varying the size and shape of a non-reactive substituent, allows evaluation of the effect on shape or size of the structural features of coal. The spin probe technique has been described in detail.[6] Briefly the coal sample is swelled in a mM nitroxide spin probe solution for approximately 18 h until equilibrium is reached. The coal slurry is then filtered and the solid is vacuum dried to remove the swelling solvent. The samples are then washed with cyclohexane, a non-swelling solvent, to remove any spin probes not trapped in the coal structure. The samples are again vacuum dried and then sealed in evacuated EPR tubes for subsequent measurement of the concentration of the nitroxide radicals trapped in the coal structure.

EXPERIMENTAL

Spin probe VII (Tempamine) was obtained from Aldrich and used as received. This probe contains an amino group which can react with acidic sites in the coal, or in the absence of such sites, it can be trapped in small pores. Ca. 4 g of APCS coal samples, obtained from the Argonne Premium Coal Sample program,[3,4] were O-alkylated according to a literature method,[5] although the work-up procedure was modified as follows. Warm water (100 mL) was added to the reaction mixture and the pH was adjusted to 7. Volatiles were removed by distillation under vacuum for 2 h at 22°C and then at 40°C for 3 h. The residue was treated with hot water (500 mL) to dissolve ammonium salts. The mixture was left to stand overnight; the aqueous layer was decanted, and the procedure was repeated 5 times. The product was isolated by filtration and washed with hot water (4-6 L) until the washings were devoid of halide ions. The alkylated coal was first dried over $CaCl_2$ under N_2, then under vacuum for 2 days and finally at 110°C for 3 days. The alkylated coal was sealed underN_2. Infrared analysis was used to follow the decrease in adsorption in the 3300-3600 cm^{-1} region (loss of hydroxyl groups) and the adsorption increase in the 1730 cm^{-1} region (esterification of the carboxylic acids).

RESULTS AND DISCUSSION

The retention of spin probe VII in BZ APCS lignite is given in Figure 3 as a function of percent pyridine present in toluene swelling solvent. The important feature to note is that large variations occur in the spin probe retention. In the absence of pyridine 1.2 x 10^{18} spins/g of probe VII is retained in the BZ lignite. When very small amounts of pyridine are present the spin probe retention drops to 0.8 x 10^{18} and then increases to 1.8 x 10^{18} with 0.1% pyridine. A decreasing variation in the amount of spin probe retained occurs as the percent pyridine in toluene is increased, becoming more or less constant near 0.4 x 10^{18} spins/g .

Totally different behavior, shown in Figure 4, of spin probe VII retention as the percent pyridine is increased occurs with O-alkylated BZ. The highest spin probe retention (4.1 x 10^{18} spins/g) is obtained in the absence of pyridine and this then decreases without any evidence of oscillation to ca. 2.4 x 10^{18} spins/g with a pyridine content of $\geq$ 0.5%.

Similar plots for Wyodak-Anderson coal and alkylated Wyodak-Anderson coal are given in Figures 5 and 6, respectively. As the percent pyridine increases from 0% to 0.01% (Figure 5) the retained spin probe concentration in units of 10^{18} spins/g drops from 6.1 to 4.8, then rises to 5.5 at 0.02%, drops to 3.6 at 0.08%, rises to 4.9 at 0.1%, drops to 3.2 at 0.2%, rises to 5.5 at 0.6%, and drops to 3.1 at 1%. Further variation is observed as the pyridine content increases to 5%. Above 5% the retained spin concentration equals approximately 3.7±.5. For the alkylated coal (Figure 6), the spin concentration is nearly constant at $9.0 \pm 0.2 \times 10^{18}$ spins/g with the variation close to the relative error of ±0.1.

Figures 7 and 8 show the results of a similar study for Lewiston-Stockton and alkylated Lewiston-Stockton coal, respectively. The spin probe concentration in units of 10^{18} spin/g (Figure 7) varies from 2.2 at 0% pyridine to 1.8 at 0.06%, increases to 2.1 at 0.08%, decreases to 1.7 at 0.4%, increases to 2.0 at 0.6%, and then decreases to 1.6 at 1%, 1.4 at 2% and 1.2 at 4%. In contrast, the spin probe retention in the alkylated coal (Figure 8) decreases from 7.6 at 0% pyridine to 6.9 at 0.2% and then gradually increases to 7.4 at 2%.

In all three coals, the absolute value of the spin probe concentration increased upon alkylation (a factor of 4 for Beulah-Zap, lignite; 2.5 for Wyodak-Anderson subbituminous and 5.4 for Lewiston-Stockton high volatile bituminous coal). Previous porosity measurements[5] indicated that an increase in microporosity occurs upon alkylation and that this increase is more pronounced in high ranked coals than in the lower ranked coal. This is confirmed by this study. It is also clear that upon alkylation the cyclical variation is nearly eliminated, confirming the role of the hydrogen-bonding scheme outlined in the introduction. The largest variation in spin concentration with % pyridine occurred for Wyodak-Anderson coal suggesting more extensive changes in local structure with pyridine at less than 1% than for the high ranked Lewiston-Stockton coal. Beulah-Zap, which loses water upon exposure to air, has a lower tendency to retain the spin probe than the high rank Lewiston-Stockton coal.

ACKNOWLEDGMENT

This work was supported by the U. S. Department of Energy, University Coal Grant program, Grant no. DE-FG22-93PC 93202.

REFERENCES

1. Tucker, D. Ph.D. dissertation, University of Alabama, 1994 Entitled. "The Use of the EPR Spin Probe Method to Study Structural Changes in Solvent Swelled, Weathered Coal."

2. Green, T. K.; Larsen, J. W. *Fuel* **1984**, *63*, 1538.

3. Vorres, K. S. "User's Handbook for the Argonne Premium Coal Sample Program," **1989**, ANL/PCSP-89/1.

4. Vorres, K. S. *Energy and Fuels* **1990**, *4*, 420.

5. Liotta, R.; Rose, K.; Hippo, E. *J. Org. Chem.* **1981**, *46*, 277.

6. Kispert, L. D.; Tucker, D.; Sady, W. *Prepr. Pap. Am. Chem. Soc., Div. Fuel Chem.* **1994**, *39*, 54 and references cited therein.

Figure 1
A cartoon depicting a possible pore structure with the location of (OH) sites that can hydrogen bond with guest molecules and localized hydrogen bonding (~~).

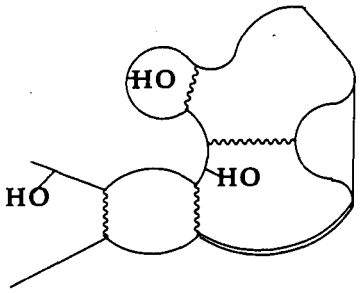

Figure 2
(a) General structure of a nitroxide spin probe,
(b) Structure of spin probe VII (TEMPAMINE)

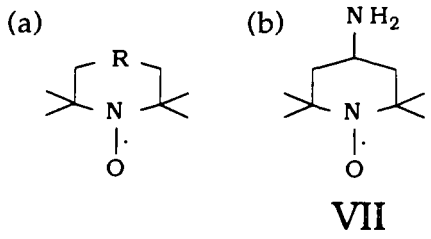

VII

Figure 3
Retention of spin probe VII in Beulah-Zap APCS lignite after swelling with toluene spiked with pyridine.

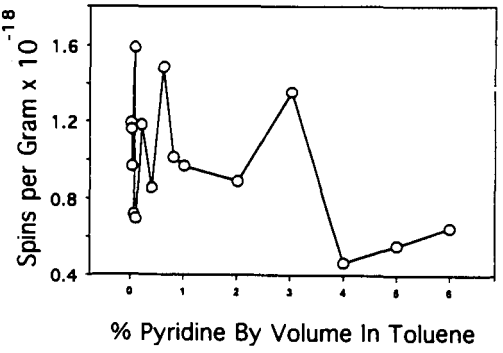

Figure 4
Retention of spin probe VII in O-alkylated Beulah-ZAP APCS lignite after swelling with toluene spiked with pyridine.

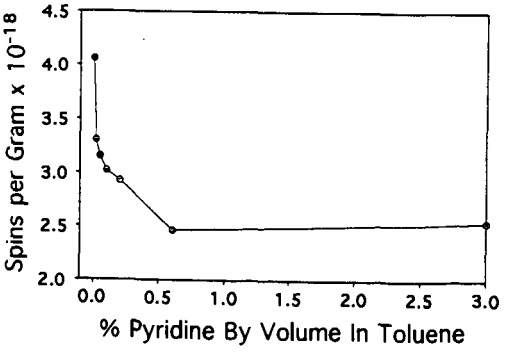

Figure 5
Retention of spin probe VII in Wyodak-Anderson sub-bituminous APCS coal after swelling with toluene spiked with pyridine.

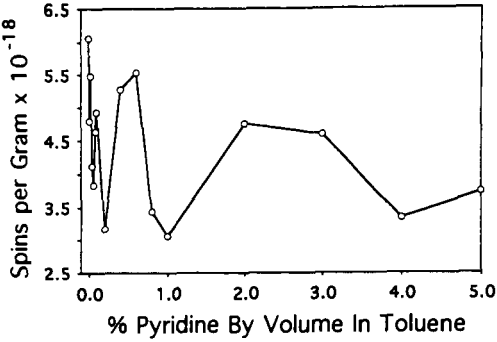

Figure 6
Same as Figure 5 except with O-alkylated Wyodak-Anderson coal.

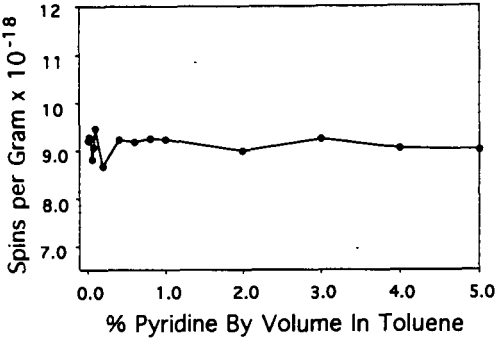

Figure 7
Same as Figure 5 except with Lewiston-Stockton high volatile bituminous APCS coal.

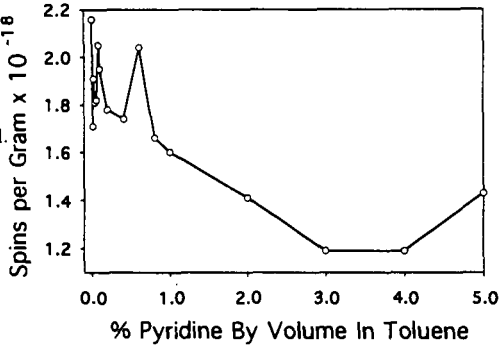

Figure 8
Same as Figure 5 except with O-alkylated Lewiston-Stockton coal.

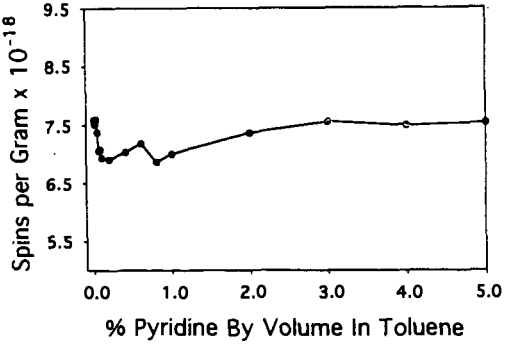

THE CHARACTERIZATION OF FLUORINATED GRAPHITE

Edward W. Hagaman, Andrei A. Gakh and Brian K. Annis

Chemical and Analytical Sciences Division
Oak Ridge National Laboratory
P.O. Box 2008
Oak Ridge, Tennessee, 37831-6201

Keywords: Fluorine, X-ray photoelectron spectroscopy, atomic force microscopy

INTRODUCTION

The characterization of solid fossil fuels by chemical and spectroscopic methods requires extensive modelling in less complex systems for chemical proof of principle and technique development. In previous work coal was fluorinated with dilute, elemental fluorine under conditions that were expected to lead to materials that contain only fluoromethine moieties. The solid state, cross polarization/magic angle spinning (CP/MAS) ^{13}C NMR spectra of the fluorinated coal are complex, indicating more chemical modification than originally anticipated.

Our goal in the coal derivatization was to sequentially increase the severity of the fluorination and observe by ^{19}F and ^{13}C NMR the type and concentration of fluorine functional groups created in the coal milieu. This requires the ability to discriminate between C, CF, CF_2, and CF_3 moieties in the coal matrix. The task can be accomplished by implementing the spectral editing technique of Wu and Zilm[1] which distinguishes different kinds of carbon resonances, especially CH and CH_2 resonances. These experiments utilize cross polarization (CP) and polarization inversion (PI) to effect the discrimination. Our version of this experiment is a triple resonance experiment that incorporates ^{19}F-^{13}C CP, PI, and simultaneous ^{1}H and ^{19}F dipolar decoupling.

In order to evaluate the elemental fluorine chemistry in a matrix simpler than coal, fluorinated graphite was prepared. X-ray photoelectron spectroscopy (XPS) was used to characterize the surface species, i.e., count CF, CF_2 and CF_3 species. These well-characterized samples are the models we will use to test the NMR editing experiments. The XPS and atomic force microscopy (AFM) data on the first fluorinated graphites we have prepared are reported in this paper.

EXPERIMENTAL

Fluorination of Graphite. Highly oriented pyrolytic graphite (HOPG), 0.7 g, was ground in a ceramic mortar and placed in a 19 mm quartz tube. The tube was placed in an oven and the powder was dried in a flow of nitrogen (2-3 cm^3/min) at 250 °C for 2 h. The flow of nitrogen was replaced by pure fluorine (2 cm^3/min) over 30 min and fluorination was continued for an additional 20 h at 250-260 °C. At the end of the fluorination the fluorine gas stream was replaced with nitrogen and the sample was cooled. The nitrogen purge was continued for 2 h at room temperature. The sample was then transferred to a glass vial under nitrogen and flushed for an additional 2 min to displace traces of air and moisture. The visual appearance of the sample did not change significantly during the fluorination.

A second sample of HOPG, a single platelet with dimensions of 0.4 x 0.8 x 0.05 mm, was subjected to the fluorination under similar conditions for 21 h. The isolated platelet was stored under nitrogen in a glass vial. No change in the visual appearance of the sample was found and the weight loss of the sample during the fluorination was lass than 0.1%.

Atomic Force Microscopy (AFM). The atomic force microscope used in this investigation was a Digital Instruments Inc., Nanoscope II which uses a Si_3N_4 tip attached to cantilever to scan the surface. Tip motion is monitored by light deflected from the cantilever.

X-ray Photoelectron Spectroscopy (XPS). The XPS data were acquired on a Kratos Ltd. spectrometer The energy analysis chamber is a Kratos Axis system designed for general purpose XPS using a small spot lens. In this instrument the standard orientation of the detector is orthogonal to the sample surface. The data reported in Table 1. are from experiments performed in this configuration. The spectrum of the HOPG platelet was also recorded after tilting the platelet 35° from its normal orientation to the detector. The x-ray source used in this work was an Al Kα monochromator (15 kV, 60 ma maximum). A UV flood lamp was used to charge

neutralize the fluorinated HOPG powder sample. The pass energy of the HOPG platelet was 20 eV. The pass energy of the HOPG powder was 40 eV. The instrument was calibrated to Au 4f at 84.0 eV. The graphitic component of the C 1s peak was observed at 284.5 eV for the conductive HOPG platelet, as expected. The graphitic component of the powdered, nonconductive HOPG was assigned this same value.

RESULTS AND DISCUSSION

Figure 1 compares the AFM image of the surface of a platelet of HOPG prior to fluorination (a) with the surface after fluorination (b). The images depict a 250 x 250 nm surface area (note the expanded z scale). At the resolution used for these measurements the graphite surface is flat. The surface after fluorination exhibits random rutted or channeled features with dimensions on the order of tens of nm. Features are etched into the surface to a depth of ca 1 nm. Since the XPS results discussed below are compatible with the surface functionality being CF_x moieties, the surface features shown in Fig. 1b likely represent fluoridation of the surface with loss of surface carbon extending to a depth equal to several graphite layers.

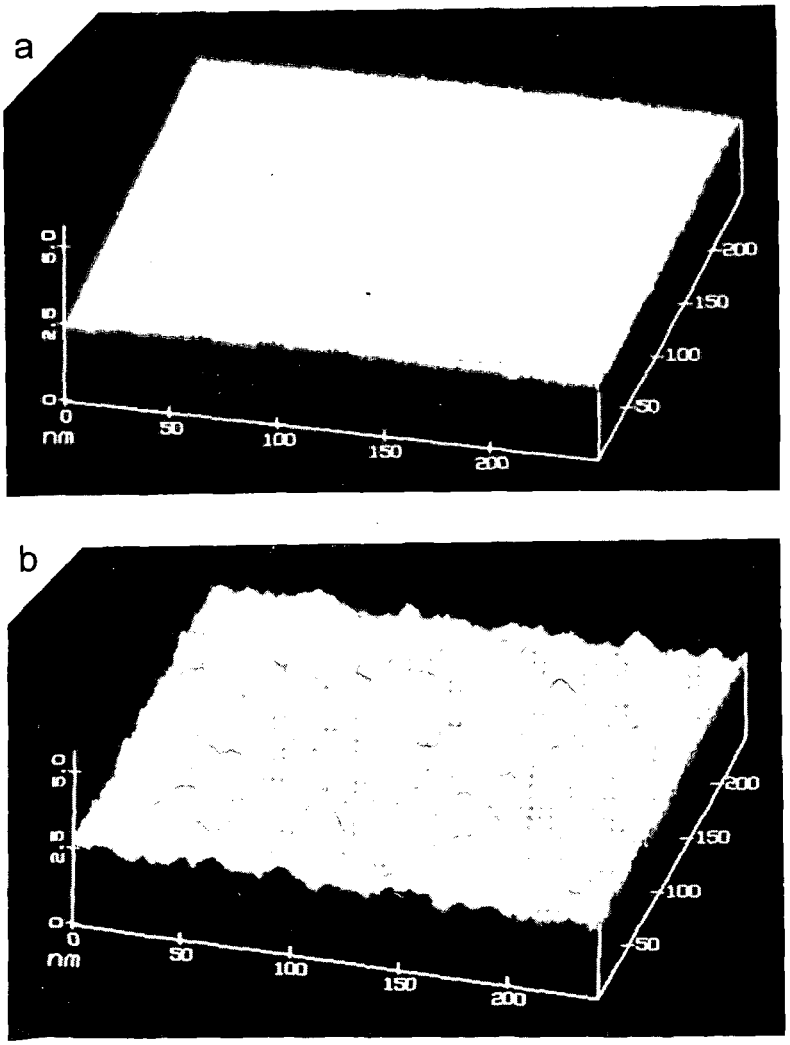

Figure 1. Atomic Force Microscopy Images of a: HOPG and b: Fluorinated HOPG

Two fluorinated samples were analyzed by XPS: the first is the sample of HOPG used for the AFM measurements shown in Fig. 1b; the second was a fluorinated graphite powder described in the experimental. Qualitative XPS survey scans showed only carbon, fluorine and oxygen on both surfaces. Figures 2 and 3 show the C 1s, F 1s and O 1s spectra of the platelet and powder sample, respectively. The powder had to be charge neutralized, which may account for some of the increase in peak width. Each spectrum has been band fitted, showing the different components which comprise the spectrum. Table 1. lists the atomic concentrations, peak position and width of each component.

Table 1. XPS Data for Fluorinated Platelet and Powdered HOPG

Platelet HOPG			
XPS Peak	Binding Energy eV	Peak Width, eV	Atomic Conc., %
C 1s 1	284.5	0.6	49.8
C 1s 2	285.7	1.42	6.7
C 1s 3	287.0	2.03	4.4
C 1s 4	289.8	1.55	13.0
C 1s 5	291.8	1.70	5.0
C 1s 6	294.1	2.49	2.6
F 1s 1	688.6	1.50	15.7
O 1s 1	532.1	2.28	0.9
O 1s 2	535.1	1.45	2.0
Powdered HOPG			
C 1s 1	284.5	2.17	33.2
C 1s 2	285.7	1.93	0.6
C 1s 3	287.0	1.48	3.5
C 1s 4	289.2	2.37	24.4
C 1s 5	292.0	2.30	1.8
C 1s 6	293.9	2.65	0.2
F 1s 1	686.1	3.05	5.5
F 1s 2	688.1	2.49	24.6
O 1s 1	532.9	3.95	5.2
O 1s 2	534.8	1.51	0.9

The C 1s peak at 284.5 eV is from pure graphite. Bonding an electronegative atom to carbon shifts the C 1s peak to higher binding energy. The second major carbon peak at 289 eV represents CF and a shift at approximately 292 eV represents CF_2. The C 1s peak at 294 eV is attributed to CF_3.[2] The CF_2 moiety has an F 1s peak at ca 690 eV; the CF F 1s peak shifts to approximately 689 eV. The assignments of chemical shifts to bonding type indicated here are from XPS data bases.[3]

The spectra indicate that the surface of both materials has been fluorinated. The dominant peak in the carbon spectrum for both samples is at 284.5 eV and is due to graphitic carbon. The majority of the fluorine is in the form of CF. Both the C 1s and the F 1s peaks corresponding to CF are approximately equal in both samples, supporting these assignments. There are minor components in the C 1s spectrum which indicate CF_2 and CF_3. The XPS analysis was repeated for the platelet sample of fluorinated HOPG after tilting the platelet 35°. This orientation biases the sensitivity of the analysis to the surface layer relative to the underlayers. An increase in the F 1s and the C 1s of the CF component relative to the graphitic C 1s peak is observed, showing fluorine to be concentrated on the surface.

The fluorinated HOPG platelet has a 2.6:1 ratio of CF:CF_2. The ratio in the powder is 13.6:1. The platelet has more comparable concentrations of CF_2 and CF functional groups (desirable in an NMR test sample) but a low absolute concentration of all CF species that may make the NMR analysis difficult. The XPS correlation between the fluorinated platelet and powder reveals the same qualitative chemistry occurs in both materials. Attempts to increase the CF_2 component in the powder are in progress.

ACKNOWLEDGEMENTS

This research was sponsored by the Division of Chemical Sciences and the Division of Material Sciences, Office of Basic Energy Sciences, U.S. Department of Energy, under Contract No. DE-AC05-840R21400 with Martin Marietta Energy Systems, Inc.

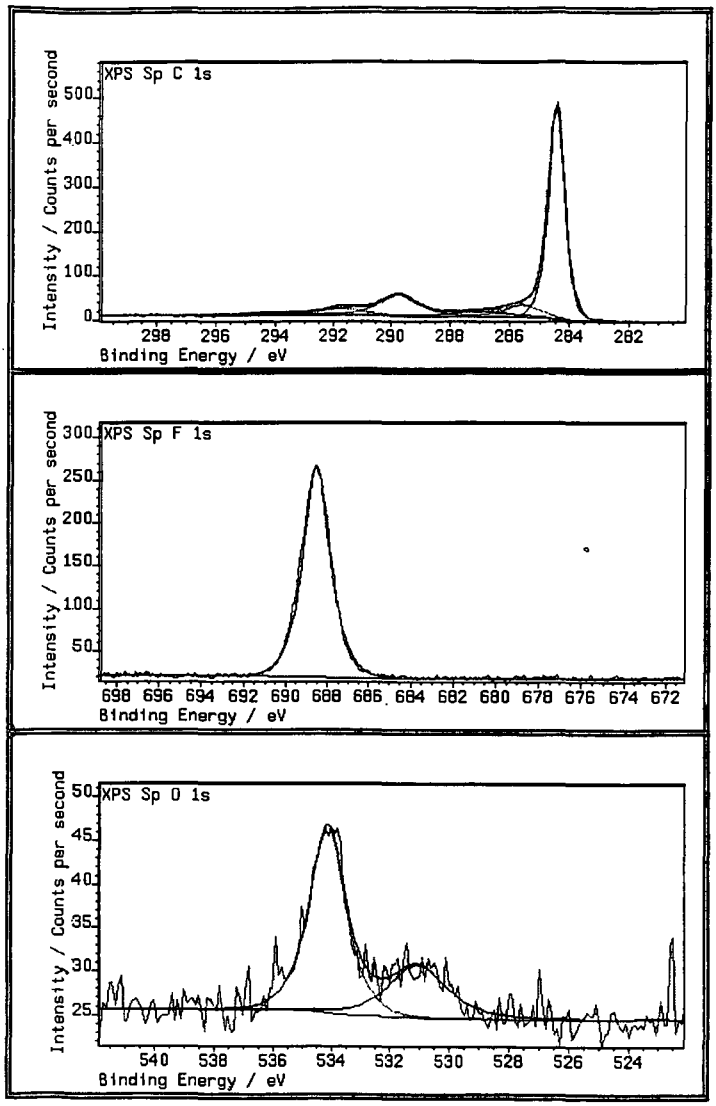

Figure 2. Carbon, Fluorine, and Oxygen X-ray Photoelectron Spectra of a Fluorinated HOPG Platelet.

REFERENCES

1. Wu, X.; Zilm, K. W. *J. Magn. Reson. Ser. A*, **1993**, *102*, 205.

2. Cox, D. M.; Cameron, S. D.; Tuinman, A.; Gakh, A.; Adcock, J. L.; Compton, R. N.; Hagaman, E. W.; Kniaz, K.; Fischer, J. E.; Strongin, R. M.; Cichy, M. A.; Smith III, A. B. *J. Am. Chem Soc.*, **1994**, *116*, 1115.

3. (a) Moulder, J. F.; Stickle, W. F.; Sobol, P. E.; Bomben, K. D. "Handbook of X-ray Photoelectron Spectroscopy" Jill Chastain, Ed., Perkin Elmer Corp. 1992. (b) "NIST Standard Reference Database 20" entitled "NIST X-ray Photoelectron Spectroscopy Database" ver. 1.0, compiled by C. D. Wagner, Surfex Co., Program written by D. M. Bickman, copyright 1989.

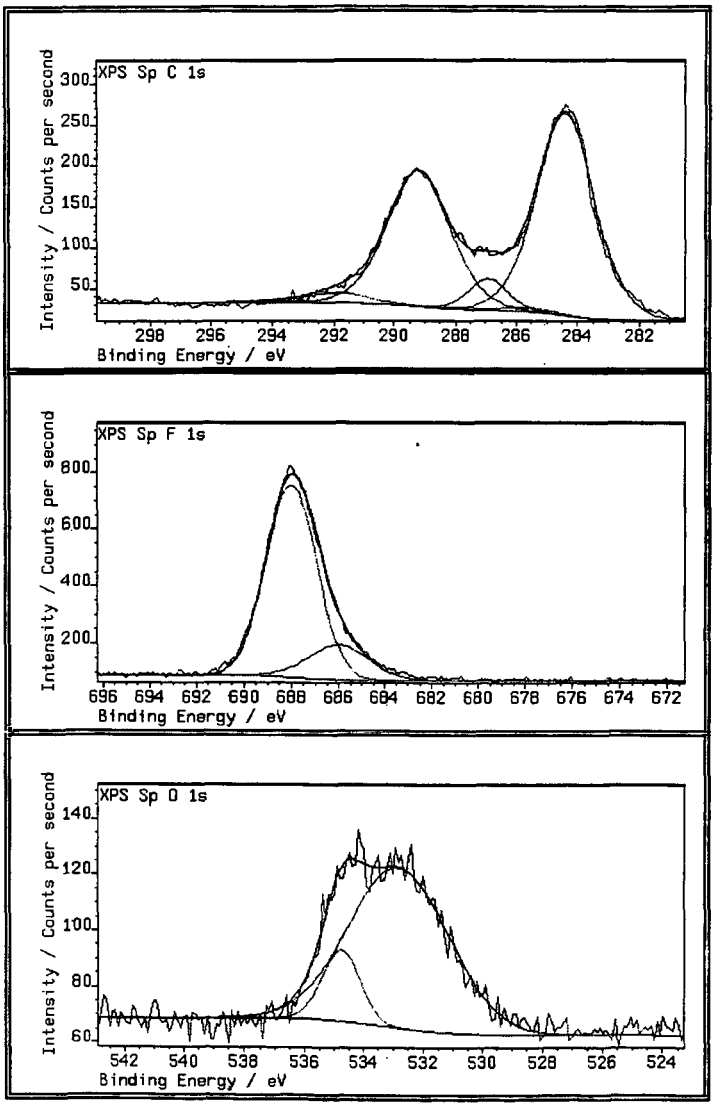

Figure 3. Carbon, Fluorine and Oxygen X-ray Photoelectron Spectra of a Fluorinated HOPG Powder.

CHARACTERIZATION OF CARBON MATERIALS USING QUANTITATIVE OPTICAL MICROSCOPY

J. C. Crelling and D. Bensley

Geology Department, Southern Illinois University
Carbondale, IL 62901

Keywords: reflectance, density gradient centrifugation, carbon density

INTRODUCTION

Research which was directed towards the characterization of ultra-fine coal has been utilized in the analysis of vitrinite and high-temperature carbon materials. Equipment and procedures have been developed which permit full reflectance characterization on particles as small as 1.5 micrometers diameter using rotational polarization techniques. Microstructural characterization using optical methods in conjunction with density gradient centrifugation (DGC) have been employed to assess carbon density within its spacial context. Using reflectance mapping techniques with apparent density data obtained from DGC processing, reflectance "images" recorded on the sample can be correlated to reflectance data obtained from DGC fractions. By comparing reflectance values associated with specific density fractions to reflectance values obtained from specific areas within the mapped reflectance image the spacial distribution of reflectance and density can be determined for a complex heterogeneous material.

PROCEDURES

Samples are processed for both petrographic examination and DGC processing. Petrographic samples are processed using standard metalurigical mounting and polishing techniques used for vertical white-light observation. Reflectance data is obtained using a Leitz MPVIII compact microscope modified for rotational polarization reflectance. The modified optical configuration uses the same components that are employed in conventional reflectance. The only variance with convention is the adaptation of the polarizer to permit rotation through 360 degrees, instead of the standard fixed 45 degree orientation, and the use of a fixed stage position during analysis. All polarizer rotation, data acquisition and data processing functions are computer controlled using a 80386/20 mHz computer. Microscope interfacing is made via a gear coupled polarizer and stepping stage, stepping stage controller and IEEE bus. A separate A/D converter controls data acquisition. Optical correction is made on all measurements to remove the effect of residual polarization within the vertical illuminator and transmission optics. Without this correction a pronounced anisotropic signal, induced by rotating one polarizer against a "stationary polarizer" within the light path, would be recorded. This "stationary polarizer" should not be confused with an actual optical component but represents the optical effect caused by residual polarization within the vertical illuminator. Sequential measurements are made across samples with both the maximum reflectance and the spacial orientation of the point stored within a data file.

DGC processing requires samples to be crushed to a particle size >15μm. The sample is then dispersed in a brig 35 solution to obtain a uniform suspension. The suspension is applied to the top of a vessel filled with an aqueous sodium polytungstate gradient ranging from 1.0 to 2.2 g/mL. The vessel is centrifuged forcing particles to their appropriate density level. After centrifugation the vessel is fractionated by pumping, filtering and weighing the resulting density layers from the density gradient. The resulting density profile accurately represents the density composition of the samples constituents.

DISCUSSION

Figures 1 and 2 illustrate the results obtained from sequential reflectance measurements. The area boxed out with squares represent the point locations where individual reflectance measurements were made. Figure 1 illustrates the results obtained from a vitrinite maceral in coal while figure 2 illustrates reflectance mapping of a C-C composite sample. Figures 3 and 4 represent DGC profiles of the coal sample and C-C composite sample respectively. The indicated points on the DGC profile indicate measured fractions with the average fraction density and reflectance values indicated. Figures 5 and 6 illustrate the spacial density relationships calculated for the "mapped" telocollinite and C-C composite samples respectively.

Figures 1 and 5 illustrate the level of heterogeneity present in vitrinite macerals in both reflectance and density properties. Figures 2 and 6 show the effects of "stress" graphitized phenolic pitch. In both cases heterogeneity of the carbon can be quantitatively evaluated using combined DGC/Ro mapping techniques.

CONCLUSIONS

Both reflectance mapping and DGC analysis can be used to quantitatively assess carbon heterogeneity. By combining these analysis the spacial distribution of reflectance and density can be determined enabling assessment of physical properties within a morphological context.

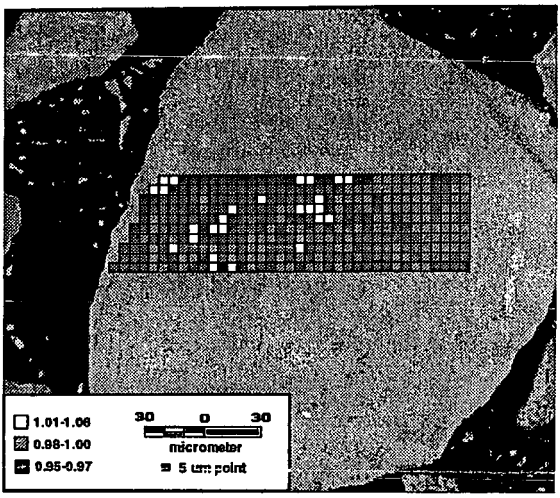

Figure 1: Reflectance distribution as measured on a apparently homogeneous vitrinite maceral.

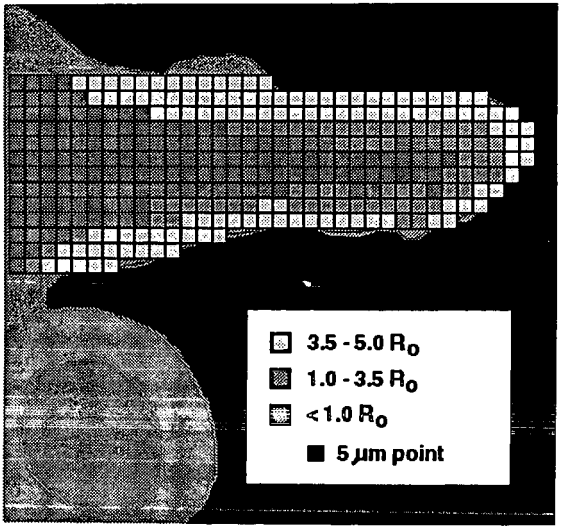

Figure 2: Reflectance distributions measured on a C-C composite sample.

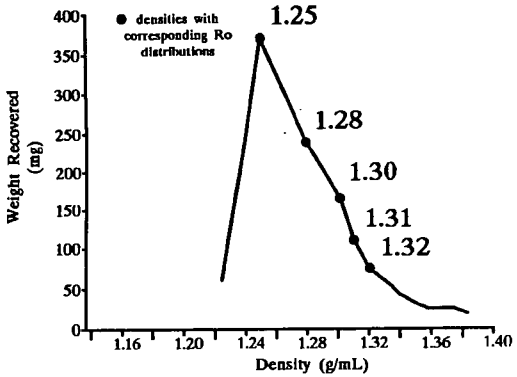

Figure 3: DGC profile of coal sample from which a single vitrinite maceral was mapped (figure 1).

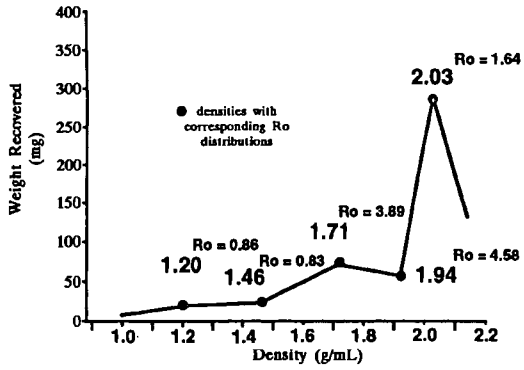

Figure 4: DGC profile of a C-C composite sample from which a single area was mapped (figure 2).

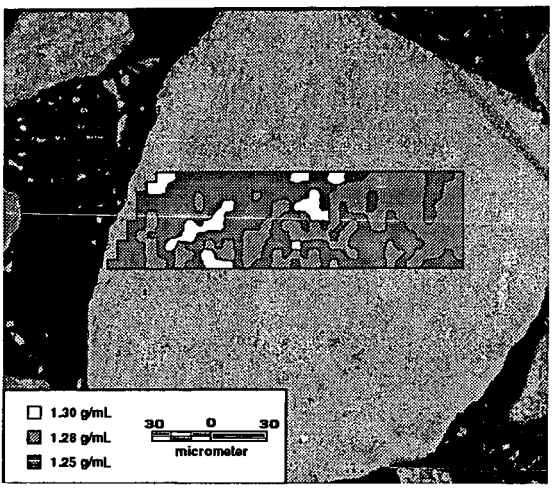

Figure 5: Density correlations made on the mapped vitrinite maceral using combined reflectance mapping/DGC techniques.

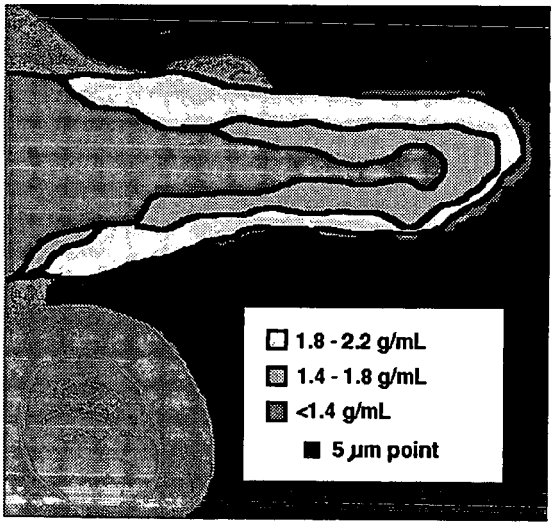

Figure 6: Density correlations made on the mapped C-C composite area using combined reflectance mapping/DGC techniques.

COUPLED LC-GC TECHNIQUES FOR THE CHARACTERISATION OF PAC IN FUEL AND ENVIRONMENTAL SAMPLES

Alastair C Lewis[1], Stuart C. Mitchell[1], Robert E Robinson[2] and Keith D Bartle[1]

[1]School of Chemistry, University of Leeds, Leeds, UK LS2 9JT.
[2]On leave from Triton Analytics Corp., Houston, Texas 77084.

Keywords: Polycyclic aromatic compounds, Coupled liquid chromatography - gas chromatography, mass spectrometry, atomic emission detection.

INTRODUCTION

Exposure to polycyclic aromatic hydrocarbons has long been identified as of considerable environmental concern[1]. Originating from both natural and anthropogenic sources, many PAC exhibit significant carcinogenic and mutagenic[2,3] properties which are critically dependent on structure. Although PAC occur naturally in fossil fuels, the predominant contributions to environmental pollution are caused by the combustion of organic fuels. Recent studies have identified characteristic source fingerprints for coke ovens, diesel and gasoline engines, road tunnels and wood combustion emissions[4]. However, despite the wealth of literature on the identification of parent polycyclic aromatic hydrocarbons[5,6] and polycyclic aromatic heterocycles[7,8], little is known about the composition and concentration of the many substituted and heteroatom-containing PAC that are produced either by combustion processes or as products of atmospheric reactions[9] and are potentially more of a health risk than parent PAH or are simply unknown[3,10]. Due to the complexity of fuel and environmental samples which contain many hundreds of aliphatic, aromatic and polar compounds, multidimensional chromatographic methods which provide separation by virtue of chemical class (group-type) or by molecular mass can greatly simplify the identification of individual PAC. LC-GC has been used previously for quantitative analysis of PAH in diesel exhaust emission extracts[11,12] urban air particulates[13,14] and other fuel related applications[15]. In this study, on-line coupled LC-GC techniques have been investigated for the identification of trace level PAC in a range of fuel feedstocks, combustion products and urban air particulate extracts. Positive identification of individual PAC was obtained by direct coupling of LC-GC to mass spectrometry and atomic emission detection.

EXPERIMENTAL

Samples: An urban air particulate sample was collected by high volume air sampler (Graseby Anderson, UK) drawing air at a rate of $0.4m^3$ through a quartz microfibre filter (Whatman UK), using a previously described method[14]. The filter was placed in an extraction vessel at 110°C and was extracted with CO_2 and 10% toluene at 400 atm, for 90 minutes using an ISCO SFX 2-10 extractor with Model 100D and 260D syringe pumps. Pressure was maintained within the cell using a 25 mm i.d. x 10 cm length of fused silica capillary tubing. The extract was collected in 3 ml of dichloromethane, which was subsequently reduced to dryness and re-dissolved in *ca.* 2 ml *n*-hexane, for compatibility with the subsequent normal phase LC step. Previous extractions of standard dust samples (NIST SRM-1649) have showed that Soxhlet equivalent or better recoveries were obtained for all certified PAH; the results have been reported earlier[14]. A typical UK diesel sample was used for a preliminary investiagtion by LC-GC-AED.

LC-GC-MS Analysis: A Carlo-Erba Dualchrom 3000 Series LC-GC instrument (Fisons, Italy), consisting of two HPLC syringe pumps, a UV detector, on-column interface, early solvent vapour exit and GC was coupled via a heated transfer line to a Finnigan Mat ion trap detector mass spectrometer (ITD/MS)[10,13]. HPLC separation was performed using a 100 mm x 2 mm i.d. column containing 5 µm 'Spherisorb' silica (Phase Separations, UK) packing. Pentane and dichloromethane were used as the mobile phase, with a stepped polarity gradient. Sample injection was via a 20 µl loop injector. LC separation was monitored by UV detection (254 nm), and was recorded by chart recorder. From the detector the eluent passed into the on-column interface which in stand-by position routed the flow through to waste. On transfer a pneumatically actuated valve was used to switch the flow through a fused silica capillary column which transfers the sample onto the retaining pre-column. GC separation was performed on a 25 m x 0.32 mm i.d. fused silica capillary column coated with a 0.33 µm film of dimethyl siloxane (BPX-5 SGE, UK). The column inlet was connected by means of a press-fit connector to a 4 m section of the separation column which was used as a retaining pre column. The pre-column was connected to 10 m x 0.53 mm i.d. uncoated fused silica retention gap, deactivated by phenyldimethyl silylation. This connection also includes an early solvent vapour exit for the evaporation of mobile phase. The exit has a twofold advantage; firstly reducing the time required

to evaporate the mobile phase and, more importantly minimising the amount of mobile phase entering the detector(s). The partially concurrent solvent evaporation rate at 65°C for a 50:50 *n*-pentane : dichloromethane (%v/v) mobile phase using the solvent vapour exit was determined to be 100 µL/min at an inlet carrier gas pressure of 120 kPa. With an LC solvent flow rate of 100 µL/min, the helium carrier gas was essentially free of solvent contamination prior to the ion trap detector (ITD). On completion of the sample transfer via on column interface, the fused silica capillary column was removed from the GC inlet, to eliminate possible vaporisation of the polyamide coating and subsequent bleed into the carrier gas at high oven temperatures. Transfer of eluent from the GC oven to the ITD/MS for detection was via a heated transfer line at 250°C. Mass scans were performed at 1 scan/sec with a mass range of 50-350 amu.

LC-GC-AED Analysis: Normal phase HPLC was performed using an in-house built LC system[12]; a Brownlee Micro gradient dual syringe HPLC pump (Brownlee Labs, Santa Clara, USA), a Rheodyne 7040 injection valve (Berkley, USA) with a 20 ml sample loop and a 100 mm x 2 mm i.d. column packed with 5mm 'Spherisorb' silica (Phase Separations, UK). Detection was by means of a Uvikon 735LC UV detector (Kontron Instruments, UK) equipped with a 1 ml flow cell and operated at a wavelength of 254 nm. Eluate passes from the UV detector entering a ten-port valve fitted with a pneumatically activated valve interface (Valco Instruments Co., Inc., Houston, Texas, USA). Selected fractions were transferred to a Hewlett Packard 5890 Series II GC via a 350 µl loop interface and a short length of deactivated silica capillary. The speed of concurrent solvent evaporation optimised by venting through an early solvent vapour exit prior to the pre-column and analytical column. Following solvent evaporation the solvent exit was closed. A Hewlett Packard 5921A Atomic Emission Detector (AED) was used for multi-element detection. Transfer of the eluate from the GC was via a heated transfer line (320°C) into the cavity of the AED, which houses a microwave induced helium plasma (MIP).

RESULTS AND DISCUSSION

The LC solvent program developed, provided the initial elution of essentially all polycyclic aromatic hydrocarbons as a single unresolved peak 4 mins into the analysis. Polarity differences appear to be the major basis for class separation between the other classes of PAC present in the samples. Alkylated PAH species such as methyl chrysenes elute with the parent PAH compounds and require a less polar mobile phase to separate them from the bulk of components, therefore using a LC mobile phase of 15% DCM and 85% pentane, the parent and alkylated PAH species could be separated into distinct ring size fractions, and the ring size fractions produced can then be transferred directly to MS. Whilst the LC stage provides much improved PAC type selectivity the separation into particular groups eg parent, heterocycles, nitrated, oxygenated etc, is not totally complete since there is some polartity overlap of species in different groups. For example, large parent PAH compounds such as coronene, have similar retention characteristics as 2 ring nitro-PAC species.

Separation /Identification of Alkylated Polycyclic Aromatic Hydrocarbons: For the urban air particulate extract using LC-GC-MS, alkylated pyrene and chrysene compounds were found to make up the majority of alkylated substituted PAH in the air particulate, in the form of methyl/dimethyl/ethyl compounds. Using a 15% DCM and 85% pentane a ring size fraction of parent and alkylated PAH corresponding to the benz[a]anthracene/chrysene group was transferred to the MS. This separation is of particular interest in view of the marked difference in carcinogenic activity of methyl chrysenes.

Separation/Identification of Nitro-Polycyclic Aromatic Compounds: Most nitro-PAC produce an abundant molecular ion peak (M^+) and several characteristic fragments: $(M\text{-}NO)^+$ and $(M\text{-}NO_2)^+$. The fractions analysed were examined for the presence of mononitro-, dinitro-, methyl-nitro, and dimethyl-nitro PAC. 9-nitroanthracene (mass 223) and 1-nitropyrene (mass 247) were identified by comparison with GC retention times and mass chromatograms of reference compounds. An isomer of nitroanthracene was also identified. Derivatives of nitrated PAC (eg. alkyl or hydroxyl) are more difficult to identify via mass spectrometry, since they fragment differently from the mono-substituted nitro-PAC compound. No compounds of this type were identified have been identified to date by this technique, however attempts are continuing to develop a LC-GC-MS procedure for this analysis. Nitrated PAC are considered to be the most carcinogenic group of PAC[3], and their formation and atmospheric reactions are little understood, although there is some evidence that some are formed as artifacts of sampling by reaction with atmospheric OH followed by NO_2 attack[16,17].

Separation/Identification of Oxy-Polycyclic Aromatic Compounds: Oxygenated PAC are considered to be as carcinogenic as many of the parent PAH due to their similarity in structure and properties to the products of the PAH metabolic process. The metabolites formed can

decompose via triol intermediates which form adducts with DNA which then cause carcinogenic or mutagenic effects[3]. Detection of oxy-PACs was greatly simplified by their separation as a class from the nitro PACs. The identification of 9-anthraldehyde, 9-phenanthraldehyde and 9-fluorenone was confirmed by co-injection of standards. 9,10-anthracenedione (anthraquinone), plus its mono and di-substituted methyl derivatives which were all identified as being present in an urban air particulate extracts. A summary of the separation of urban air particulate extract by HPLC is shown in Table 1. Quinone-PAC are thought to be formed in the atmosphere from parent PAH by reaction with singlet molecular oxygen[18,19], formed either via a sensitization mechanism[20], or via ozonolysis[21].

Separation/Identification of Polycyclic Aromatic Heterocycles: The coupling of LC-GC separation with the Hewlett Packard atomic emission detector has vastly improved the ability of the instrument to speciate trace level heterocyclic PAC in complex hydrocarbon samples. Fractionation by LC enables interference from co-eluting hydrocarbons and more polar species to be eliminated, thus allowing sulphur (181 nm), nitrogen (174 nm) and oxygen (777 nm) PAC rich fractions to be transferred directly to the GC. For a typical diesel a series of substituted dibenzothiophenes, carbazoles and quinones were readily identified from the transfer of discrete LC fractions. For each element, the response was significantly enhanced due to increased sample concentration and the reduction in the formation of molecular species in the plasma. Indeed, the improved sensitivity of the detector operating within the LC-GC system, particularly for nitrogen has increased the reliability of elemental formulation.

CONCLUSIONS

Both LC-GC techniques provide an excellent technique for the rapid and much improved separation and identification of polycyclic aromatic compounds in fuel and environmental samples. Furthermore, the combination of elemental and compositional information from AED with molecular and structural information from MS offer a powerful approach to speciation of complex sample matrices. The increased compound-type selectivity in the primary separation improves the detection of very level species, by coupling on-line advantages with reduced sample complexity at the final separation stage. The limitations of systems are the individual detection capabilities of the mass spectrometer and atomic emission detector and the solubility of some of the most polar PACs in a solvent compatible with normal phase HPLC. However, both techniques so far have provided valuable insight into the source, formation and distribution of such compounds pre- and post combustion.

REFERENCES

(1) United States National Academy of Sciences. *Particulate Polycyclic Organic Matter.* Committee on the Biological Effects of Atmospheric Pollution, National Research Council, National Academy Press, Washington DC, USA.,1972.

(2) Bridford K, J Finklea, J.Wagoner, J.Moran, P.Coplan (Eds.). Human exposure to polynuclear aromatic hydrocarbons. In: R Freudental and P.Jones (Eds.), *Polynuclear Aromatic Hydrocarbons:Chemistry, Metabolism and Carcinogenesis.* Rave Press, New York, 1976, Vol. I., 319-324.

(3) Merschundermann V., Mochayedi S., Kevekordes, S., Kern, S., Wintermann F. *Anticancer Res.*1993, **13,** 2037-2043.

(4) Khalili, N.R., Scheff, P.A., Holsen, T.M., *Atmospheric Environment*, 1995, **29**, 4, 533-542.

(5) Lee M.L., Novotny N.V., Bartle K.D., *Anal. Chem.*, 1976, **48**,1566-1572.

(6) Grimmer G., in *Handbook of Polycyclic Aromatic Hydrocarbons*, A.Bjorseth (Ed.) Marcel Dekker, Inc New York. 1983, **Vol.1**, 154-156.

(7) Palmer, S.R., Kruge, M.A., Hippo, E.J., Crelling, J.C., *Fuel*, 1994, **73**, 1167-1172.

(8) Xiaoling, M., Sakinishi, K., Mochida, I., *Ind. Eng. Chem. Res.*, 1994, **33**, 218-222.

(9) Broddin G., Cautreels W., Cauwenberghe K.A., *Atmos. Environ.* 1980, **14**, 895-910.

(10) Lee M.L., Novotny N.V., Bartle K.D., *Analytical chemistry of polycyclic aromatic compounds*. Academic Press (London) Ltd 1981, 441-451.

(11) Davies I.L., Raynor M.W., Williams P.T., Andrews G.E., Bartle K.D. *Anal. Chem.* 1987, **59**, 2579-2583.

(12) Kelly G.W., Bartle K.D., Clifford A.A., Robinson R.E., *J. High Resol. Chromatogr.* 1992, **15**, 526-530.

(13) Kelly G.W., Bartle K.D., Clifford A.A., Scammells D., *J. Chromatogr. Sci.* 1993, **31**, 73-76.

(14) Lewis A.C., Kupiszewska D., Bartle K.D., Pilling M.J., *Atmos. Environ.* 1995 **29**, .

(15) Kelly G.W, Bartle K.D., *J. High Res. Chrom.* 1994, **17**, 390-397.

(16) Later D.W. *The handbook of polycyclic aromatic hydrocarbons.* 1985 **Vol. 2**. pp 265-349. Bjorseth A and Ramdahl T (Eds) Marcel Dekker Inc. New York.

(17) Atkinson R., Lloyd A.C., Darnall K.R., Winer A.M., Pitts J.N., *Advances in Photochemistry* 1980 **Vol. 11**. Pitts J.N, Hammond G.S, Gollnick K. (Eds), Wiley, New York.
(18) Konig J., Balfanz E., Funcke, W., Romanowski, T., *Polynuclear aromatic Hydrocarbons: Mechanisms, Methods and Metabolism* 1985 pp 739-740 M. Cooke and A.J. Dennis (Eds), Battelle Press, Columbus, Ohio.
(19) Lane D.A., Katz, M., *Environ. Sci. Technol.* 1977, **8**, 137-154.
(20) Van Cauwenberghe K.A., *The handbook of polycyclic aromatic hydrocarbons.* 1985 **Vol. 2**. pp 351-384. Bjorseth, A., and Ramdahl, T., (Eds) Marcel Dekker Inc. New York.
(21) DeMore, W.B., Raper O.W., *J. Phys. Chem.* 1966, **44**, 1780-1785.

Table 1. Separation of Urban Air Particulate Extract by HPLC.

Time Interval / min	Isolated Class / Compound(s)[a]
0 - 2.7	Solvent[b] Aliphatic compounds[b]
2.7 - 3.7	Polycyclic aromatic hydrocarbons[b] Alkylated PAH[b]
3.7 - 5.5	9-Nitroanthracene[b] Nitroanthracene isomer[b] 1-and 2-Nitronaphthalene 1-Nitropyrene[b]
5.5 - 6.5	2-Nitrofluorene[b]
11.5 - 14.0	9-Anthraldehyde[b] 9-Phenanthraldehyde[b] 2-Naphthaldehyde 9-Fluorenone[b]
14.0 - 17.0	9,10-Anthracenedione[b] Benzanthrone[b] 7,8 Benzoquinoline[b] benz[a]anthracene 7,12-dione[b] 2-Methyl-9,10-anthracenedione[b] 2-Fluorenealdehyde[b] 2-Nitro-9-fluorenone[b,c] 9-Anthracenone[b]
17.0 - 19.0	2-Methyl-1,4-naphthoquinone
19.0 - 21.0	1,4- Naphthoquinone[b]
24.0 - 25.0	Acenaphthenequinone[c]

[a]LC elution order based on reference standards
[b]Compounds identified in Leeds urban air particulate extract
[c]Compound only partially soluble in *n*-hexane.

$\delta^{13}C$ GC-IRMS CHARACTERISATION OF EXTRACTABLE AND COVALENTLY-BOUND ALIPHATIC HYDROCARBONS IN PETROLEUM SOURCE ROCKS TO REVEAL COMPOSITIONAL FRACTIONATION EFFECTS.

Gordon D. Love(1), Colin E. Snape(1), Anthony E. Fallick(2) and Christopher Taylor(2).
(1) University of Strathclyde, Dept. of Pure & Applied Chemistry, Thomas Graham Building, 295 Cathedral St., Glasgow G1 1XL, UK.
(2) Scottish Universities Research & Reactor Centre (SURRC), East Kilbride, Glasgow G75 OQU, UK.

Keywords : stable isotope geochemistry, kerogen formation, selective preservation .

INTRODUCTION

The structural elucidation of sedimentary fossil organic matter at a molecular level remains a challenging task, on account of its heterogeneous, largely insoluble nature. An elaborate sequential extraction/degradation scheme to differentiate between molecular alkanes (both easily extractable, and those physically-trapped or clathrated within the macromolecular structure) and alkyl moieties covalently bound within the kerogen network, was recently devised by the Strathclyde group. Briefly, the scheme incorporates exhaustive solvent extraction with dichloromethane (DCM) followed by pyridine to remove physically trapped material and then a mild batch hydrogenation step is performed to cleave weak heteroatomic bonds (principally ester, thioether and possibly ether linkages). The key and final stage in this procedure to release strongly-bound hydrocarbons is pyrolysis at high hydrogen pressures (up to 15 MPa, about 150 atmospheres) which is known as hydropyrolysis. Thermolysis in a high hydrogen pressure (reducing) environment eliminates the problem of low yields often associated with the use of sterically-bulky chemical reagents and limits the extent of retogressive, char-forming chemistry. Hydropyrolysis gives rise to overall carbon conversions approaching 100% for Type I and Type II kerogens (these have higher H/C ratios than coals, which are classified as Type III kerogens on the basis of elemental composition) with low hydrocarbon gas yields.

The attractiveness of the scheme lies in the fact that it recognises that the structure of sedimentary organic matter is three dimensional, comprising an organic macromolecular network (kerogen) in which material is trapped with differing degrees of mobility. The increase in severity of the reaction conditions as the sequence proceeds, produces a series of soluble products whose constitution is determined by the strength of association of structural units. The differences in the yield and distribution of selected classes of aliphatic hydrocarbons (such as biomarkers) produced from sequential degradation of a series of vitrinite concentrates [1] and petroleum source rocks [2] are reported elsewhere.

The carbon isotopic signature of the bulk organic matter and individual molecules can be helpful in determining the types of organisms contributing to sediments. Stable carbon isotopic analysis of whole oils, source rock kerogens and bulk hydrocarbon fractions has been used for several years to aid source-oil and oil-oil correlations.[3] However, since kerogens are usually composed of components derived from different biological sources, bulk carbon measurements by conventional isotope mass spectrometry (following combustion) yields only a composite value. Thus, the complexity of fractionation processes and the information they can convey may be hidden within the bulk isotopic measurements. In order to resolve these separate contributions, the isotopic compositions of individual molecular constituents must be determined. Compound-specific carbon isotope measurements became practical with the recent development of reliable computer controlled gas chromatography-isotope ratio mass spectrometry (GC-IRMS).[4, 5] In this technique, a gas chromatograph is coupled to a combustion furnace and the resultant CO_2 is subsequently continuously analysed by a stable isotope mass spectrometer. The isotopic composition of a specific compound is determined by integrating and ratioing the ion currents of masses 45 ($^{13}CO_2$) and 44 ($^{12}CO_2$) measured during the time that the compound of interest is eluting through the mass spectrometer. Similar isotopic compositions for a series of compounds often implies that they have originated from the same biological sources. Differences in isotopic composition of carbon-bearing substances are usually expressed in terms of the conventional δ-notation giving the permil deviation of the isotope ratio of a sample (sa) relative to that of a standard (st), i.e.

$$\delta^{13}C_{sa} = \left[\frac{(^{13}C/^{12}C)_{sa}}{(^{13}C/^{12}C)_{st}} - 1 \right] \times 10^3 \quad (‰, \text{PDB}) \qquad 4.1$$

The standard commonly used is Peedee belemnite (PDB), a Cretaceous marine carbonate sample, whose $\delta^{13}C$-value defines 0‰ on the δ-scale.

Biological (autotrophic) carbon fixation proceeds by a limited number of assimilatory pathways that transfer carbon dioxide (CO_2), bicarbonate ions (HCO_3^-) and carbon monoxide (CO) from the inorganic carbon reservoir to the biosphere. All pathways of autotrophic carbon fixation entail isotope fractionations of varying magnitude, which, in sum, discriminate against ^{13}C and thus lead to preferential incorporation of isotopically light carbon into cell material. C_3 plants which rely exclusively on the C_3 pathway and constitute the bulk of higher plants, range from about -23 to -34‰ with a mean close to -27‰. Higher plants and some bacteria

utilising the C_4 dicarboxylic pathway are isotopically heavier, displayng average $\delta^{13}C$-values between -12 and -14‰ and a total spread from -6 to -23‰. Compounds derived from methanotrophic bacteria exhibit an unusually light isotopic signature, typically lighter than -50‰. The isotopic signature of eukaryotic algal-derived hydrocarbons are often extremely variable from sample to sample (-8 to -35‰) despite the fact that the C_3 path operates in most algal species and are sensitive to the conditions prevailing in the aquatic environment, such as pH.[6]

In ancient sedimentary systems, the structure and stable isotope ($\delta^{13}C$) content of lipid components may still be (partially) preserved and are often diagnostic of their biological source. GC-IRMS, used in conjunction with the sequential degradation scheme, offers an attractive route to probe compositional fractionation effects that might occur in sedimentary fossil organic matter, due to differences in the mode and extent of incorporation of the different initial biological inputs. As an example, the interesting preliminary results from the sequential degradation of an immature type I oil shale (Göynük) are presented and the implications of these findings, in terms of our present understanding of kerogen formation, are discussed. Göynük oil shale (Oligocene, lacustrine, NW Turkey) represents an important world deposit, with reserves estimated at 10^9 tons, occurring in 100-150 m thick seams underlain by lignites.

EXPERIMENTAL

The bulk geochemical data for the Göynük oil shale[2] and the experimental procedure for the sequential extraction/degradation scheme[1] are reported elsewhere. The Göynük sample used in this study was highly aliphatic (liptinite rich, principally alginite) and was especially organic-rich (ash content < 25%). The aliphatic fractions produced from sequential degradation were analysed by GC-FID using a Varian 3400 gas chromatograph. Separation was achieved with a WCOT 25m fused silica capillary column (0.39mm i.d.) coated with CP-Sil 5CB (0.12µm thickness). Helium was employed as the carrier gas and a temperature program of 50°C (4 mins) to 320°C (12 mins) at 4°C min^{-1} was used. The injection and detection temperatures were both set at 320°C. Compound specific $\delta^{13}C$ measurements were carried out on aliphatic fractions using a VG Isochrom II GC-IRMS instrument. Chromatographic conditions were similar to that used for GC-FID. Urea adduction was employed to separate the straight chain aliphatic components from co-eluting branched/cyclic alkane components, prior to analysis. In general , the reproducibilitiy of multiple analyses for n-alkanes and n-alkenes was excellent (± 0.5‰), after urea adduction had been performed. $\delta^{13}C$ of bulk kerogens (carbonate-free) were also determined by conventional isotope mass spectrometry to provide a suitable reference. All delta values are reported relative to the PDB standard.

RESULTS AND DISCUSSION

DCM extraction of Göynük oil shale released 4.1% w/w of total extract (dry, ash-free basis) of which only a small amount (0.1% w/w) consisted of aliphatic hydrocarbons. The GC-FID trace of the total aliphatic fraction is shown in Figure 1 and it can be seen that the major constituents present were C_{21}, C_{23}, C_{25}, C_{27}, C_{29} and C_{31} n-alkanes (max. C_{23}). An odd carbon predominance of n-alkanes is usually associated with a continental higher plant input; although this is generally in the range n-C_{25} to n-C_{31}. The distribution observed in the case of Göynük may be explained by bacterial reworking of higher plant material during early diagenesis. This can result in the reduction of the chain length of n-alkane components while preserving a noticeable odd over even carbon number predominance. One cannot, however, rule out an input from aquatic organisms. This highlights the speculative nature of interpreting the compound distribution in geological samples. Hopanes were also visible in the GC trace. Monitoring of the m/z 191 fragmentogram by gas chromatography-mass spectrometry (GC-MS) showed that these were hopanes (C_{27} and C_{29}-C_{32}) whose biological configurations had been preserved [17β(H)- for C_{27}; 17β(H), 21β(H)- for C_{29}-C_{32}] indicating a contribution from bacteria. The preservation of the original stercochemistries reflects the immaturity of the sample.

The results of the GC-IRMS analysis for the solvent-extractable n-alkanes isolated from Göynük, as displayed in Figure 3, provided definitive evidence the that n-C_{21}-n-C_{31} alkanes in the bitumen phase of Göynük were not derived from the same parent organisms. The C_{21} and C_{23} n-alkanes had the heaviest isotopic signatures (ca -20‰) and appeared to be derived solely from freshwater algae. The C_{30} and C_{31} members were relatively depleted in ^{13}C (-26.5 and -28.1‰, respectively) indicating an origin from allochthonous higher plant matter. This is consistent with the negative (-7 to -9‰) isotopic fractionation which prevails in the assimilation of atmospheric or dissolved CO_2 in comparison with the assimilation of dissolved HCO_3^- inorganic species by aquatic organisms. The intermediate n-alkanes had isotopic ratios from -22 to -24‰ indicating these chain lengths could be derived from both sources. Thus, analysis of the solvent-extractable alkanes implied an input from diverse sources, including algae, higher plants and bacteria.

Sequential catalytic hydropyrolysis of Göynük (following exhaustive solvent extraction with DCM then pyridine, followed by low temperature catalytic hydrogenation) produced a high yield of aliphatic products from the residual kerogen (approx. 23% w/w on a dry, ash-free basis) and a high overall conversion (over 90% w/w). A bimodal distribution of n-alkanes/n-alk-1-enes (maximum C_{20} and submaximum C_{28}) was produced, with the n-alk-1-enes

paralleling the distribution of their saturated analogues. The GC profile of aliphatics produced from sequential hydropyrolysis are shown in Figure 2 and in each case the n-alk-1-enes elute immediately before the n-alkanes. Interestingly, GC-IRMS indicated that the $\delta^{13}C$ values for the n-alkanes and n-alk-1-enes products were identical within the limits of experimental reproducibility (± 0.5‰) and therefore, were almost certainly derived from the same biological source. These findings are in contrast with the generally accepted rationale that alkyl moieties in the molecular weight range (n-C_{12}-n-C_{20}) are derived principally from phytoplankton while longer-chain n-alkanes (principally n-C_{25}-n-C_{33}) are products of the defuctionalisation of the cuticular waxes of continental higher plants. Thus, a bimodal distribution of aliphatics found in a crude oil or produced from pyrolysis of a sediment may either indicate an input from a single class of organism or may be the result of an input from two or more sources. The observation of isotopic uniformity in the major aliphatic pyrolysis products from a number of kerogens was recently reported[7] and appears to support an origin of the long alkyl chains in these kerogens from aliphatic macromolecular networks derived from the selective preservation of highly resistant aliphatic biopolymers. Non-hydrolysable highly aliphatic biomolecules have been identified in leaf cuticles, sporopollenins and algal cell walls may be a possible source of long-chain n-alkanes (>C_{20}) in sediments and high wax crude oils[8], as well as of shorter chain homologues. The heavy values of $\delta^{13}C$ (ca. -19‰) obtained for n-alkanes produced by sequential hydropyrolysis were typical of those found in some eukaryotic algal species.[9]

It is therefore proposed that Göynük oil shale was largely derived from the highly aliphatic resistant biomacromolecules occurring in the outer cell walls of freshwater green algae, termed *algaenans*. The results for Göynük support the view that kerogens may be composed almost exclusively from selectively preserved or partly altered resistant biomacromolecules rather from random polymerisation and condensation of the remnants from microbial degradation of the initial biomass. This mechanism of kerogen formation is often termed the *Selective Preservation* pathway.

Another point which should be noted from the data displayed in Figure 3 is the fact that the aliphatics produced from sequential hydropyrolysis (ca. -19‰) were distinctly isotopically heavier than the bulk organic carbon of the oil shale (-23.8‰). Even allowing for the presence of vitrinite (around 30% vol), an isotopic balance indicates that liptinite other than lamalginite, with a lighter isotopic signature than the bulk oil shale, must be present. Small quantities of higher plant liptinite can be identified from petrographic analysis of Göynük. GC-IRMS analysis of the n-alkanes (approx. 1.5% w/w on a dry, ash-free basis) released by mild catalytic hydrogenation (320°C, 7.0 MPa H_2) prior to hydropyrolysis, indicated that these were largely derived from higher plant sources (-26 to -28‰ for n-alkanes >C_{22}). Whether this reflects the isotopic composition of the whole hydrogenation product requires further investigation. However, it was observed that with increasing conversion (at higher temperatures) and consequently with higher yields of aliphatic products, the isotopic composition of n-alkanes released by hydrogenation and fixed-bed pyrolysis assumed a less negative (heavier) isotopic composition (approaching the algal isotopic signature). Thus, it was proposed that the more thermally labile n-alkyl components of the kerogen structure were derived largely from allochthonous higher plant material (isotopically light) while the additional n-alkanes released by higher conversion regimes originated from an autochthonous (algal) source (isotopically heavy). As a check, non-sequential hydropyrolysis was conducted on a pyridine-extracted GOS sample. The isotopic signatures of the n-alkanes produced (ca. -24.0‰) were similar to the $\delta^{13}C$ value determined for the bulk carbon of the Göynük kerogen (-23.8‰). Thus, the compositional fractionation effect observed was real and not produced by a kinetic isotope effect associated with hydropyrolysis. The heavy isotopic values of algal-derived aliphatics was likely to reflect low concentrations of dissolved CO_2 in the environment of carbon fixation for Göynük. In such circumstances, many carbon-fixing organisms utilise special pathways (such as assimilation of HCO_3^-) for accumulation of inorganic carbon. The isotopic fractionation effects associated with such pathways are small in comparison to those produced by the regular C_3 pathway, and the resultant organic carbon is relatively enriched in ^{13}C. A thermally-resistant algal backbone for Göynük is consistent with petrographic analysis, which showed alginite (and in particular, lamalginite) to be the dominant maceral.

Additionally, the sequential degradation procedure was applied to the Dunnet torbanite (Type I, Scotland) and a Kimmeridge clay from Dorset (Type II, SW England). Both samples were immature source rocks (< 0.4% R_o) and thus offered a good comparison with Göynük Oil Shale. A lack of any noticeable compositional fractionation for either sample was reflected in the GC-IRMS data for the aliphatic fractions produced (Figures 4 and 5). It was observed that the $\delta^{13}C$ values of aliphatic products from low temperature DCM extraction, mild catalytic hydrogenation and hydropyrolysis were very similar in magnitude, although in the case of Dunnet, the bitumen phase (DCM-extractable) aliphatics were slightly isotopically lighter. A relative lightness of solvent-extractable lipids (usually ca. 2-4‰) relative to the $\delta^{13}C$ value for the bulk kerogen has been widely observed however.[5] The only report of compositional fraction that has appeared in the geochemical literature to date, that parallels that of Göynük, is that of the Messel oil shale (type I, Western Germany). Robinson *et al.*[10] concluded from a study of the extractable lipids that the major sources of organic matter in the Messel oil shale were dinoflagellates and bacteria, especially cyanobacteria. Compound-specific carbon ($\delta^{13}C$) isotope measurements showed that the aliphatic components of the bitumen phase were derived

from diverse sources, including methanotrophic bacteria.[5] However, the analytical pyrolysis products from this oil shale showed a striking similarity to those of algaenans isolated from cultured *Tetraedron Minimum* algae.[11] Scanning electron microscopy (SEM) confirmed that the bulk of the organic matter of Messel oil shale was composed of a *Tetraedron*-type fossilised algal species. While these results for Messel at first seem at variance, it should be recognised that the extractable organic matter of the Messel shale, like that of Göynük, represented at best a few percent of the total organic matter, whilst the kerogen represented 95% or more. In such cases, conclusions based on analyses of solvent extracts probably suffer from a severe bias. Thus, the interpretation of biomarker data with respect to major sources of organic matter should be performed with great caution as it may lead to false interpretations being made.

In the case of Dunnet shale, the similarity in the distribution of aliphatics released at each stage in the degradation scheme (not shown here) together with the observance of isotopic uniformity in the n-alkane/n-alkene products from sequential hydropyrolysis, supported an origin of the aliphatic constituents of this torbanite as being derived almost exclusively from fresh- to brackish-water alga, *Botryococcus*.. A mechanism of selective preservation of resistant aliphatic biopolymers in algal cell walls, as with Göynük, can explain the formation of torbanite. Largeau and co-workers demonstrated the presence of highly resistant biopolymers, termed PRB (Polymère Resistant de *Botryococcus*), in cell walls of Botryococcus.[12,13] Structural and morphological similarities between PRB A and immature Torbanite demonstrated that the resistant polymer was selectively preserved and thus afforded a major contribution to Torbanite formation.[14] Unlike the algal precursor of ultralaminae-type alginite, *Botryococcus* appears to impart a molecular fingerprint (the characteristic n-alkane distribution observed for DS) to the bitumen phase at low maturities. This might be explained by the fact that Botryococcus is anomolously hydrocarbon-rich and can contain up to 76 percent of its dry cell weight as extractable lipids .[15]

CONCLUSIONS

The application of a sequential degradation scheme to an immature oil shale (Göynük), in conjunction with compound specific carbon ($\delta^{13}C$) measurements, highlighted the fact that significant compositional fractionation effects may exist between aliphatic constituents of the free molecular (bitumen) phase and those covalently bound to the insoluble kerogen network. It thus appears, particularly for immature type I source rocks, that the bitumen phase is not necessarily a low molecular weight indicator of the constituents of the bulk kerogen. The isotopic uniformity of the aliphatics released by the high-conversion hydropyrolysis step lends further support to the theory that selective preservation is an important mechanism in kerogen formation.

REFERENCES

1. Love, G.D., Snape, C.E. and Carr, A.D. *Prep. Am. Chem. Soc. Div. Fuel Chem.* **1993**, 38(4), 1281-12 and *Energy & Fuels*, submitted.
2. Love, G.D., Snape, C.E., Carr, A.D. and Houghton, R.C. *Org. Geochem.*, submitted.
3. Schoell, M. In *Advances in Petroleum Geochemistry, Volume 1.* (Eds. J. Brooks and D.H. Welte) pp. 215-245. Academic Press, London, 1984
4. Bjorøy, M., Hall, K. and Jumeau, J. *Trends in Analytical Chemistry* **1990**, 9(10), 331-336.
5. Freeman, K.H., Hayes, J.M., Trendel, J.-M. and Albrecht, P. *Nature* **1990**, 343, 254-256.
6. Schidlowski, M. In *Biological Markers in the Sedimentary Record* (Ed. R.B. Johns) pp. 347-361. Elsevier, Amsterdam, 1986.
7. Eglinton, T.I. *Org. Geochem.* **1994**, 21, 721-736.
8. Tegelaar, E.W., Matthezing, R.M., Jansen, J.B.H., Horsfield, B. and de Leeuw, J.W. *Nature* **1989**, 342, 529-531.
9. Hayes, J.M., Takigiku, R., Ocampo, R., Callot, H.J. and Albrecht, P. *Nature* **1987**, 329, 48-51.
10. Robinson, N., Eglinton, G. and Cranwell P.A. *Chem. Geol.* **1989**, 76,153-173.
11. Goth, K., de Leeuw, J.W., Püttman, W. and Tegelaar, E.W. *Nature* **1988**, 336, 759-761.
12. Largeau, C., Derenne, S., Casadevall, E., Kadouri, A. and Sellier, N. In *Advances in Organic Geochemistry 1985* (Eds. D. Leythaeuser and J. Rullkotter) pp. 1023-1032. Pergamon Press, Oxford, 1986.
13. Berkaloff, C., Casadevall, E., Largeau, C., Metzger, P., Peracca, S. and Virlet, J. *Phytochemistry* **1983**, 22, 389-397.
14. Rohmer, M., Dastillung, M. and Ourisson, G. *Naturwissenschaften* **1980**, 67, 456-458.
15. Maxwell, J.R., Douglas, A.G., Eglinton, G. and McCormick, A. *Phyochemistry* **1968**, 7, 2157-2171.

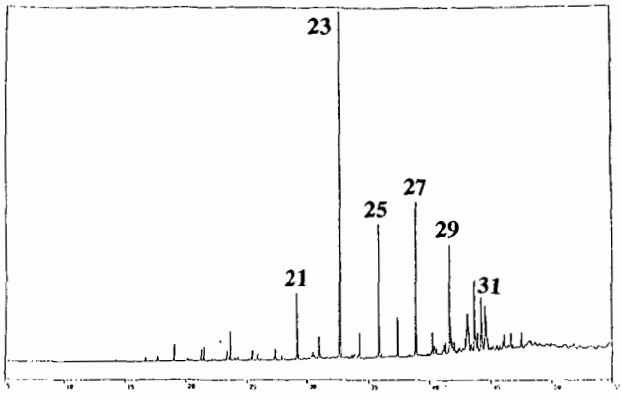

Figure 1. GC-FID trace of the free aliphatic hydrocarbons released by dichloromethane extraction of Göynük Oil Shale.

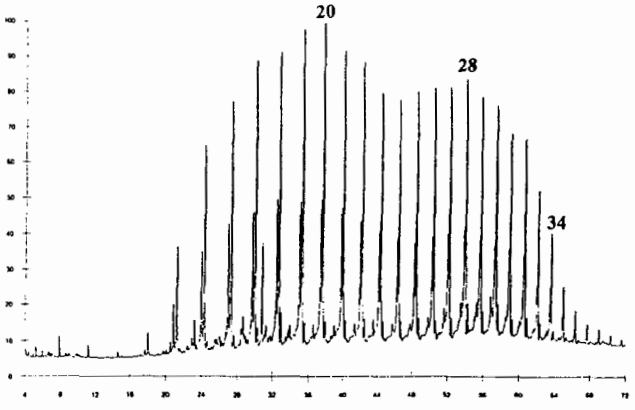

Figure 2. GC-FID trace of the aliphatic hydrocarbons produced from sequential hydropyrolysis of Göynük Oil Shale.

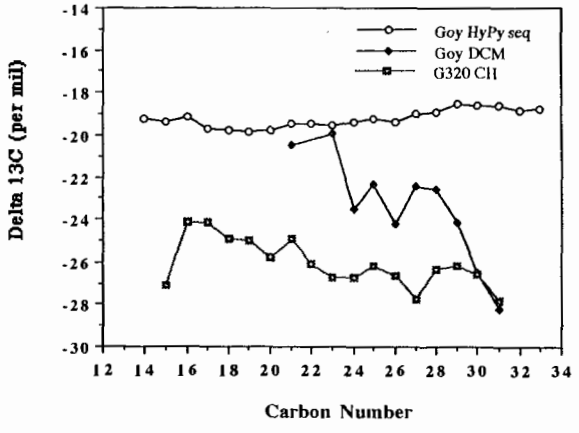

Figure 3. GC-IRMS analysis of *n*-alkanes produced from sequential degradation of Göynük Oil Shale.

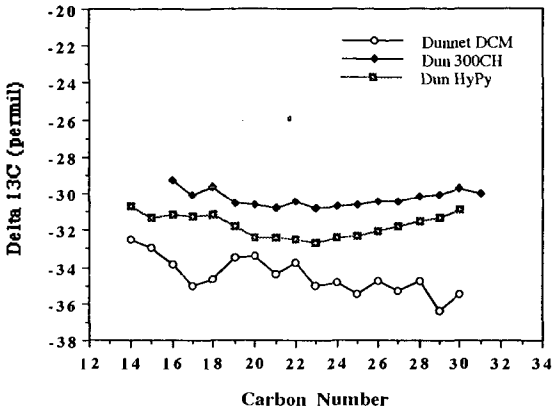

Figure 4. GC-IRMS analysis of n-alkanes produced from degradation of Dunnet torbanite. ($\delta^{13}C$ of bulk TOC = -29.2‰)

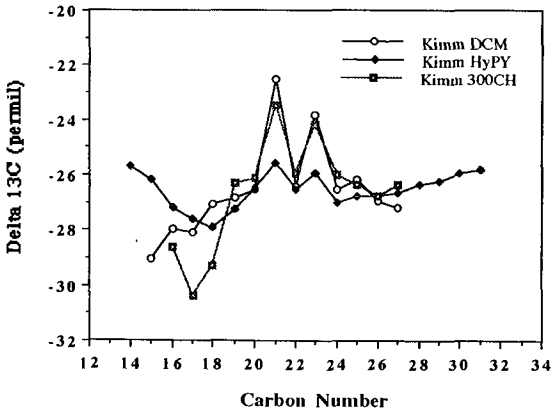

Figure 5. GC-IRMS analysis of n-alkanes produced from degradation of Kimmeridge clay. ($\delta^{13}C$ of bulk TOC = -23.8‰)

FOSSIL FUEL CHARACTERIZATION USING LASER DESORPTION MASS SPECTROMETRY: APPLICATIONS AND LIMITATIONS

Jerry E. Hunt and Randall E. Winans
Argonne National Laboratory, Chemistry Division
Argonne, IL 60439 USA

Keywords: Argonne Premium Coals, laser desorption, matrix-assisted laser desorption

INTRODUCTION

High molecular weight compounds (>600 amu) in fossil fuels have been overlooked in the past principally because of inappropriate analytical techniques. Most of the techniques have accessed only the easily volatilizable fraction. Mass spectrometry characterization of any presumed heavy components has mostly depended on pyrolysis to break up the larger molecules prior to analysis, especially by pyrolysis gas chromatography mass spectrometry. The material that is outside of the volatilizable fractions has received little attention. However, laser desorption mass spectrometry (LDMS) and matrix-assisted laser desorption/ionization mass spectrometry (MALDI) are particularly applicable to those molecules which resist intact ionization by traditional gas-phase methods. The application and limitations of these techniques to model compounds and fossil-derived materials is discussed in this study.

LD and MALDI mass spectrometry are increasingly used to detect intact molecular species, such as proteins with masses from 1000 to 100,000 amu and beyond.[1] MALDI is also being used for a few high molecular weight polymers.[2] A good example, related to coal-type systems, is the report on lignin mass spectrometry by MALDI.[3] Here the mass spectrum shows a wide molecular distribution of several hundred to larger than 16000, with the center of gravity of the distribution around 2600. The results are interpreted in terms of oligomeric lignin molecules. Thus, if there are indeed large molecular species in a polymeric content in fossil fuel extracts, MALDI is an attractive technique.

We have previously reported laser desorption of coal extracts that show only low molecular weight ions (<2000 amu).[4-6] We compare LD with fast atom bombardment and desorption chemical ionization mass spectrometry, two other soft ionization techniques. All of these techniques produce similar data that differ only in minor details. We have used our two TOF mass spectrometers for coal analysis by MALDI, have carefully analyzed our data and the instrumental conditions and conclude that the bulk of coal material produces only low molecular weight ions (up to 2000 amu). In agreement with these reports, Hanley showed LD and MALDI data of pyridine extracts which produced a distribution of ions between 150 and 1500.[7] In addition, field ionization mass spectrometry has found similar pattern in the low mass region.[8] Recently, Herod et. al[9-12] have interpreted their LD and MALDI data in terms of high mass species being desorbed. We have presented alternate interpretations for these results.[6]

In our hands, LD or MALDI of coals and extracts do not show any reproducible ion intensity over mass 2000. The conditions whereby large molecular ions can be desorbed intact are very specialized. This paper will describe the scope and limitations of laser desorption and matrix-assisted laser desorption in time-of-flight mass spectrometers as applied to high molecular weight molecules, such as proteins and polymer systems.

EXPERIMENTAL

The coals used in this study are the Argonne Premium Coal Samples. The procedures for the pyridine extract of the Argonne Premium Coals have been reported previously.[5] The laser desorption mass spectra and matrix-assisted laser desorption mass spectra were recorded on a linear time-of-flight mass spectrometer constructed at Argonne and a Kratos Kompact MALDI III linear/reflectron time-of-flight mass spectrometer. The spectra were produced by exposing the samples distributed as thin layer on a stainless steel sample holder to laser pulses from either a Nd:YAG or a

nitrogen laser. The laser is operated close to the ionization threshold to minimize possible fragmentation of the desorbing material and to optimize resolution.

The matrices used were dihydroxybenzoic acid, sinapinic acid, indoleacrylic acid and 2-(4-hydroxyphenylazo)-benzoic acid (HABA) purchased from Aldrich. The polyethylene sample were purchased from Petrolite. The polyethylene glycol was purchased from Aldrich.

RESULTS

Coals

Coals are a unique sample for LD and MALDI. They are chemically very complex, heterogeneous, and most likely polydisperse in mass. Figure 1 shows a positive ion LD mass spectrum of the pyridine extract of APCS 1 mv bituminous coal produced using 337 nm laser pulses, displaying a distribution of ions between roughly 200 and tailing to 2000 amu. The major ion series seen are alkyl-pyrenes (-fluoranthenes), -chrysenes, -benzopyrenes, -phenlypyrenes (-pyreneobenzofurans), -carbazoles, and -benzoperylenes. Laser desorption favors the aromatic compounds. Laser desorption with the Nd:YAG fundamental wavelength of 1064 nm, 532 nm (frequency doubled), and 266 nm (frequency quadrupled) show similar spectra.

The MALDI spectrum of the same sample from sinapinic acid is shown in figure 2. The matrix/laser combination is sinapinic acid with 337 nm laser light. At first glance the data indicate a continuum of high mass peaks, but the observed "signal" is actually a result of chemical noise from the matrix and ion saturation of the detector creating a false signal at the detector which is not correlated with the laser blast or sample. In an attempt to see higher mass ions, we have deflected the low mass ions using time-gated pulsed deflection, so that these intense ions do not impact the detector. The results show no high mass ions. Matrix-assisted laser desorption/ionization using 2,5-hydroxybenzoic acid, HABA, nicotinic acid, sinapinic acid, 3-hydroxypicolinic acid, silver nitrate, silver acetate, silver picolinate and indole acrylic acid, have been attempted on the pyridine extracts of Argonne coals. No higher mass or other ions are observed in the MALDI experiments beyond those of the matrix and those seen in the neat coal extracts.

The Nature of the MALDI Event

In order to assess the characteristics of the MALDI mass spectrum, we present a protein mass spectrum. The inset in the figure 2 shows the MALDI of a protein in the sinapinic acid matrix. Here the molecular ion is easily observed above the background without detector saturation. A feature of MALDI in time-of-flight instruments is that at higher masses the resolving power decrease. The peak with for each of the two protein ions using this matrix is about 4000 mass units a the baseline. An important aspect of MALDI is the low resolution, especially at higher masses. In the case of two single proteins the mass resolution in ~150 $m/\Delta m$ full width at half maximum. This means that a distribution of molecules, for example from 10000 to 200000 amu, would appear only as a broad unresolved hump in the mass spectrum. In fact, MALDI for polymers above 10,000 amu the resolution for a linear time-of-flight mass spectrometer is insufficient to identify individual oligomers. Sharp peaks are not be observed. The amount of available charge in the MALDI event to span such a large mass region is also questionable.

The MALDI mass spectrum (HABA matrix) of polyethylene glycol 3000 is shown in figure 3. The distribution of oligomers is clearly observed. In the case of more nonpolar species, such as polyethylene, we have found that common organic matrices do not result in mass spectra. Silver nitrate or other silver salt must be added to polyethylene to produce mass spectra of silver cationized oligomers. We have easily observed polyethylene up to 2500MW with this method.

CONCLUSIONS

LDMS and MALDI time-of-flight instruments are easy to operate, fast, and are suitable for quantitative measurement of molecular weight distributions of certain coal components. LD, in particular, is better suited to mixture analysis than MALDI.

Although matrix-assisted laser desorption time-of-flight analysis has been touted as a universal molecular weight distribution tool, it is hardly that. The successful application of the MALDI is greatly dependent on the chemical structure of the system under investigation. Different chemical structures may require significantly different sample preparation. The sample preparation step is perhaps the most important component of a MALDI experiment. First, nonpolar compounds (e.g., polyethylenes) have not been successfully analyzed by any organic matrix-assisted technique that the authors are aware. Second, ion intensities from mixtures of compounds rarely show true abundances. Third, in mixed systems the lowest concentration species may be not observed at all because of the high background noise levels that are a feature of matrix-assisted laser desorption. The fact that spectra are easy to obtain should not overshadow the fact that sample preparation is the critical factor in successful analyses. Furthermore, the conditions useful for one system may not be useful for others. The conditions and matrices presently used for coal in MALDI are most appropriate for proteins. Thus, there is a strong possibility that any observed high mass ions may be from contaminant proteins contained in the coal.

However, the fact remains that LDMS and MALDI are capable of producing intact, unfragmented molecular ions from biopolymers, macroscopic molecules based on aromatic building blocks, and polymers. MALDI can provide values for the molecular weight as well as shows the entire distributions of polymer species. The question arises, if there were high mass material in coals and extracts, would they be detected by this technique. First, optimal matrices must be found. There is good reason to believe that good miscibility of matrix and the coal in the condensed form is the prerequisite for a good matrix, as has been found to be true for protein desorption. Matrices working well for polar biopolymers will not be optimal for coals. Most of the protein matrices actively exclude ionic components, which are needed for cationizaton. Second, if the mass distribution is extremely polydisperse it may be difficult to detect the high mass material above background as the contribution at any mass may be low even if the contribution to the total mass over a wide range is high. Finally, the mass spectrum is sensitive to the number average molecular weight; a low value, however, does not preclude the presence of high molecular weight species.

ACKNOWLEDGMENT

This work was performed under the auspices of the Office of Basic Energy Sciences, Division of Chemical Sciences, U.S. Department of Energy, under contract number W-31-109-ENG-38.

REFERENCES

1. R. C. Beavis, *Org. Mass Spectrom.* **27**, 653-659 (1992).
2. J. E. Campana, L.-S. Sheng, S. L. Shew, B. E. Winger, *trends in analytical chemistry* **13**, 239-247 (1994).
3. J. O. Metzger, et al., *Angw. Chem. Int. Ed. Eng.* **31**, 762-764 (1992).
4. J. E. Hunt, K. R. Lykke, R. E. Winans, *Preprints Am. Chem. Soc., Div. Fuel Chem.* **36**, 1325-1328 (1991).
5. R. E. Winans, R. L. McBeth, J. E. Hunt, P. E. Melnikov, Monomers in Coal Macromolecules, 1991 International Conference on Coal Science, University of Newcastle upon Tyne, UK, September 16-20, (1991).
6. J. E. Hunt, R. E. Winans, *Preprints Am. Chem. Soc., Div. Fuel Chem.* **39**, 831-934 (1994).
7. J. A. Burroughs, B. M. Cadre, L. Hanley, presented at American Society for Mass Spectrometry Meeting, San Francisco, CA, (1993).
8. A. A. Herod, B. J. Stokes, H.-R. Schulten, *FUEL* **72**, 31-43 (1993).
9. A. A. Herod, et al., *Rap. Commun. Mass Spectrom.* **8**, 815-822 (1994).
10. A. A. Herod, et al., *Rap. Commun. Mass Spectrom.* **8**, 808-814 (1994).
11. A. A. Herod, et al., *J. Chem. Soc., Chem. Commun.*, 767-769 (1993).
12. A. A. Herod and R. Kandiyoti, *FUEL* **74**. 784-786 (1995).

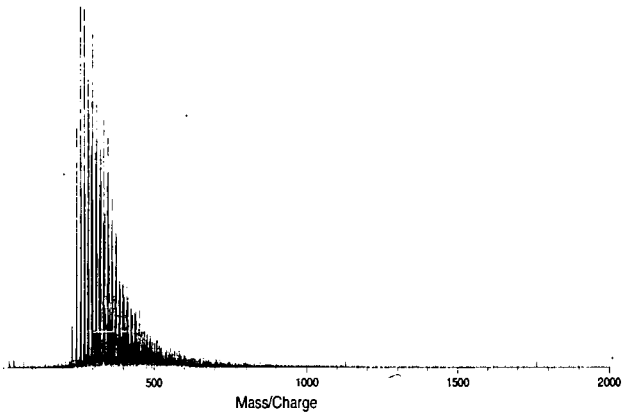

Figure 1. LD mass spectrum of the demineralized pyridine soluble fraction of APCS 1 (Upper Freeport).

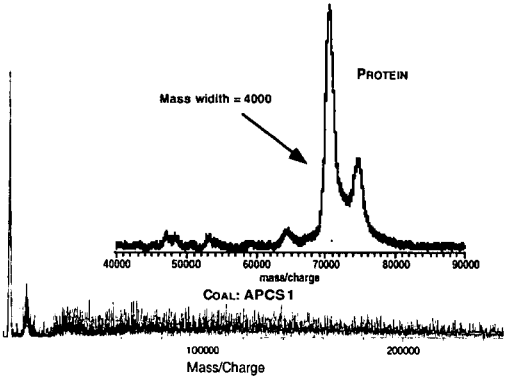

Figure 2. MALDI linear mass spectrum of APCS 1 (Upper Freeport) using sinapinic acid as matrix showing the effect of detector saturation. The inset is the MALDI of two proteins, synapsin IA, IB, in sinapinic acid.

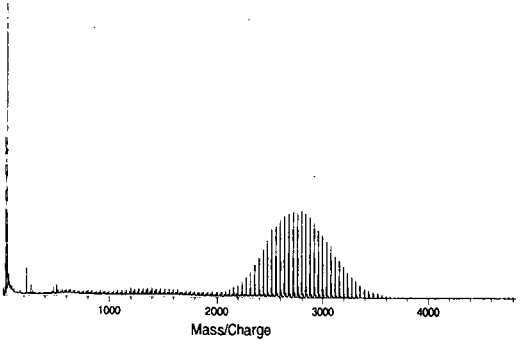

Figure 3. MALDI reflectron spectrum of polyethylene glycol showing intact cationized molecular ion formation.

HIGH RESOLUTION MASS SPECTROMETRY FOR THE CHARACTERIZATION OF COMPLEX, FOSSIL ORGANIC MIXTURES

Randall E. Winans, George W. Haas, Yeonhee L. Kim, and Jerry E. Hunt
Chemistry Division
Argonne National Laboratory
Argonne, IL 60439

Keywords: Argonne Premium Coals, Desorption Chemical Ionization High Resolution Mass Spectrometry (DCIHRMS)

INTRODUCTION

The nature of molecules with heteroatom functionality in the pyridine extracts of the Argonne Premium Coal Samples is being explored using high resolution mass spectrometry (HRMS), with desorption chemical ionization (DCI). Structural information is obtained from tandem MS experiments using high resolution to select the ions to fragment. The first DCIHRMS spectra of complex mixtures are shown. Molecular weight distribution determined by DCI are similar to those determined by laser desorption and field ionization mass spectrometry with very little ion intensity observed at greater than 1000 Daltons. Results are correlated with other techniques such as NMR, XPS, and XANES.

PyMS has been used extensively to examine coals and separated macerals. Results from electron impact (EI) in high resolution mode have demonstrated the importance of not only single heteroatom containing molecules in coals, but also multiple heteroatom containing molecules.[1] Both PyGCMS and PyMS have been used to analyze the more volatile pyrolysis components. Thermogravimetric MS techniques yield quantitative data with rather slow heating rates.[2] Also, a standard technique now used to provide molecular weight distribution of volatile tars is field ionization MS (FIMS).[3] FIMS results are published for all eight Argonne coals,[4] while Meuzelaar, Schulten and co-workers have correlated the results from PyFIMS, low voltage EI and TGAMS on the same coal.[5] They found similar patterns in the low mass regions. FABMS has been applied to coal pyrolysis products yielding data similar to FIMS.[6] Finally, the first DCIMS results have been discussed[7] and will be expanded in this paper with the addition of high resolution data.

EXPERIMENTAL

The Argonne Premium Coal samples used in this study have been described[8] and further information is available on World Wide Web - http://www.anl.gov/PCS/pcshome.html. Pyridine extracts[7] were thermalized directly in the source of a Kratos MS50 TA using a desorption chemical ionization probe heated from 200 to 700 °C @ 100 °C/min. The spectrometer was operated at a dynamic resolution of 10,000 and scanned at 10 s/decade of mass. Isobutane was used as the CI gas and poly(dimethylsiloxane) (PDMS) was used as the internal mass calibrant. For group analysis, all scans with ions above background are averaged and only those which occur a minimum of four times are saved. Formulae which fit within ±3.5 millimass units are assigned for each averaged ion peak. The formula are then sorted by hydrogen deficiency and heteroatom content.

RESULTS AND DISCUSSION

In general, the data from DCIHRMS are similar to those found by field ionization (FIMS).[4] A major problem is finding an internal mass calibrant because perfluorokerosene (pfk), which is used in electron impact, does not ionize in isobutane CI. PDMS is an effective calibrant,[9] but the measurements are not consistently as good as with pfk because the reference peaks are spaced at larger increments of mass. Therefore, we are looking at some alternative reference materials. Recently, a resolving power of 80,000 was achieved by the source used in this study.

Samples of averaged spectra are shown for four of the Argonne coals in Figure 1. The spectra typically show ion intensity out to $m/z \approx 700$ and useful information ends at the low mass end of 90, due to the isobutane. Normally $[M+H]^+$ ions are observed under these conditions.

The subbituminous coal (Figure 1a) gave a distribution similar to bituminous coals, except for a series of fatty acids C_{25}, C_{27}, C_{29}, C_{31} (major) and C_{26}, C_{28}, C_{30} (minor). Also, pyrolysis fragments of lignin remnants are observed at m/z = 111, 125, 139, 153, which correspond to the series $Ph(OH)_2(CH_2)_xH$, x = 0-3. The acids were also observed in the lignite coal by DCIMS. With FIMS,

they were only observed in the lignite, but the lignin fragments are observed in both low rank coals.[4] It is interesting to note that these are not the major species seen by PyGCMS of low rank coals.

In the Illinois No. 6 coal (Figure 2b), the fatty acids are absent and the lignin derived pyrolysis fragments are alkylated C_0-C_4 monohydroxybenzenes. However, the molecular size distribution is very similar to the low rank subbituminous coal. Another difference is the large number of sulfur containing ions in the Illinois coal as one would expect.[1]

The hvA bituminous Pittsburgh seam coal gave a higher molecular size distribution of the ions. However, alkylated hydroxybenzene species are still observed, but their overall contribution to the total ion current found is significantly less than with the low rank coals.

The Blind Canyon coal (APCS 6) (Figure 1d) is unusual in that it contains significant amounts of resinite and sporinite macerals. Ions at m/z = 320 ($C_{25}H_{20}$), 321, 324 ($C_{25}H_{24}$), 325 (100), 342 ($C_{26}H_{30}$), 343 correspond to triterpenoid hydrocarbons from resinite, which has also been observed in Curie point pyrolysis MS[10] and by GCMS in benzene-methanol extract.[11]

All of the total ion response curves are bimodal such as is seen in Figure 2a for the Lewiston-Stockton hvA bituminous coal (APCS 7). This effect has also been seen in the temperature programmed thermolysis of whole coals. For the whole coal, the first peaks had been thought to be small molecules such as those that are solvent extractable. The extract also contains larger molecules which are released as pyrolysis temperatures where weak bond cleavage is occurring. No evidence is found for very large polycyclic aromatics volatilizing at the higher temperatures.

The change in the ion mass distribution with temperature for APCS 7 is shown in Figure 2b. The ions at m/z = 157 and 111 are artifacts from the extraction solvent, pyridine, representing the dimer of pyridine and an oxygenated alkyl pyridine molecule, respectively. At increasing desorption temperature, the size of the ions increases from scan 9 to scan 12. Around scan 18, pyrolysis begins and distribution shifts to small ions and finally the mass distribution shifts higher in scan 21. It is interesting to note that the distributions are similar in scan 12 and 21 even though the temperatures differ by 220 °C. In addition, over the entire temperature range, a series of distinct peaks are observed between 470 and 600. Exact mass measurements suggest that they are alkylated aromatic hydrocarbons with 4 rings. This was confirmed by tandem MS experiments and are possibly greatly modified biomarkers. They were not observed by FDMS, but have been seen in both FAB and EI MS experiments.[6,7]

Finally, from the exact mass measurement, formulae can be calculated resulting in information on ring size and heteroatom distribution. An example is shown in Figure 3 for the Pocahontas lv bituminous coal (APCS 5). The ring size varies from 4 to 7 with the most abundant being six (rings + double bonds = 18, 19). Even though the heteroatom content combined is lower than all the other coals, from statistical viewpoint every polycyclic aromatic with 6 rings should have a heteroatom in it. This is what we are observing in the extract. Some preliminary MSMS results suggest that annelated furans are the likely form of the single oxygen molecules, which agrees with NMR experiments.[12] XPS results indicate that over 60% of nitrogen exist in pyrrole type structures which is analogous to furan for oxygen and thiophene for sulfur.[13] These structures are probably important in determining the tertiary structure of high rank coals.

CONCLUSIONS

High resolution CIMS data further support the notion that the size of the stable aromatic clusters is not large in coals except the very high rank coals and inertinite macerals. The DCI spectra appear to be very representative of the sample with little discrimination for molecular types such as aliphatics.

ACKNOWLEDGMENT

This work was performed under the auspices of the Office of Basic Energy Sciences, Division of Chemical Sciences, U.S. Department of Energy, under contract number W-31-109-ENG-38.

REFERENCES

1. Winans, R. E. and Neill, P. H. In Geochemistry of Sulfur in Fossil Fuels, W. L. Orr and C. M. White, Eds., ACS Symposium Series 429, ACS, Washington, D.C., 1990, Ch. 15, p. 249-259.
2. Szabo, P.; Varhegyi, G.; Till, F.; and Szekely, T. *Thermochimica Acta*, **1990**, *170*, 167-177.

3. Schulten, H.-R. and Marzec, A. *Fuel*, **1986**, *65*, 855-860.
4. Solomon, P. R.; Serio, M. A.; Despanda, G. V.; and Kroo, E. *Energy Fuels*, **1990**, *4*, 42-54.
5. Yun, Y.; Meuzelaar, H. L. C.; Simmleit, N.; and Schulten, H.-R. *Energy Fuels*, **1991**, *5*, 22-29.
6. Winans, R. E. *J. Anal. & Appl. Pyrolysis*, **1991**, *20*, 1-13.
7. Winans, R. E.; McBeth, R. L.; Hunt, J. E.; and Melnikov, P. E. *Proceedings, 6th International Conference on Coal Science*, University of Newcastle-upon-Tyne, England, September 16-20, 1991, pp. 44-47.
8. Vorres, K. S. *Energy Fuels*, **1990**, *4*, 420-425.
9. McCamish, M.; Allan, A. R.; and Roboz, J. *Rapid Comm. Mass Spectrom.*, **1988**, *1*, 124-125.
10. Meuzelaar, H. L. C.; Huai, H.; Lo, R.; and Dworzanski, J. *Fuel Proc. Tech.*, **1991**, *28*, 119-134.
11. Hayatsu, R.; McBeth, R. L.; Neill, P. H.; Xia, Y.; and Winans, R. E. *Energy Fuels*, **1990**, *4*, 456-463.
12. Winans, R. E.; McBeth, R. L.; Melnikov, P. E.; and Botto, R. E. *Proceedings, 7th International Conference on Coal Science*, Banff, Canada, September 12-17, 1993, pp. 515-518.
13. Kelemen, S. R.; Gorbaty, M. L.; and Kwiatek, P. J. *Energy Fuels*, **1994**, *8*, 896.

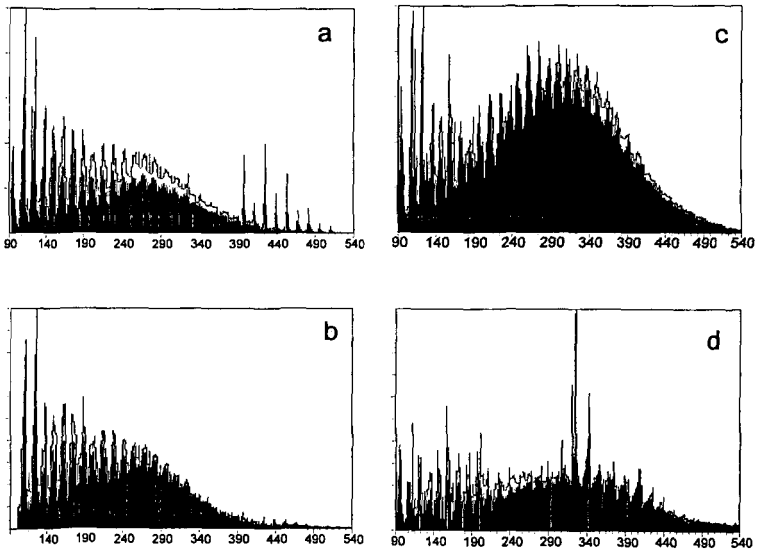

Figure 1. DCI mass spectra of selected Argonne coals. Data are derived from averaging over the total heating range. (a) Subbituminous coal (APCS 2); (b) Illinois No. 6 hvC (APCS 3); (c) Pittsburgh seam (APCS 4); and (d) Blind Canyon (APCS 6).

a

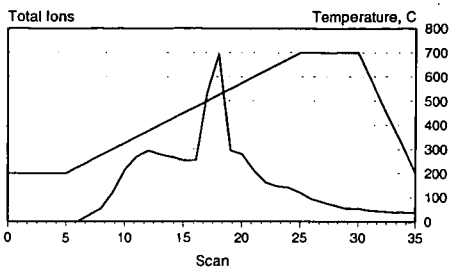

b

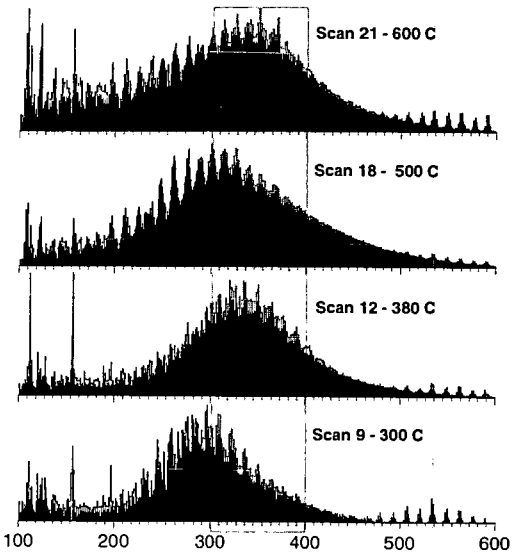

Figure 2. Data from Lewiston-Stockton bituminous coal(APCS 7). (a) Total ion response. (b) Selected scans labelled with scan numbers from Figure 2(a).

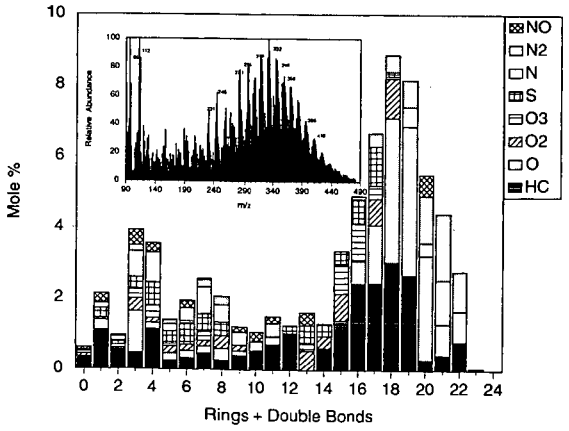

Figure 3. Group analysis of DCIHRMS data from Pocahontas extract(APCS 5). The inset is the averaged spectrum used to calculate the distributions.

IMPROVED SIZE EXCLUSION CHROMATOGRAPHY OF COAL DERIVED MATERIALS USING N-METHYL-2-PYRROLIDINONE AS MOBILE PHASE

Barry R. Johnson, Keith D. Bartle, Alan A. Herod* & Rafael Kandiyoti*
School of Chemistry, University of Leeds, Leeds LS2 9JT, UK
*Department of Chemical Engineering, Imperial College, London SW7 2BY,UK

Keywords Size exclusion chromatography, molecular mass distribution, coal derived materials

INTRODUCTION

A detailed knowledge of the molecular mass distribution (MMD) in coal and its derived products is essential for a fundamental understanding of coal structure, and of the processes occurring during pyrolysis, liquefaction and combustion. Indeed with increased economic and environmental pressure to use natural resources more effectively such knowledge can be applied to gaining more from finite coal reserves. Of the methods available for determining MMDs size exclusion chromatography (SEC) is perhaps the most routinely employed. In SEC tetrahydrofuran (THF) is the most commonly employed mobile phase. However THF has limited solvating power for coal derived materials and consequently a significant proportion of such materials goes undetected. In addition the interpretation of chromatograms with reference to calibration of the column with polystyrene standards is flawed[1]. By comparison, N-methyl-2-pyrrolidinone (NMP) is capable of solvating more of the coal sample and therefore gives the opportunity to determine an improved MMD. In this contribution the extended capabilities of NMP as the mobile phase are demonstrated primarily through the analysis of a coal tar pitch. Both NMP and THF are used as mobile phases for SEC using a number of detection techniques, allowing comparison and evaluation of different chromatographic systems to the analysis of coal derived materials.

EXPERIMENTAL

The principle coal product used in these investigations was a high temperature coal tar pitch, with observations confirmed by similar experiments on a Point of Ayr Pilot Plant extract of Point of Ayr (PoA) coal, and a synthetic pitch. Neither pitch sample was wholly soluble in THF, unlike the PoA sample. The systems developed were then applied to the examination of char material from the British Coal, Coal Technology Development Division (CTDD) Gasification Pilot Plant (Stoke Orchard). The gasifier feed stock was power station grade Daw Mill coal. Char samples were derived from experiments at atmospheric pressure and 960^{o}C. Organic material was extracted from the char using three different techniques. Supercritical fluid extraction, carbon dioxide with toluene modifier (400atm, 200^{o}C), and liquid solvent extraction (1:1 NMP:CS_2 and sonication) both produced greater yields than the more conventional soxhlet extraction. However, in each case the yield was low indicating destruction of potential tar forming materials within the gasifier.

The chromatographic analyses and separations were performed on three systems:

For the THF based analytical system two Jordi gel (5µm, polydivinylbenzene packing) analytical SEC columns (250 x 10 mm, 500 & 100-A^{o}), with guard column, were operated at room temperature with a THF flow rate of 1.0ml/min. Detection was through fixed wavelength (254 or 280 nm) uv absorption and evaporative light scattering detection (ELSD).
Fractionation of the coal tar pitch was performed on two PL Gel (10 µm, styrene-divinylbenzene copolymer packing) preparative scale (600 x 25 mm, 500 & 100-A^{o}) columns. 40 mg of the pitch, in THF, was injected onto the columns with a THF flow rate of 10 mL/min and uv absorption detection used at 254 nm. Using this apparatus the pitch eluted over a volume range of some 40mL. A continuous series of aliquots of the column effluent were collected for each of 22 separate injections. The fractions from the same collection times were then combined and dried in a vacuum oven to remove the solvent.
The NMP based apparatus consisted of a single PL gel (3µm, styrene-divinylbenzene copolymer packing) SEC column (250 x 10 mm, Mixed Bed E) with guard column connected in series to a variable wavelength uv absorption detector (260-700 nm) and a uv/vis fluorescence detector (280-750 nm). Columns were operated at a temperature of 80^{o}C, with an NMP flow rate of 0.5 mL/min.
All SEC apparatus were calibrated using narrow polystyrene standards (162 - 410,000 g/mol, Polymer Labs Ltd). Injection volumes were 20-µl of a 1-10 mg/mL solution for the analytical systems, and 2ml for the preparative scale experiments.

RESULTS AND DISCUSSION

The THF-SEC chromatograms, from both uv absorption and ELSD, of the THF soluble portion of the soft pitch are shown in Figure 1. The range of the calibration with polystyrenes is marked on the figure. This clearly illustrates the difficulties being addressed in the present work[1,2]. However before these are examined two other interesting features are revealed in this figure. The two monitoring wavelengths employed give very similar profiles, and so are detecting similar material. The ELSD chromatogram shows material eluting over the same time range, but gives a different profile, and therefore more

information, at the shorter elution times. This ELSD detection method produces excellent results for the heaviest material within the sample, a portion often underestimated by other detectors.

Returning to the main point of Figure 1. The pitch sample elutes over a much greater time range than the calibrants. In fact the majority of the pitch sample elutes at retention volumes greater than the smallest calibrant. Obviously this 'late' material is not of very small mass, but is interacting with the column packing material, and so the separation occurring is through both adsorption and size exclusion mechanisms. This multimode separation phenomena is well documented[1,2] and means that a MMD cannot confidently be assigned to the sample.

The application of NMP as a mobile phase for analysing such material was investigated next. The dried THF extract of the coal tar pitch was redissolved in NMP, and appeared to be completely soluble. This was analysed on the NMP-SEC apparatus together with the NMP extract of the pitch. The resulting chromatograms are presented in Figure 2. The polystyrene calibration for this apparatus gave an exclusion limit at ~550s and a total permeation limit (peak of toluene elution) at ~1365s. The NMP extract shows two unresolved maxima in the chromatogram. The first is at the exclusion limit indicating large molecular material, with the second within the columns resolving range. The important feature to note here is that there is no material eluting after the total permeation limit. This observation is repeated in the fluorescence detected chromatogram. In the case of the THF extract of the soft pitch, again there are two maxima, one at the exclusion limit and one within the columns resolving range. However, here the two peaks are baseline resolved. Again there is no material eluting after the total permeation limit.

These chromatograms indicate that the molecular material solvated by NMP has a continuous mass range limited only by the exclusion limit of the columns (~30,000 polystyrene equivalent mass units, p.e.m.u. - manufacturers figures). Indeed, by consideration of the intensity of the excluded peak a large proportion of the pitch has a high molecular mass. The majority of the THF soluble material has a much smaller mass, < 5000 p.e.m.u. The presence of the excluded material in this sample may be due to processes occurring during drying and removal of the original THF. A similar effect has been reported during experiments to measure molecular mass by vapour pressure osmometry, where accurate weighing of solvent free sample is essential.

The examinations in Figures 1 & 2 raise an important question about the mechanism of separation occurring in the THF and NMP systems[2,3]. Clearly there is adsorption chromatography occurring within the THF system, so what effect is this having on the size separation mechanism of the porous column packing? Figure 3 presents some results from an investigation of the order of elution of coal derived material with NMP or THF as the mobile phase. The preparative scale separation of the coal tar pitch produced narrow retention volume defined fractions with known elution order, confirmed on the analytical THF system. These fractions were dissolved in NMP and injected on to the NMP-SEC system. Figure 3 illustrates the finding that the elution order remains largely the same. There is however a greater peak broadness in this NMP system for each individual fraction.

These observations indicate that the non-size exclusion contribution to the separation mechanism is much less when NMP is the chromatographic mobile phase. This may well be due to both the greater solublising powers of NMP and the higher temperatures at which the NMP columns are operated. This is supported by the fact that no thermally treated coal derived material has been found to elute after the retention time of toluene.

We now turn to an examination of material extracted from the gasifier char. The supercritical fluid extraction, Figure 4, yields material which is generally of low molecular weight. There is no excluded peak. This is consistent with previous SFE of coal and environmental materials[4]. Also illustrated is the extension of extraction to larger molecules as more modifier is used. It is interesting to note that SFE produces material up to the total permeation limit of the column.

Chromatograms produced from the analysis of the mixed solvent extract are shown in Figure 5. This is a powerful technique capable of solvating 60% of some raw coals[5]. This increased extraction power over SFE is seen by the presence of a large peak in the chromatogram corresponding to excluded material. Indeed there appears to be more excluded than retained material. The lowest molecular weight material indicated by Figure 4 to be present in the original char may well be lost from the material examined in Figure 5 by the processes used to remove CS_2 from the extract filtrate. This last figure also illustrates that the excluded material is absorbing significant amounts of uv light at 500nm. The corresponding fluorescence chromatograms show very little fluorescence at any wavelength. This supports the assumption that this excluded material consists of larger molecular structures and not aggregated low molecular weight compounds which generally have strong fluorescence spectra.

CONCLUSIONS

From the results reported here it is clear that NMP surpasses THF as a mobile phase for SEC of coal derived materials. It offers the opportunity to analyse more of the sample, and has shown much reduced adsorption effects. Investigation has shown that this technique can be applied to materials of industrial relevance. Polystyrene calibration for these materials remains a source of error particularly for higher mass materials, but is probably less inaccurate for low masses with NMP-SEC. The combination of

NMP-SEC and new MS techniques (LIMA, MALDI), might provide a possible route to the manufacture of relevant coal calibrants and thus accurate MMDs.

ACKNOWLEDGEMENTS

The authors gratefully acknowledge the permission given by CTDD allowing collection and analysis of the gasifier samples and supply of the PoA liquefaction extract, in particular Drs Nigel Patterson and Sam Moore. We would also like to thank the EPSRC and ETSU for funding this work.

REFERENCES

1. K. D. Bartle, M. J. Mulligan, N. Taylor, T. G. M. & C. E. Snape, Fuel 63 (1984) 1556.
2. A. L. Lafleur & M. J. Wornat, Analytical Chemistry 60 (1988) 1096.
3. A. L. Lafleur & Y. Nakagawa, Fuel 68 (1989) 741.
4. S. B. Hawthorne & D. J. Miller, Anal Chem 66 (1994) 4005
5. M. Iino, T. Takanohashi, H. Ohsuga & K. Toda, Fuel 67 (1988) 1639

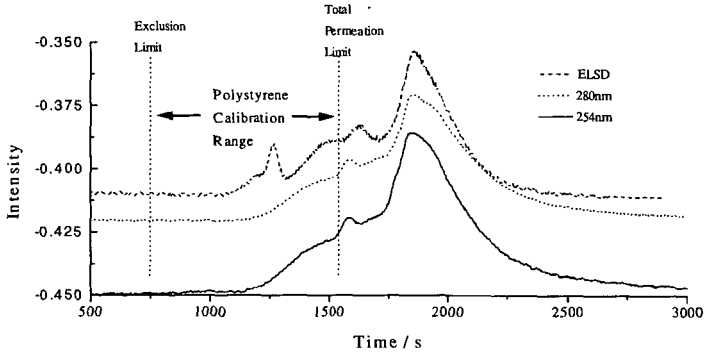

Figure 1 Size exclusion chromatographic analysis of coal tar pitch using multiple detectors with tetrahydrofuran as the mobile phase.

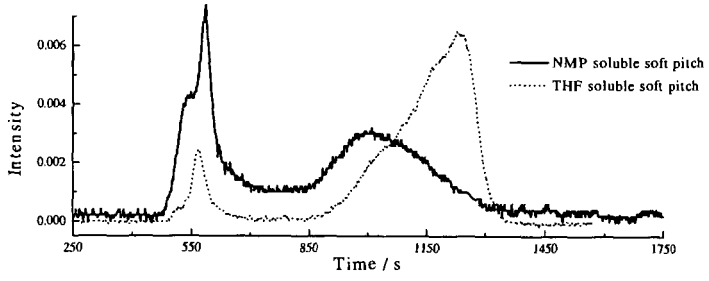

Figure 2 SEC chromatograms of solvent separated coal tar pitch fractions using uv absorption detection at 280nm and N-methyl-2-pyrrolidinone as the mobile phase.

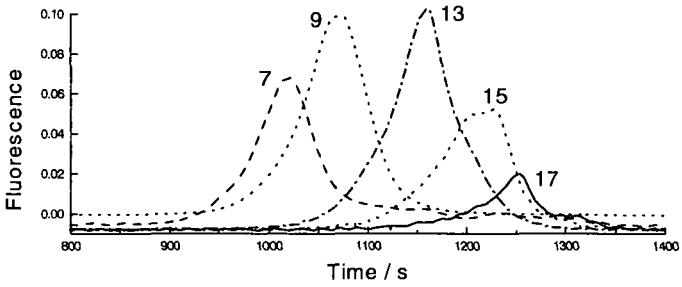

Figure 3 NMP-SEC chromatograms of pitch fractions from preparative scale THF-SEC.

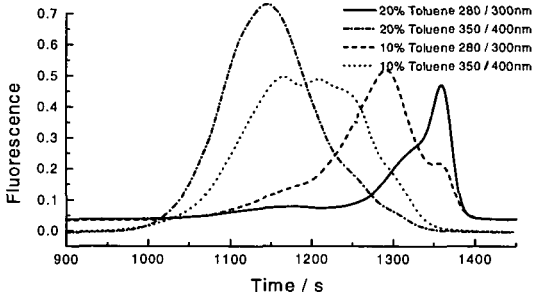

Figure 4 Chromatograms of supercritical fluid extracts from gasifier char.

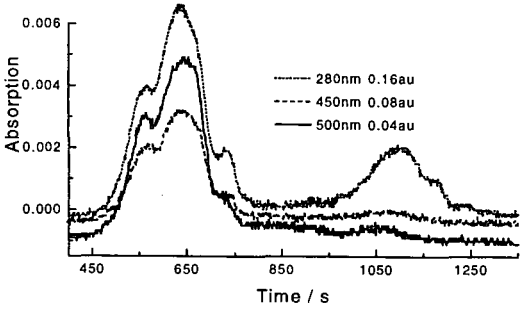

Figure 5 Chromatograms of mixed solvent extract from gasifier char.

DETERMINATION OF ORGANIC SULFUR FORMS IN SOME COALS AND KEROGENS BY ATMOSFERIC PRESSURE TEMPERATURE PROGRAMMED REDUCTION (AP-TPR).

J. Yperman[a], I. I Maes[a], D. Franco[a], C. E. Snape[b], S. C. Mitchell[c], S. R. Palmer[d], J. Mullens[a] and L.C. Van Poucke[a]

a) Laboratory of Inorganic and Physical Chemistry, Limburgs Universitair Centrum, B-3590 Diepenbeek, Belgium
b) Department of Pure and Applied Chemistry, University of Strathclyde, 295 Cathedral Street, Glasgow G1 1XQ, United Kingdom
c) School of Chemistry, University of Leeds, Leeds LS2 9JT, United Kingdom
d) Mechanical Engineering and Energy Processes, Southern Illinois University at Carbondale, Carbondale, IL 62901, U. S. A.

ABSTRACT

The following samples have been investigated as examples for the applicability of the atmospheric pressure temperature programmed reduction (AP-TPR) technique : Indiana #5, Herrin #6, and Upper-Freeport (Argonne Premium coal, USA), Kimmeridge Dorset-Cuddle (Type II kerogen, UK) and Mequinenza (lignite, Spain). The Mequinenza lignite has been treated with diluted nitric acid in order to remove pyrite while for the Upper Freeport and the Kimmeridge the pyrite was removed by a $LiAlH_4$ treatment. The Indiana #5 and Herrin #6 were treated with a peroxy-acetic acid solution at room temperature in order to remove beside pyrite also other sulfur groups. The AP-TPR profiles of the treated and untreated samples are discussed and compared with each other. It is demonstrated that $LiAlH_4$ as the peroxide treatment not only removes pyrite, but also changes and removes other sulfur functionalities. The AP-TPR technique proved that the pyrite signal is clearly resolved and that possible retrogressive reactions might be hidden under other sulfur functionalities, which has no important influence on the interpretation of the AP-TPR profile after pyrite reduction.

INTRODUCTION

As often discussed, the presence of sulfur is undesirable in metallurgical coke, as well as in the production of smokeless and formed fuels. Therefore a prior desulfurization is recommended. While inorganic sulfur can mostly be removed by simple physical methods, the removal of organic-bound sulfur always needs a chemical treatment. Herefore, it is necessary to know which sulfur forms occur in the coal in order to choose a suitable method of desulfurization and to estimate the extent of desulfurization as well as the kind of sulfur functionalities that have been removed. At the moment a number of chemical and instrumentation methods are used for the determination of these different sulfur functionalities in coal [1]. AP-TPR[2-5] proved to be a powerful technique to gain more insight into the sulfur form distribution in the raw as well as in the treated coal.

EXPERIMENTAL

Samples : the treatments and the analyses of the coals and kerogens have been described previously[6-7] and are listed in table I and II.
Apparatus : the atmospheric pressure TPR setup has been described previously[3-5].
Samples were heated from 20° to 1000°C, at a rate of 5°C/min. Experiments were always recorded in a pure H_2-atmosphere.

RESULTS AND DISCUSSION

a) Mequinenza Lignite

In figure 1 the AP-TPR-results are shown for the Mequinenza lignite as received (a) and treated (b) with diluted nitric acid. Based on model compound work[5], it is possible to assign the regions in the AP-TPR profiles to specific organic sulfur groups. For the raw Mequinenza lignite figure 1 curve (a), the first peak at 395°C must be attributed to alifatic sulfide as well as to mixed aryl-alkyl sulfides. The quite pronounced shoulder around 500°C can be attributed to pyritic sulfur. The second peak at 605°C represents the di-aryl sulfides. Above 700°C, simple thiophenes are visible. Above 800°C, even more complex thiophenic structures can be observed. The total amount of sulfur detected by the AP-TPR-technique is 6.0%, or an overall 76% sulfur recovery.

Looking at the HNO_3-treated Mequinenza lignite AP-TPR profile [figure 1 curve (b)] and comparing it with curve (a) of the native coal, pyrite as well as alifatic sulfides have been mostly removed. This results in a less pronounced first signal still demonstrating the presence of aryl-alkyl sulfides. But also aryl sulfides are present as shown by the peak at 645°C. A well pronounced signal at 730°C refers to the presence of simple thiophenes. It is believed that due to the effect of the HNO_3 treatment also a better accessibility of the coal towards the reduction proces is established. The sulfur yield of this AP-TPR-experiment is 4.6%, i.e. a 53% sulfur recovery of the total amount of sulfur present in the coal sample.

b) Kimmeridge Kerogen

In figure 2 the Kimmeridge Dorset-Cuddle AP-TPR-profiles are shown. The sulfur recovery is quite high for the native kerogen (a) as for the $LiAlH_4$-treated (b). The changes in the AP-TPR-profiles [see curve (a) vs. (b)] are spectacular. This was also the case for the HP-TPR plots[6]. The pyrite peak is not visible in the raw material kinetogram. The first main peak for the kerogen can be attributed to aryl-alkyl sulfur forms (T_{max} at 410°C). The second corresponds with di-aryl sulfur functionalities. The onset of the first peak starts later suggesting the absence of pure alifatic sulfur forms in Kimmeridge Kerogen. The AP-TPR results show some differences with the HP-TPR findings, probably due to the disturbing role

of pyrite.
Looking at figure 2 curve (b), the $LiAlH_4$ treatment not only removes pyrite, but obviously has also a drastic influence on the other sulfur groups. Beside pyrite aliphatic sulfur forms as well as certain amounts of aryl-alkyl sulfides are also removed. The signal starting at 175°C, indicates that beside some desulfurization also some new, easy to reduce, sulfur compounds are formed, in this case thiols. The main peak (T_{max} at 630°C) in figure 2 curve (b) is much more narrow than the corresponding one in figure 2 curve (a) with a maximum at 600°C. This indicates that the $LiAlH_4$ treatment also partly removes or changes di-aryl sulfides. It is quite clear that the $LiAlH_4$ treatment disturbs the other sulfur forms in the kerogen as well during the desulfurization by breaking certain sulfur bonds and creating others.

c) Bituminous coal
Figure 3 gives the AP-TPR-spectra of the raw and $LiAlH_4$-treated Upper Freeport samples (both with almost a 100% sulfur recovery). The peak at 530°C is believed to be the pyrite signal. The shoulders at lower and higher temperatures must be assigned to alifatic sulfides and aryl-alkyl sulfides, and pure aryl sulfides (T_{max} at 585°C), respectively.
Because of the high amount of pyrite, the $LiAlH_4$ treatment is quite effective. .This is shown by the AP-TPR-profile in figure 3 curve (b). Only simple thiophenic structures are detected, but only in very small amounts. These findings are in agreement with the one of the HP-TPR experiment. It is clear that according to the coal type, the $LiAlH_4$-treatment can cause different effects during the desulfurization process.

d) Argonne Premium coals
In figure 4 the AP-TPR profiles of Indiana #5 as received [curve (a)] and after treatment with peroxy-acetic acid for 6 hours [curve (b)] and 24 hours [curve (c)] are shown. The sulfur amount in wt % detected by the set-up is 2.9%, 1.1% and 0.73%, respectively. Using the model compound work[5], the signal at 460°C can be attributed to alifatic sulfides and aryl-alkyl sulfides. The shoulder around 540°C is attributed to pyrite and the peak at 595°C refers to di-aryl sulfur compounds. The feature at higher temperature is caused by simple thiophenes.
Comparing figure 4 curve (a) with curves (b) and (c), it is clear that beside the removal of pyrite [minimum in both profiles (b) and (c) at 540°C] the other non-thiophenic compounds are also partly removed by the peroxy-acetic acid treatment. The longer the treatment is performed, the less non-thiophenic sulfur is found. One can conclude that the peroxide method is an overall desulfurization method as many sulfur forms are affected by this oxidation. In how far condensed or complex thiophenic sulfur is attacked by this treatment is not clear at the moment. At the moment AP-TPR is not capable to reduce these sulfur functionalities effectively.
In figure 5 the AP-TPR results are shown for the Herrin #6. The profile for the raw material is given by figure 6 curve (a). The peak at 425°C corresponds with alifatic sulfides. The one at 485°C refers to aryl-alkyl sulfur functionalities. In this case the pyrite peak is not visible because of its low presence. The 485°C signal and the huge signal with a maximum at 605°C refer to aryl sulfur compounds and even some simple thiophenic structures. For the oxidised samples, the AP-TPR profiles in figure 5 curves (b) and (c) show the same trends as for the Indiana #5, i.e. all sulfur forms present in the raw coal are attacked by the peroxide treatment. The longer the experiment is performed the more sulfur forms of all kind are removed. The sulfur recoveries in wt% for the AP-TPR experiments in figure 5 are again quite high: 3.4%, 2.0% and 1.3%, for curves (a), (b) and (c) respectively.

CONCLUSIONS

It is demonstrated that AP-TPR provides differentiated profiles which can be explained in terms of different organic sulfur functionalities. The pyrite signal can be distinguished very easily from the organic sulfur peaks. It is shown by the AP-TPR technique that different desulfurization treatments not only removed the specific sulfur group, but also affect other sulfur forms present in the coal as well. This is also found by other treated coal samples using the same or other methods.

ACKNOWLEDGEMENT

The authors like to thank mrs. M. Vanhamel and Mr. J. Kaelen for their technical assistance with the TPR experiments. I. I. Maes is supported by a specialisation grant from the "Vlaams Instituut voor de bevordering van het wetenschappelijk-technologisch onderzoek in de industrie (IWT)".

REFERENCES

1. Davidson, R., Organic Sulfur in Coal, IEA Coal Research, London, 1993.
2. Majchrowicz, B.B., Franco, D.V., Yperman, J. , Reggers, G., Gelan, J., Martens, H., Mullens, J. and Van Poucke, L.C., Fuel, 1991, **70**, 434.
3. Majchrowicz, B.B.,Yperman, J., Mullens, J. and Van Poucke, L.C. , Anal. Chem., 1991, **63**, 60.
4. Yperman, J., Franco, D., Mullens, J., Reggers, G., D'Olieslaeger, M., Van Poucke, L.C. and Marinov, S.P. in *Composition, Geochemistry and Conversion of Oil shales*, C. Snape (ed.), Kluwer academic Publishers, 1995, 449.
5. Ismaïl, K., Mitchell, S.C., Brown, S.D., Snape, C.E., Buchanan III, A.C., Britt, P.F., Franco, D.V., Maes, I.I. and Yperman, J., Energy & Fuel, in press.
6. Mitchell, S.C., Snape, C.E., Garcia, R., Ismaïl, K. and Bartle, K.D., Fuel, 1994, **73**, 159.
7. Palmer, S.R., Kruge, M.A., Hippo, E.J. and Crelling, J.C., Fuel, 1994, **73**(7), 1167.

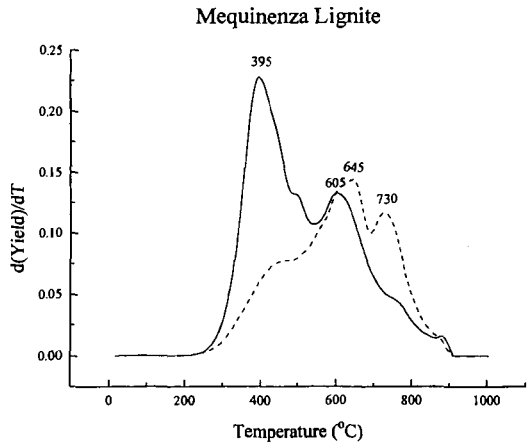

Figure 1: TPR-profiles of a Mequinenza Lignite as received (a) and after HNO_3 treatment (b).

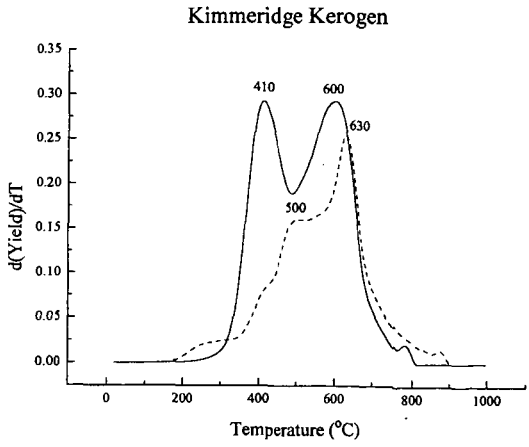

Figure 2 : TPR-profiles of Kimmeridge Kerogen as received (a) and after $LiAlH_4$-treatment (b).

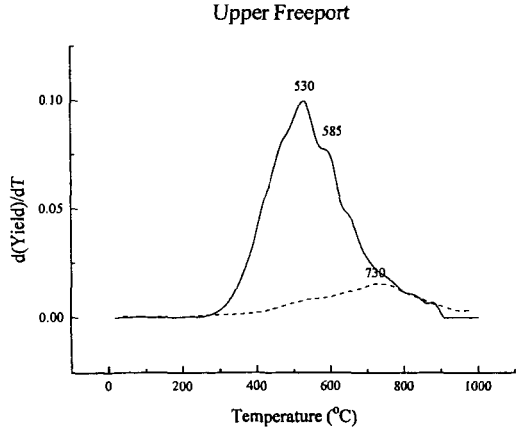

Figure 3 : TPR-profiles of Upper Freeport as received (a) and after $LiAlH_4$-treatment (b).

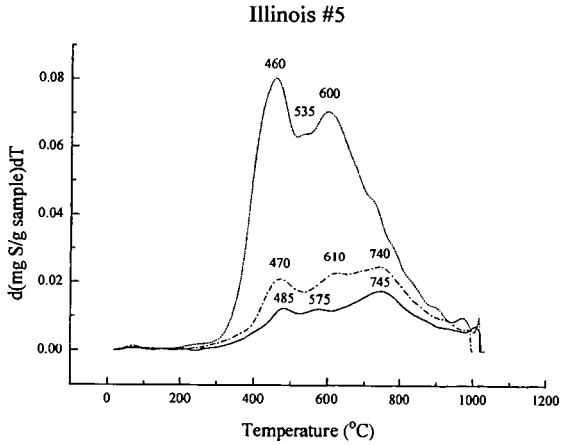

Figure 4 : TPR-profiles of Indiana #5 as received (a) and after 6 hours (b) and 24 hours (c) oxidation.

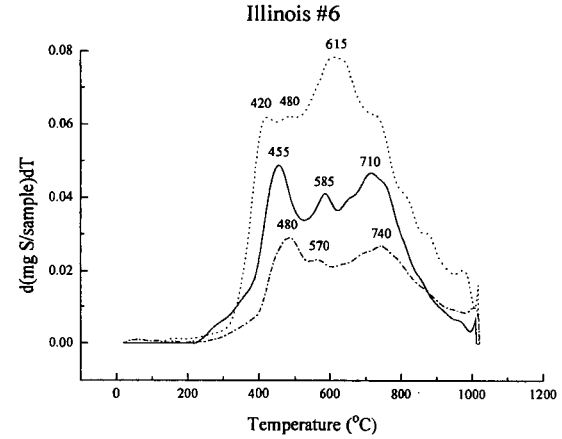

Figure 5 : TPR-profiles of Herrin #6 as received (a) and after 6 hours (b) and 24 hours (c) oxidation.

Table I

sample (wt % dmmf)		Mequinenza	Kimmeridge	Upper Freeport
	C	66.4	55.5	88.0
	H	5.8	6.2	4.8
	N	1.6	2.1	1.6
Sulfur (wt % db)	Total	9.0	8.3	2.32
	pyritic	0.5	n.d.	1.77
	sulfatic	0.5	n.d.	0.01
	organic	8.0	n.d.	0.54
after treatment Sulfur (wt % db)	Total	8.6	5.8	0.48

Table II

sample (wt % db)		Herrin #6	Indiana #5
	C	69.1	72.1
	H	5.1	5.1
	N	4.4	1.5
	O	9.5	8.4
Sulfur (wt % db)	Total	4.4	3.8
	pyritic	1.2	1.8
	sulfatic	0.1	0.0
	organic	3.1	2.0
After 6 hours ox. total sulfur (wt % db)		3.1	2.2
After 24 hours ox. total sulfur (wt % db)		1.9	2.0

DETERMINATION OF COAL RANK BY THERMOGRAVIMETRIC ANALYSIS

He Huang, Keyu Wang, M. T. Klein and W.H. Calkins*
Department of Chemical Engineering
University of Delaware, Newark, Delaware 19716

Key words: thermogravimetric analysis, coal rank, coal pyrolysis

INTRODUCTION

The thermogravimetric analysis patterns of coals and their residues reveal subtle differences between coals and changes which occur during the processing. It is the purpose of this paper to call attention to some of the various processes occurring during the TG analysis, and to show how these patterns can be interpreted in terms of changes or differences in coal structure. It is also our purpose to show how manipulation of the various TGA parameters, i.e., heating rate program, purge gas type, and the way in which the TG data are treated, can be used to reveal important aspects of the coal structure. Finally, the use of TGA as an objective criterion for determining coal rank is discussed.

EXPERIMENTAL

Apparatus. A horizontal thermogravimetric analyzer (TGA), TA Instruments model 51 (New Castle, Delaware), was employed. An approximately 30 mg sample of the coal or coal residue was loaded in a quartz pan and mounted in the instrument. The program of manipulation of the TG variables were determined by the objectives of the particular experiment.

RESULTS AND DISCUSSION

A representative TG scan on Illinois #6 coal from the Argonne Premium Coal Sample program dried in a vacuum oven with a nitrogen purge at 105 °C for 48 hours is shown in Figure 1. The weight loss resulting from heating at a ramp rate of 10 °C/min to 950 °C in nitrogen at 100 cm^3/min defines the amount of Volatile Matter (VM) in the coal. Further weight loss occurred at 950 °C after the introduction of oxygen, which was caused by the combustion of the organic material remaining. This defines the Fixed Carbon content (FC). The residue represents the ash content, which is in agreement with ash content determined by ASTM D3174.

The differential of the weight loss (DTG) curve highlights the various TG processes more clearly. The DTG curve for Illinois #6 shows a pattern which is more complex than the other Argonne coals. This becomes even more distinct and complex if the heating rate is slowed down to about 1 °C/min. The curve shown in Figure 2 has been smoothed by a rigorous mathematical treatment (1) of the numerous data points obtained in the analysis. There is a low temperature peak representing the loss of residual moisture below 200 °C. The main Volatile Matter peak starts at 350-400 °C and actually consists of three or perhaps four individual weight loss processes. The large peak is broad and probably consists of a number of pyrolysis processes. The well defined peak at 571 °C is tentatively identified as due to pyrite decomposition to pyrrhotite and sulfur because this peak is absent in coals containing little or no pyrite. Also, the decomposition temperature corresponds closely to that reported for pyrite (2). Two other small peaks are not yet identified but are fairly broad. They disappear gradually during coal liquefaction.

The DTG curves of the Illinois #6 coal in nitrogen and in hydrogen given in Figure 3 show similar patterns. However, all three peak temperatures in hydrogen, especially the highest temperature peak, are shifted to lower temperatures than those run in nitrogen. This might be due to the quenching by hydrogen of free radicals generated in the pyrolysis process to form more volatile products. The difference in the effect of the different gases is particularly apparent when the Volatile Matter produced is compared. Figure 4 shows the Volatile Matter produced in hydrogen and in nitrogen over a wide range of heating rates. The Volatile Matter yields are consistently higher, and therefore the Fixed Carbon yields are lower, in hydrogen than in nitrogen.

The heating rate also has a strong effect on the yields of Volatile Matter in either hydrogen or nitrogen (Figures 4a, 4b, and 4c). In hydrogen, the Volatile Matter yields decrease somewhat as the heating rate increases. This may be because, at the higher heating rates, the pyrolysis times are shorter, providing less time for reaction with the molecular hydrogen to form more volatile products. However, in nitrogen, the Volatile Matter yields increase with heating rate. At the low heating rates, the unquenched free radicals react to form more retrograde products (fixed carbon). This is in agreement with

the well known observation of the increase in yield of flash pyrolysis products compared with that of slow pyrolysis. This is shown by experiments on three coals of differing rank.

TGA of Coal Liquefaction Residues. When the Illinois #6 coal is reacted in tetralin (8:1 tetralin to coal by weight) at 400 °C, the fine structure of the DTG profile of the partially reacted coal residue gradually disappears. This is shown in Figure 5, which suggests that liquefaction promotes the removal of the materials producing the fine structure peaks.

It is interesting that the changes in Volatile Matter of the residue during liquefaction are insensitive to whether the liquefaction is run in nitrogen or hydrogen, or in the presence of catalyst and hydrogen (Figure 6). This is not true, however, for the formation of Fixed Carbon. In general, more Fixed Carbon is formed as the liquefaction proceeds. However, the amount formed is greatly diminished when the liquefaction is carried out in the presence of hydrogen and a hydrogenation catalyst (Figure 7).

TGA of Coals of Various Ranks. DTG curves for all eight Argonne Premium Coals, dried at 105 °C for 48 hours and run at 10 °C/min with a nitrogen gas purge rate of 100 cm^3/min, are shown in Figure 8. This clearly shows the gradual shift of peak temperature as the coal rank increases from Lignite to low volatile bituminous coal. At the same time, the peak height increases to a maximum and then decreases again as the rank increases. This trend is more clearly evident in the plot of peak temperature vs carbon content (in wt%) shown in Figure 9. If peak height is plotted against carbon content, a volcano type curve is obtained. This is shown in Figure 10. While there are a number of measures of coal rank (3 - 12), this provides an independent and objective measure of coal rank which can be useful particularly in borderline cases.

SUMMARY AND CONCLUSIONS

1). Thermogravimetric Analysis (TGA) provides sensitive, rapid and reproducible results concerning the various weight loss processes that can be a reflection of the physical and chemical structure of coals. Additional information can be obtained by variation of TG variables, such as heating rate and purge gas type.

2). TGA also reveals changes in the physical and chemical structure of coal as it undergoes coal liquefaction. This technique also is capable of revealing the onset and rate of the retrograde reactions occurring during the liquefaction process.

3). TGA provides an independent measure of coal rank.

ACKNOWLEDGEMENTS

The support of this work by the Department of Energy under DE22-93PC93205 is gratefully acknowledged. The use of Argonne Premium Coal Samples provided by Dr Karl Vorres is also acknowledged. Additional funds for purchase of thermal analysis equipment was provided by the University of Delaware.

REFERENCES

1. Wang, Keyu; Huang, He; Wang, Shaojie; Klein, M.T.; Calkins, W.H. 'A novel smoothing technique for thermogravimetric analysis data', to be submitted in *Anal. Chem.*
2. Luganov, V.A.; Schebalin, V.I. Can. Metall. Q. *Fuel*, 1982, **21**, 157.
3. Krevelen, D.W. van 'Coal Typology, Physics, Chemistry, Constitution' 3rd ed., Elsevier Publishers (1994).
4. 'Classification of Coals by Rank' *ASTM D388*, 1966 (Reapproved 1972).
5. 'Gross Calorific Value of Solid Fuel by the Adiabatic Bomb Calorimeter' *ASTM D2015*, 1966 (reapproved 1972).
6. 'Preparing Coal Samples for Microscopical Analysis by Reflected Light' *ASTM D2797*, 1972.
7. 'Microscopical Determination of the Reflectance of the Organic Components in a Polished Specimen of Coal' *ASTM 1798*, 1972.
8. 'Proximate Analysis of Coal and Coke' *ASTM D3172*, 1973.
9. 'Volatile Matter in the Analysis Sample of Coal and Coke' *ASTM D3175*, 1973.
10. 'Ultimate Analysis of Coal and Coke' *ASTM D3176*, 1974.
11. 'Carbon and Hydrogen in the Analysis Sample of Coal and Coke' *ASTM D3178*, 1973.
12. 'Gross Calorific Value of Solid Fuel by the Isothermal-Jacket Bomb Calorimeter' *ASTM 3286*, 1973.

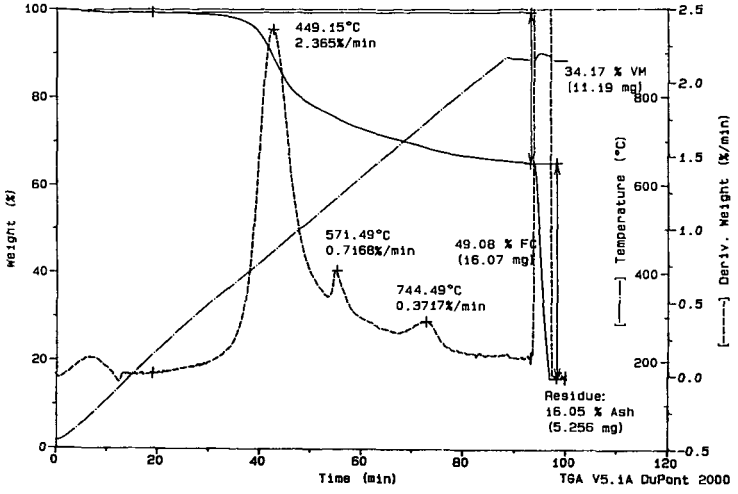

Figure 1 A TG scan on the Illinois #6 coal at 10 °C/min

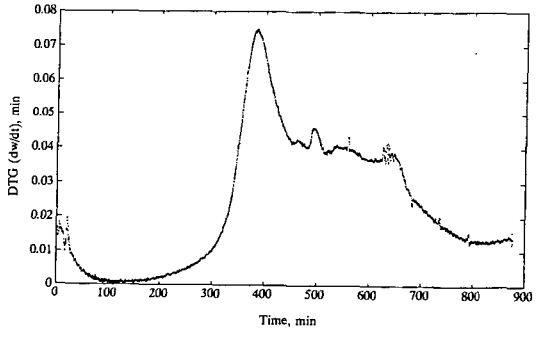

Figure 2 A TG scan on the Illinois #6 coal at 1 °C/min

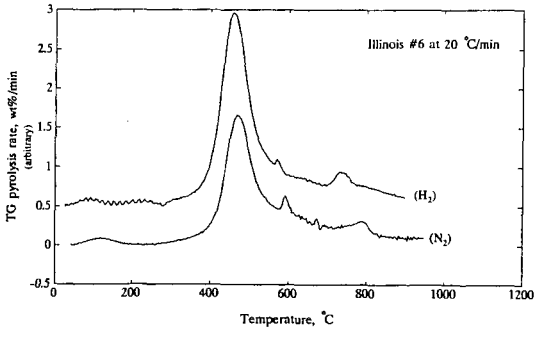

Figure 3 - Effect of gas atmospher on DTG of the Illinois #6 coal pyrolysis

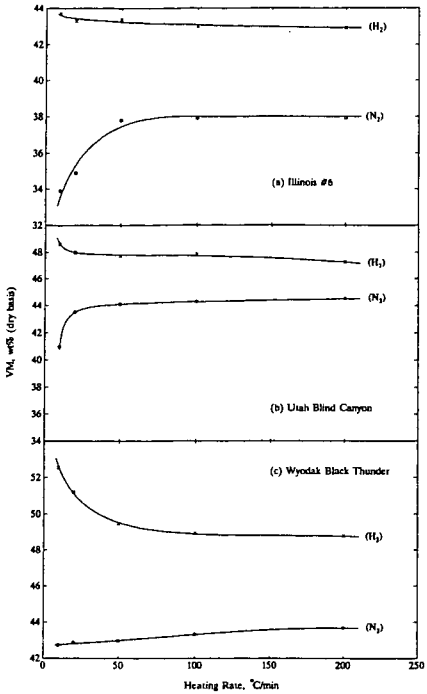

Figure 4 Effect of heating rate on the VM yields determined by TG pyrolysis in N_2 and H_2 of a). Illinois #6, b). Utah Blind Canyon, and c). Wyodak Black Thunder

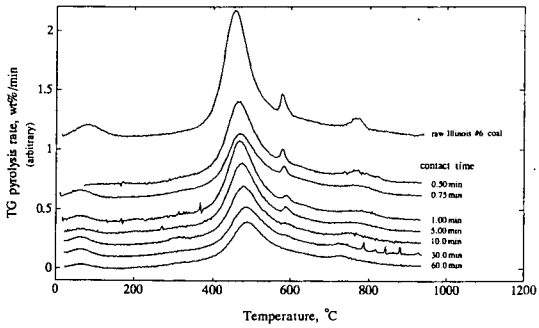

Figure 5 DTG profiles for residues of the Illinois #6 coal after liquefaction in tetralin at the selected contact times (TG scan at 10 °C/min; Liquefaction run at 390 °C under 1000 psig N_2)

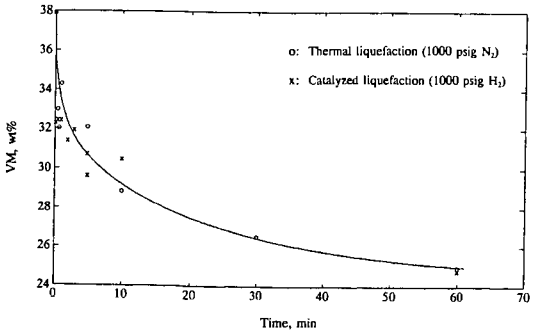

Figure 6 VM (volatile matter) in the liquefaction residues determined by TGA

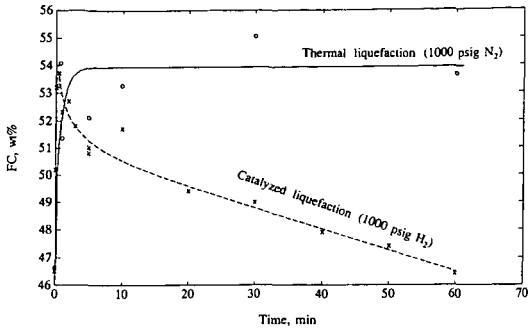

Figure 7 FC (fixed carbon) in the liquefaction residues determined by TGA (Liquefaction run: T:C = 8:1; 390 °C; TG scan: 100 cm^3(STP)/min N_2; 100 °C/min)

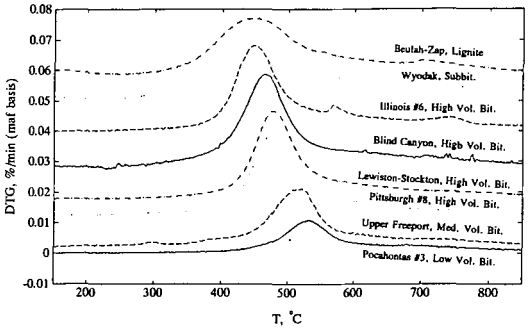

Figure 8 Pyrolysis DTG profiles of the Argonne Premium Coal samples

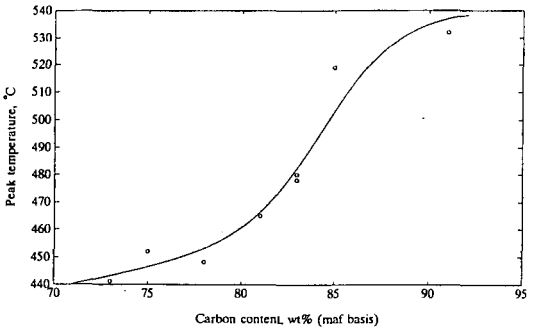

Figure 9 Peak temperature vs. carbon content of the Argonne Premium Coal samples

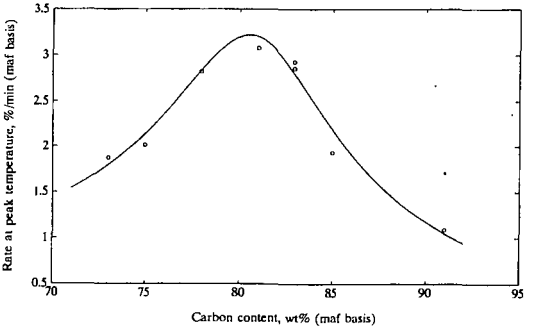

Figure 10 Rate at peak temperature vs. carbon content of the Argonne Premium Coal samples

A THERMOGRAVIMETRIC ANALYSIS OF CATALYTIC HYDROPROCESSING OF A COAL-DERIVED LIQUID

X. Song[1], S. Lu[2], H. Fu[2] and I.G. Dalla Lana[2]
[1]Corresponding author, Department of Chemical Engineering, Laval University
Ste-Foy, Quebec, Canada G1K 7P4
[2]Department of Chemical Engineering, University of Alberta
Edmonton, Alberta, Canada T6G 2G6

Keywords: Thermogravimetric analysis, coal-derived liquids, hydroprocessing.

INTRODUCTION

Thermogravimetric analysis (TGA) has normally been used to study thermal behaviours of solid materials. The extension of this technique to materials in fluid phases is less common. So far there have been very few reports dealing with the application of TGA to solid-catalyzed gas-phase reaction system. Massoth and Cowley [1] described the use of a stirred flow microbalance in studying the catalytic hydrogenation of 1-butene under steady-state reaction conditions. More recently, TGA was combined with techniques such as online MS or GC analysis to study catalytic reactions [2,3]. However, the use of TGA in studying a solid-catalyzed gas-liquid reaction, especially when the liquid is a relatively non-volatile complex feedstock, is very limited.

Laboratory-scale experiments on the hydroprocessing of complex feedstocks such as coal-derived liquids (CDLs) involve considerable preparation and time as well as chemical analysis to obtain useful information. The application of TGA to studies of such a complex reaction system appears appealing because of its small sample size requirement, short running period, simple operation and thus low running expense. In the present work, an attempt was made to explore the usefulness of TGA to catalytic hydroprocessing of a CDL. A programmed heating of an organic complex such as a CDL usually involves vaporization and chemical reactions such as thermal cracking, coking, etc., depending on temperature and operation conditions. If the system contains an active solid catalyst, the process will be more complicated. We found that many operating parameters have significant effects on the TGA data of CDL-catalyst mixture samples. For such a complex system, it is essential to set-up standardized operating conditions. The effects of various operating parameters on TGA curves were investigated in order to establish a reliable procedure. This paper reports TGA results of catalytic hydroprocessing of a CDL, the influence of TGA atmosphere (carrier gas) on CDL weight loss, and the comparison of performances of different catalysts in TGA of CDL.

EXPERIMENTAL

TGA experiments were carried out using a Perkin Elmer TGS-2 Thermogravimetric Analyzer. In most runs, the amount of CDL in a CDL-catalyst mixture sample was about 20 mg. H_2 or N_2 was used as a carrier gas (100 ml/min, atmospheric pressure). Temperature was programmed from 50 °C to 450 °C at a heating rate of 5 °C/min. The weight loss of a catalyst itself due to removal of moisture was obtained under these conditions, and was usually less than 5%. The weight loss of CDL in contact with the catalyst was obtained by subtracting the weight loss of the catalyst from total weight loss of the mixed sample.

RESULTS AND DISCUSSION

In our preliminary experiments, we found that many TGA operating conditions such as heating rate, sample weight, pan material and carrier gas flow rate significantly influenced TGA data. Efforts were therefore made to find reasonable conditions, and the following were chosen: heating rate = 5 °C/min; CDL sample weight = 20 mg; pan material = quartz; carrier gas flow-rate = 100 ml/min.

Effect of catalyst particle size What occur in the samples under our operating conditions involve gas-liquid-solid heterogeneous reactions, such as thermal/catalytic cracking, hydrogenation, coking, etc. Weight loss percentage and weight loss rate can be considered as measurements of overall conversion and conversion rate, respectively. Conversion is strongly dependent on the contact among gas (carrier gas), liquid (CDL) and solid (catalyst). In the present work, the mixed samples of CDL and catalyst were made by simply immersing a catalyst into CDL. Particle size of the catalyst will influence the contact among the three phases, and thus conversion. Fig. 1 shows the influence of catalyst (Ni-Mo/Al_2O_3) particle size on weight loss of CDL, where the weight of CDL in the mixed samples (catalyst content 50 wt%) was 20 mg and hydrogen was used as the carrier gas. It can be noted that the presence of the catalyst has a significant effect on CDL weight loss. Compared to the data obtained in the absence of the catalyst, CDL in contact with the catalyst has an increased weight loss at lower temperatures and a decreased weight loss at higher temperatures. The finer the catalyst particles, the greater the CDL weight loss (Fig. 1a). In addition, the presence of catalyst brings about a lower temperature at which maximum CDL weight loss rate occurs (maximum weight loss rate temperature). The finer the catalyst particles, the greater the maximum of CDL weight loss rate (Fig. 1b).

In order to examine whether the difference between the curve for pure CDL and the curves for CDL in contact with the catalyst resulted from the catalysis (a chemical factor) or from the better contact between CDL and atmosphere (H_2) provided by CDL dispersion on fine solid catalyst

particles (a physical factor), a mixture of fine glass beads (0.10 - 0.12 mm) with CDL was subjected to TGA. It was found that TGA curves with and without glass beads almost overlapped, indicating that inert materials such as glass beads cannot result in substantial change in TGA curve of CDL. In other words, the increased CDL weight loss at lower temperatures and the decreased at higher temperatures in the presence of a catalyst is mostly caused by the interaction between CDL and active sites on the catalyst surface, not by a larger exterior area exposing to hydrogen. Finer catalyst particles resulted in a greater CDL weight loss and a greater weight loss rate. This is because there are more accessible catalytic sites for CDL to reach on smaller catalyst particles.

An anomalous observation is that, at relatively high temperatures the presence of catalyst always suppresses CDL weight loss. The coke formation on catalyst surface at higher temperature is the most probable reason for the phenomenon. To examine this speculation, following calcination was carried out. A residue in a sample pan was calcined at 600 °C in air in a muffle furnace for 30 minutes after TGA. The residue was weighed before and after the calcination respectively. The weight loss of the residue during the calcination accounts for the coke formed during the TGA run. CDL weight loss was obtained by subtracting catalyst weight loss from total weight loss of the sample. The results listed in Table 1 indicates that coking on catalyst surface does occur at higher temperatures. This may result from the high content of aromatics in the CDL. In subsequent runs, the catalyst particles finer than 0.12 mm were used.

Influence of the catalyst content in CDL-catalyst mixture Fig. 2 shows the influence of catalyst content in a mixture sample on CDL weight loss. Hydrogen was used as a carrier gas. CDL weight in the sample was 20 mg. The important point is that the presence of a catalyst in the feedstock resulted in an increased CDL weight loss at low temperatures. This increased weight loss is shown in Fig. 3, which was obtained by subtracting CDL weight loss observed in the absence of the catalyst from that in the presence of the catalyst. It is seen from Fig. 3 that a high catalyst content (> 50%) or a low one (< 40%) is not favourable for CDL weight loss. The fact that too high a catalyst content suppresses weight loss suggests that the weight loss is affected not only by catalytic effects but also by adsorption of CDL on the catalyst surface. When the catalyst content is increased to a certain extent (> 50%), enhanced adsorption causes somewhat stabilized adsorbed species on the catalyst surface. On the other hand, when catalyst content is too low (< 40%), it is difficult to make a uniformly mixed CDL-catalyst sample. Therefore, an intermediate catalyst content is suggested in order to obtain reliable data. In subsequent runs, a catalyst content of 40% or 50% is used.

Reproducibility of TGA results The above discussions indicate that the TGA data of CDL strongly depend on the operating conditions. Strictly controlled operating conditions are essential because of the small sample size and high sensitivity of the TGA system. Several operating parameters have been chosen. Using these standardized parameters, tests of TGA reproducibility for CDL without and with a catalyst were carried out, and the maximum deviation in CDL weight loss observed among three independent runs is 0.7% for pure CDL sample and 1.2% for CDL-catalyst mixture sample, respectively.

Effect of gas atmosphere This series of runs was carried out with Ni-Mo/Al_2O_3 catalyst. CDL weight and the catalyst content in the feedstock were 20 mg and 40 wt% respectively. Fig. 4a shows that CDL weight loss is higher when the sample is heated in hydrogen than in nitrogen. This observation is in agreement with that of Kordulis et al. [4] for Safaniya asphaltene. A lower maximum weight loss rate was also observed in an inert atmosphere (Fig. 4b). The same tendency was observed in the presence of a catalyst. In both hydrogen and nitrogen, the effect of the catalyst was displayed at lower temperatures (< 300°C), as evidenced by the higher weight loss and the lower temperature for maximum weight loss rate. At temperatures above 300 °C, weight loss was suppressed by the catalyst because of coke formation as discussed earlier. The fact that a hydrogen atmosphere is conducive to weight loss suggests that contacting the CDL plus catalyst with H_2 suppresses the formation of coke on the catalyst to some extent. Comparison between curves 2 and 4 indicates that, for CDL feedstock which is of high aromaticity, catalytic *hydroprocessing* is much more effective than catalytic processing without the participation of hydrogen.

Comparison between different catalysts Fig. 5 summarizes the results obtained from CDL with three different catalysts at identical TGA conditions. A comparable run with pure CDL is also included. All the experiments were run in hydrogen (100 ml/min). Mixed samples contained 20 mg of CDL and 40 wt% of catalyst. Compared to the curve for pure CDL (Fig. 5, curve 1), all three curves for catalyst presence show a similar tendency, i.e., below 300 °C, the presence of catalysts has a positive effect on CDL weight loss, while above 300 °C, it suppresses CDL weight loss. Three residues from these runs were subjected to calcination using the same method as described earlier, and the results are shown in Table 2.

It is indicated in Fig. 5 and Table 2 that the interactions between three catalysts and CDL are different. The retention of CDL on the catalysts while being heated is likely to be caused by the combination of two factors, i.e., (1) surface adsorption affinity for the components present in CDL and (2) the condensation of aromatic compounds. The former predominates at lower temperatures while the latter does at higher temperatures. The additional weight loss of CDL in

the presence of catalysts may be attributed to catalytic (hydrogenation/hydrocracking) activity of the catalysts, which may occur over the whole temperature range tested. The differences between the TGA curves for different catalysts likely represent different catalytic selectivities for competing reactions such as thermal and catalytic cracking, hydrocracking, hydrogenation and coking. Coking is favoured at higher temperatures with a deficiency of H_2. Among the three commercial catalysts tested, Co-Mo/Al_2O_3 exhibits the maximum retention of CDL mass over the entire programmed temperature range. One may deduce that there is a stronger interaction between CDL and Co-Mo/Al_2O_3, which brings about somewhat stabilized adsorbed species. Because of the stable adsorption, on the one hand, it becomes more difficult for volatile components to evaporate and for reactive heavier species to be converted into lighter ones, and on the other hand, it becomes easier for aromatic species to condense on active sites of the catalyst.

If the catalyst which exhibits the minimum retention of CDL mass during the temperature-programmed heating to 450 °C is considered to be the superior one, the Ni-Mo/Al_2O_3 appears to be the best for hydroprocessing of CDL. The TGA curves have shown a different extent of CDL weight loss for each catalyst. These real differences in weight loss suggest that TGA may be useful as a tool for a quick but rough evaluation of hydrocracking catalysts.

A comparison between hydrocracking catalyst test results using the TGA method and from high-pressure batch tests To evaluate the ability of TGA to indicate the relative activities of catalysts for hydroprocessing CDL, additional runs at 13.9 MPa and 400 °C were carried out in a catalytic stirred tank reactor operated in a closed (batch) mode [5]. The following comparisons were obtained from analysis of the product liquid:

Hydrodesulfurization activity:	Ni-Mo/Al_2O_3 > Ni-W/Al_2O_3 > Co-Mo/Al_2O_3
Hydrodenitrogenation activity:	Ni-Mo/Al_2O_3 > Ni-W/Al_2O_3 > Co-Mo/Al_2O_3
Hydrodeoxygenation activity:	Co-Mo/Al_2O_3 > Ni-Mo/Al_2O_3 > Ni-W/Al_2O_3
Aromaticity-reducing ability:	Ni-Mo/Al_2O_3 > Ni-W/Al_2O_3 > Co-Mo/Al_2O_3
H/C ratio of the product liquid:	Ni-W/Al_2O_3 > Ni-Mo/Al_2O_3 > Co-Mo/Al_2O_3
Conversion to gas-oil (343-524 °C):	Ni-Mo/Al_2O_3 > Ni-W/Al_2O_3 > Co-Mo/Al_2O_3

While some of the above differences may be small, these results suggest that the Ni-Mo/Al_2O_3 catalyst provided the best overall performance. The TGA results yielded the weight loss in the following sequence (see Fig. 5):

Ni-Mo/Al_2O_3 > Ni-W/Al_2O_3 > Co-Mo/Al_2O_3.

Thus there may be some qualitative relation between overall catalyst performance and weight loss during a temperature-programmed TGA experiment.

SUMMARY

Because of small sample size and high sensitivity of TGA, its results will be significantly affected by operation conditions, especially when the sample involves a complicated system like the mixture of a relatively non-volatile CDL and a solid catalyst. In order to ensure reproducibility and to make valuable comparisons of experimental data, strictly standardized procedures need to be pre-defined in applications such as catalytic hydroprocessing (gas-liquid-solid systems).

TGA can provide useful information about solid-catalyzed relatively non-volatile liquid phase reaction systems. Such an application to hydroprocessing of a CDL was demonstrated in the present work. The weight loss of CDL as a function of increasing temperature is increased at lower temperatures and lowered at higher temperatures when a catalyst is present, irrespective of whether the atmosphere is H_2 or N_2. Preliminary results suggest that the catalyst most active for hydroprocessing of the CDL tested is the catalyst producing the greatest weight loss.

Our experimental results suggest that many of the molecular fragments are strongly absorbed on the surface of the catalyst. In a batch-type experiment such as in a TGA weighing pan, this adsorption may persist over the entire range of temperature tested and its magnitude may vary with the type of catalyst tested. At higher temperatures (>300 °C), the reactions involving coking increasingly dominate.

What occurs during TGA of CDL in H_2 atmosphere in the presence of a catalyst is so complicated that some ambiguities in TGA results exist. So far it is not yet possible to comment in depth about the chemistry involved because TGA only provided a mass-temperature record of the process. Additional work using TGA combined with some means of identifying the chemical character of the evolved gases seems to be valuable. Recent designs of TGA equipment available enable mass changes as large as ten grams to be monitored. Access to such equipment would enable chemical analysis of the residue as well as the evolved gases to be determined.

REFERENCES

[1] F.E. Massoth and S.E. Cowly, Ind. Eng. Chem. Fund., 15 (1976) 218.
[2] J.W. Dean and D.B. Dadyburjor, Ind. Eng. Chem. Res., 27 (1988) 1754.
[3] D.E. Rogers and L.M. Parker, Appl. Catal., 51 (1989) 181.
[4] C. Kordulis, F.M. Faus and B. Delmon, Appl. Catal., 23 (1986) 367.
[5] I.G. Dalla Lana, "Hydroprocessing of Coal-Derived Liquids", Final Report to Alberta Office of Coal Research and Technology, (1990).

Table 1 Coke formation from pure CDL and from CDL-catalyst mixture

Sample for TGA	Weight loss after TGA (wt%)	Weight loss after calcination (wt%)	Coke formed during TGA (wt%)
pure CDL	82.38	98.80	16.42
CDL-catalyst mixture	77.47	98.79	21.32

Table 2 Coke formation on three commercial catalysts

Mixture samples for TGA	$Ni\text{-}Mo/Al_2O_3$ & CDL	$Co\text{-}Mo/Al_2O_3$ & CDL	$Ni\text{-}W/Al_2O_3$ & CDL
Weight loss of CDL after TGA (%)	77.47	74.08	75.44
Weight loss of CDL after calcination (%)	98.79	98.82	98.78
Coke formed during TGA (%)	21.32	24.74	23.34

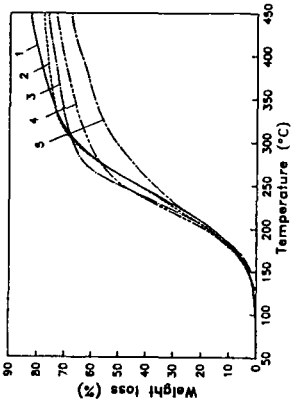

Fig. 2 Influence of catalyst content (wt%) in mixture sample: (1) 0%; (2) 25%; (3) 40%; (4) 50%; (5) 60%. Carrier gas = H_2.

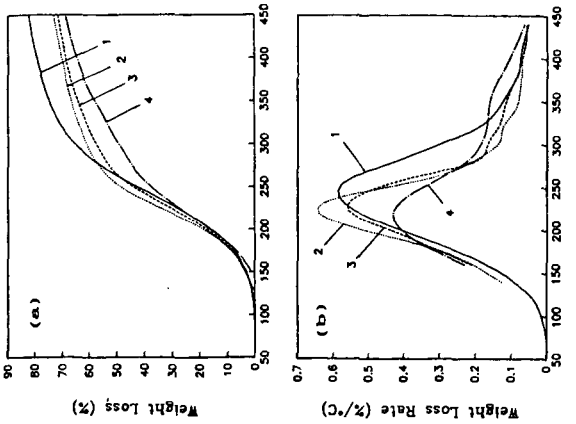

Fig. 1 Effect of catalyst particle size on TGA curve of CDL: (1) no catalyst; (2) <0.12 mm; (3) 1.59 mm; (4) 3.18 mm. Catalyst content = 50 wt%; carrier gas = H_2.

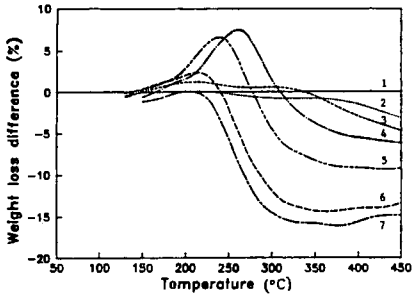

Fig. 3 The difference between CDL weight losses in the present of the catalyst and that in the absence of the catalyst. Catalyst content: (1) 0; (2) 10%; (3) 25%; (4) 40%; (5) 50%; (6) 57%; (7) 60%.

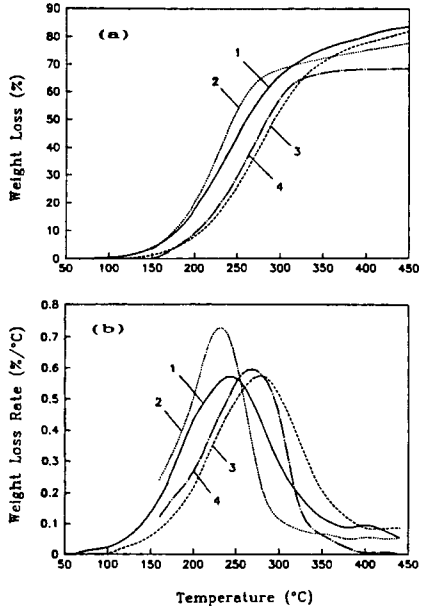

Fig. 4 Effect of atmosphere on TGA curve of CDL with and without the catalyst: (1) H_2, without catalyst; (2) H_2, with catalyst; (3) N_2, without catalyst; (4) N_2, with catalyst. Catalyst content = 40%.

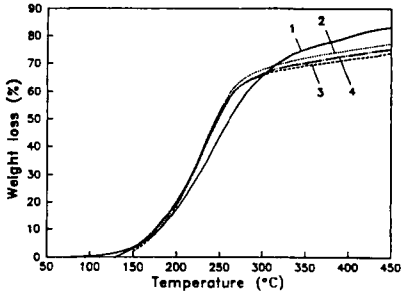

Fig. 5 TGA curves of CDL in the presence of different commercial catalysts: (1) no catalyst; (2) Ni-Mo/Al_2O_3; (3) Co-Mo/Al_2O_3; (4) Ni-W/Al_2O_3. Carrier gas = H_2.

ANALYSIS OF ORGANIC / INORGANIC ANALYTES IN ENVIRONMENTAL SAMPLES BY PACKED CAPILLARY CHROMATOGRAPHY

Mark D. Burford[1], Neil G. Smart[2], Mark M. Robson[1], Stuart C. Mitchell[1], Keith D. Bartle[1] and Antony A. Clifford[1]

[1] School of Chemistry, University of Leeds, Leeds LS2 9JT, UK

[2] British Nuclear Fuels plc, Springfield Works, Salwick, Preston PR4 OXJ, UK.

Keywords: Packed capillary columns, organic and inorganic analytes, metals.

INTRODUCTION

Recent progress in the development of techniques for packing of high efficiency capillary columns has enabled the concept of unified chromatography to be realised [1]. Packed capillary columns offer the advantages of both packed column (high loading capacity, wide range of stationary phases) and capillary column (speed of analysis, high resolution) techniques to produce a versatile and efficient analytical procedure. For the detailed investigation of fossil fuel and environmental samples the rapid growth of packed capillary chromatography offers the unique opportunity to analyse both organic and inorganic components as the column can be operated in both gas chromatography (GC) and supercritical fluid chromatography (SFC) modes. In this study, the use of packing capillary columns, prepared in-house, is investigated for both high pressure GC and SFC using helium and CO_2 as the mobile phase respectively. Several spiked and real world samples have been used to demonstrate the potential of packed capillary columns in the analysis of organic and inorganic analytes in fuel and environmental samples.

EXPERIMENTAL

Column packing procedure

A number of fused silica capillary columns, of varying length, were packed using supercritical CO_2 at 300 bar. The fused silica tubing was connected to a packing reservoir, cleaned with methanol and dried. The packing material was then placed in the reservoir. The end of the reservoir was connected to a high pressure valve which facilitated the introduction of the mobile phase. The end of the column was connected, via a Valco union containing a metal screen (2 μm), to a linear restrictor (12 μm i.d. x 30 cm fused silica tubing). The column tubing and restrictor were then immersed in an ultrasonic bath (~60-70°C). Liquid CO_2 was introduced into the system by opening both valves. The column was continuously sonicated at constant pressure throughout the packing procedure. On completion, sonication was stopped whilst the pressure was maintained for a further 30 minutes approximately, prior to depressurisation. The depressurisation step was performed slowly to avoid backflushing and possible deformation of the packed bed. At a pressure of 70-80 bar, both valves were closed and the system vented. The column was then ready for use.

High pressure gas chromatography

Two different packed capillary stationary phases were evaluated for the analysis of light hydrocarbons. The fused silica columns, i.d. of 250 μm, were packed with either 5 μm ODSII (C_{18}) or 5 μm hexyl (C_6) (Phase Separations, Deeside, UK). Three different column lengths (10, 20 and 30 cm) were installed in a Lee Scientific 600 Series SFC oven fitted with a Valco AC14LTWP injection valve and an FID. All samples were injected neat by varying the injection time. The system was evaluated using high pressure helium (20-100 bar) and carbon dioxide (40-65 bar).

Supercritical fluid chromatography (SFC)

The chromatographic system comprised an RPT 9400 (RPT Inc., San Jose, California) micro SFC pump, Lee Scientific 600 Series SFC oven, Lee Scientific micro UV detector and a Merck-Hitachi D2500 integrator. A valco AC14LTWP injection valve with an injection volume of 200 ηl was used. The various components were connected via silica capillary. A 12 μm linear restrictor was located after the UV-VIS detector and heated to 350°C to avoid blockages. The system was operated manually.

RESULTS AND DISCUSSION

High pressure gas chromatography

Microcolumns packed with conventional gas GC packings have previously been investigated at high pressures by Giddings and coworkers [2]. However, only recently has the use of LC packings been explored in high pressure packed capillary GC by Liu and Yang [3]. Conventional packing techniques introduce the stationary phase as a slurry but a new packing technique using supercritical CO_2 have been shown to provide a significant improvement in packing and column efficiency [1]. In the present study, to evaluate column performance helium

was used as the mobile phase in the analysis of low molecular weight hydrocarbons. Figure 1 shows the chromatogram obtained from the analysis of a 12 component synthetic mixture of C_5-C_8 hydrocarbons using a 20 cm x 250 μm i.d. column packed with 5 μm octadecylsilica (ODS-C_{18}). At 120 bar helium pressure, complete separation of all 12 compounds was achieved within 20 minutes. The resolution obtained from the analysis of the mixture containing six C6 isomers and four C8 isomers demonstrates the high efficiency provided by high pressure packed capillary GC for the separation of light hydrocqrbon geometrical isomers. The separation is comparable to that acheived using open tubular capillary columns but with a considerably reduced analysis time. Furthermore, due to the higher sample loading of the pacvked column, it is possible to inject the sample directly thus avoiding any possible discrimination effects normally associated with split-splitless injection when using open tubular capillary columns. The full range of the ODS column with helium as the mobile phase is shown in Figure 2 for the analysis of a light naphtha standard (Supelco 4-8265) conducted under the same conditions as above. From the chromatogram it is clear that the low molecular weight compounds are well-resolved but as the molecular weight increases the resolutin tails off indicating the current limit of the technique. Analysis of the standard by an open tubular chromatography confirmed this observation, with separation of the higher molecular weight compounds reduced considerably. However, the overall analysis time was also reduced by approximately one third.

Supercritical fluid chromatography (SFC)

The chromatographic analysis of the organic and metallic components recovered from fuel and oil related environmental samples generally involves two specific separation techniques due to the distinctive chemical and physical characteristics of both types of analytes. The organic components of interest such as polycyclic aromatic hydrocarbons (PAHs), polychlorinated biphenyls (PCBs) and petroleum hydrocarbons are sufficiently volatile to be amenable to capillary gas chromatography (GC). However, the organometallic and inorganic species, which in general cannot be volatilized or are thermally unstable at GC operating temperatures are chromatographically separated using ion-exchange or high performance liquid chromatography (HPLC) [4].

The use of supercritical fluid chromatography (SFC) has proved to be a suitable technique for the analysis of a wide range of organic compounds. For example, the separation and identification of the EPA priority PAHs in a coal tar oil can be achieved using a 30 cm x 250 μm i.d. capillary column packed with 5 μm ODS1 stationary phase (See Figure 3). The use of this short column which contained a tailor made PAH stationary phase (Phase Separations, Deeside, UK) eluted the 16 priority PAHs within 30 minutes. Whilst the elution of organic components by supercritical fluids is readily attainable, the elution of metal ions is considerably more difficult due to the charge neutralisation required to solvate ions in the mobile phase [5]. Furthermore, previous studies have demonstrated that ionic organometallic compounds result in poor peak shapes due to their chemical reactivity with the stationary phase [6]. However, by chelating the metal ion with a ligand to form a neutral metal complex the solubility and hence the chromatography of the metal species can be significantly improved [7].

Initial SFC investigations of common metal complexes such as metal dialkyldithiocarbamates (DDC) used packed columns with an organically modified carbon dioxide (CO_2/MeOH) mobile phase. More recently, capillary GC with pure carbon dioxide has offered improved resolution [8], but the technique requires that the metal DDC complex be sufficiently soluble in the mobile phase to avoid broad peak shapes and poor reproducibility [7]. Packed capillary chromatography offers the advantages of both a packed column (e.g. high loading capacity and a wide range of stationary phases) and a capillary column (e.g., speed of analysis and high resolution) and therefore metal DDC complexes with relatively low solubility can be adequately resolved using just pure CO_2. Figure 4 shows the chromatogram of an organic extract containing the DDC ligand and the metal complexes $Fe(DDC)_3$ (7 μg) and $Ni(DDC)_2$ (14 μg).

Organometallic compounds can also be separated using the same 20 cm packed capillary ODS1 column (Figure 5) with pressure programming. Both ionic (triphenyltin chloride) and non-ionic (tetraphenyltin, triphenylarsenic and ferrocene) species were detected with good chromatographic peak shapes. Earlier studies have found that the presence of an anionic functional group increases the polarity and chemical reactivity of the organometallic compounds, which consequently results in poor peak shapes [6] and/or incomplete recovery of injected samples [9]. Thus the elution of the ionic components has previously required an organic modifier to avoid peak tailing [6], however this addition step was not necessary with the packed capillary system.

The wide range of metal complexes and organometallic species that are amenable to SFC should also be amenable to supercritical fluid extraction (SFE), and several researchers have adequately demonstrated this application [5,10]. For example, the diethyldithiocarbamate (DDC) metal complexes analysed by packed capillary are generally poorly soluble in low pressure (150 atm) and low temperature (50°) carbon dioxide [5], with solubility values in the region of 10^{-7} - 10^{-6} mol/L. Consequently, the complexes are difficult to elute from the packed capillary column without high pressures (350 atm) (See Figure 5). Thus, if the temperature and pressure of the supercritical fluid is substantially increased the solubility of the metal DDC complexes will also increase, as shown in Table 1.

Table 1. Solubility of cadmium (II) diethyldithiocarbamate in CO_2.

CO_2 conditions	Solubility (mol/L)
250 atm, 50°C	3.6×10^{-6}
250 atm, 100°C	1.6×10^{-5}
350 atm, 50°C	5.3×10^{-6}
350 atm, 100°C	6.5×10^{-5}

Using high pressure carbon dioxide (400 atm) to solvate the DDC ligand it was possible to recover between 50 and 70% of spiked Pb^{2+} and Cd^{2+} from filter paper. It is envisaged that further extractions of the metal ions with fresh complexing agent at this rigorous extraction condition could potentially achieve quantitative SFE recoveries.

REFERENCES

[1] D. Tong, K.D. Bartle and A.A. Clifford, *J. Microcol. Sep.*, 6 (1994) 249.
[2] M.N. Myers and J.C. Giddings, Anal. Chem, 38 (1966) 29.
[3] Y. Liu and F.J. Yang, J. Microcolumn Separations, 3 (1991) 251.
[4] B.R. Willeford and H. Veening, *J. Chromatogr.*, 251 (1982) 61.
[5] C.M. Wai, Y Lin, R. Brauer, S. Wang and W.F. Beckert, *Talanta*, 40 (1993) 1325.
[6] J.W. Oudsema and C.F. Poole, *Fresenius J. Anal. Chem.*, 344 (1992) 426.
[7] K.E. Laintz, J.-J. Yu and C.M. Wai, *Anal. Chem.*, 64 (1992) 311.
[8] P. Manninen and M-L. Riekkola, *J. High Resolut. Chromatogr.*, 14 (1991) 210.
[9] E. Blake, M.W. Raynor and D. Cornell, *J. Chromatogr.*, 683 (1994) 223.
[10] J. Wang and W.D. Marshall, *Anal. Chem.*, 66 (1994) 3900.

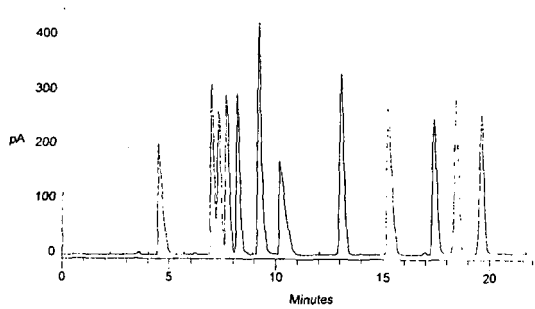

Figure 1
High pressure gas chromatogram of a mixture of: 1 Pentene, 2 Methyl Pentene, 3 Methyl Pentane, 2 Methyl Pentane, 2, 3 Dimethyl Butane, Methyl Cyclopentane, Cyclohexane, 3 Methyl Hexane, 3 Methyl Heptane, Octane, 2, 2, 4 Trimethyl Pentane, 2, 2, 4 Trimethyl Pentane.
Conditions: 20 cm, 250 μm ID, octadecylsilica column (Phase-Separations, Deeside, UK), Helium mobile phase at 120 bar, with the following temperature program: 4 minutes isothermal at 40 C, 5° C per minute ramp to 220 °C

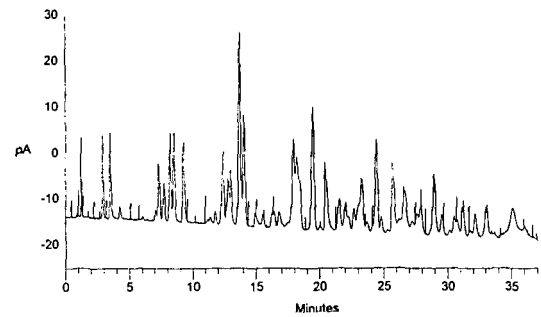

Figure 2
High pressure gas chromatogram of a light naphtha standard (Supelco 4-8265)
Conditions: 20 cm, 250 μm ID, octadecylsilica column (Phase-Separations, Deeside, UK), Helium mobile phase at 120 bar, with the following temperature program: 4 minutes isothermal at 40 C, 5° C per minute ramp to 220 °C

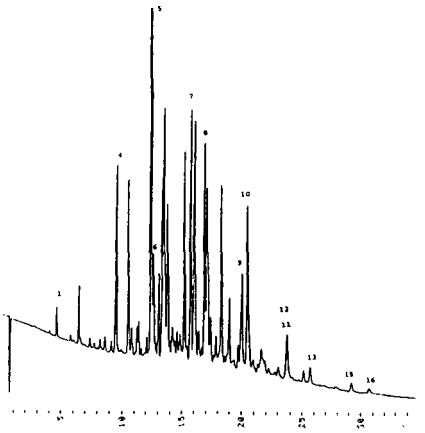

Figure 3
Supercritical fluid chromatogram of base coal tar oil analysed using the following conditions:
Column: PAH 5 μm (Phase-Separations, Deeside, UK), 30 cm column. 250 μm ID. column oven temperature 100°C, detector wavelength 254, with the following gradient 100 to 300 bar CO_2 and 0.10 to 1.00 μL/min methanol over 30 minutes.
Peak identification; 1 naphthalene; 2 acenaphthene; 3 acenaphthylene, 4 fluorene; 5 phenanthrene; 6 anthracene; 7 fluoranthene; 8 pyrene; 9 benzo[*a*]anthracene; 10 chrysene; 11 benzo[*b*]fluoranthene; 12 benzo[*k*]fluoranthene; 13 benzo[*a*]pyrene; 14 dibenzo[*a,h*]anthracene; 15 benzo[*ghi*]perylene; 16 indeno[1,2,3-*cd*]pyrene.

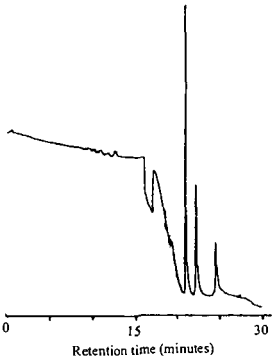

Figure 4. SFC separation of a mixture of DDC, $Fe(DDC)_3$ and $Ni(DDC)_2$ using a 20 cm x 250 μm I.D. capillary column packed with 5μm ODS1 stationary phase. Separation obtained with carbon dioxide pressure programme starting at 100 atm and increasing the pressure at 16 atm/min to 350 atm, then holding the pressure at 350 atm for 15 minutes. UV detection at 220 nm.

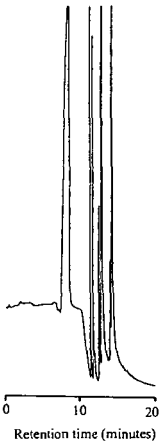

Figure 5. SFC separation of organotin, organoarsenic and ferrocene compounds using a 20 cm x 250 μm I.D. capillary column packed with 5μm PAH stationary phase. Separation obtained with carbon dioxide pressure programme starting at 100 atm and increasing the pressure at 16 atm/min to 350 atm, then holding the pressure at 350 atm for 15 minutes. UV detection at 220 nm.

INVESTIGATION OF JET FUEL THERMAL STABILITY USING PHOTON CORRELATION SPECTROSCOPY AND A QUARTZ CRYSTAL MICROBALANCE

Wayne M. Trott
Energetic and Multiphase Processes Department 1512
Sandia National Laboratories
P. O. Box 5800
Albuquerque, New Mexico 87185-0834

Keywords: Jet Fuels, Particle Size Distribution, Mass Deposition

INTRODUCTION

The thermal stability of aviation fuels is an important concern in designs for enhanced aircraft performance. In addition to its primary use as a propellant, jet fuel serves as a coolant for the environmental control system, engine lubrication, avionics, etc. in present military applications. Thermal loads on the fuel are anticipated to increase concurrently with the demands of advanced aircraft. Unfortunately, elevated temperatures in hydrocarbon-based fuels lead to oxidative degradation, producing insoluble products in the bulk liquid as well as deposits on contacting surfaces.[1] These processes reduce heat exchanger efficiencies and can result in obstructions of critical components, including valves, filters, and injection nozzles.

Efforts to develop highly stable jet fuels and thereby mitigate loss of heat-transfer efficiency and fouling problems in flight systems would certainly benefit from a predictive model that adequately accounts for the global physics and chemistry leading to insoluble particle formation and solids deposition. Recent experiments by Jones and Balster[2,3] have illustrated the complexity of these processes. In particular, their studies of Jet-A, POSF-2827 fuel[3] have demonstrated that observed insolubles are early products of autoxidation chemistry and that the "yield" of these products is directly correlated with O_2 availability. Their results also suggest that surface deposits arise from a precursor material formed in the bulk fuel in one of several independent reaction channels leading to the formation of various degradation products. Additional experimental work incorporating sensitive, real-time diagnostic methods for monitoring incipient particle formation as well as mass deposition on surfaces is clearly needed. To address this need, an experimental assembly designed for simultaneous application of photon correlation spectroscopy (PCS) and a quartz crystal microbalance (QCM) has been assembled and tested. The main aspects of this assembly and preliminary results obtained from integrated PCS and QCM measurements are described in this paper.

EXPERIMENTAL

PCS is a well established and widely used dynamic light scattering technique for quantitative measurement of particle size distributions in liquid samples. Briefly summarized, this technique monitors fluctuations in the intensity of scattered light due to Brownian motion of particles in a laser-illuminated volume. The scattered light is viewed by a photomultiplier, converted into pulse trains by an amplifier/discriminator and processed by a digital correlator, which performs an autocorrelation of the time-dependent intensity signal. For a monodisperse suspension of particles, the autocorrelation exhibits an exponential decay rate $G(\tau) \propto e^{-2\Gamma\tau}$. The decay constant, Γ, is related to the translational diffusion coefficient, D, of the scattering particles and to the geometry of the experiment through the relations

$$\Gamma = q^2 D;\ q = \frac{4\pi n \sin(\theta/2)}{\lambda}$$

where q represents the magnitude of the scattering wave vector which can be determined from the refractive index of the liquid (n), the scattering angle, (θ), and the wavelength of the incident light (λ). For spherical particles, the particle size can be determined from the Stokes-Einstein equation

$$D = \frac{kT}{3\pi\eta d}$$

where k is the Boltzmann constant, T the absolute temperature, η the fluid viscosity, and d the particle diameter. Detailed discussions of PCS instrumentation and data reduction methods are available elsewhere.[4,5] Under favorable circumstances, PCS can be used for accurate, noninvasive sizing of particles over a diameter range of a few nm to several microns. Successful application of this technique to real-time, *in situ* measurements of particle formation in heated jet fuels has been reported previously.[6] Under isothermal conditions, thermally stressed fuels appear to generate simple, monomodal particle size distributions that exhibit a systematic increase in mean particle diameter as a function of time at elevated temperature.

The QCM provides a sensitive, compact system for complementary measurements of surface deposition. This device is a bulk-wave resonator, consisting of a piezoelectric quartz wafer with metal

electrodes on each face, that can be electrically excited into resonance. When the crystal is excited in this manner, it undergoes a shear deformation with displacement maxima at the crystal faces. Mass accumulated on the crystal faces moves synchronously with the oscillating surfaces, resulting in a shift of the resonant frequency. The QCM is typically incorporated in an oscillator circuit, where the oscillation frequency decreases with mass accumulation. The theory that relates measured frequency changes to mass deposition has been presented in detail elsewhere.[7] Under conditions of constant fluid density and viscosity, the surface mass density (mass/area), ρ_s, is related to the measured decrease in frequency, $\Delta\nu$, as follows:

$$\rho_s = \left(-2.21 \times 10^5 \frac{g}{cm^2 s}\right) \frac{\Delta\nu}{\nu_0^2}$$

where ν_0 is the unperturbed resonant frequency of the device (~5 MHz). The QCM permits quantitative measurements at very low deposition rates; a typical system can easily achieve a resolution of ~0.1-0.2 $\mu g\text{-}cm^{-2}$. The utility of QCM instrumentation in jet fuel thermal stability studies was demonstrated by Klavetter et al.[8] Most of these initial tests were performed under conditions of abundant oxygen availability. Recently, Zabarnick and co-workers have used QCM systems to investigate the thermal stability of various jet fuels at relatively low oxygen availability[9] and to evaluate the effect of several jet fuel additives.[10]

A schematic diagram of the jet fuel test system designed for integrated PCS and QCM measurements is shown in Figure 1. The stainless steel pressure vessel (300 ml. capacity, Parr Instruments) provided optical access for the PCS source laser (typically a HeNe laser, 35 mW peak power) as well as a viewing port for the PCS collection optics at a 90° angle to the incident light. The lid of the vessel was modified to accommodate a mounting clamp for the QCM sensor and a hermetic, rf feedthrough assembly, as described previously.[8] The QCM was mounted vertically in the fuel in order to mitigate gravitational effects on deposition. Gas inlet and outlet ports were also located on the fixture lid, permitting fuel exposure to an oxidative or inert atmosphere at variable pressure, as desired. In order to reduce the time required to attain the target temperature and to optimize temperature uniformity in the cell, heating was supplied by band heaters attached to the window "arms" in combination with the heating mantle provided with the vessel. Temperatures were monitored by thermocouples positioned in the fuel sample and at several points on the outside of the vessel. The desired stress temperature was maintained by using one of the thermocouples as a feedback device for a programmable temperature controller (Eurotherm Model 818).

In all tests described in this paper, samples were prepared by filtering the fuel through a 0.2-μm PTFE filter, sealing the vessel, and then sparging with the desired gas (oxygen or nitrogen) for ~45 minutes. Typically, the vessel was filled to within 0.75" of the lid. For some tests, a 50 psig atmosphere of O_2 or N_2 was imposed prior to heating. In other experiments, the fuel was heated under ambient pressure conditions. Data acquisition included the frequency and dc voltage output of the QCM oscillator circuit as well as the output of the digital correlator (Langley-Ford, Model 1096). Intensities of transmitted and scattered laser light were monitored by a laser power meter (located at the output port of the test vessel) and a frequency counter (coupled to the amplifier/discriminator), respectively. In reducing the PCS data, several available algorithms were utilized, including a discrete exponential fitting program and two Laplace inversion routines.[11]

RESULTS AND DISCUSSION

Previous investigations[6,8] of jet fuel thermal stability have shown that the rates of both particle growth and mass deposition are sensitive to the temperature of the sample. Hence, reasonable uniformity of the temperature field in the test vessel is required for facile, quantitative interpretation of PCS and QCM data. Evaluation and optimization of temperature conditions in the assembly described above has been achieved by conducting heating tests employing an array of thermocouples. The results of one test are given in Figure 2. In this case, five thermocouples were placed in the fluid. Measurements were obtained near the bottom (TC1), center (TC4), and top (TC5) of the fluid volume, as well as along the side of the vessel (TC3) and within one of the three arms containing window ports (TC2). Another device (TC6) was used to monitor the outside wall temperature. The target temperature for this test was 150 C. Both fairly rapid heating and acceptable temperature uniformity in the fuel were achieved. At the target point, temperatures throughout the main body of the cell were uniform to within 0.8 C. The temperature in the extension arms was slightly hotter (~2 C). Similar results have been obtained in tests with other target temperatures.

Thus far, integrated PCS and QCM tests have been performed on Jet A 91-POSF-2827, a non-hydrotreated fuel that is known to resist oxidation but produce surface deposits in appreciable quantities at elevated temperatures, and Jet A-1 POSF-2747, a hydrotreated fuel that is highly stable with regard to surface deposition even though it consumes O_2 rapidly.[9] Results on the first substance are more developed and will be described here. Jet A 91-POSF-2827 contains a relatively high level (up to 0.1 mass percent) of sulfur compounds; these components are thought to play a significant role in both inhibition of oxidation and deposit formation.[3] A summary of mass

deposition results from QCM measurements in this fuel is provided in Table 1. Figures 3 and 4 illustrate selected QCM data in graphical form; relevant particle growth curves (as determined by PCS) and transmitted/scattered light intensity plots are shown in Figures 5 and 6, respectively.

The data obtained in this work are generally consistent with results of previous jet fuel thermal stability tests performed under similar conditions. The critical role of dissolved oxygen has been emphasized in earlier studies[3,8,9] and is again demonstrated by the tests conducted near 150 C using O_2 and N_2, respectively, as the sparge and confining gas (cf. Table 1). With abundant oxygen, the QCM system registered a mass deposition rate of 0.88 $\mu g\text{-}cm^{-2}\text{-}hr^{-1}$. A substantially lower rate was obtained when oxygen was effectively purged from the system. In fuel sparged with nitrogen and heated to 148 C under 50 psig N_2 confinement, the observed rate was only 0.13 $\mu g\text{-}cm^{-2}\text{-}hr^{-1}$. This low value compares favorably with previous QCM results acquired under oxygen-depleted conditions.[8,9] Similarly, particle formation in the fluid was very heavy with abundant oxygen but largely suppressed when the fuel was stressed with severely limited oxygen availability. In the latter case, the PCS technique was unable to provide meaningful correlations at any time during testing at elevated temperature; however, some hints of particle generation were seen in the raw data and, after the fuel cooled to room temperature, a small concentration of particles with mean diameter near 200 nm was observed. Processes leading to the generation of bulk and surface insolubles in the absence of O_2 are evidently minor but not negligible.

The remaining tests have also addressed the role of oxygen availability. For example, Figure 3 shows QCM results for a Jet A 91-POSF-2827 sample sparged with O_2 and heated to 139 C under ambient pressure. A plot of temperature measured by a thermocouple positioned in the fuel is also included in this figure for comparison. After the sample attained a constant temperature, mass accumulation closely corresponding to a linear deposition rate of 0.23 $\mu g\text{-}cm^{-2}\text{-}hr^{-1}$ was registered. The rate determined in this test compares favorably to the results of Zabarnick[9] which indicate similar deposition behavior (accumulation of 3.6 $\mu g\text{-}cm^{-2}$ at a nearly linear rate in 15 hours) for Jet A POSF-2827 sparged with air and heated to 140 C under ambient pressure. The most significant difference in experimental conditions for these two tests was the choice of oxygen vs. air for the sparging gas. The similarity in recorded mass accumulation rates suggests that the additional oxygen availability has a negligible effect on surface deposition at this temperature. In this case, added oxygen in the confining atmosphere should also play a minor role. The slightly higher deposition rate of 0.27 $\mu g\text{-}cm^{-2}\text{-}hr^{-1}$ seen in Jet A 91-POSF-2827 heated to 138 C under 50 psig O_2 (cf. Table 1) supports this expectation. Similarly, Klavetter et al.[8] reported nearly identical rates for the same fuel sparged with O_2 and heated to 160 C under 50 psig O_2 and N_2 overpressures (1.18 vs. 1.23 $\mu g\text{-}cm^{-2}\text{-}hr^{-1}$, respectively). These results all appear to be linked to this fuel's tendency to consume oxygen relatively slowly.

An additional comparison can be made with deposition rates determined by Klavetter et al.[8] for Jet A 91-POSF-2827 (confining pressure of 50 psig O_2) over a temperature range of 160-200 C. The QCM results acquired in the present work expand this range down to 133 C. Figure 4 shows an Arrhenius plot with data from three relevant tests (1, 3, and 4; cf. Table 1) added to the earlier results obtained at higher temperature. The Arrhenius "line" derived from a linear least-squares fit to the data implies an activation energy of 20 kcal/mol for the global deposition process. This value is somewhat lower than the 26 kcal/mol activation energy calculated for this fuel in Ref. 8; however, it is consistent with the behavior of other fuels examined in that study.

The simultaneous PCS and light intensity measurements provide added insight. In all tests where *some* oxygen was supplied in the sparge gas and confining pressure, large concentrations of particles formed in the fluid within several hours. Consistent with previous PCS measurements,[6] particles were detected earlier and the mean particle diameter increased more rapidly with increasing stress temperature. The influence of added oxygen at a given temperature is illustrated by the PCS results in Figure 5. At 133 C, significant particle formation was observed earlier in the presence of abundant oxygen; however, the initial rate of increase in particle size was approximately the same in the both cases. Dissimilar behavior was observed at later times. At ambient pressure, the mean particle size inferred from the PCS data increased steadily throughout the test whereas, under 50 psig O_2 confinement, the particle size appeared to level off near 300 nm. This phenomenon is probably an artifact arising from multiple scattering effects that can occur when particles are present in high concentration. The scattered light intensity data are consistent with this interpretation. Figure 6 demonstrates the complex behavior of the scattered light intensity vs. time for the test performed under 50 psig O_2. The intensity increased rapidly during the first two hours of this test, reaching a maximum value at approximately 150 minutes. This time period corresponds to the initial phase of particle formation and growth (cf. Figure 5). Thereafter, the intensity fell to roughly half the peak value at about 300 minutes and then recovered slightly. This period coincides with the observed "saturation" in particle diameter. The fuel exhibited a very "cloudy" appearance at these times, a further indication that particle formation had occurred to such an extent that the laser intensity reaching the PCS measurement volume (i.e., center of the cell) was

severely attenuated by particle absorption and scattering. In contrast, the scattered light intensity was observed to be still slowly increasing after five hours of heating Jet A 91-POSF-2827 at 133 C under ambient pressure and the fuel appeared to be only slightly "cloudy" at this point.

Figure 6 also provides results of laser power measurements taken at the exit optical port of the test vessel during the test under 50 psig O_2 confinement. The maximum in scattered light intensity accompanied a steep decline in the transmitted laser power, illustrating the important role of particle scattering and absorption at this point in the experiment. The late-time recovery of both signals shown in Figure 6 may be due in part to particle settling as the mean size increased. Also, Mie theory predicts a complex dependence of scattering cross section vs. particle diameter at sizes > 400 nm. Estimates of the relative mass involved in particle formation under an O_2 overpressure vs. ambient pressure were calculated from Mie intensity parameters in combination with the light intensities. A Beer's Law-type relationship was used to infer the laser power reaching the center of the cell from power measurements incident on and transmitted by the sample. Attenuation of the scattered light intensity by particles in the sample was accounted for in a similar fashion. These calculations suggest that the mass associated with particle formation in the fuel heated under 50 psig O_2 is 3-5 times higher (for a given time during the test) than in fuel heated at ambient pressure. For Jet A 91-POSF-2827 under these conditions, excess oxygen clearly affects the generation of bulk insolubles more substantially than it accelerates surface deposition.

CLOSURE

An experimental setup for simultaneous, real-time investigation of particle formation and surface deposition in heated jet fuels has been assembled and tested. The design permits integrated PCS and QCM measurements in a nearly isothermal environment. Data obtained from integrated measurements on Jet A 91-POSF-2827 are generally consistent with earlier results from tests performed with the individual techniques. With this fuel, oxygen availability is a factor in both particle formation and mass accumulation on surfaces. In particular, excess oxygen (at a given temperature) leads to substantially larger concentrations of particles in the bulk liquid. Integrated PCS and QCM measurements should find application in thermal stability tests of a wide range of fuel types and should permit detailed evaluation of various additives, including antioxidants, dispersants, etc. Under some conditions leading to extensive generation of bulk insolubles, quantitative particle sizing using PCS may be limited by multiple scattering effects.

ACKNOWLEDGMENTS

This work was jointly supported by the U. S. Air Force, Aero Propulsion and Power Directorate of Wright Laboratory, Wright-Patterson AFB, and the U. S. Department of Energy, Pittsburgh Energy Technology Center (PETC) through Sandia National Laboratories under contract DE-AC04-94AL85000. The support of W. E. Harrison III and Dr. W. M. Roquemore of Wright Laboratory as well as S. Rogers of the U. S. DOE PETC is gratefully acknowledged. The excellent technical assistance of Jaime Castañeda is greatly appreciated.

REFERENCES

1. R. N. Hazlett, *Thermal Oxidation Stability of Aviation Turbine Fuels*, ASTM Monograph 1 (American Society for Testing and Materials, Philadelphia, PA, 1991).
2. E. G. Jones and W. J. Balster, "Application of a Sulphur-Doped Alkane System to the Study of Thermal Oxidation of Jet Fuels," ASME Paper 92-GT-122 (American Society of Mechanical Engineers, New York, 1992).
3. E. G. Jones and W. J. Balster, "Phenomenological Study of the Formation of Insolubles in a Jet-A Fuel," *Energy & Fuels* 7, 968 (1993).
4. B. B. Weiner, "Particle Sizing Using Photon Correlation Spectroscopy," in *Modern Methods of Particle Size Analysis*, H. G. Barth, Ed. (Wiley, New York, 1984), pp. 93-116.
5. B. J. Berne and R. Pecora, *Dynamic Light Scattering with Applications to Chemistry, Biology and Physics*, (Wiley, New York, 1976).
6. E. A. Klavetter, S. J. Martin, W. M. Trott, and T. J. O'Hern, "Advanced Thermally Stable, Coal-Derived, Jet Fuels Development Program Annual Report: Experiment System and Model Development," Wright Laboratory Report, WL-TR-94-2003, December 1993.
7. S. J. Martin, V. E. Granstaff, and G. C. Frye, "Characterization of a Quartz Crystal Microbalance with Simultaneous Mass and Liquid Loading," *Anal. Chem.* **63**, 2272 (1991).
8. E. A. Klavetter, S. J. Martin, and K. O. Wessendorf, "Monitoring Jet Fuel Thermal Stability Using a Quartz Crystal Microbalance," *Energy & Fuels* 7, 582 (1993).
9. S. Zabarnick, "Studies of Jet Fuel Thermal Stability and Oxidation Using a Quartz Crystal Microbalance and Pressure Measurements," *Ind. Eng. Chem. Res.* **33**, 1348 (1994).
10. S. Zabarnick and R. R. Grinstead, "Studies of Jet Fuel Additives Using the Quartz Crystal Microbalance and Pressure Monitoring at 140 °C," *Ind. Eng. Chem. Res.* **33**, 2771 (1994).
11. P. Russo, K. Guo, and L. Delong, "A New Look at Distribution Analysis of Dynamic Light Scattering Data, Using Only a Microcomputer," Society of Plastics Engineers, 46th Annual Technical Conference Proceedings, 1988, pp. 983-985.

Table 1: QCM Results in Jet A 91-POSF-2827

Test #	Sparge Gas	Confining Pressure	Temp. (C)	Deposition Rate ($\mu g\text{-}cm^{-2}\text{-}hr^{-1}$)
1	O_2	50 psig O_2	151	0.88
2	N_2	50 psig N_2	148	0.13
3	O_2	50 psig O_2	138	0.27
4	O_2	50 psig O_2	133	0.39
5	O_2	Ambient	133	0.63 (early) 0.15 (late)
6	O_2	Ambient	139	0.23

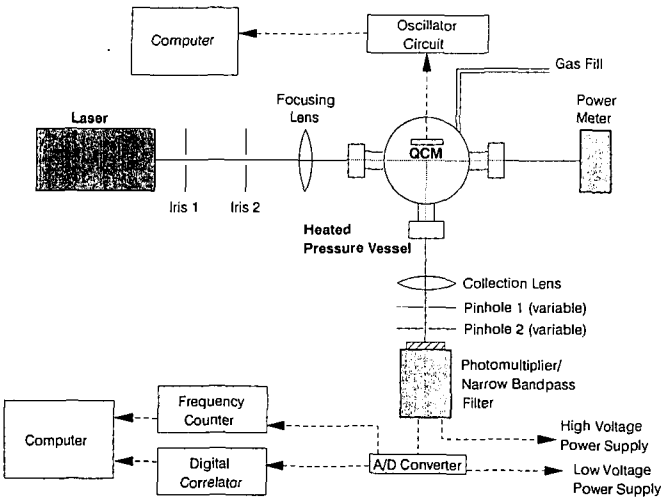

Figure 1. Schematic representation of integrated PCS/QCM system for studies of heated jet fuels.

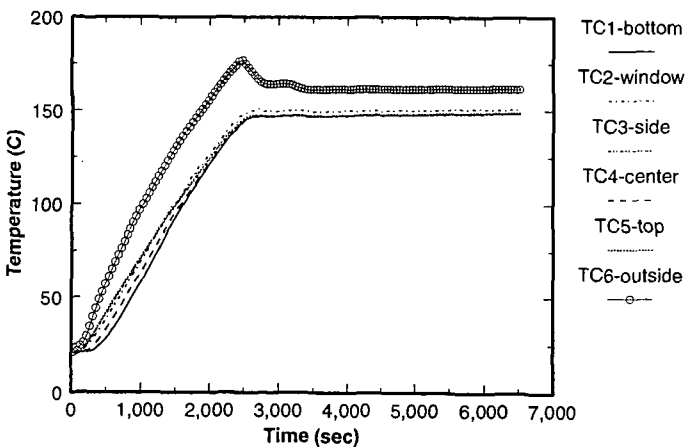

Figure 2. Temperature measurements at various points in the pressure vessel during heating of Jet A fuel. Target temperature was 150 C. Thermocouple locations are noted on legend.

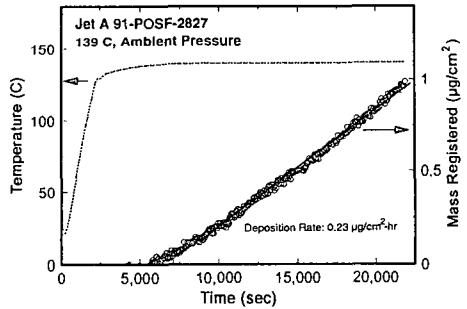

Figure 3. Mass deposition recorded by QCM in Jet A 91-POSF-2827 heated to 139 C. Test performed at ambient pressure. Temperature history in fuel is also shown.

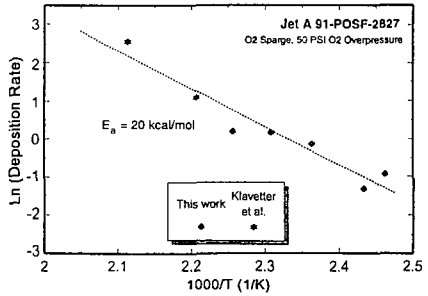

Figure 4. Arrhenius plot for Jet A 91-POSF-2827 tested at temperatures in the range 133-200 C.

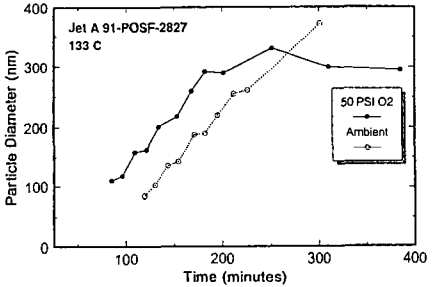

Figure 5. Particle growth measured by PCS for Jet A 91-POSF-2827 heated to 133 C. Tests conducted at two different pressure conditions.

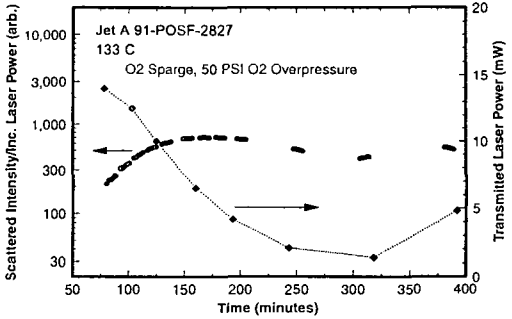

Figure 6. Normalized scattered light intensity (logarithmic scale) and transmitted laser power (linear scale) for Jet A 91-POSF-2827 heated to 133 C.

A NOVEL METHOD FOR THE DETERMINATION OF THE BOILING RANGE OF LIQUID FUELS BY THERMOGRAVIMETRIC ANALYSIS

He Huang, Keyu Wang, Shaojie Wang, M.T. Klein, and W.H. Calkins*
Center for Catalytic Science and Technology, Department of Chemical Engineering
University of Delaware, Newark, Delaware 19716

Key words: boiling range, liquid fuels, SimDis TGA

INTRODUCTION

The most widely used separation technique in the petroleum industry as well as in much of the chemical industry is distillation. This is particularly true of all liquid fuel production processes, including coal-derived liquid fuels, and shale oil as well as petroleum. To design and operate a suitable distillation column system requires a knowledge of the boiling point distribution of the materials to be separated. In recognition of this need, the ASTM developed the classical distillation procedures of ASTM D86, D216, D447, D850, and D1078. Since these methods required a relatively large sample and are not particularly precise, the widely used simulated distillation analysis based on gas chromatography (ASTM D3710-83) was introduced. This method requires only a small sample size and is reasonably rapid. However, it is limited to materials boiling below about 350°C. Above that temperature the column packing becomes unstable and the materials being analyzed tend to crack. Also the results measured by the SimDis GC method are determined by the interactions between the tested sample and the selected column packing. Therefore the GC method is not fundamentally a determination of the boiling range of the sample mixture but rather a measure of the range of interactions of the sample with the packing.

To avoid the limitation in the higher boiling range of the tested material in the SimDis GC method, Schwartz et al developed a capillary supercritical fluid chromatography (SFC) method (1). When the SFC is properly calibrated, it has been shown to be a suitable simulated distillation method, even for materials having atmospheric equivalent boiling points as high as 760 °C or 1400 °F. However this does not eliminate the problem of interactions of the sample with the packing material.

In their work, Schwartz et al also used both atmospheric "flow"thermogravimetric analysis (FTGA) and vacuum thermogravimetric analysis (VTGA) methods to distinguish between evaporation and thermal decomposition. They have observed a bimodal distribution of DTG (the rate of weight loss) on Arabian heavy atmospheric residue in both FTGA and VTGA runs. The first peak in the VTGA (about 0.2-0.5torr) profile is shifted towards lower temperature as compared with the FTGA profile since the sample vaporization was enhanced by a reduced pressure. However, the reduced pressure had no effect on the position of the second peak in the VTGA curve since the thermal decomposition or pyrolysis rate was not significantly affected by the reduced pressure. Therefore, the low temperature peak in each DTG curve is interpreted as the sample vaporization profile and the high temperature peak as the thermal decomposition or pyrolysis reactions.

In the investigation of the hydrocracking of high boiling coal derived vacuum resids, it became important to measure the degree to which the resids had been broken down to lower boiling products. This plus the importance of a simple, rapid, and accurate analytical distillation technique mentioned above motivated the development of an analytical TGA method for boiling range measurement, i.e. atmospheric equivalent boiling point (AEBP) curve, of a variety of samples. While supercritical chromatography was an alternative, the use of thermogravimetric analysis to determine the AEBP curve was an attractive approach. Such a SimDis TGA method would not be affected by interactions with column packing and not limited by sample boiling point range. Development of this novel SimDis TGA method and the preliminary results on a variety of samples are presented in this paper.

EXPERIMENTAL

TGA Apparatus. A horizontal thermogravimetric analyzer (TGA), TA Instruments model 51 (New Castle, Delaware), was used. In this particular instrument, dual thermocouples were used for the system temperature control. One is a furnace thermocouple and the other is a sample thermocouple, which is located very close to the test sample. The sample thermocouple is always used for the temperature measurements. Only the furnace thermocouple is used for control in the ramp method (constant heating rate). However, either the furnace thermocouple or the sample thermocouple can be used for isothermal control, depending on the purpose. If the "Isothermal" mode is selected, the

furnace thermocouple is used. On the other hand, if the "Isotrack" mode is selected, the sample thermocouple is used. The isotrack mode gives much better temperature control, for example, ± 0.01 to ± 0.05 °C for the range of 60 to 280 °C, compared to the Isothermal mode.

Nitrogen was used as an inert carrier gas at 100 ml/min volumetric flow rate. Vacuum TGA (VTGA) was carried out by attachment of the thermogravimetric analyzer to a vacuum pump. A vacuum gauge from 0-760 mmHg (0-1 atm.) range was used to monitor the pressure. After a sample was loaded onto the sample pan, the vacuum metering valve (shown in Figure 1) was gradually opened, and the pressure was adjusted to a predetermined value (down to 30 mmHg or 0.0395 atm). By this control and use of a ballast tank (buffer), the pressure (or vacuum) of the TGA chamber was found to be very stable during the VTGA analysis.

TGA Sample Pan. The SimDis TGA method requires a change in the conventional TGA sample pan because the rate of weight loss in the open pan system is controlled not only by the vapor pressure of the test sample but also by mass transfer. The TGA sample characteristics in the pan as well as the diffusion out constantly change with the sample amount as the TG analysis proceeds. For those reasons, a new sample pan configuration with a small aperture at the top, as shown in Figure 2, was devised. The objective of this change is to make the rate of the weight loss from the sample pan primarily determined by the partial pressure of the sample molecules. This partial pressure has been shown from thermodynamic considerations and experimentation to be essentially equal to the vapor pressure of the sample. Three cylindrical quartz TGA sample pans with different sizes of circular aperture at the top were fabricated. The diameters of the apertures were 0.615, 0.974, and 1.538 mm. In each TGA test, about 80 mg of liquid sample was injected into the sample pan by a syringe before the TG analysis.

SimDis TGA Methods. Analytical variables, such as carrier gas flow rate, pressure, and temperature or heating rate, were held constant during a TG analysis. Two methods, i.e., a ramp method and an isotrack method, have been used in the SimDis TGA technique. In the ramp method, a constant heating rate was used and the rate of the weight loss determined versus temperature. In the isotrack method, the temperature of the sample is very rapidly heated to a predetermined temperature within 2 minutes, and precisely controlled at this preset temperature within 0.01 to 0.05 °C after 5 minutes. The weight change and the DTG (the differential of the weight loss curve) decay are determined as a function of time.

Materials Studied. A light paraffinic vacuum distillate from Amoco and a converted resid liquid were used to test the SimDis TGA technique.

SimDis TGA Calibration. A SimDis TGA system can be calibrated by either a synthetic mixture which contains compounds of known boiling range or a 'standard' mixture for which distillation curves are available. In either case, the calibration sample should be similar to the sample for which the boiling range is to be determined. For the synthetic mixture, the paraffins, especially n-alkanes, provide a wide range of boiling components for calibration purposes. For the 'standard' mixture, any petroleum sample with known boiling range distribution could be selected. Some variation between samples of the same boiling point but different chemical structure are to be expected due to variation in molecular characteristics (such as molecular weight and shape) and heats and entropies of vaporization of the samples.

n-Alkane standards, C-10 to C-32, were purchased from Aldrich Chemical Co (Milwaukee, NJ). The SimDIS TGA was calibrated with a synthetic mixture of these n-alkane standards shown in Table 1.

SimDis TGA Data Processing. The smoothed and noise-free DTG curves were acquired by an 11 point smoothing technique (2).

RESULTS AND DISCUSSION

Strategies for Selection of the Optimum Method for Determining Boiling Point Range of an Unknown Sample. The analytical variables of the SimDis TGA technique include: 1). time-temperature profile: ramp method or isotrack method; 2). pressure: atmospheric pressure or under vacuum (down to 0.03 atm.); 3). size of the aperture at the top of the pan; and 4). carrier gas type and flow rate.

For a pure compound, SimDis TGA can be run using either the ramp or isotrack method. For an unknown mixture, the ramp method provides information concerning the vaporization range of the sample. If run under at least two pressures (vacuum), it can distinguish quantitatively between the material boiling so high that pyrolysis will occur and that fraction volatilizing under distillation conditions.

To accurately obtain the boiling range curve for a mixture, the isotrack method is the preferred technique. This method translates the decay of the rate of weight loss into the boiling point distribution. Therefore, the optimum conditions to run a simulated distillation by TGA are those conditions which give the highest sensitivity and stable decay curve. To accomplish this, the optimum conditions for a SimDis TGA run is dependent on the boiling range of the test sample. For example, for light samples, it is better to run the SimDis TGA at a low isotrack temperature, small hole size of pan, and atmospheric pressure. For very high boiling mixtures, SimDis TGA should be run at a higher isotrack temperature, larger hole size of pan, and high vacuum (for example, 30 mmHg). For a mixture containing a very broad boiling range, the test can be run at either more than one temperature or more than one pressure (vacuum) or both to detect the very volatile fraction as well as the higher boiling components.

The recommended general steps to run an unknown sample using the SimDis TGA technique are:

1). ramp at 1 to 5 °C/min to 600 °C at 1 atm and/or under vacuum (down to ca. 0.03 atm.) at 100 cm^3/min N_2. Oxygen is then introduced to burn off the combustible material remaining (if any). In this run, IBP (Initial Boiling Point), FBP (Final Boiling Point) and/or PT (Pyrolysis Temperature), the boiling range and volatile fraction, and ash fraction (if any) are determined.

2). based on the results obtained from Step 1, select the optimum conditions of aperture size of pan, isotrack temperature, pressure, etc. to run a SimDis TGA.

SimDis TGA by the Ramp Method. Typical DTG curves from SimDis TGA runs using the ramp method at two pressures on a light paraffinic vacuum distillate from Amoco are shown in Figure 3. The rate-of-weight-loss curves show a distinct shift to lower temperatures as the pressure is reduced. No pyrolysis is evident in this determination since the DTG curve is entirely shifted under vacuum. The volatilization range for this sample at atmospheric pressure is between about 200°C and 470 °C. Under the vacuum of 0.238 atm., it is shifted to between about 180°C and 420 °C. The volatilization ranges are somewhat lower than the actual boiling range because of the nitrogen gas sweep and controlled diffusion.

SimDis TGA Calibration. Temperature-time plot for a calibration run using a synthetic mixture of hydrocarbons of C_{10} to C_{32} is shown in Figure 4. The predetermined isotrack temperature was 280 °C. The DTG decay curve for this calibration is shown in Figure 5. Although the temperature of the sample reached the predetermined temperature of 280 °C within 2 minutes, the loss of the light fractions in the synthetic mixture, such as C_{10} and C_{15}, occurred before the temperature became stable. In other words, the light fractions in the synthetic mixture of C_{10} and C_{15} were evolved from the sample pan within this initial 2-5 minutes. This is clearly illustrated in Figures 6 and 7, the plot of wt% of sample in the pan vs. temperature and wt% of sample in the pan vs. DTG decay, respectively. From the concentrations of the C_{10}-C_{32} components in the synthetic mixture given in Table 1, we can find the rates of weight loss at which the components were evolved from the pan. The plot which describes a linear relationship of log (rate of weight loss) vs $1/T_b$ (T_b, the boiling point of C_{20}-C_{32}) is shown in Figure 8, in accordance with the Clausius-Clapeyron equation. This shows that the DTG decay determined by TGA technique is indeed measuring the vapor pressure and therefore boiling range.

SimDis TGA Test. For a mixture containing a wide range of boiling materials, such as the light paraffinic vacuum distillate from Amoco, the DTG decay determined under the same conditions of running the calibration mixture can be translated into a boiling range distribution using the equation of

$$T_b = \frac{B}{\ln(r) - A} \qquad (1)$$

where r is the decay rate of the test sample and A and B are parameters determined by calibration (for this case, A = -21.06 and B = 12778).

Temperature-time plot for the test sample of the light paraffinic vacuum distillate is similar to that as shown in Figure 4. The DTG decay curve is shown in Figure 9. Although the temperature of the sample reached the predetermined temperature of 280 °C within 2 minutes, the 10 wt% of light fractions in the vacuum distillate were lost before the temperature became stable, i.e., the 10 wt% of light fractions in the vacuum distillate were evolved from the pan within this initial 2-5 minutes. This is clearly illustrated in Figure 10, the plot of wt% of sample in the pan vs. temperature. The simulated distillation curve for this vacuum distillate is shown in Figure 11.

A simulated distillation run by the isotrack method has been made on a sample of Wilsonville # 258 resid converted using sulfided molybdenum naphthenate at 403°C for 60 minutes. The boiling range curve derived from the DTG decay of this sample is shown in Figure 12. The fraction of material in which the product boiled below 850 °F (the cut-off point for resid) was 93.8 wt% (including tetralin fraction).

Advantages of the SimDis TGA Method. The most significant advantages to using the TGA technique for simulated distillation are:

1). SimDis TGA is run at much lower temperature than other techniques, especially if combined with vacuum.
2). there is no limitation to the sample type. The sample can be very light or very heavy. Even a sample with a very wide range of boiling materials can be tested by this technique.
3). Highly reproducible results can be obtained. The experimental cycle for one run can be 1 to 12 hrs, depending on sample and purpose. No cleaning is required as would be necessary in a distillation column.
4). Very small amounts of sample (30-80 mg) are required for each SimDis TGA run;
5). The SimDis TGA method measures the true boiling characteristics of the sample and is not affected by interactions between the test sample and packing, as is the case with the chromatographic methods.

SUMMARY AND CONCLUSIONS

1. Two analytical methods (a ramp and an isotrack method) have been developed for determining the boiling range of an unknown sample based on the use of thermogravimetric analysis.

2. These methods require the use of a special cylindrical sample pan with a small hole in the top to control the rate of weight loss (diffusion of the sample vapors exiting the pan). Under these conditions, the diffusion rate is proportional to the vapor pressure of the sample at the particular temperature of the analysis.

3. For screening an unknown sample, the "ramp method" is used in which the temperature of the sample is increased at a predetermined rate while holding the purge gas flow rate constant. The temperature range of volatilization is measured. If high boiling material is present which involves pyrolysis of the sample rather than only volatilization, a similar "ramp method" is run under vacuum. This indicates which portion of the sample is volatilized and what portion is pyrolyzed under the conditions of the test.

4. For more precise determination of the boiling range of a sample, the isotrack method is used. In this method, the sample is rapidly heated to a predetermined temperature and then held constant while the rate of weight loss (DTG) is measured. When the system is properly calibrated with a known sample, the rate of weight loss (DTG decay) can be translated by a computer program into an actual boiling range.

ACKNOWLEDGEMENTS

The support of this work by the subcontract from CONSOL under DOE Contract DE-AC22-94PC93054 and by the Department of Energy under DE22-93PC93205 is acknowledged. Helpful discussions with F.P. Burke, R.A. Winschel, and S.D. Brandes are gratefully acknowledged. Additional funds for purchase of thermal analysis equipment was provided by the University of Delaware.

REFERENCES

1. Schwartz, H.E.; Brownlee, R.G.; Boduszynski, M.; Su, F. *Anal. Chem.* 1987, 59, 1393.
2. Wang, Keyu; Huang, H.; Wang, S.; Klein, M.T.; Calkins, W.H.* "A Novel Smoothing Technique for Thermogravimetric Analysis Data", to be submitted to *Anal. Chem.*

Table 1 Concentrations and properties of the C_{10}-C_{32} components in the synthetic mixture

No. of Carbon	Name	MW	b.p.,°C	m.p.,°C	W, g	C, wt%
10	Decane	142.28	174.1	-29.7	1.2298	18.26%
15	Pentadecane	212.41	270.6	10.0	1.2068	17.92%
20	Eicosane	282.54	343.0	36.8	1.1238	16.69%
25	Pentacosane	352.67	401.9	55.0	1.0716	15.91%
30	Triacontane	422.80	449.7	65.8	1.0402	15.45%
32	Dotriacontane	450.85	467.0	69.7	1.0618	15.77%

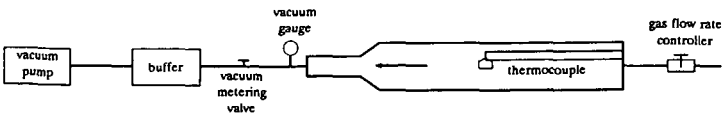

Figure 1 Instrumentation of vacuum thermogravimetric analyzer (VTGA)

Figure 2 A SimDis TGA sample pan

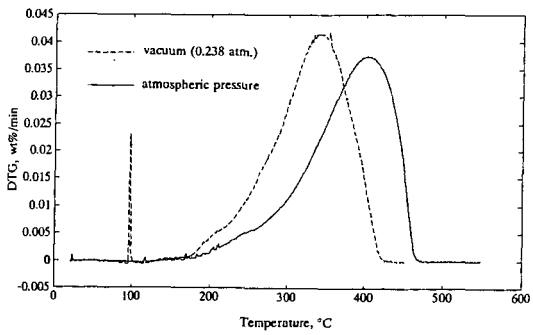

Figure 3 DTG curves from SimDis TGA runs using the ramp method at two pressures on a light paraffinic vacuum distillate from Amoco

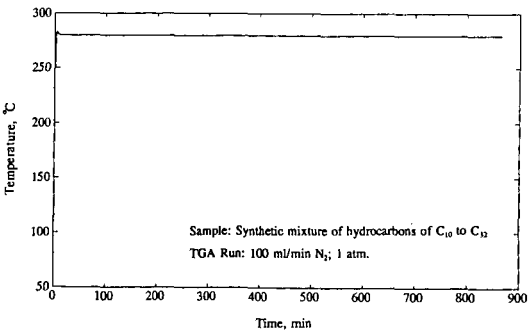

Figure 4 Temperature-time plot for the calibration sample of a synthetic mixture of n-alkanes

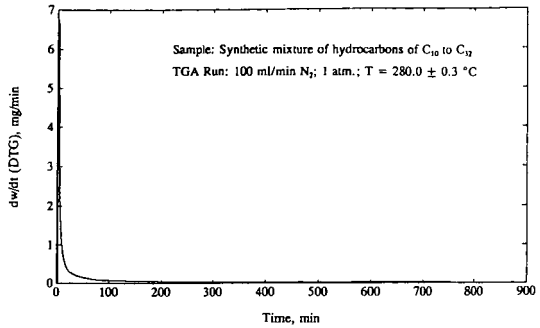

Figure 5 DTG decay curve for the calibration run

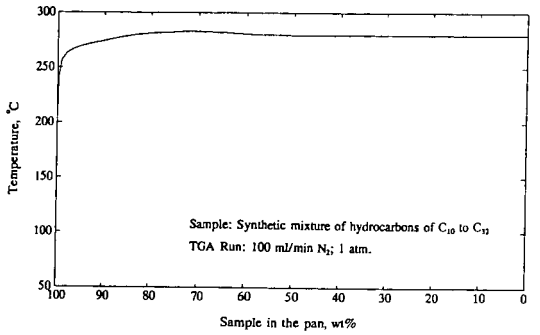

Figure 6 Plot of wt% sample in the pan vs. temperature for the calibration run

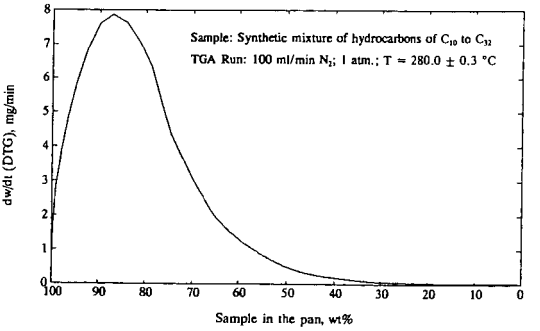

Figure 7 Plot of wt% sample in the pan vs. DTG decay for the calibration run

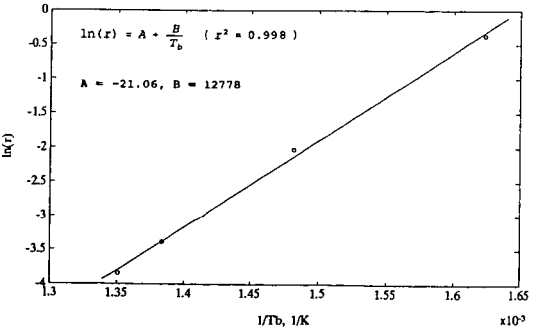

Figure 8 ln(r) vs. $1/T_b$ (r: rate of weight loss; T_b: boiling point of C_{20}-C_{32})

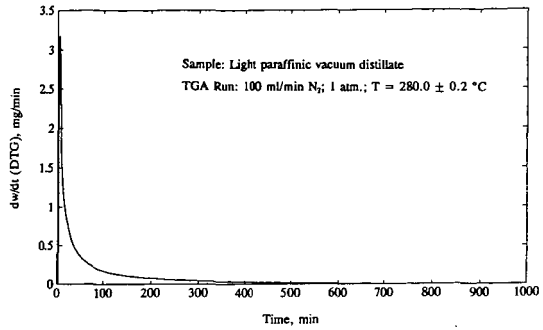

Figure 9 DTG decay curve for the light paraffinic vacuum distillate

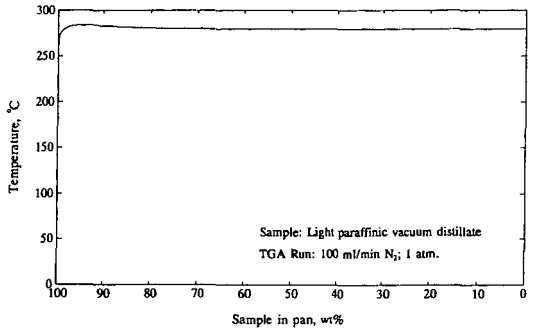

Figure 10 Plot of wt% sample in the pan vs. temperature for the light paraffinic vacuum distillate

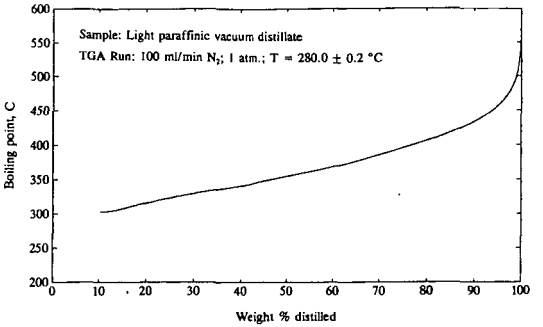

Figure 11 Simulated distillation curve (AEBP) for the light paraffinic vacuum distillate

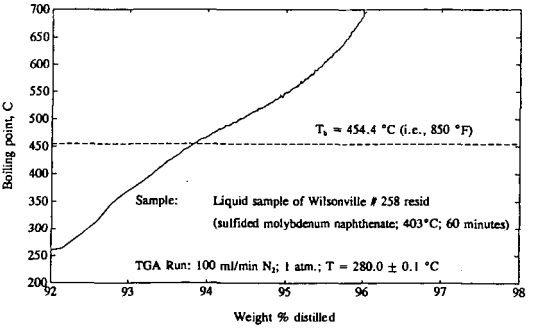

Figure 12 Simulated distillation curve (AEBP) for the liquid sample of a resid conversion run under 1500 psig H_2

Cloud Point Determination Using a Thickness Shear Mode Resonator

James J. Spates[1], Stephen J. Martin[2], Arthur J. Mansure[2], and Jeffrey W. Germer[3]

[1]Ktech Corporation, Albuquerque, NM 87110
[2]Sandia National Laboratories, Albuquerque, NM 87185
[3]Petrolite Corporation, St. Louis, MO 63119

Keywords: cloud point, thickness shear mode resonator, viscosity

Introduction

Crude oils and crude oil products contain substantial amounts of petroleum waxes, consisting of a distribution of high molecular weight hydrocarbons. These waxes or paraffins have limited solubility in oil and tend to precipitate out at a temperature determined by the concentration and constituents of the wax. Precipitation and deposition of wax results in narrowing of pipelines, making crude oil recovery difficult.

A parameter of practical importance is the wax precipitation temperature, traditionally known as the *cloud point*, at which visible crystallization occurs. Deposition problems arise in oil field operations at or below this temperature. Several techniques can be used to determine the cloud point [1]: (1) visual observation, (2) viscosity measurement, (3) differential thermal analysis, and (4) pulsed nuclear magnetic resonance.

In this paper we describe a new technique for measuring cloud point based on measuring properties of the fluid and accumulated deposit using a quartz resonator. The thickness shear mode (TSM) resonator consists of a thin, highly polished disk of AT-cut quartz with circular electrodes on both sides (Figure 1). Applying an RF signal to the electrodes causes the piezoelectric quartz crystal to be excited into a shear mode of vibration in which crystal faces undergo in-plane displacement.

The TSM resonator is instrumented as a sensor by incorporating it as the frequency-control element of an oscillator circuit. Wessendorf [2] has described an oscillator circuit capable of exciting the crystal in liquid media. This oscillator tracks the resonant frequency of the crystal and has level-control circuitry to measure the amplitude of the oscillation voltage; it provides a feedback voltage to maintain this at constant level. The level control compensates for changes in resonator damping caused by (1) changes in the viscosity of the contacting fluid and/or (2) deposits that form on the crystal. Since both of these changes occur with oil at the cloud point, the feedback voltage is a good indicator of the cloud point.

When a TSM resonator operates in contact with a fluid, the shear motion of the surface radiates a critically damped shear wave into the contacting fluid (Fig. 2). This mechanical coupling causes both a change in stored and dissipated energy in the crystal, leading to a change in resonant frequency and crystal damping (oscillator feedback voltage). Kanawaza and Gordon showed that resonant frequency decreases proportionally with $(\rho\eta)^{1/2}$, where ρ and η are liquid density and viscosity, respectively [3]. The change in crystal damping or feedback voltage due to liquid contact is also proportional to $(\rho\eta)^{1/2}$ [4].

A rigid film deposited onto the resonator surface moves synchronously with the oscillating surface. This causes a change in the stored (kinetic) energy of the resonator. This results in a decrease in resonant frequency proportional to the areal mass density (density times thickness) contributed by the layer [5]. Since moving the rigid layer does not result in dissipation of energy, however, there is no change in crystal damping or oscillator feedback voltage.

A compliant film deposited on the resonator surface behaves differently than a rigid one. While the lower film surface moves synchronously with the resonator surface, the upper film region may lag behind [6]. This induces a shear strain in the film. Since compliant films are typically viscoelastic, i.e., having both elastic and viscous character, strain in the film leads to both energy storage and dissipation. As the thickness of the compliant film increases, it initially leads to a decrease in resonant frequency; at larger

thicknesses, however, the film causes an increase in frequency [6]. Thus, frequency alone is not a good indicator of deposit thickness. Initially, the feedback voltage increases with film thickness; at larger thicknesses, voltage tends to saturate. At the cloud point, the precipitation of wax results in both a change in the viscosity of the fluid, as well as formation of a viscoelastic deposit on the resonator surface. Since both effects lead to an increase in crystal damping, this parameter is a good indicator of the cloud point.

System Description

Figure 3 is a block diagram describing the cloud point detector system. The system consists of a test cell and peripheral equipment for temperature control and data acquisition. The temperature controller allows sample temperature to be easily varied to determine the cloud point of the test fluid. The data acquisition system is made up of a voltmeter (HP 3478A), frequency counter (HP 5384A), and scanning thermometer (Keithley 740). A personal computer acquires data from these instruments.

The test cell, shown in Fig. 4, has two parts: the cell body and the cell head. The cell body holds a glass sample cup with a volume of 25 cm^3. The body, made of stainless steel, has thermoelectric coolers on each of the four vertical surfaces. Heat sinks are attached to the coolers so that waste heat can be efficiently transferred to the room air, facilitated by a fan. The thermoelectric units heat and cool samples over the range of 5°C to 85°C. A stir bar is inserted in the sample cup to maintain sample uniformity; this is driven magnetically from below. The cell body also contains an o-ring seal on the surface that maintains pressure and prevents the loss of the more volatile sample constituents. Overpressurization is prevented by a 100 psi pressure-relief valve.

The cell head includes the sensor, oscillator, a thermocouple, and electrical connectors to output the oscillator frequency and feedback voltage. The electrical connector that holds the sensor was designed to allow rapid sensor changeout.

Experimental Section

A clean and dry TSM resonator was installed in the cell head and reference measurements were made of the resonant frequency and oscillator feedback voltage. A crude oil simulant, consisting of Shell wax 300 and kerosene, was then placed in the test cell at room temperature. The lid, with sensor attached, was bolted onto the cell, sealing the test volume. At the start of a test, the cell temperature was elevated to 80°C. After the temperature stabilized, the controller was set for a certain cooling rate and final temperature; data acquisition was initiated.

The cloud point of the sample was also determined by visual observation. This was done by placing a mirror beneath the sample cup and observing a change in clarity as the sample was cooled. The sample was initially heated to 80°C and then cooled to 40 °C with the lid on to contain volatile components. The lid was removed at 40°C so that the cloud point could be observed.

Figure 5 shows the change in oscillator feedback voltage and resonant frequency vs. temperature for two different cooling rates for a wax/kerosene sample. A dashed line indicates the visually-determined cloud point at an intermediate cooling rate of 1°C/min. The oscillator damping voltage, in particular, shows an abrupt increase at the visually-observed cloud point due to the onset of wax precipitation. This is due to increased resonator damping from a combination of increased fluid viscosity and wax depositing on the resonator. The resonant frequency also shows an abrupt change at the cloud point. It is clear that the best indication of cloud point (i.e., agreement with visual observation) obtained from the resonator measurement is the point at which the damping voltage first changes slope during cooling.

The cloud point determined from resonator measurements is slightly higher for the lower cooling rate. This is to be expected since the lower rate provides more time for the nucleation of wax crystals to occur. Below the cloud point, the responses are quite dependent upon the cooling rate. This may be due to a dependence of the crystal properties on the cooling rate. Graham [7] has noted that slower cooling rates lead to crystals that are larger, more irregularly-shaped, and more aggregated.

Figure 6 shows the change in oscillator feedback voltage and resonant frequency vs.

temperature for two wax concentrations. The samples are both cooled at a rate of 1°C/min. The "original" sample shows a cloud point of 34.4°C, while the sample with added wax shows a cloud point of 36.6°C. As expected, the higher concentration of wax precipitates out at a higher temperature. The oscillator voltage clearly indicates the onset of wax precipitation in each case. The oscillation frequency shows a more complicated behavior, resulting from the fact that oscillation frequency initially decreases with accumulated layer thickness, then increases.

Conclusion

The resonator exhibits large responses in both oscillator feedback voltage and resonant frequency at the cloud point. The temperature at which the feedback voltage first changes slope during the cooling process is an indication of cloud point that is consistent with visual determination. This technique is less subjective and operator dependent than visual means and works equally well with opaque samples. Moreover, since the resonator operates at extremely low shear rates, it perturbs the sample less than a rotating-cup viscometer.

Acknowledgements

The authors are grateful for assistance from J. E. Miller, R. S. Sandoval, R. W. Cernosek, K. O. Wessendorf, and T. W. Schneider of Sandia National Laboratories. This work was performed at Sandia National Laboratories, supported by the U.S. Department of Energy under contract No. DE-AC04-94AL85000.

References

[1] Newberry, M. D., *SPE Production Engineering* (SPE#11561), 151.

[2] Wessendorf, K. O. *Proc. 1993 Frequency Control Symp.* (IEEE, New York, 1993) pp. 711-717.

[3] Kanazawa, K. K.; Gordon II, J. G. *Anal. Chem.* **1985**, *57*, 1770-1771.

[4] Martin, S. J.; Frye, G. C.; Wessendorf, K. O. *Sensors and Actuators A* **1994**, *44*, 209-218.

[5] Sauerbrey, G. Z. *Phys.* **1959**, *155*, 206-222.

[6] Martin, S. J.; Frye, G. C. *Proc. 1991 Ultrasonics Symposium*, (IEEE, New York, 1991), 393-398.

[7] Graham, D. E.; Stockwell, A.; Thompson, D. G. *Chemicals in the Oil Industry* (Royal Society of Chemistry, 1983) Special Publication no. 45.

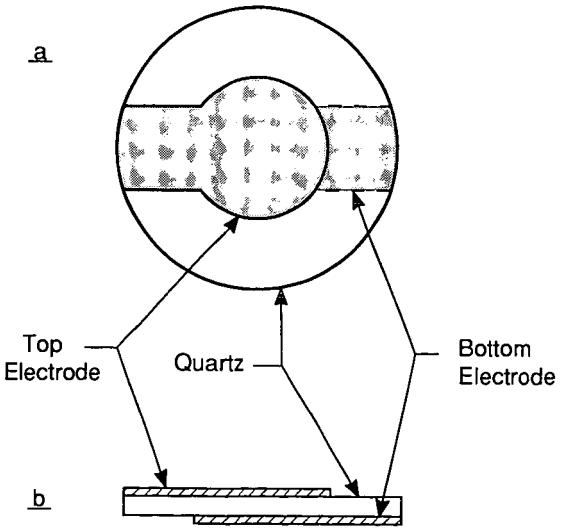

Fig. 1. *Top (a) and side (b) views of a quartz thickness shear mode (TSM) resonator.*

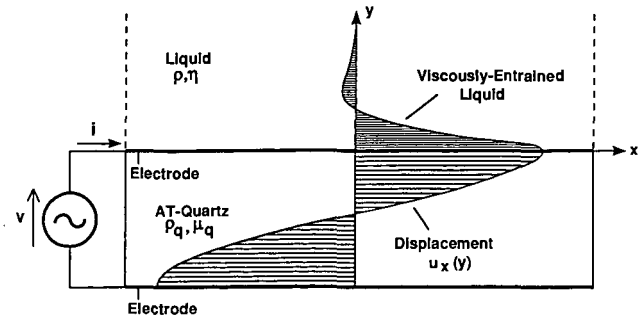

Fig. 2. *Cross-sectional view of a smooth TSM resonator with the upper surface contacted by a liquid. Shear motion of the smooth surface causes a thin layer of the contacting liquid to be vicously entrained.*

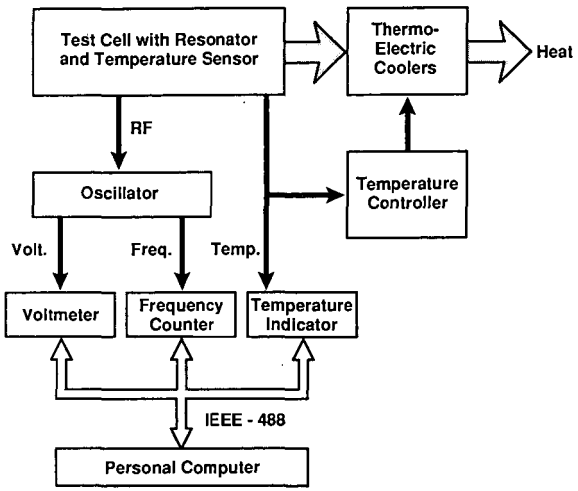

Fig. 3. *Block diagram of the cloud point detector system used for TSM resonator and visual cloud point determinations.*

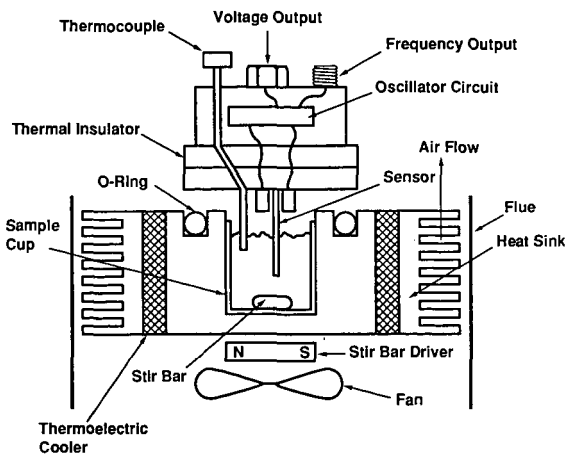

Fig. 4. *Cloud point detector test cell with TSM resonator (sensor), oscillator circuit, thermocouple, sample cup, stir bar with driver, thermoelectric coolers, heat sinks and fan.*

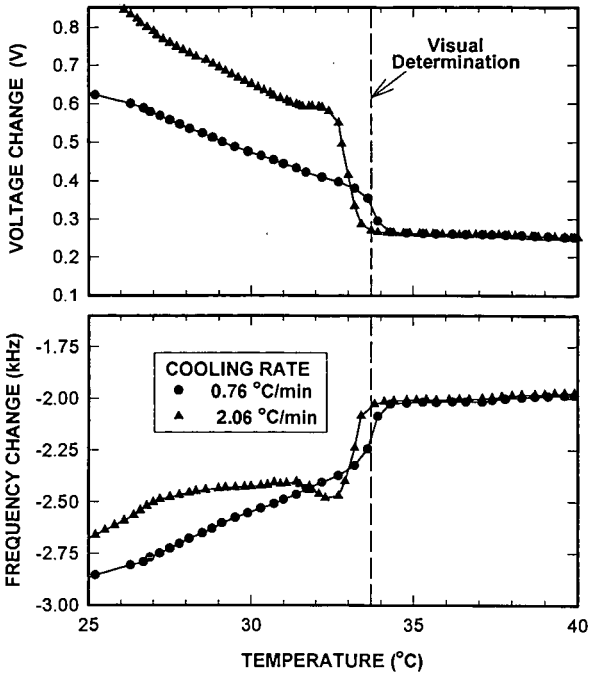

Fig. 5. *Voltage change and frequency change measurements of TSM resonator vs.temperature for a Shell wax 300/kerosene mixture cooled at two rates. Dashed line indicates the visually determined cloud point.*

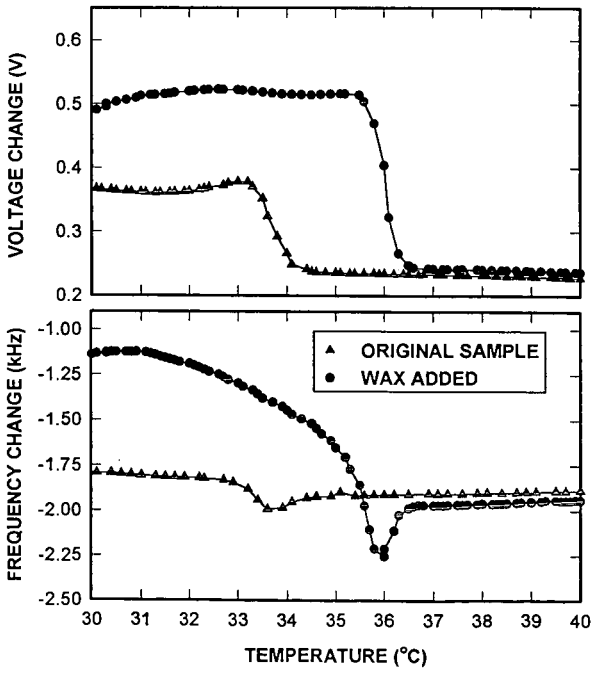

Fig. 6. *Voltage change and frequency change measurements of TSM resonantor for two different Shell wax 300/kerosene concentrations cooled at the same rate.*

CHARACTERIZATION OF PETROLEUM RESID COMPONENTS FRACTIONATED BY HIGH VACUUM SHORT-PATH DISTILLATION AND GEL PERMEATION CHROMATOGRAPHY

Frank Sen-Chun Lee
Department of Chemistry
Hong Kong Baptist University
Kowloon, Hong Kong

Keywords: petroleum resids; heavy oils; hydrocarbon type analysis

INTRODUCTION

The traditional cut point between distillable oils and resids by vacuum distillation is 1000°C. The recent advent of high vacuum, short-path distillation (DISTACT molecular still) makes it possible to cut deeper into resid components (see references cited in ref 1). By varying the wall temperature and pressure of the DISTACT unit, the 1000+°F resid components can be further cut into narrow boiling fractions up to an atmospheric equivalent end point of about 1350°F. In this study, this additional resid components distillable between 1000 and 1350°F was fractionated and characterized. Furthermore, the asphaltenes in the bottom material were separated into molecular weight cuts by GPC (Gel permeation Chromatography). Such fractionation scheme allows us to compare systematically the composition and properties of the full range petroleum resid components as a function of AEBP (Atmospheric Equivalent Boiling Point) or molecular weight.

EXPERIEMNTAL

The two feedstocks used in this study were both high sulfur 1000+°F petroleum vacuum resids originated from different crude blends. The two are similar in general properties as shown in Table 1. The DISTACT fractionation scheme is illustrated in Figure 1, which lists the different temperature and pressure combinations used to cut the different boiling fractions. The AEBPs of the fractions were measured by GC simulated distillation. The GPC separation was carried out on a Waters GPC system using a set of Water Styregel columns arranging in the order of 60, 100, 100 and 500 A pore sizes. The dimensions of each of the columns were 7 mm i.d. and 100 cm long. The elution solvent was tetrahydrofuran and the flow rate was 5 ml/min. Multiple runs were made in order to collect sufficient material for characterization. The VPO (Vapor Pressure Osmometry) measurement were made in nitrobenzene solvent at 120°C, using infinite dilution method.

Three LC (Liquid Chromatographic) procedures were used for compound type separation. The IX (Ion Exchange) separation used two sequentially connected columns each packed with anion (MP 1 resin for trapping acids) or cation (MP 50 resin for trapping bases) exchange resins obtained from Biorad. The neutrals were eluted by toluene from the column sequence while the acidic and basic material were desorbed from their respective columns by isopropanol/toluene solvent mixed with minor amounts of formic acids or isopropylamine, respectively. The ABN (Acid/Base/Neutral) separation by alumina LC was carried out on two sequentially connected columns packed with acidic (for trapping bases) and basic (for trapping acids and pyrrolics) alumina, respectively. The neutrals were eluted from the column sequence by cyclohexane (neutral I) and toluene (Neutral II). Afterwards, the two columns were disconnected and the pyrrolics in the basic alumina column was first eluted by dichloromethane. Finally, a mixture of dichloromethane and methanol was used to elute the acids and bases from their respective columns. In ORA separation, the asphaltenes and maltenes were first separated by hexane dissolution. The maltenes were then separated by Silica Gel LC into oil and resin fractions.

The NMR hydrocarbon analysis was based on data from combined H-1 and C-13 solution NMR analysis using the Brown-Lader model (2).

RESULTS AND DISCUSSION

1. Properties of DISTACT fractions: The boiling curves of the fractions from GC simulated distillation are shown in Figure 2. In Table 2, the wt % yield and the boiling ranges are listed. The BP data show a progressive increase in boiling range from the lighter to the heavier fractions, indicating the validity of the DISTACT distillation technique in terms of BP separation. The four distillable fractions from O3 through O6 account for 61% of the total resid material, with their T50 temperature (temperature at which 50 wt% is distillable) increases regularly from 840, 980, 1080 to 1090°F. The end points of the two bottom cuts, R1 and R2, are both above 1400°F. Their T50 points are in the 1320-1350°F range. Overall, about 80 wt% of the total 1000+°F resid mass is DISTACT distillables.

The ORA yield and elemental composition in Tables 3 and 4 indicate that as the BP of the fractions increases, the H/C ratio decreases and the concentrations of asphaltenes, Rams carbon and heteroatoms increase regularly. On a resid feed basis, the four distillate fractions account for 16% of the Ramscarbon, 29% N, 43% S and 10-12% Ni/V. Thus, while the higher cut point of the DISTACT technique significant increases the distillable yield, it also allows the carryover of significant amounts of catalyst poisons.

The MW data for the DISTACT fractions are listed in Table 8 along with the NMR results to be discussed later. The number average MWs of the fractions obtained by GPC and VPO agree very well. The MW increases regularly from 400 for fraction O6 to 8-900 for O3 and 14-1500 for the bottom fraction R1, in the same direction as the BP.

2. Compound Type Separation: The compound type distribution of the DISTACT distillables was studied by IX and Alumina ABN separation using resid B as the sample. In both cases, a "normal" and a "reversed" column separation procedures were carried out. The yield distribution and the elemental composition of the fractions from the two separations are summarized in Tables 5 (IX) and 6 (Alumina). In IX separation, the total mass recovery is 98% in the normal sequence and only 93.7 % in the reversed one, indicating small material losses due to irreversible adsorption by IX resins, especially the cation IX resin. The mass recovery in the alumina separation is essentially quantitative irrespective of the column sequence. The yield of the total polar material (acids plus bases) in alumina separation is lower than those of IX (12-13 vs 18-20%). Furthermore, the alumina LC gives similar acid/base yield distributions after column switching whereas different results were obtained in the IX case. It is likely that the IX resins adsorb significant amounts of extra high MW polyaromatics in addition to the N/O containing polar species because of their high adsorptivities. This extra material can locate themselves in either the acid or base fractions depending on the order of the columns.

Based on the more consistent alumina ABN separation, the neutral material amounts to about 88-90% of the total distillables. The three polar fractions--pyrrolics, acids and bases--account for only 10-12% of the total mass but 98-99% of the total N and metals. The S is more evenly distributed (IX results). The low H/C ratios of the polar fractions (1.0-1.3) indicate their highly aromatic nature. The MWs of the ABN fractions differ only slightly: 570 for neutrals compared to 580-600 for acids and bases. The order is consistent with the BP curves as shown on the right of Figure 2.

The highly functionalized structure of the three polar fractions are evidenced from their FTIR spectra shown in Figure 3. The pyrrolic fraction shows a strong band around 3500 cm^{-1}, indicative of N-H absorption. The acids show a series of bands from 3400-3650 cm^{-1}, indicative of phenolic O-H with varying extent of H bondings. All three polar fractions distinguish themselves from the two neutral fractions by their prominent carbonyl absorption bands around 1650-1750 cm^{-1}. The pyrrolics and the bases also show the aromatic C-C and C-N bands around 1550-1620 cm^{-1}, suggesting the presence of N in the ring systems. On the other hand, the spectra of the two neutral fractions show only typical hydrocarbon structure free of any heteroatom functionalities.

In Table 7, the MW, % aromatic C, MW and ABN yield distribution between the gas oils and the DISTACT distillates are compared.

3. NMR Average Structure: The polyaromatic structure of the DISTACT fractions were determined by combined C-13 and H-1 NMR analyses using the improved Brown-Lader model (2). The model assumes that all the molecules being analyzed are aromatic with the aliphatics present only as side chains on the polyaromatic core. Thus, before NMR analysis, the aliphatics in the ABN neutrals of the DISTACT fractions were further separated by Silica Gel LC. Such separation showed that the DISTACT bottom fractions (R1 and R2) contain only 0.04-0.05 wt% of pure aliphatic components. In the distillate portion, the aliphatics in the four lighter fractions O4 through O6 is less than 5%, but as much as 41% was found in the heaviest fraction O3.

Table 8 lists the NMR-derived average molecular structural parameters for the DISTACT fractions of resid A. The C_A increases smoothly from 21.4 to 36.9% with increasing boiling range of the fractions. The cluster ring number (number of aromatic rings in the polyaromatic core) also increases with boiling range from an average of 1.6 rings for O6 to 5.4 rings for the heaviest fraction R1. The cluster weights of the average molecule in the fractions are compared with their

corresponding MWs measured by VPO and GPC. For the four distillate fractions 03 through 06, the cluster weight and the MW for each fraction is fairly close. Within the uncertainties of the average structure determinations, the data suggest that the molecules in the distillates on the average contain only one cluster. This is opposed to the residue fraction R1 where the MW is about twice that of the cluster weight. Thus, the average molecule in R1 contains about 2 clusters.

4. Asphaltenes: Asphaltenes represent the heaviest component in resids. As shown earlier, nearly all the asphaltenes are in the DISTACT bottom material. The asphaltenes in the DISTACT bottom of resid B was fractionated by GPC into seven MW fractions. Essentially quantitative mass recovery was observed in GPC separations.

The MW of the separated fractions were further determined by both VPO and analytical GPC. The yield distribution, elemental composition, MW and NMR derived structural parameters of the GPC fractions are summarized in Table 9. The data show that the major differences among the different fractions are MW and NMR structure parameters, while the elemental and metal concentrations are grossly similar. The MW increases smoothly from less than 620 for the lightest cut 7 to 50-5100 for the two heaviest cuts 1 and 2.

The NMR data show that about 55 wt% of the asphaltenes (sum of cuts 4 through 7) has an average cluster size of 4-6 rings. The total of cuts 2 and 3, which account for 35% of the asphaltenes, has about 6-7 rings. The heaviest asphaltenes (cut 1), which accounts for 10 wt% of the total asphaltenes and 1.2 wt% of the resid mass, has an average of 14 rings. Comparing the cluster weight with the MW of the fractions, it is seen that all but fraction 6 have multiple clusters per average molecule. The number of clusters per molecule increases with the MW of the fractions from 3-4 clusters for fractions 4 and 5 to 6-10 clusters for fractions 2 and 3. The heaviest fraction 1 has the highest number of rings per cluster (14) but only 5 clusters per average molecule.

SUMMARY

The composition and properties of resid components as a function of increasing BP or MW are compared in Table 10. Results show satisfactory BP separation of the maltenes by DISTACT and MW separation of the asphaltenes by GPC. A comparison among the properties of gas oils, DISTACT fractions and GPC MW cuts show that there is a continuous and smooth increase of aromaticity, polarity and NMR derived polyaromatic cluster size with BP or MW. The same compound types exist in different boiling fractions but the relative amounts of the different types change with BP. The commonly suggested "structural discontinuity" between asphaltenes and other heavy oil components is not apparent except for the heaviest asphaltene fractions, which account for about 1.2 wt% of the total resid mass. However, the analytical data for this fractions of heavy and highly polar material remain questionable because of their reactive nature.

REFERENCES

1. Boduszynski, M.M., Energy and Fuels (1988) 2, 597-613; (1987) 1, 2-11 and the references therein.
2. Hasan, M.A., M.F. Ali and A. Bulchar (1983) Fuel, 62, 518 and the references therein.

ACKNOWLEDGEMENT

The experimental work of this paper was carried out when the author was working at Amoco Research Center of Amoco Corporation in Naperville, IL. The author would like to express his sincere appreciation to Amoco for supporting this research, and the many capable colleagues who helped me on this project including in particular Mr. Al Hensley, Dr. L. J. Duffy, Mr. Wayland Chan, Dr. Om Mahajan, Dr. Naresh Sethi, Mr. D. Maciejewski and Dr. R. L. Ollendorff.

Figure 1. DISTACT Fractionation Scheme

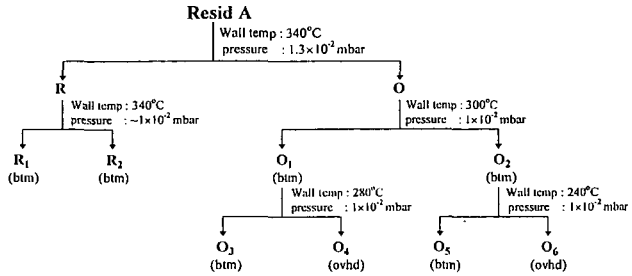

Figure 2. GC Simulated Distribution of DISTACT Fractions

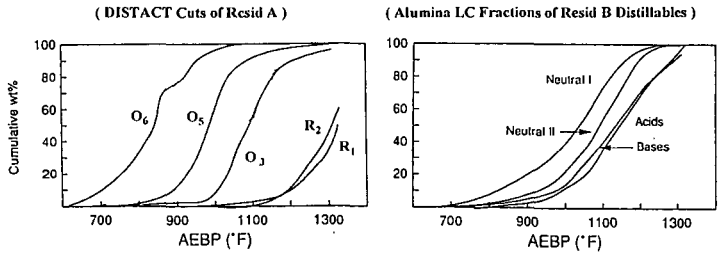

Figure 3. FITR Spectra of Alumina LC Fractions (Resid B DISTACT Distillables)

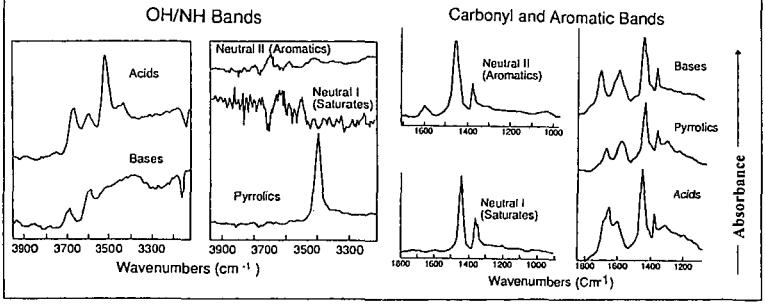

TABLE 1

RESID FEED PROPERTIES

Properties	Virgin High-S Resid A	Virgin Resid B
Wt% C	84.10	84.72
Wt% H	10.29	10.35
Wt% S	4.64	3.75
Wt% N	0.51	0.52
PPM, Ni	50	56
PPM, V	228	222
H/C	1.46	1.47
% C_A	30.0	32.6
Wt% Rams	17.1	20.0
Wt% 1000-°F	18	0
ORA (Wt%) :		
Oil	30.0	40.9
Resin	58.2	46.2
Asphaltene	9.6	12.9

TABLE 2

DISTACT FRACTION YIELD AND BOILING RANGE BY GC SIMULATED DISTILLATION (RESID A)

	Boiling Range			
Fraction Code	Wt%	IBP	T50	T90
R_1	37.4	900	1350	> 1400
R_2	6.6	1000	1320	> 1400
O_3	5.6	700	1080	1250
O_4	23.0	700	1090	1220
O_5	12.3	700	980	1090
O_6	15.0	600	840	960

IBP = Initial Boiling Point; T50 and T90 = °C when 50 and 90 wt%, respectively, of materials are distillable.

TABLE 3 ORA AND RAMSCARBON YIELDS OF DISTACT FRACTIONS (RESID A)

Fraction	Oil	Resin	Asphaltenes	Total	Rams C
	Wt%				
R_1	5.7	68.5	22.7	96.9	32.9
R_2	7.5	69.3	21.3	98.1	33.1
O_3	28.5	66.8	4.0	99.3	12.8
O_4	39.6	58.9	1.2	99.7	7.4
O_5	53.4	46.6	0.2	100.2	2.2
O_6	65.2	34.4	0.1	99.7	0.3
Weighted Sum of Above Fractions	29.7	58.4	10.5	98.6	17.2
Feed by Direct Analysis	30.0	58.2	9.6	97.8	–

TABLE 4 ELEMENTAL COMPOSITION OF DISTACT CUTS (RESID A)

Fraction	C	H	N	O (by difference)	S	Total Metals	H/C
	Wt%						
R_1	83.50	9.09	0.70	0.49	6.16	0.06	1.31
R_2	83.77	9.39	0.69	0.03	6.07	0.05	1.35
O_3	83.98	10.61	0.37	0.74	4.28	0.02	1.51
O_4	84.54	11.07	0.27	0.22	3.89	0.01	1.57
O_5	85.13	11.26	0.21	0.24	3.61	< 0.01	1.59
O_6	85.28	11.69	0.12	0.05	2.86	< 0.01	1.64

TABLE 5

ELEMENTAL COMPOSITION OF COMPOUND-TYPE FRACTIONS SEPARATED BY ION-EXCHANGE LC (Resid B; DISTACT distillate)*

	Original Sample* (Direct Measurement)	Reversed Column Sequence (Cation + Anion Resins)				Normal Column Sequence (Anion + Cation Resins) †			
		Neutrals	Acids	Bases	Calculated Sum of Fractions	Neutrals	Acids	Bases	Calculated Sum of Fractions
Wt% Yield	= 100	80.4	8.0	9.9	98.3	74.0	14.1	5.6	93.7
Wt% C	85.31	84.87	82.56	82.29	84.43	85.09	83.45	81.55	84.63
Wt% H	11.17	11.54	9.28	8.51	11.05	11.59	8.87	8.94	11.02
Wt% N	0.28	< 0.01	1.66	1.45	0.28	< 0.01	1.79	0.81	0.30
Wt% S	3.06	2.18	3.81	2.93	2.39	2.15	3.5	2.12	2.35
Wt% Total Metals	–	< 0.01	0.05	0.07	–	< 0.01	0.07	< 0.01	< 0.01
Elemental Sum : Wt%	96.8	98.8	97.3	95.3	98.2	98.9	97.1	93.4	98.3
PPM Ni	9	0.4	102	15	10	0.4	85	< 5	12
PPM V	68	0	151	153	27	0.2	430	< 2	60
H/C	1.57	1.63	1.35	1.22	1.57	1.63	1.28	1.32	1.56

*The fraction has an ORA distribution of 65.1% oil, 34.6% resin, and 0.3% asphaltenes.

† In ion exchange separation, two columns, one packed with cation resin and the others packed with anion resins, are connected in series. The basic material is trapped on the cation resins whereas the acidic material is trapped on the anion resins. The reverse sequence has the cation column in front of the anion column, whereas the reverse is true in the normal sequence.

TABLE 6

ELEMENT COMPOSITION OF COMPOUND-TYPE FRACTIONS SEPARATED BY ALUMINA LC (Resid B; DISTACT distillate)

Fraction	Normal LC Sequence (Basic + Acidic Alumina, Acid Material First)					Reversed LC Sequence (Acidic + Basic Alumina, Basic Materials First)				
	Yield	C	H	N	H/C	Yield	C	H	N	H/C
	wt %									
(Standard As-Received Alumina, 2% H_2O)										
Neutral I (Cyclohexane Elution)	35.6	86.21	13.34	(2 ppm)	1.86	56.4	85.38	12.69	(6 ppm)	1.78
Neutral II (Toluene Elution)	53.5	84.35	9.95	(128 ppm)	1.42	34.0	84.91	9.00	(270 ppm)	1.27
Total Neutrals (I and II)	88.1	85.09	11.30	(78 ppm)	1.59	89-90	85.20	11.30	(103 ppm)	1.59
Pyrrolics	3.36	83.75	8.29	1.93	1.19	2-3	–	–	2.0	–
Bases	7.52	70.87	7.25	1.51	1.01	8.26	–	–	1.65	–
Acids	2.74	82.20	9.13	1.31	1.33	1.39	–	–	1.60	–
Sum of Fractions	101.7	–	–	0.22	–	100-102	–	–	0.23	–

TABLE 7

COMPARISON OF PROPERTIES BETWEEN GAS OILS AND DISTACT DISTILLABLES

	Heavy Vac Gas Oil A	Heavy Vac Gas Oil B	Resid B DISTACT distillate
% C_A (by C-13 NMR)	21.8	24.9	25.0
Total N (ppm)	1540	2820	2700
Avg MW	400 ± 30 (by MS)	350 ± 30 (by MS)	570 (VPO)
Alumina ABN Yield (wt%, normalized)			
1. Neutrals	93	90	87
2. Pyrrolics	0.49	0.88	3.3
3. Acids	3.5	5.0	2.6
4. Bases	3.0	4.0	7.3
5. Total polars (2 + 3 + 4)	7.0	9.9	13
N Concentration in ABN Fractions (Wt% observed) :			
1. Neutrals	0.013	0.024	0.008
2. Pyrrolics	3.0	3.2	1.9
3. Acids	2.3	3.2	1.4
4. Bases	1.3	0.82	1.6

TABLE 8

CALCULATED AVERAGE MOLECULAR STRUCTURAL PARAMETERS OF RESID A DISTACT FRACTIONS

1. Calculated Structural Parameter				
Sample	# Condensed Aromatic Rings	NMR Cluster Wt	VPO MW	GPC MW
R_1	5.4	749	1380	1500
O_3	4.3	918	800	900
O_4	3.4	838	500	500
O_5	2.5	701	470	–
O_6	1.6	526	400	450

2. Experimental Data							
Sample	H/C	C_A	Ha	H_{alpha}	$H_{methylenes}$	H_{methyl}	C_{methyl}
R_1	1.35	36.9	8.0	15.3	59.4	17.3	9.7
O_3	1.51	26.8	5.5	11.2	63.3	20.0	11.6
O_4	1.57	25.0	5.7	10.3	63.7	20.3	10.1
O_5	1.59	23.4	5.3	11.2	62.0	21.5	9.4
O_6	1.64	21.4	5.4	11.6	59.5	23.5	13.5

TABLE 9 PROPERTIES OF GPC CUTS OF RESID B ASPHALTENES

GPC Cut Number	1	2	3	4	5	6	7
H/C	1.09	1.09	–	1.14	1.13	1.07	–
GPC Number Avg. MW	5160	5020	3720	2410	1330	620	–
VPO Number Avg. MW	–	6830	–	2460	1370	–	–
Yield (wt%)	9.7	14.3	20.5	17.4	17.1	12.4	8.5
Elemental Composition (wt%) :							
C	83.72	84.23	–	84.30	84.16	84.08	–
H	7.60	7.66	–	8.00	7.90	7.52	–
N	1.13	1.11	–	1.01	1.02	1.16	–
S	6.37	6.49	–	6.18	6.09	5.96	–
O (by difference)	1.2	0.5	–	0.5	0	1.3	–
Metal Concentration (ppm) :							
Fe	134	29	34	87	35	320	–
Ni	228	130	122	127	144	450	–
V	590	490	490	530	490	1230	–
Ca	101	141	44	64	50	344	–
Zn	66	34	21	43	29	82	–
Total Metals	1120	830	711	850	750	2430	–
NMR Parameters							
C_A (by C_{13}-NMR)	51	48	–	47	47	53	–
Number of condensed aromatic rings	14	7.0	–	5.7	4.4	5.1	6.4
Cluster weight	1004	654	–	595	501	490	470

TABLE 10

SUMMARY OF PROPERTIES OF HEAVY OIL COMPONENTS AS A FUNCTION OF BP

Chemical Properties	Vacuum Gas Oil (FHD-756)	1000+ Resid								
		DISTACT Distillables				DISTACT Bottom		Asphaltenes		
T90 BP (°F)	850	960	1090	1220	1250	Total	Asphaltene Removed	> 1300°F		
Ave. MW	400	400	470	500	800	1380	800	500-600	1300-2400	4000-5000
% C_A by NMR	22	21	23	25	27	37	32	53	47	48
Number of Condensed Aromatic Rings	1.5	1.6	2.5	3.4	4.3	5	5	5	4-6	7
Atomic H/C Ratio	1.7	1.64	1.59	1.57	1.51	1.31	1.4	1.07	1.13	1.09
Wt% S in fraction	–	2.9	3.6	3.9	4.3	6.2	6	6.0	6.1	6.5
Wt ppm Ni + V	< 1	1	12	80	130	490	410	1700	620	620
Wt% N in fraction	0.15	0.12	0.21	0.27	0.37	0.7	0.6	1.16	1.01	1.11
ABN Separation by Alumina LC										
Neutral Material :										
Wt% Aromatics	47	82				50-70		20-30		
Wt% Saturates	45	6				0.1		< 0.1		
Ave. MW	400	570				–		–		
Polar Materials (Acids Plus Bases) :										
Wt%	8	10-13				30-40		70-80		
Ave. MW	400	580-600				–		2000		

SPECTROSCOPIC CHARACTERIZATION OF VISBREAKING TARS

R. Scotti, M. Clericuzio, C. Pirovano

Eniricerche S.p.A., via Maritano, 26 - 20097 San Donato Milanese (MI) - Italy

Keywords: Fluorescence spectroscopy, NIR spectroscopy, Visbreaking tar.

INTRODUCTION

Visbreaking (VB) is a thermal cracking process, widely used in the refineries of Western Europe to obtain distillates (gasoil, naphtha) from a petroleum residue (feedstock). The visbroken residue (tar) is used to produce fuel oil, after addition of the appropriate amounts of cutter-stock.

Even if the highest conversion of feedstock would be desirable, the severity of the VB process is limited by the stability of the resulting VB tars. The stability index (SI) here employed is:

$SI = 1 + V_{cet}$, where V_{cet} is the maximum amount of *n*-cetane, expressed as *ml* of cetane for *g* of sample, that can be added before the flocculation of asphaltenes starts. VB tars having SI<1.1 are considered to be unstable and cannot be used in the preparation of fuel oils with the appropriate specifications.

Several papers can be found in the literature dealing with the molecular changes occuring during the VB process [1-3]. The present paper is aimed at verifying the amount of information that can be extracted from optical spectroscopies and, in particular, the possibility of directly monitoring the physico-chemical modifications caused by VB process. To this purpose a series of VB tars, produced from a single feedstock at different severities, were investigated by a number of spectroscopic techniques, viz.: NIR; UV-Vis; Fluorescence; ^1H and ^{13}C NMR; EPR.

EXPERIMENTAL

The lab visbreaking apparatus has already been described in detail elsewhere [4]. VB experiments were carried out in a continuous bench-scale unit under isothermal conditions (442 °C); the severity of the process was therefore determined only by residence times, varying from 3.5 to 9 minutes. The feedstock employed in the VB experiments was a 500°C + vacuum residue (VR) produced from a mixture of different crudes. VB tars were produced after distillation at 350 °C (350+, atmospheric pressure) or at 500 °C (500+, under vacuum). Asphaltenes were separated according to the IP 143 method. Deasphalted oil (DAO) was fractionated into saturate, aromatic and polar components via liquid chromatography according to a partially modified ASTM D 2549 method, using n-hexane, n-hexane/toluene, clorophorm/diethylether/ethanol as eluents. The feedstocks was also characterized in terms of elemental analysis (ASTM D5291), total sulphur (ASTM D1552), Conradson Carbon Residue (CCR, ASTM D5430), specific gravity (ASTM D4052) and viscosity, measured at 50 and 100 °C by a RMS 800-Rheometrics.

Near-Infrared spectra were collected on a Guided Waves model 260, UV-Vis spectra on a diode-array Hewlett-Packard 8452A spectrophotometer.

Fluorescence spectra (corrected both in excitation and in emission using the standard Perkin-Elmer procedure of the instrument) were recorded on a Perkin-Elmer MPF-66 spectrofluorimeter.

^1H and ^{13}C NMR spectra were recorded on a Bruker AMX-300, operating at 300.130 MHz for proton and 75.470 MHz for carbon. ^{13}C quantitative spectra were obtained using an Inverse Gate decoupling technique. $CDCl_3$ was used as solvent.

EPR spectra were recorded on a Bruker ESP 300 E operating at X-band (9.5 GHz). Strong pitch (3×10^{15} spin/cm ± 15%) was used as quantitative reference.

RESULTS AND DISCUSSION

The physico-chemical properties of feedstock, VB tars, and the fractions obtained from 350+ tars are reported in tabs. 1, 2 and 3, respectively.

The molar ratio of aromatic carbon (F_a) and the main lengths of side chains (*n*) were calculated by NMR analysis, according to Dickinson [5,6].

A general increase of F_a and of asphaltene content with increasing VB severity is evident (tabs. 2-3). From the analysis of tar fractions (tab. 3) it turns out that the increase in F_a and the decrease in *n* mainly occurs in asphaltenes. This is in agreement with previous studies of the molecular effects of VB [2]: at relatively low severity asphaltene dealkylation occurs via breaking of aliphatic side chains, dehydrogenation and ring-opening of naphthenic moieties occurs, leading to more aromatic structures.

The relative amount of radicals (from EPR) increases with VB severity (tab. 2). *g* factors are not significantly affected by thermal treatment within each series. These radicals are associated with non-localized π systems stabilized by resonance over polyaromatic centers [7]. The slight difference between 350+ and 500+ tars ($g_{350+} = 2.0026 \pm 0.0001$; $g_{500+} = 2.0029 \pm 0.0001$) could be assigned to the different content in heteroatoms of the two series.

The electronic absorption spectrum of a typical VB tar shows a broad and unstructured band spanning the UV and visible regions of the spectrum, with absorption maxima around 260-270 nm (data not shown). For each sample the extinction coefficient $\varepsilon_w = A/cl$ (c expressed as w/v) was calculated as the slope of the straight line fitting the absorbances at 0.1, 0.05, 0.025, 0.0125 mg/ml in CCl_4. The use of w/v concentrations, rather than molar, is justified by the critical values of average molecular weights in heavy petroleum derivatives, owing to association phenomena [8]. ε_w, obtained at 280 and 320 nm, increases with increasing VB residence time within each of the two series, 350+ and 500+ (fig.1, only 500+ shown).This is in agreement with the increase of aromatic chromophores.

Fluorescence spectra were recorded both in THF and CCl_4 solutions (0.0125 mg/ml).

The excitation spectra show, in both solvents, two main maxima, centered at about 330 and 390 nm (data not shown). Emission spectra were recorded with excitation centered at 394 nm: in THF a maximum in emission is observed at 453 nm (fig. 2, top). In fig. 3 emission intensities at 453 nm (in THF) are plotted for the eight samples: they show an increase with increasing VB severity in both series, which is related to the increase in aromaticity.

Spectra recorded in CCl_4 are markedly different (fig. 2, bottom). The overall intensity is approximately 4-fold smaller in CCl_4 than in THF, and maxima in emission are red-shifted about 25 nm . This clearly shows that in CCl_4 VB tars are much more aggregated: in fact, formation of molecular complexes is expected to lead to fluorescence quenching and red-shifted emissions. Molecular association is a well-known phenomenon in the chemistry of asphaltenes, even at very low concentrations [8-9]. Our explanation is that the polar THF is more effective in disrupting the aggregation state of VB tars.

An interesting phenomenon is observed when fluorescence spectra are recorded in CCl_4. Immediately after the solution is prepared, the intensity of the spectrum decreases gradually with time until a plateau is reached, generally within one hour (fig. 4). The phenomenon is partially reversible after stirring the solution, and is much less evident in THF. Slow diffusion phenomena in solution, or a simple sedimentation effect might be responsible for this. NMR-Imaging studies are in progress to have more information.

An analogous phenomenon is observed in the NIR spectrum. The freshly prepared solution in CCl_4 (10 mg/ml) shows an increase of baseline with time (fig. 5), probably due to Rayleigh scattering. It is likely that rather large particles are formed.

To avoid changes in baseline, NIR spectra were recorded under stirring, using optical fibers.

The spectra show a broad continuum with increasing absorption at higher energy, which is attributed to electronic transitions of large aromatic ring systems [10], and a second region at lower energies, which is attributed to vibrational overtones and combination bands of predominantly saturated hydrocarbons [10]. The ratio between I_{1200} (electronic transitions) and I_{2300} (C-H stretch plus bend) increases with severity (fig. 6).

CONCLUSIONS

1) Our data suggest that it is possible to monitor the severity of VB by means of optical spectroscopies (potentially also on-line). In fact UV and NIR absorption intensities, as well as fluorescence emission intensities, are all sensitive to the molecular changes occurring during the VB process.

2) The solvent has a marked effect on the solution structure of VB tars; in particular in CCl_4, as compared to THF:

- a) solute molecules are in a higher aggregation state;
- b) the equilibrium structure is reached rather slowly, and is at least partially reversible by stirring;
- c) rather large particles are probably formed.

Care should therefore be taken in analytical applications when using CCl_4 as solvent, otherwise the reproducibility of measures will be strongly affected.

REFERENCES

1) Singh I.D., Kothiyal V., Kapoor M.P., Ramaswamy V. and Aloopwan M.K.S. - *Fuel* **72**, 751, 1993.

2) Tatsumi T. J., Nakasuga A., Yoshida H., Suhara S., and Tominaga H. - *J. Japan Pet. Inst.* **28**, 318, 1985.

3) T. Zerlia and G. Pinelli - *Fuel* **72**, 1109, 1993.

4) Del Bianco A., Garuti G., Pirovano C. and Russo R. - *ACS Preprints, Division of Petroleum Chemistry* 408, 1994.

5) Dickinson E.M. - *Fuel* **59**, 290, 1980.

6) Calemma V., Iwanski P., Nali M., Scotti R. and Montanari L. - *Energy Fuels* **9**, 225, 1995.

7) Yen T.F., Erdman J.G. and Saraceno A.J. - *Fuel* **34**, 694, 1962.

8) Speight J.G., Wernick D.L, Gould K.A., Overfield R.E., Rao B.M.L. and Savage D.W. - *Revue de l'Institut Francais du Petrole* **40**, 51, 1985.

9) Sheu E.Y., De Tar M.M., Storm D.A. and De Canio, S.J. - *Fuel* **71**, 299, 1992.

10) Mullins O.C. - *Anal. Chem.* **62**, 508, 1990.

Table 1: Physico-chemical properties of feedstock

Specific gravity 15°C	0.9896	CCR wt%		14.3	*Dist. fractions*	°C
Viscosity 50 °C [cSt]	30,800	SI		6.3		
Viscosity 100°C [cSt]	660				Initial Boiling Point	306
H wt%	10.9				5 wt%	434
C wt%	86.3	C7-Asphaltenes wt%		5.8	10 wt%	478
N wt%	0.8	*DAO composition*:			30 wt%	563
S wt%	1.4	Saturates	wt%	25.4	50 wt%	618
V [ppm]	79	Aromatics	wt%	46.2	70 wt%	680
Ni [ppm]	58	Polars	wt%	22.6	90 wt%	756

Table 2: Physico-chemical properties of 350°C+ and 500°C+ VB-tars

Time [min]	SI	Sp.Gr.	V. 50 [cSt]	V. 100 [cSt]	H/C	N %wt	S %wt	Coke %wt	F_{ar}	N_r x10^{16}
350 °C +										
3.5	1.8	1.000	26,700	400	1.42	1.1	1.3	0.03	0.26	5.5
5	1.5	1.004	30,100	450	1.40	1.1	1.3	0.04	0.29	6.8
7	1.2	1.006	30,200	440	1.36	1.2	1.3	0.22	0.30	8.0
9	1.1	1.008	31,200	470	1.36	1.2	1.3	0.40	0.32	8.5
500 °C +										
3.5	1.9	1.011	259,750	1,600	1.35	1.5	1.3	0.04	-	6.5
5	1.6	1.013	429,700	2,250	1.33	1.5	1.3	0.06	-	6.7
7	1.3	1.025	1,155,400	3,750	1.30	1.4	1.3	0.28	-	10.8
9	1.2	1.032	1,862,500	6,050	1.27	1.4	1.4	0.53	-	12.9

Time: residence time; SI: stability index; Sp.Gr: specific gravity at 15°C; V.50, V.100: viscosity at 50 and 100°C; F_{ar}: molar ratio of aromatic C by NMR; N_r: spin density [spin/g] by ESR.

Table 3: Composition of VB-tars 350 °C +

Time [min]	SI	Satur.	Aromatics			Polars			Asphaltenes		
		wt %	wt%	F_{ar}	*n*	wt%	F_{ar}	*n*	wt%	F_{ar}	*n*
3.5	1.8	25.4	41.5	-	-	22.2	-	-	10.9	0.56	-
5	1.5	25.7	40.3	0.35	6.1	22.4	0.42	5.3	11.6	0.62	4.7
7	1.2	24.2	36.6	0.33	5.9	26.4	0.45	5.5	12.8	0.67	4.2
9	1.1	24.0	36.9	0.34	6.2	25.5	0.44	5.3	13.6	0.68	3.7

Time: residence time; SI: stability index; F_{ar}: molar ratio of aromatic C by NMR; *n*: main length of side chains.

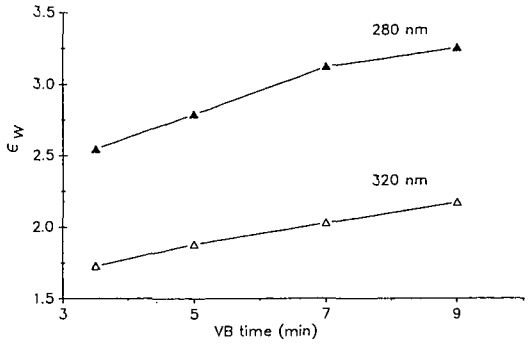

Fig. 1 - Extinction coefficients of 500+ tars (per gram) vs. VB severity.

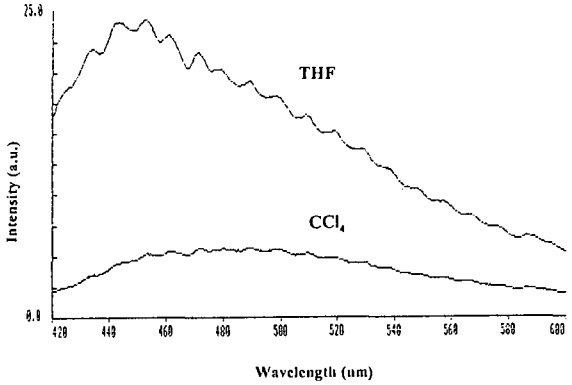

Fig. 2 - Fluorescence emission spectra of a selected VB tar. Excitation: 394 nm.

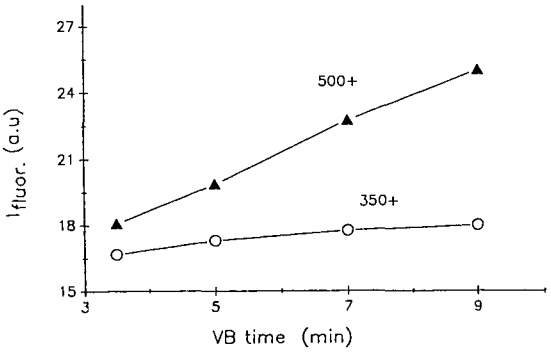

Fig. 3 - Intensity of fluorescence emission at 500 nm (exc. 394 nm) vs. VB severity. Solvent: THF.

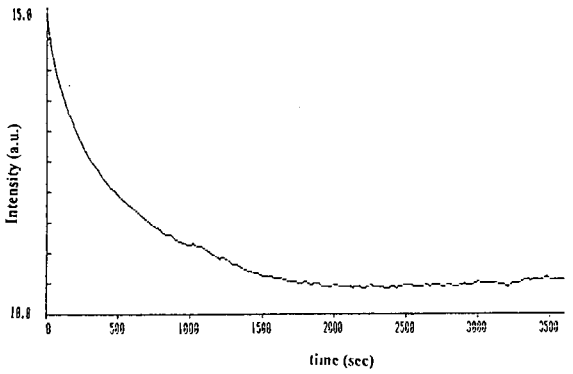

Fig. 4 - Time evolution of the intensity of fluorescence emission at 500 nm (exc. 394 nm). The solution is prepared by 1:100 dilution of an initial sol. in CCl_4.

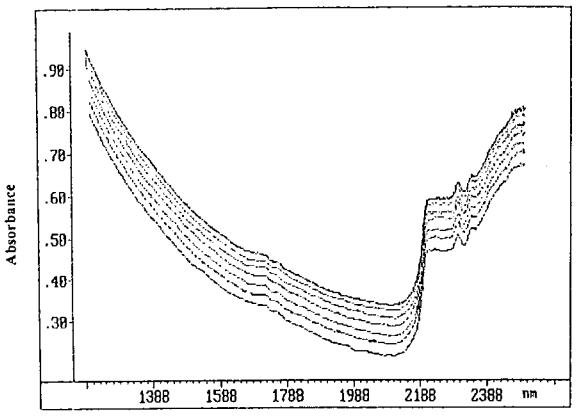

Fig. 5 - NIR spectra of a selected VB tar in CCl_4. Spectra were recorded every 8 minutes from 0 (bottom trace) to 48 min. (top trace).

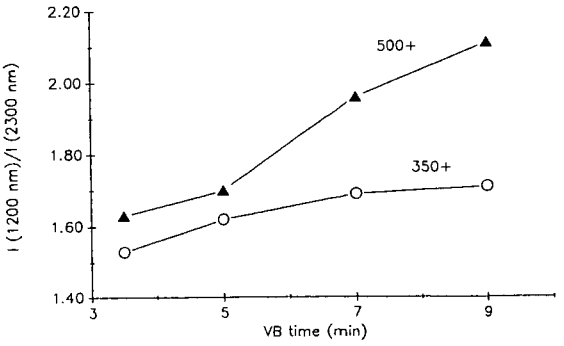

Fig. 6 - NIR intensity ratio between the bands at 1200 and 2300 nm vs. VB severity. Solvent: CCl_4.

THE STUDY OF COAL-DERIVED PYRITE USING ATMOSPHERIC PRESSURE TEMPERATURE PROGRAMMED REDUCTION (AP-TPR) AND TGA

Inge I. Maes, Jan Yperman, Dirk V. Franco, Jules Mullens and Lucien C. Van Poucke
Laboratory of Inorganic and Physical Chemistry
Limburgs Universitair Centrum
B-3590 Diepenbeek, Belgium

Grazyna Gryglewicz and Piotr Wilk
Institute of Chemistry and Technology of Petroleum and Coal,
Technical University of Wroclaw
50-344 Wroclaw, Poland

Keywords: pyrite, coal, AP-TPR

ABSTRACT

It is possible with AP-TPR to determine qualitatively as well as quantitatively the different organic sulfur forms in coal. The presence of pyrite might disturb an accurate sulfur determination by AP-TPR as is the case in other thermal techniques. Therefore it is important to have an insight into the behaviour of pyrite under the reducing experimental conditions. This study presents an explanation for the behaviour of pyrite subjected to a linear temperature increase up to 1000°C in an inert (TGA) as well as reducing (AP-TPR) atmosphere. Two pyrite samples were extracted from coal of the Halemba and Jastrzebie mine. As an example of the consequences of the presence of pyrite in coal, a discussion of the AP-TPR kinetogram of the Siersza coal of high pyritic sulfur content is included.

INTRODUCTION

Pyritic and organic sulfur are the two major sulfur forms in coal. Pyritic sulfur occurs mainly as iron sulfide, FeS_2. There are two naturally occurring forms of FeS_2, pyrite and marcasite of which pyrite is a major contributor to the total sulfur content of coals.

The AP-TPR technique is used to determine the organic sulfur functionalities in coal-derived materials. It is recommended to record pyrite free samples in order to overcome interference and to have an accurate view of the organic sulfur functionalities present in the raw coal. In the past, extraction with diluted nitric acid was commonly used to obtain pyrite free coal samples. Nevertheless, using this method, a complete removal is not always achieved when the pyrite is highly disseminated and present in particles of < 5 μm [1]. In addition, it has been demonstrated that the nitric acid treatment may have an influence on the coal structure and consequently some other organic sulfur functionalities might be changed [2]. More and more this treatment has been replaced by the lithium aluminium hydride procedure [3,4]. At the moment, $LiAlH_4$ is thought to cause selective desulfurization of the pyrite, although there is still a possibility that cleavage of di- and polysulfide linkages can occur. Moreover, a reduction of other organic sulfur compounds is not excluded.

The AP-TPR technique proved to be very promising for monitoring the consequences of different types of selective chemical treatments on coal [5]. In those cases, the ability in distinguishing pyritic sulfur from organically-bound sulfur is very desirable. The AP-TPR analysis has appeared to be useful in following the changes in the organic sulfur functionalities induced by heat treatment of coal as well [6].

The purpose of this paper is to present results of our study on the conversion of coal pyrite during the AP-TPR experiment. For this purpose coal pyrite was chosen to avoid a discrepancy which could be arised from the use of mineral pyrite. Moreover, coal-derived pyrite can be enriched in trace elements which can affect on its reactivity [7].

EXPERIMENTAL

a) Samples

The two pyrite samples studied in this paper are extracted from the Halemba and Jastrzebie coal. The pyrite concentrates are firstly cleaned by means of gravity separation and consequently by magnetic separation. The obtained coal-derived pyrites show a high degree of purity, which is determined by X-ray diffraction analysis.

The subbituminous coal sample originates from the Siersza mine (Poland) and is chosen for its high pyritic sulfur content of 4.17 wt%.

b) Used Techniques

Powder X-ray diffraction (XRD) with Mo K_α radiation was used for identification and purity control of the extracted pyrite samples.

Atmospheric Pressure-Temperature Programmed Reduction (AP-TPR) experiments are recorded

according to the procedure mentioned in previous papers [5,8,9]. A further optimization is performed by using a MKS flow controller (Model 2476). This set-up guarantees a flow of 50 cm^3 min^{-1} H_2-gas through the reactor during the entire AP-TPR experiment. All experiments are recorded with a heating rate of 5 °C min^{-1} and without the use of a reducing mixture. In this study the experimental AP-TPR data are smoothed by a more narrow 11 point Savitsky-Golay-Gorry filtering algoritm [10,11]. This change results in sharper signals and more detailed AP-TPR profiles. All samples were grounded before analysis to a particle size of less than 147 µm.
The Thermographical Analysis (TGA) experiments are performed with a TA Instruments (formerly Du Pont) Model 2000-951 apparatus. The samples (20-30 mg) are heated up to 1000°C at a heating rate of 5 °C min^{-1} in a pure argon gas stream of 50 cm^3 min^{-1}. The TGA data manipulation was performed using a 13 point smoothing filter of the Savitsky-Golay procedure.

RESULTS AND DISCUSSION

In Figure 1 the AP-TPR kinetogram of the Halemba pyrite sample is presented. The profile consists of two well separated maxima. The first temperature maximum is found at approximately 570 °C and the second at 690 °C. From this point it is clear that the pyrite (FeS_2) is not reduced in one step, but in two. The difference in shape between the two peaks also suggests a difference in reducing conditions. For the pyrite extracted from the Jastrzebie coal, the AP-TPR profile is comparable, as can be seen in Figure 1. In this kinetogram the maximum reducing temperatures are at 575 °C and 675 °C. Here the difference between the two reducing step mechanisms is even more obvious. Relatively, the first reducing peak has gained in intensity and the second peak has broadened even more in comparison to the Halemba pyrite curve.
In order to understand better the reason for this phenomenon, a TGA experiment is carried out under an argon atmosphere on the Halemba pyrite sample. The TGA plot is shown in Figure 2. Undoubtly, there is only one sharp peak at 600 °C visible. Calculations have proven that the mass decrease of 27.73 % during the experiment corresponds with a loss of 0.19 mmol sulfur for an amount of 0.18 mmol pyrite which was originally present in the examined sample. Taking into account the experimental error, this calculation illustrates that indeed only one sulfur is liberated for each FeS_2 molecule. Consequently, the signal in Figure 2 has to result from the thermal decomposition of pyrite into troilite (FeS) and elemental sulfur. The corresponding chemical reaction can be written as follows:

$$FeS_2\ (s) \xrightarrow{T\nearrow,\ Ar} FeS\ (s) + S\ (g)$$

In an inert atmosphere this reaction takes place at approximately 600 °C. The first Halemba pyrite maximum reduction temperature of the AP-TPR kinetogram in Figure 1 is found at 570 °C. From non-isothermal kinetic studies it is known that the removal of sulfur from pyrite under hydrogen is more favorable than under an inert atmosphere [12,13]. This can explain the 30 °C temperature difference between the thermal decomposition under argon and the AP-TPR reduction under H_2 atmosphere. Consequently, this means that probably the first reduction step of pyrite takes place after thermal liberation of the elemental sulfur. In the gaseous phase this sulfur will then react with the H_2-gas forming H_2S and is as such detected. This gas phase reaction proceeds rapidly, which is translated in a corresponding sharp, high peak in the AP-TPR kinetogram. The same profile characteristics can be seen in the Jastrzebie pyrite kinetogram in Figure 1. It also seems that the first reduction peak of both pyrite samples is at almost the same temperature.
The TGA experiment shows that the troilite does not decompose thermally at temperatures up to 1000 °C. In consequence, the second reduction peak in both pyrite AP-TPR kinetograms can thus be attributed to the direct reduction of FeS. In contrast with the first reduction peak, this reaction occurs between the H_2-gas and FeS in the solid phase according to:

$$FeS\ (s) + H_2\ (g) \xrightarrow{T\nearrow} Fe\ (s) + H_2S\ (g)$$

This solid phase mechanism causes the broadening of the second pyrite reduction peak. The H_2-gas reacts with the surface of the solid troilite which causes a slower reduction and consequently a broader reduction peak in comparison to the former gas-gas reaction. Consequently, the second reduction peak of the Halemba and Jastrzebie kinetograms are not so similar as the first. The peaks do not have the same maximum reduction temperatures, nor the same shape. Assumed is that this reduction in the solid phase is strongly dependent on the morphology. Minor physical differences of the troilite surface can affect the course of the reduction process. In consequence, the AP-TPR kinetogram can look a little different for each experiment if the troilite particles originating from the thermal decomposition of pyrite have a different particle size or different surface characteristics. Because of the nature of the solid-gas reduction, the peaks exhibit a broad contour. Depending on the relative concentrations, this band can usually be seen as a background on which possible reducing peaks of other sulfur groups present in for instance coal are superimposed.

As an example, the kinetograms of two AP-TPR experiments of the same Siersza coal sample are shown in Figure 3 and 4. Both profiles exhibit one sharp, intense peak that can easily be recognised as the first reduction peak of pyrite: the reduction of elemental sulfur in the gaseous phase. The Siersza coal was chosen for its high pyrite content (4.17 wt%) which explains the rather stupendous appearance of the first pyrite reduction peak in the kinetogram. As predicted, the second reduction peak is not so reproducible. This does not disturb the organic sulfur reduction peak characterization at 750-760 °C. The coal sample kinetograms prove that a qualitative analysis can be possible, even though the troilite reduction peaks are not exactly reproducible and the reduction conditions are hard to control. Also, it can be stressed upon that these experiments also suggest that most of the elemental sulfur, thermally liberated from pyrite, is reduced by the H_2-gas under AP-TPR conditions. However, still a smaller amount of elemental sulfur could have reacted with the organic matrix to form organic sulfur groups which will be reduced at higher temperatures. The extend of this taking place is not known at this point, but will be the subject of further investigations. If the objective of the AP-TPR analysis is to study the organic sulfur distribution in coal, than it may be opportune to remove the pyrite in advance. In this way, no elemental sulfur can react with the organic matrix and the troilite reduction peak can not interfere with the organic sulfur reduction peaks.

CONCLUSIONS

In this study the mechanism of pyrite reduction is explained. It is demonstrated that in the first reduction step sulfur is thermally liberated from FeS_2. In the AP-TPR experiment this S-gas is then reduced into H_2S at approximately 570 °C. Around 680 °C, the solid FeS is transformed under a reducing atmosphere into Fe and H_2S.

The kinetogram of a pyrite sample exhibits at first a sharp reduction peak followed by a broader and less intense reduction band. Because of the characteristic reduction peak at approximately 570 °C, pyrite can easily be recognised in the AP-TPR kinetogram of most coal samples. The troilite reduction peak at approximately 680 °C is in most cases too broad to be of great disturbance for the AP-TPR analysis of coal. The organic sulfur group reduction peaks will only be superimposed upon the FeS band.

ACKNOWLEDGEMENTS

The authors would like to thank Mrs. M. Vanhamel and Mr. J. Kaelen for their technical assistance with the AP-TPR experiments. I. I. Maes is supported by a specialisation grant from the "Vlaams Instituut voor de bevordering van het Wetenschappelijk-Technologisch onderzoek in de industrie".

REFERENCES

1. Davidson, R. *Organic Sulphur in Coal*, IEA Coal Research, London, 1993
2. Calkins, W. H. *Fuel* **1994**, 73, 475
3. Gryglewicz, G.; Jasienko, S. *Fuel* **1992**, 71, 1225
4. Lawlor, D. L.; Fester, J. I.; Robinson, W. E. *Fuel* **1963**, 42, 239
5. Yperman, J.; Franco, D. V.; Mullens, J.; Reggers, G.; D'Olieslaeger, M.; Van Poucke, L. C.; Marinov, S. P. *Nato ASI, "Composition, Geochemistry and Conversion of Oil Shales, Ackay", Series C, Vol. 455*, Kluwer, Dordrecht, The Netherlands,1995, pp 449
6. Yperman, J.; Franco, D.; Mullens, J.; Van Poucke, L.C.; Gryglewicz, G.; Jasienko, S. *Fuel* (in press)
7. Spears, D. A.; Martinez Tarazona, M. R.; Lee, S. *Fuel* **1994**, 73,1051
8. Mullens, J.; Yperman, J.; Carleer, R.; Franco, D. V.; Van Poucke, L. C.; Van Der Biest, J. *Applied Clay Science* **1993**, 8, 91
9. Ismail, K.; Mitchell, S. C.; Brown, S. D.; Snape, C. E.; Buchanan III, A. C.; Britt, P. F.; Franco, D. V.; Maes, I. I.; Yperman, J. *Energy & Fuels* **1995**, accepted
10. Savitsky, A.; Golay, M. J. E. *Analytical Chemistry* **1964**, 36, 1627
11. Gorry, P. *Analytical Chemistry* **1990**, 62, 570
12. Tsai,C.S. *Fundamentals of Coal Beneficiation and Utilization,Coal Science and Technology 2*, Elsevier, Amsterdam, 1982, pp 235
13. Sugawara,T.; Sugawara,K.; Ohashi,H. *Fuel* **1988**,67,1263

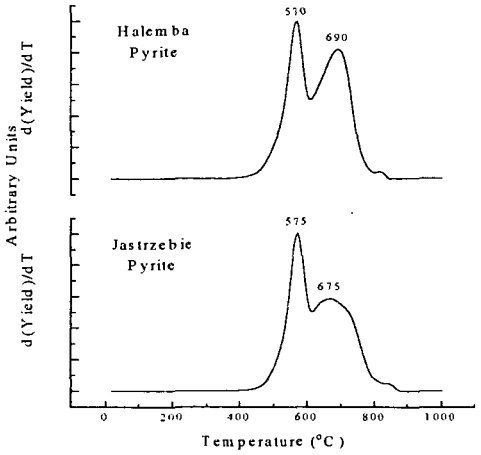

Figure 1 : AP-TPR kinetograms of the Halemba and Jastrzebie pyrite sample

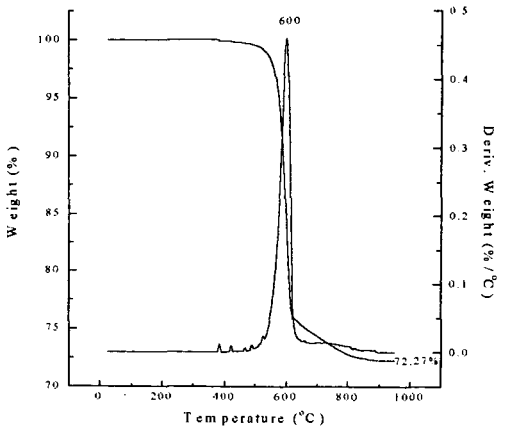

Figure 2 : TGA spectrum of the Halemba pyrite sample

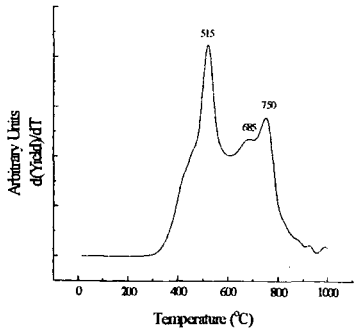

Figure 3 : AP-TPR kinetogram of the Siersza coal sample - I

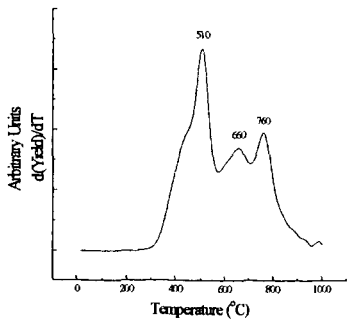

Figure 4 : AP-TPR kinetogram of the Siersza coal sample - II